University of Louisville

ThinkIR: The University of Louisville's Institutional Repository

Electronic Theses and Dissertations

5-2008

Variational methods for shape and image registrations.

Rachid Fahmi 1971-
University of Louisville

Follow this and additional works at: https://ir.library.louisville.edu/etd

VARIATIONAL METHODS FOR SHAPE AND IMAGE REGISTRATIONS

By

Rachid Fahmi
M.Sc. 1994, Applied Maths, University Of Metz, France.
Ph.D., 1998, Applied Maths/Mechanical Engineering, University Of Metz, France

A Dissertation
Submitted to the Faculty of the
Graduate School of the University of Louisville
in Partial Fulfillment of the Requirements
for the Degree of

Doctor of Philosophy

Department of Electrical and Computer Engineering
University of Louisville
Louisville, Kentucky

May 2008

VARIATIONAL METHODS FOR SHAPE AND IMAGE REGISTRATIONS

By

Rachid Fahmi
M.Sc. 1994, Applied Maths, University of Metz, France
Ph.D., 1998, Applied Maths/Mechanical Engineering, University of Metz, France

A Dissertation Approved on

    May 6, 2008

by the Following Reading and Examination Committee:

Aly A. Farag, Ph.D., Dissertation Director

Amir Amini, Ph.D.,

Mohamed N. Ahmed, Ph.D.,

Manuel F. Casanova, Ph.D.,

Tamer Inanc, Ph.D.,

Thomas Riedel, Ph.D.,

ii

DEDICATION

To the greatest persons in my life, my mother and my beautiful wife Nadia.

Thank you for your endless love, support, and sacrifices.

I love you more than anything else in this world.

ACKNOWLEDGMENTS

First of all, my deepest thanks are due to Almighty God, the merciful, the compassionate for all the blessings bestowed upon me.

I would like to express my deepest gratitude to my advisor, Prof. Aly A. Farag, for giving me the opportunity to be a member in his research group and for his support over the course of this work. He provided a very rich working environment with many opportunities to develop new ideas, work in promising applications, get experience in diverse areas, and meet well-known people in the field. I am indebted to his support and help.

I would like to thank Prof. Amir Amini, Dr. Tamer Inanc, Prof. Thomas Riedel, Prof. Manuel Casanova, and Dr. Mohamed N. Ahmed for agreeing to be on my dissertation committee and for the useful consultation and the fruitful discussions.

I would like to thank all the members of Computer Vision and Image Processing Laboratory at University of Louisville, both past and present. Special thanks to Mr. Mike Miller for his continuous dedication to help and for his support in hard times. Also, I would like to thank Mr. Chuck Sites for his valuable technical help during all these years.

Very special thanks to my family for their unwavering encouragement and support, and their unconditional love without which this dissertation and research would not have been possible. My deepest gratitude to my parents, brothers and sisters. Finally, words cannot describe how I am indebted to my mother and my wife for their pain, suffering and sacrifices made during the journey of this study. Special thanks are to my beautiful wife Nadia for loving me from all her heart and taking care of me, and for sharing with me the tough moments. This dissertation is dedicated to our first to be baby Incha Allah (God willing).

ABSTRACT

Variational methods for shape and image registrations

Rachid Fahmi

April 30, 2008

Estimating and analysis of deformation, either rigid or non-rigid, is an active area of research in various medical imaging and computer vision applications. Its importance stems from the inherent inter- and intra-variability in biological and biomedical object shapes and from the dynamic nature of the scenes usually dealt with in computer vision research. For instance, quantifying the growth of a tumor, recognizing a person's face, tracking a facial expression, or retrieving an object inside a data base require the estimation of some sort of motion or deformation undergone by the object of interest. To solve these problems, and other similar problems, registration comes into play. This is the process of bringing into correspondences two or more data sets. Depending on the application at hand, these data sets can be for instance gray scale/color images or objects' outlines. In the latter case, one talks about shape registration while in the former case, one talks about image/volume registration. In some situations, the combinations of different types of data can be used complementarily to establish point correspondences.

One of most important image analysis tools that greatly benefits from the process of registration, and which will be addressed in this dissertation, is the image segmentation. This process consists of localizing objects in images. Several challenges are encountered in image segmentation, including noise, gray scale inhomogeneities, and occlusions. To cope with such issues, the shape information is often incorporated as a statistical model into the segmentation process. Building such statistical models requires a good and accurate

shape alignment approach. In addition, segmenting anatomical structures can be accurately solved through the registration of the input data set with a predefined anatomical atlas.

Variational approaches for shape/image registration and segmentation have received huge interest in the past few years. Unlike traditional discrete approaches, the variational methods are based on continuous modelling of the input data through the use of Partial Differential Equations (*PDE*). This brings into benefit the extensive literature on theory and numerical methods proposed to solve *PDE*s.

This dissertation addresses the registration problem from a variational point of view, with more focus on shape registration.

First, a novel variational framework for global-to-local shape registration is proposed. The input shapes are implicitly represented through their signed distance maps. A new Sum-of-Squared-Differences (*SSD*) criterion which measures the disparity between the implicit representations of the input shapes, is introduced to recover the global alignment parameters. This new criteria has the advantages over some existing ones in accurately handling scale variations. In addition, the proposed alignment model is less expensive computationally. Complementary to the global registration field, the local deformation field is explicitly established between the two globally aligned shapes, by minimizing a new energy functional. This functional incrementally and simultaneously updates the displacement field while keeping the corresponding implicit representation of the globally warped source shape as close to a signed distance function as possible. This is done under some regularization constraints that enforce the smoothness of the recovered deformations. The overall process leads to a set of coupled set of equations that are simultaneously solved through a gradient descent scheme. Several applications, where the developed tools play a major role, are addressed throughout this dissertation. For instance, some insight is given as to how one can solve the challenging problem of three dimensional face recognition in the presence of facial expressions. Statistical modelling of shapes will be presented as a way of benefiting from the proposed shape registration framework.

Second, this dissertation will visit the shape-based segmentation problem. The piece-wise constant Chan and Vese segmentation models [1] are chosen as the underly-

ing segmentation models and it will be shown how the proposed global shape registration technique can serve in enhancing the segmentation results of an input image when some prior knowledge of shapes is integrated in the underlying segmentation framework. The resulting paradigm allows the recovery of a segmentation map that is in accordance with the shape prior model as well as an affine transformation between this map and the model. Furthermore, it can deal with noisy, occluded and missing or corrupted data. The classical way of solving the shape-based segmentation problems within a level set framework is by directly solving the underlying Euler-Lagrange equations using a gradient descent scheme. This is very computationally expensive given the non-linear parabolic nature of the corresponding *PDE*'s. To overcome these difficulties, a fast algorithm is designed and implemented to solve both the two-phase and the multi-phase shape-based segmentation problem. This algorithm exploits the fact that only the sign of the level set function, not its value, is needed to evolve the segmenting interface. The integration of multiple selective shape priors and the segmentation into multiple regions has never been addressed before.

Third, a new image/volume non-rigid registration approach based on scale space and level set theories, will be introduced. This contribution is the fruit of a collaborative effort with two other members of the *CVIP* Lab. New feature descriptors are built as voxel signatures using scale space theory. These descriptors are used to capture the global motion of the imaged object. Local deformations are modelled through an evolution process of equi-spaced closed curves/surfaces (iso-contours/surfaces) which are generated using fast marching level sets and are matched based on a cross correlation measure between neighboring voxels.

A novel Finite Element (*FE*)-based approach is developed to validate the performance of the proposed image registration techniques. Both two and three dimensional tissue deformations are simulated using the *FE* method. The registration accuracy with respect to the *FE* simulations is assessed by co-registering the deformed images with the original ones and comparing the recovered displacement field with the bio-mechanically simulated ones.

TABLE OF CONTENTS

LIST OF TABLES

LIST OF FIGURES

CHAPTER I

INTRODUCTION

The problem of establishing point correspondences between two or more data sets is known as the process of registration. Depending on the application at hand, this data can be either gray scale/color images or outlines of objects of interest occupying a certain image domain. In the latter case, the alignment process is referred to as shape registration while in the former case, one talks about image/volume registration. In both cases, the registration process is a very challenging problem with direct applications in various fields, including computer vision, data fusion, medical imaging, motion tracking, etc. These examples of applications are all based upon the ability to automatically map points between the respective domains of the images. Reconstructing a 3D scene from two or more views or calibrating a camera are other applications that require the ability to establish point correspondences between two images.

Numerous approaches have been developed to solve registration problems. Each of these approaches has its strengths and limitations. For shape registration, the existing techniques can be categorized based on three main aspects: the selected model to represent the shapes, the transformation model, and the mathematical framework chosen to recover the registration parameters. In the case of registering images, the developed approaches are categorized into two main families: feature-based and area-based techniques. The feature-based methods rely on extracting and matching salient anatomical structures from images (closed-boundary regions, edges, contours, line intersections, corners, etc.). The area-based methods, also known as correlation-like methods, are used directly to match image intensities without any attempt to detect distinctive objects. This chapter presents an overview of the the main ingredients of both shape and image registrations starting with a variational formulation of the matching problem.

A.   A Generic Registration Problem

The registration problem in general can be formulated as follows. Given are two images referred to as *template*, T, and *reference*, R, of the same object acquired using the same or different sensors (possibly from a sequence). The task of image registration is to find *homologuous* (corresponding) points in both images. Assume that in continuous variables, the two images can be represented by two compactly supported functions, $R : \Omega \subseteq \mathbb{R}^n \to \mathbb{R}^p$ and $T : \Omega \to \mathbb{R}^p$, with $n = 2, 3$ and $p \leq n$. This means that the functions R and T assign to each point $\mathbf{x}$, in a domain Ω, its intensities $T(\mathbf{x})$ and $R(\mathbf{x})$ (note that here, it is meant by intensities any image representing feature such as gray scale values, the edge map, a distance transform with respect to a locus of points, etc.). The image domain Ω is supposed to be a bounded region of $\mathbb{R}^n$ whose boundary, $\partial\Omega$, fulfills some regularity constraints. The goal of matching the images, T and R, is to find a displacement filed $\mathbf{u} = (u_1, \cdots, u_n)^T : \Omega \to \mathbb{R}^n$ such that the transformed template $T \circ g(\mathbf{u})$ matches the reference R, where the deformation g is given by

$$g(\mathbf{u})(.) \quad : \quad \mathbb{R}^n \to \mathbb{R}^n \tag{1}$$

$$\mathbf{x} \mapsto g(\mathbf{u})(\mathbf{x}) \doteq \mathbf{x} + \mathbf{u}(\mathbf{x}).$$

Generally, the displacement field $\mathbf{u}$ is searched for in a space of admissible functions, $\mathcal{X}$, whose definition depends on how much is known about the relation between the two images and what regularity constraints can be imposed on the unknown $\mathbf{u}$. For instance, for some camera calibration problems, it is known that corresponding points should belong to epipolar lines, and hence the mapping transformation is a homography.

The matching score is usually measured by a disparity functional $\mathcal{D}(R, T, \mathbf{u})$ which is defined in terms of statistical measures on the intensities of the images R and $T \circ g(\mathbf{u})$. Different measures, depending on the nature of the data, have been proposed to map corresponding points to each other. For example, if the intensities of the given images are comparable (i.e., the images have been acquired by the same sensors), then a reasonable way of matching the two images is by finding a geometric transformation which minimizes

the Sum of Squared Differences (*SSD*)

$$\mathcal{D}^{SSD}(R, T, \mathbf{u}) = \int_{\Omega} (T(\mathbf{x} + \mathbf{u}(\mathbf{x})) - R(\mathbf{x}))^2 d\mathbf{x}. \tag{2}$$

However, if the two images have different intensity maps, the so-called *multi-modal registration*, this simple way of measuring their similarity is no longer considered. Consider for example, the tracking problem under different illumination conditions, or the problem of registering different medical image modalities (see Fig. 1), etc. In such a case, more general measures have to be considered. This is the role of statistical and information-theoretic-based similarity measures, such as the maximization of the Mutual Information (*MI*) [10, 11],

$$\mathcal{D}^{MI}(R, T, \mathbf{u}) = \mathcal{H}(R) + \mathcal{H}(T \circ g(\mathbf{u})) - \mathcal{H}(R, T \circ g(\mathbf{u})), \tag{3}$$

where, $g(\mathbf{u})$ is given by Eq. (1), $\mathcal{H}(I)$ is the Shannon entropy of the image I, computed on the probability distribution of the grey values, $p^I(\cdot)$, and $\mathcal{H}(I_1, I_2)$ is the joint entropy between I_1 and I_2. Maximizing $\mathcal{D}^{MI}(.)$ with respect to $\mathbf{u}$ is equivalent to maximizing the *Kulback-Leibler* distance between the joint distribution $p^{R, T \circ g(\mathbf{u})}(\cdot, \cdot)$ and the product distribution $p^R(\cdot) \cdot p^{T \circ g(\mathbf{u})}(\cdot)$, given by:

$$\mathcal{D}^{MI}(R, T, \mathbf{u}) = \int_{\Omega} p^{R, T \circ g(\mathbf{u})}(l_1, l_2) \log(\frac{p^{R, T \circ g(\mathbf{u})}(l_1, l_2)}{p^R(l_1) \cdot p^{T \circ g}(l_2)}) dl_1 dl_2. \tag{4}$$

Other measures exist, including the Correlation Ratio (*CR*) [12], which have been also used to cope with the difficulty of registering images with different modalities.

Image registration is usually performed by optimizing one of these criteria over a class of deformations,

$$\text{Find } \mathbf{u} \in \mathcal{X} \quad \text{s.t.,} \quad \mathcal{D}(R, T, \mathbf{u}) \quad \text{is optimal.} \tag{5}$$

Mathematically, this problem is ill-posed in the sense of Hadamard. That is, the solution, if it exists, is neither unique nor stable. To cope with this problem, a regularization term, $\mathcal{R}(\mathbf{u})$, which measures the irregularity of the displacement field $\mathbf{u}$, is usually added to the registration criterion to guarantee the well-posedness of the problem. This leads to solving the following optimization problem:

$$\text{Find } \mathbf{u} \in \mathcal{X} \quad \text{s.t.,} \quad \mathcal{D}(R, T, \mathbf{u}) + \alpha \mathcal{R}(\mathbf{u}) \quad \text{is optimal,} \tag{6}$$
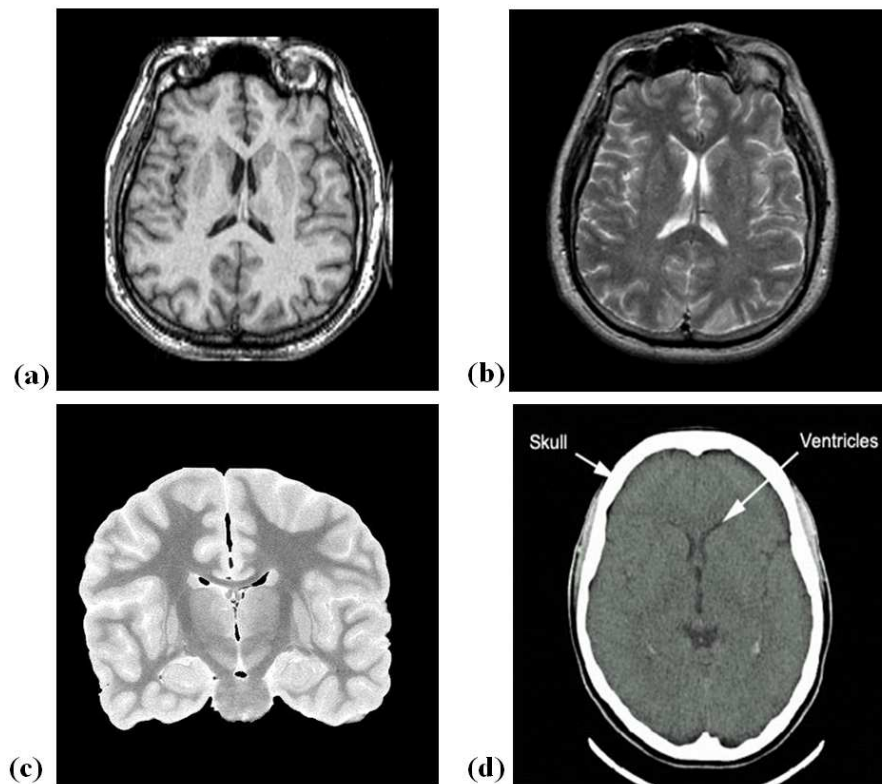
FIGURE 1 – Examples of different medical images modalities of the human brain. (a) T1-weighted MR image. (b) T2-weighted MR image. (c) Proton-Density MR image. (d) CT image.

where, $\alpha > 0$ is a regularization parameter that balances the contribution of the two terms. A simple example of $\mathcal{R}(.)$ is the *Tikhonov* model [13] which was the first regularization model to be used to solve image matching problems [14]. This regularization model is defined as follows:

$$\mathcal{R}(\mathbf{u}) = \frac{1}{2} \int_{\Omega} \|D\mathbf{u}(\mathbf{x})\|^2 d\mathbf{x}, \tag{7}$$

where $D\mathbf{u}$ denotes the Jacobian matrix of $\mathbf{u}$. Other regularization models have been proposed to deal with the ill-poseness of the problem (5). These models are physically-based functionals relying on elasticity or fluid theory [15–17].

Note that the choice of the regularization term, $\mathcal{R}$, contributes to the definition of the space $\mathcal{X}$ where the solution is to be sought. For instance, for the Tikonov model (Eq. 7), the set of admissible transformations, $\mathcal{X}$, is contained in $[H^1(\Omega)]^n$, with $H^1(\Omega)$ being the Sobolev space of order 1 on Ω [18].

In summary, the matching problem can be casted as the following minimization problem:

$$\mathbf{u}^* = \arg\min_{\mathbf{u} \in \mathcal{X}} [\mathcal{D}(R, T, \mathbf{u}) + \alpha \mathcal{R}(\mathbf{u})]. \tag{8}$$

Under sufficient regularity conditions of the functionals $\mathcal{D}$ and $\mathcal{R}$, and by assuming that the set of admissible solutions, $\mathcal{X}$, is a Hilbert space, one can derive the Euler-Lagrange equations associated with the minimization problem (8) as:

$$\begin{cases} \frac{d}{dt}\mathbf{u} = -[\nabla_{\mathbf{u}}\mathcal{D}(R, T, \mathbf{u}) + \alpha \nabla_{\mathbf{u}}\mathcal{R}(\mathbf{u})], \\ \mathbf{u}(0, \cdot) = \mathbf{u}_0(\cdot), \end{cases} \tag{9}$$

where, ∇ denotes the gradient operator on $\mathcal{X}$, and $\mathbf{u}_0 \in \mathcal{X}$ is an initial field. This problem can be solved using a gradient descent scheme.

The registration work flow is illustrated in Fig. 2. Starting from an initial estimate of the deformation field, the target image is transformed and the similarity/dissimilarity between the transformed target and the source is iteratively measured while the transformation parameters are updated through an optimization scenario. The process stops when the difference between the transformed target and the source is below a certain threshold or if a maximum number of iterations is attained.
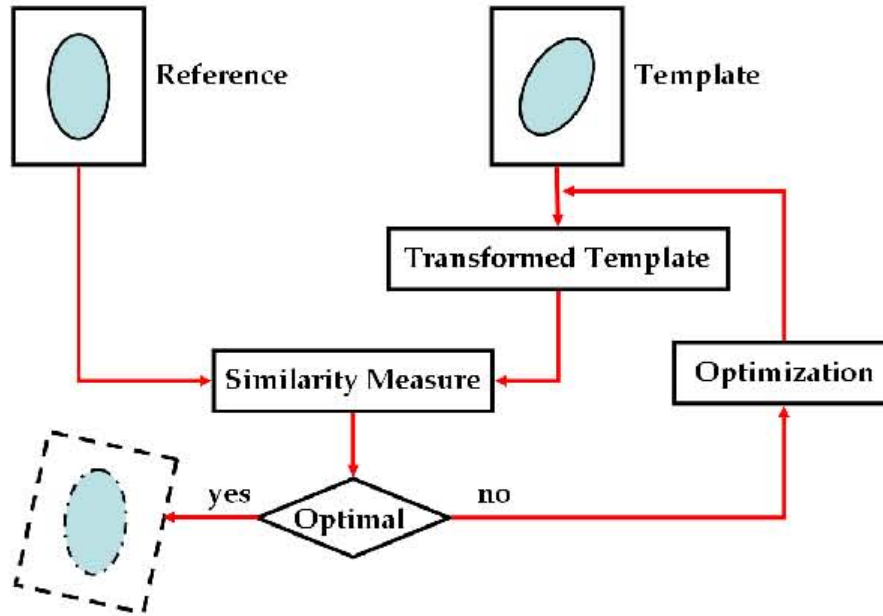
FIGURE 2 – Registration work flow. Only the main components of the registration process are shown.

A totally different approach for solving the image matching problem can be achieved through an interface evolution scenario expressed in a level set framework. Such an approach was independently adopted by Bertalmío et al. [19] for image segmentation and tracking, and by Vemuri et al. [20] for image registration. The main idea of registering two images within this framework is to evolve one image (the source), by letting the level sets of its intensity map evolve along their respective normals, towards the level-sets of the intensity map of the other image (the target). The evolution speed is proportional to the difference between the intensity values of the target and the evolving source. This leads to an intensity morphing model, but does not provide a geometric mapping between the two images. A different evolution model, expressed in vector form, is proposed in [19, 20] to explicitly recover a dense displacement field between the two images. The derivation of this equation is as follows. Let $\mathcal{C}(p,t) : \mathbb{R} \times [0,T) \rightarrow \mathbb{R}^2$ denote a family of closed planar curves. Assume that these curves deform in time according to the following general

6

evolution equation:

$$\frac{\partial \mathcal{C}}{\partial t} = \beta \mathbf{N}, \text{ with } \mathcal{C}(p, t_0) = \mathcal{C}_0(p), \tag{10}$$

where β, which does not depend on the parametrization of the curve, is the normal component of the velocity and $\mathbf{N}$ is the inward unit normal to $\mathcal{C}(p, t)$. Note that the tangential velocity was removed from the flow equation (10) since it does not affect the geometry of the deformation as shown by Epstein and Gage in 1987. Now, let $\mathcal{C}(p, t)$ be represented by the zero level set of a function $\phi : \mathbb{R}^2 \times [0, T) \to \mathbb{R}$. That is, $\mathcal{C}(p, t)$ satisfies $\phi(\mathcal{C}, t) = 0$. Differentiating this equation leads to the following level set representation of the flow, as proposed by Osher and Sethian [21]:

$$\frac{\partial \phi}{\partial t} = F \parallel \nabla \phi \parallel, \tag{11}$$

where F is the evolution speed. This equation, compared to a direct discretization of Eq. (10), offers many advantages such as the handling of topological changes. Note that this formulation has been successfully used in various 2D/3D applications, including segmentation, tracking, shape from shading, and shape registration [22].

B. Shape Registration

The process of registering shapes is based on three main components, namely 1) the way to represent the shapes, 2) the transformation model, and 3) the mathematical framework selected to recover the registration parameters. The following section briefly reviews each of these components.

1. Shape Representation

Shape representation is handled differently in each application. For instance, in [5], the authors choose to represent the shapes to be registered as the zero level sets of distance functions in a higher dimensional space. This implicit representation is known to be invariant to translation and rotation, and can efficiently handle the isotropic scaling case. Hong et al. [23] have proposed a new shape representation algorithm and showed its potential

in image matching and segmentation. This new algorithm is based on integral kernels and represents a shape as the area of intersection between the kernel and the inside and outside of the shape. The kernel scale has a major effect on the method performance, however its appropriate selection was not discussed. In [24], a new approach was proposed to solve the shape registration problem by using a volumetric representation of shapes through vector level sets. The authors claimed that this representation is more suitable for scale variations. In [25], the authors use the point-set representation for shapes in order to solve the problem of non-rigid registration of shapes. This representation, also known as clouds of points representation, was used in [26], where the authors proposed to describe each sample point by a *"shape context"*, and use this new descriptor to match shapes for object recognition purposes. These and other shape descriptors, such as medial axis [27] and Fourier descriptors [28] will be reviewed in more detail in the next chapter.

2.   Transformation Models

Transformation models can be divided into two classes: global and local. The global transformation models are usually defined by a small set of parameters. These models include, among others, the rigid transformations (translations and rotations), the similarity transformations (translations, rotations, and isotropic scalings), the affine transformations, which in addition to translations and rotations, account for anisotropic scaling and/or shearing. In some cases, such transformations can be used alone to efficiently align two shapes. However, in the case of non-rigid deformations, more complex transformations are required in order to establish dense correspondences between the two given shapes.

3.   Related Works on Shape Registration

Different techniques have been developed to solve the non-rigid registration problem of shapes [5, 7, 17, 29, 30]. In [31], the authors presented an algorithm, known as the Thin Plate Spline-Robust Point Matching (*TPS-RPM*) algorithm, to jointly estimate the rigid and non-rigid transformations between two clouds of points that may be of different

(a)   (b)
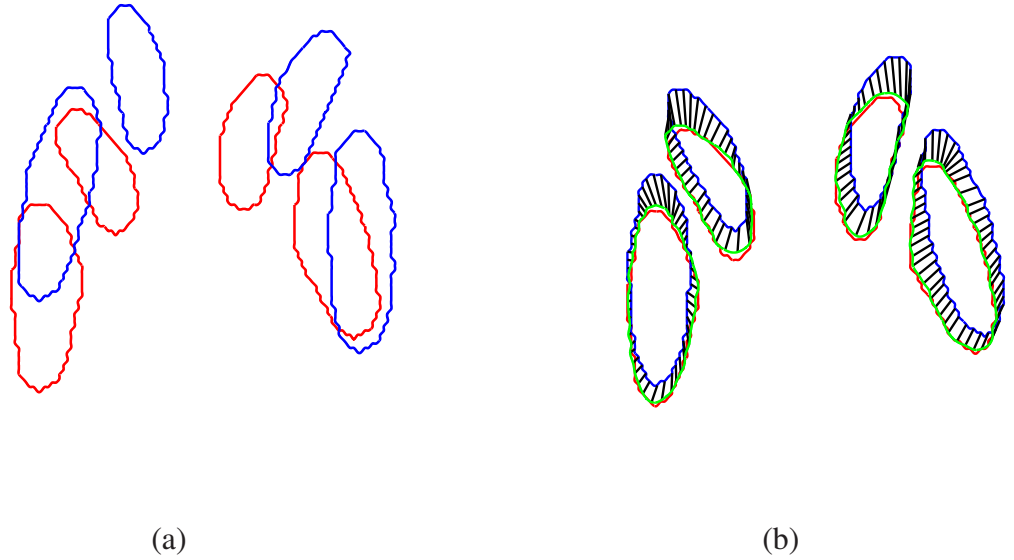
FIGURE 3 – Example of registration of a subcortical shape. (a) Initial positions of the
source shape (blue) and target (red); (b) Established shape correspondences after local
registration. The green curve represents the locally deformed source.

sizes. Thin plate splines were also adopted in [26] where corresponding points are deter-

mined by iteratively minimizing the overall *shape context* distances, and the *TPS* trans-

formation is re-estimated at each iteration to recover the local transformation maps. More

recently, Chen and Bhanu [30] introduced a global-to-local procedure to align non-rigid

shapes. The shape context descriptors are used to recover a global similarity transfor-

mation, while the local deformation is performed within an optimization formulation, in

which the bending energy of *TPS* transformation is incorporated as a regularization term.

Zheng and Doermann [29] proposed a relaxation labeling-based point matching algorithm

for nonrigid shapes. The authors formulated point matching as a graph matching prob-

lem and used the shape context distance to initialize the matching of graphs, followed by

relaxation labeling updates. Huang et al. [5] introduced a hierarchical shape registration

algorithm using a B-spline-based-Incremental Free Form Deformations (*IFFD*) model to

recover the local registration field between two globally aligned shapes.

Broadly speaking, given the transformation model and the selected shape represen-

tation model, most existing techniques that have been developed to recover the registration

parameters are based on the optimization of a disparity measure between the two shapes. For instance, the Sum of Squared Differences (*SSD*) is a popular criterion that is mostly appropriate, as mentioned above, when the two data sets have comparable values (e.g., mono-modal images) or when matching shapes with no scale variations, while the Mutual Information (*MI*) is a stochastic measure that is more appropriate for registering images with different modalities or matching shapes under scale variations [5].

Smoothness constraints, using physically based functionals relying on elasticity or fluid theory [15–18], are often be introduced to guarantee the well posedness of the problem and to retain some smoothness properties of the recovered displacement field.

An example of registering two dimensional shapes is illustrated on Fig. 3. Note that these results are obtained by the proposed registration approach (see chapter VI).

C. Shape-based segmentation

A very important image processing tool that may greatly benefit from shape registration is the segmentation of a given image into its semantically significant parts. This is one of the most fundamental problems in several application areas, including computer vision, medical imaging, etc. This problem presents several challenges that are mainly related to image noise and inhomogeneities, etc. Consequently, segmentation approaches that primarily rely on low level image cues, such as color information and/or texture may not output accurate results. One way to overcome this difficulty is to exploit the prior knowledge of shapes and other properties of the imaged structures in order to constrain the segmentation process. The incorporation of such priors into the segmentation framework becomes even more necessary in the presence of occlusion, corruption, shadows, etc.

The integration of shape priors into level sets-based segmentation methods has attracted the attention of several researchers in the past years. The basic idea consists of incorporating the prior knowledge into the interface evolution in order to recover the object(s) of interest. The segmenting interface propagates by implicitly evolving an embedding higher dimensional function according to an energy minimization formalism. Some

10
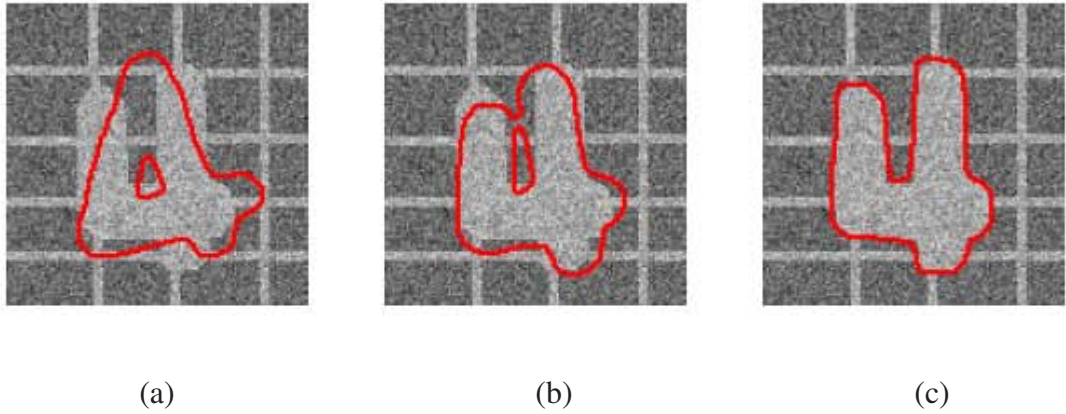
FIGURE 4 – Example of shape-based segmentation using an active contour model. (a) Initial positions of the evolving contour. (b) An intermediate evolution step. (c) Final segmentation result.

of the existing level set-based segmentation approaches with shape prior allow the recovery of a familiar object, whose shape is analogous to the shape prior, but suppress the *"unfamiliar"* image objects [32, 33]. Other methods, e.g., [34], permit the simultaneous segmentation of both familiar and unfamiliar objects. This is done through the introduction of a *"labeling"* function which indicates the image regions where the shape prior is to be enforced. Moreover, some methods, e.g., [34], assume the pose and position of the object of interest to be known and in accordance with the localization of the shape prior, while other approaches (e.g., [32, 33, 35]) assume the existence of a global transformation between the object of interest and the shape prior. The parameters of this transformation are iteratively updated during the course of evolution of the segmenting interface. This allows to segment familiar objects without knowing their pose nor their orientation in the image scene. Raviv et al. [33] presented a novel approach which accounts for projective transformations between the shape prior and the object to be segmented. However, all of these approaches are limited to segmenting a single known object in a given 2-phase image. The key question to be asked is: what if multiple known objects are present in the image scene and need to be segmented? Several attempts have been made to answer this question. For instance, in [35], the authors proposed a framework which handles an arbitrary number of regions and multiple competing shape priors by expanding the split and merge

level set based segmentation approach by Brox and Weickert [36] to deal with multiple regions. Cremers et al [37] introduced a framework which allows the integration of multiple selective shape priors into the 2-phase Chan-Vese model. The authors introduced a dynamic vector-valued labeling function to indicate where to enforce which prior. In both of these studies, the shape prior is represented by a fixed template. However, in other studies, statistical shape priors were considered. For instance, Leventon et al. [38] proposed to perform the Principal Component Analysis (*PCA*) on a collection of signed distance functions of the training shapes. The accuracy of such representation depends greatly on accurately aligning the shapes in the training set. The derived shape statistics are then used, along the gradient force of the image, to guide the evolution of the segmenting geodesic active contour. This statistical approach was adopted in other studies (see e.g., [32, 39]). Such a scenario is illustrated on Fig. 4 where both shape and image information are used to evolve the segmenting contour towards the object of interest.

D. Contributions

The main **contributions** of this work can be summarized as follows.

• In this dissertation, the shapes are implicitly embedded as the zero level set of a distance function in a higher dimensional space. The powerful distance transform is used as the embedding function. A new variational framework for a dense global to local shape registration in the implicit space is proposed. First, a new dissimilarity measure is introduced to recover the transformation parameters that globally align the two input shapes (source and target). This new measure can deal efficiently with rigid and similarity motion and leads to accurate results in the presence of anisotropic scaling. Complementary to the global registration field, the local coordinate transformation between the two globally aligned shapes is explicitly estimated by minimizing a new energy functional. This functional consists of three terms, the first of which is a discrepancy measure between the two shape representations. The second term penalizes the deviation of the distance map representation of the globally warped source shape from a signed distance function, while

the local displacement field, which aims at aligning it with the target shape, is being updated. The last term is a regularization term that enforces the smoothness of the recovered deformations. This leads to a set of coupled equations that are simultaneously minimized through a gradient descent scheme.

The proposed registration framework has many advantages over existing techniques. First, the shape representation using signed distance transform, as used in this work, provides a feature space in which minimization of energy functionals using gradient descent schemes can be used effectively. This representation has also the advantage of being relatively simple compared to other descriptors, since it is based on simple geometrical definitions. In addition, the signed distance representation is invariant to rigid transformations and is less expensive computationally compared to other representations such as the vector distance transform. This is a huge advantage especially when dealing with three dimensional shapes. Huang et al. [5] have also used the distance transform and proposed a global alignment model for shapes by maximizing mutual information. In that work, the probability density functions are approximated using Gaussian kernels with empirical width values which may lead to inaccurate results if these values are not chosen carefully. Moreover, the proposed non-rigid registration model in this dissertation has the advantage of accurately dealing with highly local deformations. This is due to the introduction of the new penalizing energy term. In [5], the authors had to use a feature-based energy term to cope with such situations. This introduces the burden of extracting corresponding features. Both in [5] and [40], the authors chose to model the displacement field using B-splines. No such restriction is imposed on the displacement field in this work. In [5, 40], the registration field is recovered by iteratively minimizing a regularized energy with respect to each component of each control point which may greatly increase the likelihood of their algorithms to be trapped in local optima, and may increase the computational complexities as well.

- A fast algorithm to solve the challenging problem of shape-based segmentation within the level set framework is proposed. Inspired by the work of Cremers et al. [34] and that of Song and Chan [6], the piece-wise constant Chan-Vese model is considered as the underlying level set formalism and it is assumed that the considered shape priors are

13

represented by fixed templates. The core idea of the proposed algorithm, which was also used in [41], is to exploit the fact that only the sign of the level set function, not its value, is needed to evolve the segmenting contour. Hence, instead of solving the Euler-Lagrange equations of the underlying variational problem, as was done for instance in [34], one directly computes the segmentation energy and checks its changes when moving image points from positive to negative regions of the level set function and vice-versa. This algorithm is extended to allow the integration of multiple selective shape priors into the multi-phase Chan-Vese segmentation model [1]. The resulting framework can handle multiple familiar objects without affecting the correct segmentation of other unknown objects. Unlike [37], more than one level set function is used, each of which is associated with a shape prior and a labelling function indicating where in the image domain each prior is to be active. This framework can deal better with multi-phase images. This is the first attempt of handling more than one shape prior within the multi-phase Chan-Vese segmentation model. Moreover, the proposed global shape registration dissimilarity measure is used to address the problem of pose invariance in the case when the object(s) of interest do not share the same location and orientation as the the shape prior(s). The advantage of the proposed global registration method in building statistical shape models and using them in a simultaneous segmentation and registration framework will be highlighted. It will be shown, through comparisons with other global registration methods, that a good alignment is required to build an accurate shape model and to output accurate segmentation results.

- A novel and accurate approach for image and volume registration is presented. The technique is the fruit of a collaborative effort with two ex-colleagues at the *CVIP* laboratory. New feature descriptors are built as voxel signatures using scale space theory. These descriptors are used to capture the global motion of the imaged object. Local deformations are modelled through an evolution process of equi-spaced closed curves/surfaces (iso-contours/surfaces) which are generated using fast marching level sets and are matched using the built feature descriptors.

- The performance of the proposed image registration method is validated using a novel technique based on the finite element method. Several 2D and 3D biomechanical

tissue deformations cases are simulated, and the registration accuracy is quantified by co-registering the deformed shapes/images with the original ones and comparing the recovered mesh point displacements with the simulated ones.

E.   Dissertation Summary and Organization

This manuscript is presented in nine chapters. In the following, a detailed summary for each chapter is given.

CHAPTER 2

In this chapter, a non-exhaustive overview of the existing shape representation models is presented. Some of the strengths and limitations of each of these models in the context of shape registration are highlighted. The choice of the implicit representation in terms of signed distance transforms is justified.

CHAPTER 3

In this chapter, a new dissimilarity measure is proposed to recover the affine matching parameters between two given shapes. The performance of this measure is compared to two other techniques, namely, the isotropic scales-based measure and the one expressed in the embedding space of vector distance functions. In addition, an empirical evaluation of the proposed criterion is presented to show the well behavior of the resulting optimization algorithm. The chapter ends by showing the potential of the proposed registration criterion in building statistical shape models.

CHAPTER 4

This chapter is devoted to discussing the proposed variational framework to solve the non-rigid shape matching problem. The chapter introduces an energy formulation that takes into account the re-initialization of the signed distance representation of the source shape while it is being deformed. The chosen regularization energy used to preserve the regularity of the solution is introduced and the overall numerical implementation is explained both in 2D and 3D cases. The chapter is ended with a novel validation technique based on the finite element method, followed by a comparison with some results that have been reported

recently in the literature. Various 2D/3D registration examples are presented to show the potential of the proposed registration model.

CHAPTER 5

This chapter shows the potential of the proposed global-to-local registration framework to dealing with three dimensional face registration. This chapters shows on several 3D face range scans that the proposed registration framework can efficiently reduce the highly local distortions caused by facial expressions, such as smiling and cheek inflating. This motivates the application of the proposed registration approach to solve the 3D face recognition problem in the presence of face expressions. The results are very encouraging.

CHAPTER 6

This chapter addresses the level set-based segmentation with shape priors. The chapter starts by a quick review of the piece-wise constant Chan and Vese segmentation models, and then shows how the shape prior as well as the *"labelling"* function are added to the segmentation functional. The chapter continues by introducing a fast algorithm and showing how it can be applied within the 2-phase and the n-phase Chan and Vese segmentation models with selective shape prior(s). The chapter ends with the introduction of a new pose invariance formulation using the global shape registration of chapter III.

CHAPTER 7

This chapter introduces a new registration method for images in two and three dimensional spaces. Level set theory is used to generate equi-spaced iso-contours/surfaces of the imaged object/organ in the two images and scale space theory is used to build feature descriptors that will subsequently be used to match these iso-contours. The chapter continues by using the *FEM*-based validation technique introduced in chapter IV, in order to validate the proposed image registration approach. Comparisons with an existing registration method is also presented.

CHAPTER 8

This chapter summarizes the main components of the proposed work, and presents a plan for future directions.

CHAPTER II

WHAT IS A SHAPE AND HOW CAN IT BE DESCRIBED?

The way of describing or representing a shape is a core component of any existing shape registration algorithm. This chapter reviews some existing shape description techniques and highlights their properties relevant to the registration process as it will be formulated in this dissertation.

Generally speaking, the shape of a geometrical figure (or object) is understood to refer to those geometrical attributes that are invariant to Euclidean similarity transformations, that is those attributes that remain unchanged when the object is rotated, translated and scaled [42]. This is reflected in Fig. 5. Two objects are said to have the same shape if one is a transformed version of the other under a similarity transformation. A shape can be classified either as static or dynamic. A static shape, also referred to as rigid shape, is a shape that does not change over time by deformation. An example of such a shape is a car model. A dynamic shape deforms over time, such as a human face which undergoes changes when speaking or smiling for example.

Various techniques have been designed to describe shapes. Each has its strengths and its limitations vis-a-vis the application for which the representation is being used. These techniques aim at providing a simplified representation of the considered shape while preserving its main characteristics. The purpose of this chapter is to provide a non-exhaustive overview of existing shape representations and a necessary background for the chosen descriptor throughout this work, namely the *"distance transform"*.

A.   Existing Shape Representation Techniques

The literature is rich with shape representation techniques. These techniques can generally be categorized as parametric, such as Fourier descriptors and spherical harmon-

FIGURE 5 – Four copies of the same shape, but under different Euclidean transformations. Image is courtesy of [2].

ics, or non-parametric, such as landmark-based techniques, medial axes, and distance transform. In many applications, in particular in image-based morphological studies in the field of medical imaging, the analysis starts with the extraction of a quantitative description of the anatomical shapes of interest from the input images. The following section overviews some existing techniques to describe or represent shapes and explains how some of these descriptors are extracted from the images.

1. Parametric Representations

Within this family, the techniques fit a parametric model to a curve outline in a 2D image or a bounding surface in a 3D image. The model parameters are typically derived from segmented images and are used to describe the considered shape. This family of descriptors include, among others, the following:

- *Geometric Moments:* The mathematical concept of moments has been around for many years and has been utilized in several fields, including mechanics, statistics, pattern recognition and image understanding. Historically, the first significant work considering moments for pattern recognition was introduced by Hu [43]. In general,

the three-dimensional $(p+q+r)^{th}$ geometric moment, $\mathcal{M}_{pqr}$, of a function $f(x,y,z)$ (an image intensity or a density distribution function) is defined as

$$\mathcal{M}_{pqr} = \int_{-\infty}^{+\infty} \int_{-\infty}^{+\infty} \int_{-\infty}^{+\infty} x^p y^q z^r f(x,y,z) dx dy dz, \qquad (12)$$

where, $p,q,r \in \mathbb{N}$. Geometric moments are not orthogonal since their basis functions, namely the monomials $x^p y^q z^r$ are not orthogonal. Moreover, according to the uniqueness theorem, the moment set $(\mathcal{M}_{pqr})_{pqr}$ is uniquely determined for a given image function f, and the existence theorem states that the moments of all orders exist [43]. These two theorems give rise to the reconstruction property of moments. Finally, note that in case the function f is a binary function with a value one inside the region enclosed by the shape, and zero outside, then the zeroth order moment is equal to the area enclosed by the shape.

Hu [43] derived a set of seven moment invariants, using non-linear combinations of geometric moments. These invariants remain the same under image translation, rotation and scaling. A number of such moments invariants can be put into a feature vector and used for matching purposes as was done for instance in [44, 45]. Recently, matching two shapes using moments was proposed in [46] in the context of affine-invariant shape-based segmentation. Mathematically, moments have the advantage of being concise, however, it is difficult to correlate high order moments with shape features.

- *Spherical Harmonics (*SPHARM*):* Surfaces in 3D can be represented by a series expansion of parametric coordinate functions in 2D parameter space. Popular among the basis functions are the spherical harmonics which were used, for instance, in [47, 48]. The surface voxels are projected onto the unit sphere, S^2, with its origin located at the center of mass of the object and the surface, $v(\theta,\phi) = (v_1(\theta,\phi), v_2(\theta,\phi), v_3(\theta,\phi))$ is expressed as a linear combination of its harmonics as follows:

$$v_i(\theta,\phi) = \sum_{l \geq 0} \sum_{|m| \leq l} C_{lm}^i Y_l^m(\theta,\phi), \text{ with } \theta \in [0,\pi], \text{ and } \phi \in [0,2\phi]. \qquad (13)$$
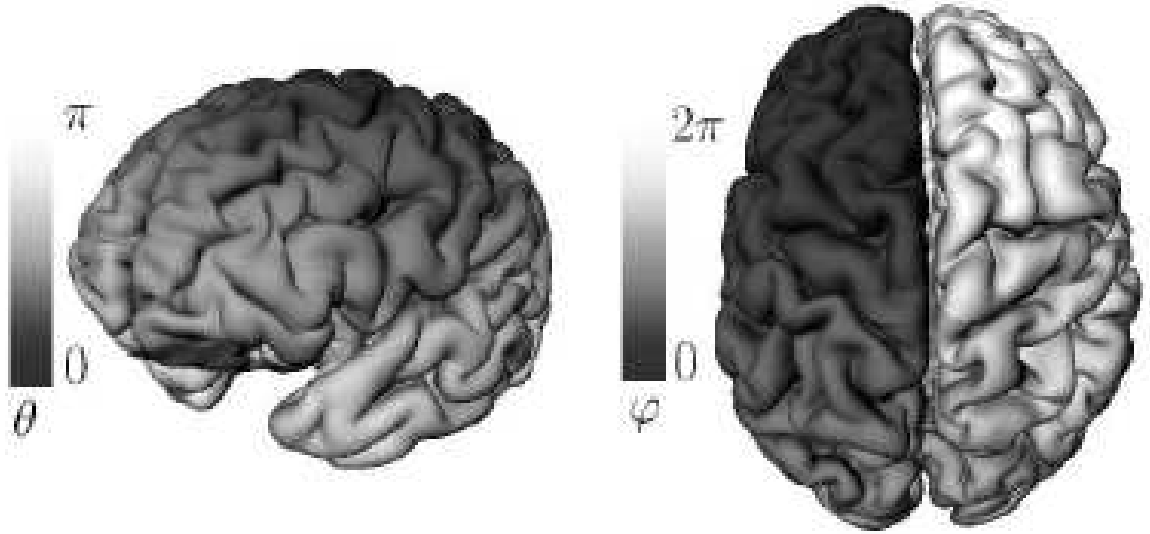
FIGURE 6 – Parametrization of cortical surface using the spherical coordinate system.. Image is courtesy of [3].

where, C_{lm}^i are the expansion coefficients given by

$$C_{lm}^i = \int_{S^2} v_i(\theta, \phi) Y_l^m(\theta, \phi) \sin \theta d\theta d\phi,$$

and $Y_l^m(\theta, \phi)$ are the harmonic of degree l and order m, which are defined as solutions to the normal Laplace equation in spherical coordinates. Truncating this expansion at a given frequency l allows the reconstruction of the original surface at the different levels. Figure. 6 illustrates the parametrization of a cortical surface using spherical harmonics.

Recently, a new mathematical tool, based on spherical harmonics, for obtaining rotation-invariant representations of 3D shapes was proposed in [48], and was used for 3D shape matching scenarios. In addition, a variant of the spherical harmonics representation, known as weighted spherical harmonics was introduced by Chung *et al.* (see e.g., [49, 50]) for the purpose of voxel-based morphometry (*VBM*) [1] and

---

[1] Voxel-based morphometry (VBM) is a fully automated image analysis technique allowing identification of regional differences in gray matter and white matter between groups of subjects without a prior region of
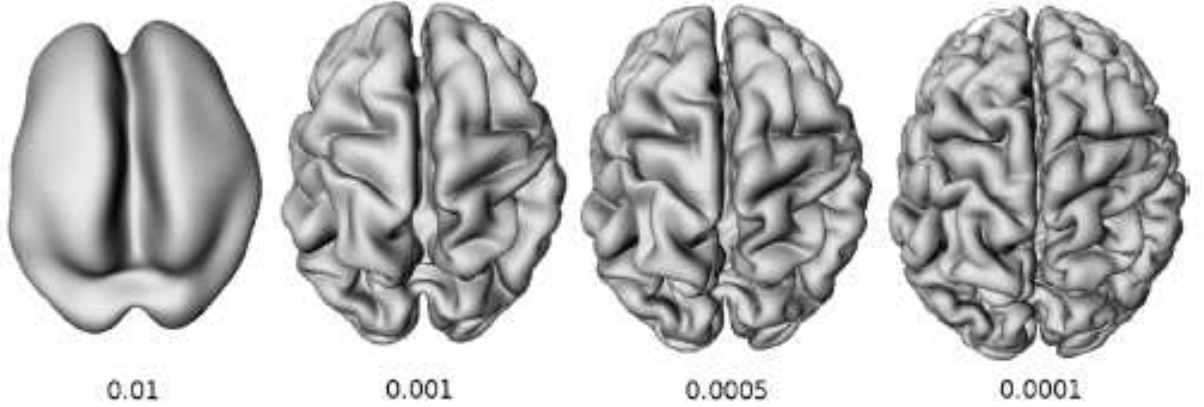
FIGURE 7 – Weighted *SPHARM* representation of a cortical surface at different scales. Image is courtesy of [4].

for the tensor-based cortical morphometry. The new representation generalizes the traditional *SPHARM* by weighting each spherical harmonic basis such that the resulting representation becomes the solution of an isotropic diffusion equation on a unit sphere. This is a multiscale representation that results in a smooth and explicit representation of unknown cortical boundary. The weighted *SPHARM* representation of $v(\theta, \phi)$ at different scales, σ, is given by

$$v_i(\theta, \phi) = \sum_{l \geq 0} \sum_{m=-l}^{l} e^{l(l+1)\sigma} C_{lm}^i Y_l^m(\theta, \phi). \tag{14}$$

Note that the weighted *SPHARM* corresponds to the traditional *SPHARM* for the particular case $\sigma = 0$. Figure 7 shows the weighted *SPHARM* representation of a cortical surface at different scales. This representation, as well as the weighted Fourier Series [4] were further used by the authors to normalize brain surfaces into a common stereotaxic space using affine transformation. The displacement field was obtained by minimizing the integral of the squared errors between the two input surfaces. The authors showed that, unlike other surface registration techniques, the optimal displacement field in the least square sense is obtained by simply taking the

interest in brain magnetic resonance imaging [49].
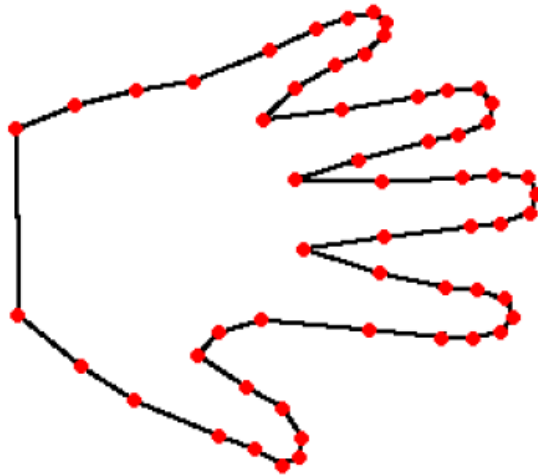
FIGURE 8 – Example of landmark representation of a shape.

difference between the two surface representations. This leads to proper alignment of sulcal folding patterns between subjects and across hemispheres within a subject. This was used as a tool for comparing the gray matter and the cortical thickness across subjects in an autism study [4].

2. Landmark-Based Representation

The boundary of a shape (a curve in 2D or surface in 3D) can be represented by a set of points known as landmarks. Figure 8 illustrates this type of description. A landmark can be defined as a point of correspondence on each object that matches between and within populations. Such points can be manually placed by a knowledgeable user of the underlying anatomy to determine *"special locations"*, or can be detected automatically using some geometric features of the boundary, such as curvature [51–53]. Both manual and automatic landmarks can be extracted either from gray scale or segmented images. Landmarks were extensively used to match shapes (see for example, [51–53]). This representation was also

used in conjunction with Procrustes analysis [2] for statistical shape analysis [2] or to build a point distribution model and use it to segment brain structures in *MR* images [54]. However, it is worth mentioning that this representation suffers from problems such as the need for point correspondences, numerical instabilities, and inability to handle topological changes.

3. Medial Axes Representation

A medial axis or skeleton of a shape was initially defined by Blum [55] as the locus of centers of a disc in 2D or sphere in 3D of maximal size that fits in the domain occupied by the shape (see Fig. 9-a). Since then, medial axes have been used extensively in various computer vision and medical imaging applications. Each point on the medial axis has a least two closest points on the shape boundary, and is associated with a radius of its corresponding maximal disc or sphere. This allows the representation of the considered shape using less information. A shape can be fully recovered from its medial axis. Note that in 3D cases, the skeleton can be a medial surface or, in case of tubular structures, a set of medial curves as shown on Fig. 9-b. This dimension reduction plays a major role in several applications, such as shape matching and retrieval [56–59], segmentation of tubular-like structures [60], and virtual endoscopy [61]. Several techniques have been proposed for medial axis extraction, most of which require a segmented image with the exception of the algorithm proposed in [62, 63] which simultaneously estimates the boundary and the medial axis from the input gray scale image. These algorithms include, among others, the thinning methods which are based on the idea of iteratively peeling off the object's boundary without altering its topology (see e.g., [64]).

---

[2]As a curiosity Procrustes was the nickname of a robber in Greek mythology called Damastes, who lived by the road from Eleusis to Athens. He offered travelers hospitality on a magical bed that would fit any guest. His humor was to stretch the ones who were too short to fit the bed until they died or, if they were too tall, to cut off as much of their limbs as would make them short enough. This rather unpleasant practice continued until Damastes was killed by Theseus, son of Æthra and the Athenian king geus. Another nickname for Damastes was The one who stretches [2].
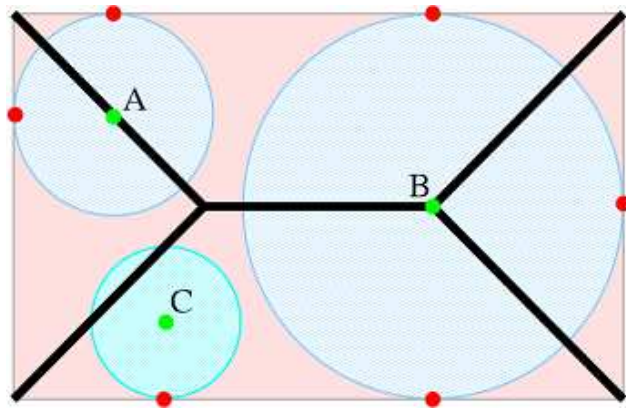
(a)
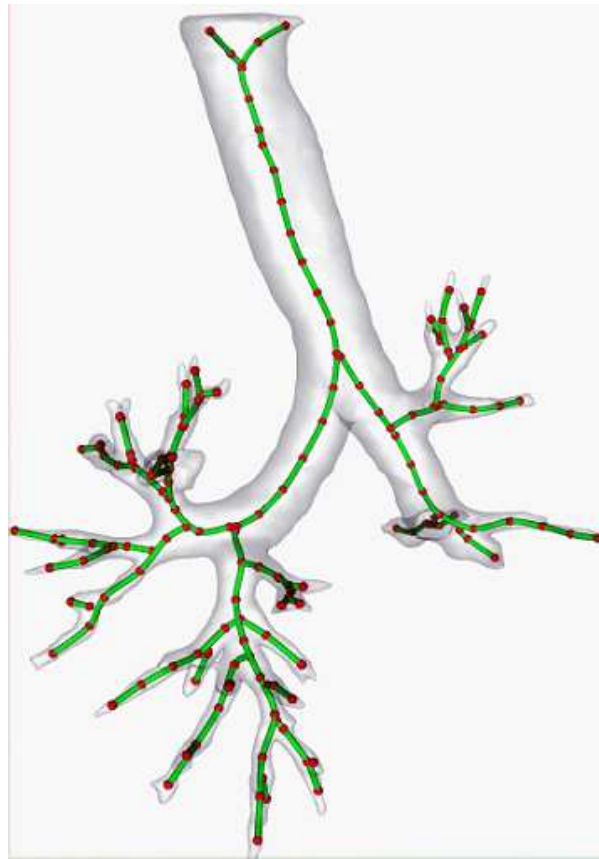
(b)

FIGURE 9 – (a) Two dimensional illustration of the maximal discs to define medial axis.
(b) Curve skeleton of a synthetic 3D shape. Images are courtesy of Dr. M. Sabry Hassouna.

4. Implicit Representation Using Vector Distance Function (*VDF*)

A shape representation (in vector form) was proposed by Faugeras and Gomes [65]. This representation was used to evolve manifolds [66], and has been popular in various image analysis applications. The method, called the Vector Distance Function (*VDF*) method, uses the vector that connects any point in space to its closest point on the object of interest. Given a manifold $\mathcal{M}$ in $\mathbb{R}^n$, $(n = 2, 3)$, let $\delta(\mathbf{x}) := dist(\mathbf{x}, \mathcal{M})$ denote the distance from a point $\mathbf{x} \in \mathbb{R}^n$ to $\mathcal{M}$. That is, $\delta(\mathbf{x}) = \|\mathbf{x} - \mathbf{x}_0\|$ with $\mathbf{x}_0$ being the closet point to $\mathbf{x}$ on $\mathcal{M}$. The function $\delta(\mathbf{x})$ is Lipschitz continuous and hence it is almost everywhere (*a.e.*) differentiable, and so is the squared distance function defined by

$$\eta(\mathbf{x}) := \frac{1}{2}\delta^2(\mathbf{x}).$$

The vector distance function $V(\mathbf{x})$ is defined as the derivative of $\eta(.)$. That is,

$$V(\mathbf{x}) := \nabla\eta(\mathbf{x}) = \delta(\mathbf{x})\nabla\delta(\mathbf{x}).$$

The *VDF*, $V(.)$, is is an implicit representation of the manifold $\mathcal{M}$, with $\mathcal{M} = V^{-1}(\mathbf{0})$, and for each $\mathbf{x} \in \mathbb{R}^n$, $V(\mathbf{x})$ is a vector of length $\delta(\mathbf{x})$ since $\delta(.)$ satisfies *a.e.* the *Eikonal* equation $\|\nabla\delta(\mathbf{x})\| = 1$.

In addition, let $\mathbf{x}$ be a point where δ is differentiable, and let $\mathbf{x}_0 = P_{\mathcal{M}}(\mathbf{x})$ be the unique projection of $\mathbf{x}$ onto $\mathcal{M}$, i.e., $\delta(\mathbf{x}) = \|\mathbf{x} - \mathbf{x}_0\|$. If $\mathcal{M}$ is smooth at $\mathbf{x}$, then the *VDF* to $\mathcal{M}$ at $\mathbf{x}$ is given by (see [65] for more details)

$$V(\mathbf{x}) = \mathbf{x} - \mathbf{x}_0 = \mathbf{x} - P_{\mathcal{M}}(\mathbf{x}).$$

Figure 10 shows a few examples of the x- and y-components of the *VDF*'s corresponding to different 2D shapes. The *VDF* representation was recently used for shape registration in [22, 40].

5. Implicit Representation Using Distance Transform

The distance transform, or the distance map, of a given shape assigns to each point $\mathbf{x}$ in the image its minimal Euclidean distance, $D(\mathbf{x})$, from the shape boundary. Some
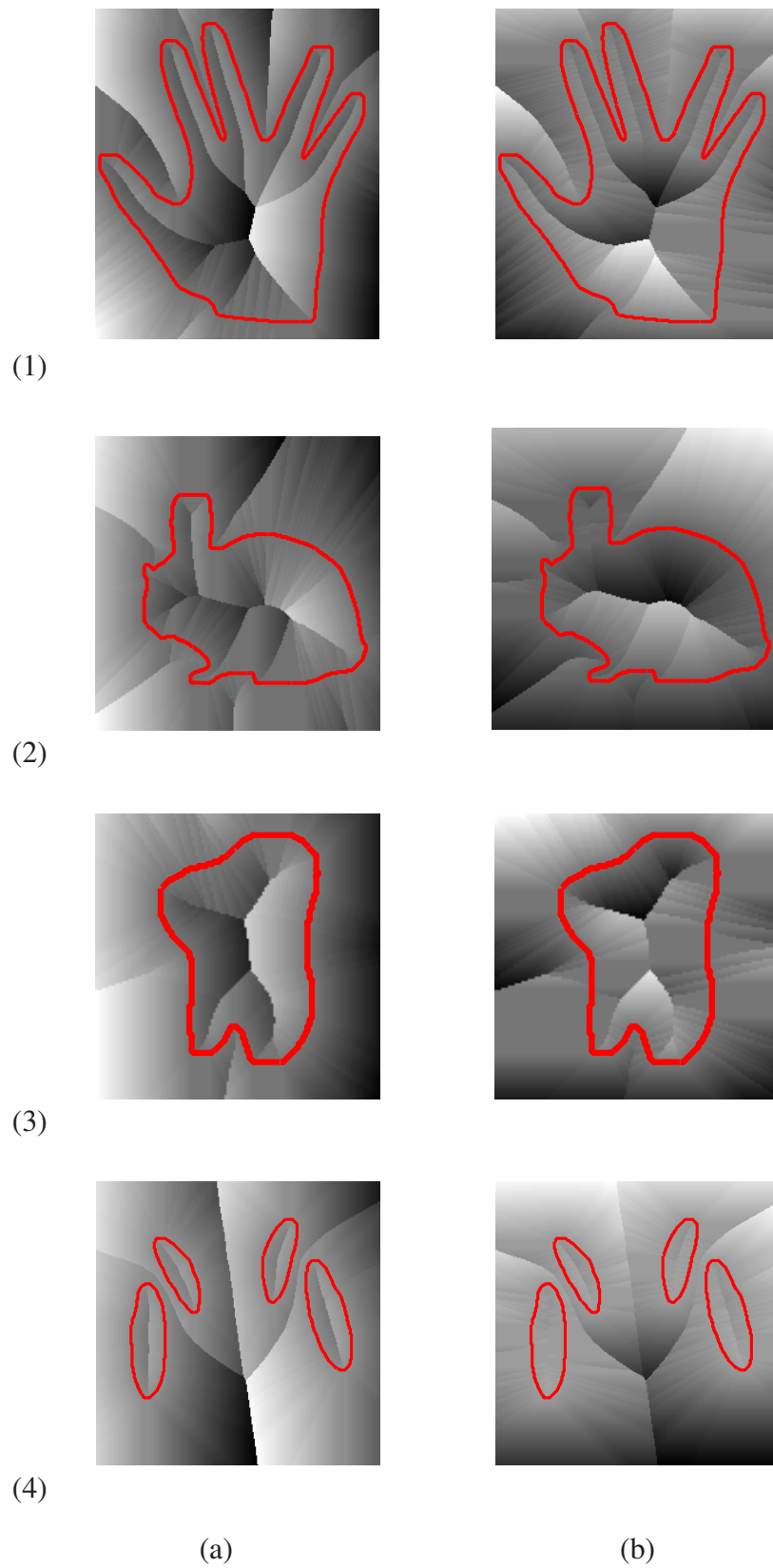
FIGURE 10 – Shape Representation Using the VDF. (a) Hand. (b) Rabbit. (c) Tooth. (d) Hippocampus. (a) the x-component of the VDF; (b) the y-component of the VDF.

two dimensional examples of such representations are shown on Fig. 14. The boundary is modelled as the zero-level set of the distance transform. In many applications, including the present work, a signed variant of the distance transform is considered. This variant negates the values of the distance transform either inside or outside the region enclosed by the shape. Indeed, let S denote an imaged shape in $\mathbb{R}^n$ which defines a partition of the image domain Ω into two regions: the region enclosed by S, Ω_S, and its complement in Ω, $\Omega \backslash \Omega_S$. The shape S can be implicitly defined by the following signed distance transform

$$
\Phi_S(\mathbf{x}) = \begin{cases} 0, & \text{if } \mathbf{x} \in S, \\ +dist(\mathbf{x}, S), & \text{if } \mathbf{x} \in \Omega_S, \\ -dist(\mathbf{x}, S), & \text{if } \mathbf{x} \in \Omega \backslash \Omega_S, \end{cases} \tag{15}
$$

where, $dist(\mathbf{x}, S)$ refers to the minimum Euclidean distance between an image point $\mathbf{x}$ and the shape S.

Examples of such representation are presented on Fig. 12 for various 2D shapes, and on Fig. 13 for a 3D example. The signed variant has the advantage of eliminating the singularities at the shape outline and leads to a linear transition as one crosses the object boundary. Note that the distance transform was used as a way of computing the medial axis of shapes. In fact, the singularity ridges of the distance transform, which are defined as the locus of points that lie inside the shape and have at least two closet points on the boundary, form the shape skeleton (see e.g., [67–69]).

The distance transform is computed from a binary segmentation of the object being considered. An exact computation of the distance transform is very time consuming, especially for large data sets and for higher dimensions. Early discrete techniques to approximate the distance transform can be found in the work by Danielson [70] and that by Borgefors [71]. Other algorithms have been designed to continuously approximate the distance transform by solving a special first order non-linear partial differential equation (*PDE*), known as the Eikonal equation, using the Fast Marching Method (*FMM*) (see appendix I).

In this work, direct computations of the distance transform were carried out for two dimen-
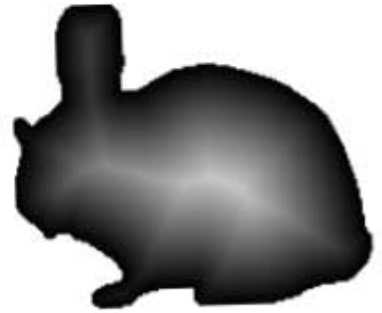
FIGURE 11 – Examples of the distance map inside of 2D shapes. (a) Hand. (b) Rabbit. (c) Tooth. (d) Hippocampus.
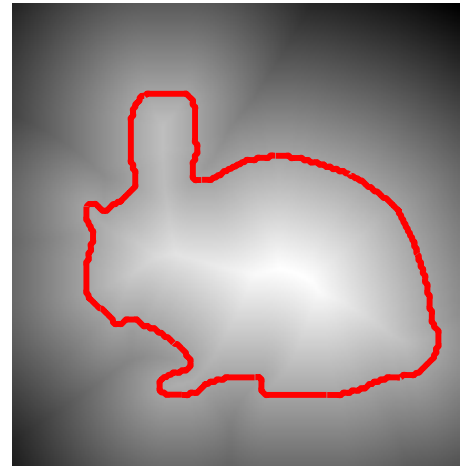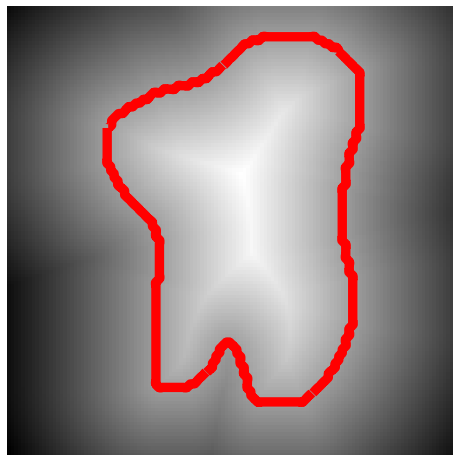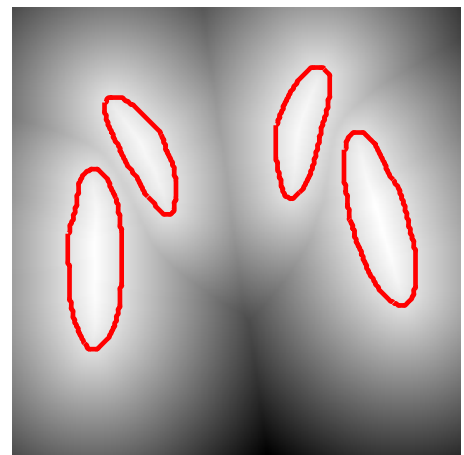
FIGURE 12 – Examples of the signed distance representation of 2D shapes by negating the distance outside the shapes. (a) Hand. (b) Rabbit. (c) Tooth. (d) Hippocampus.

(a)

(b)

(c)

(d)
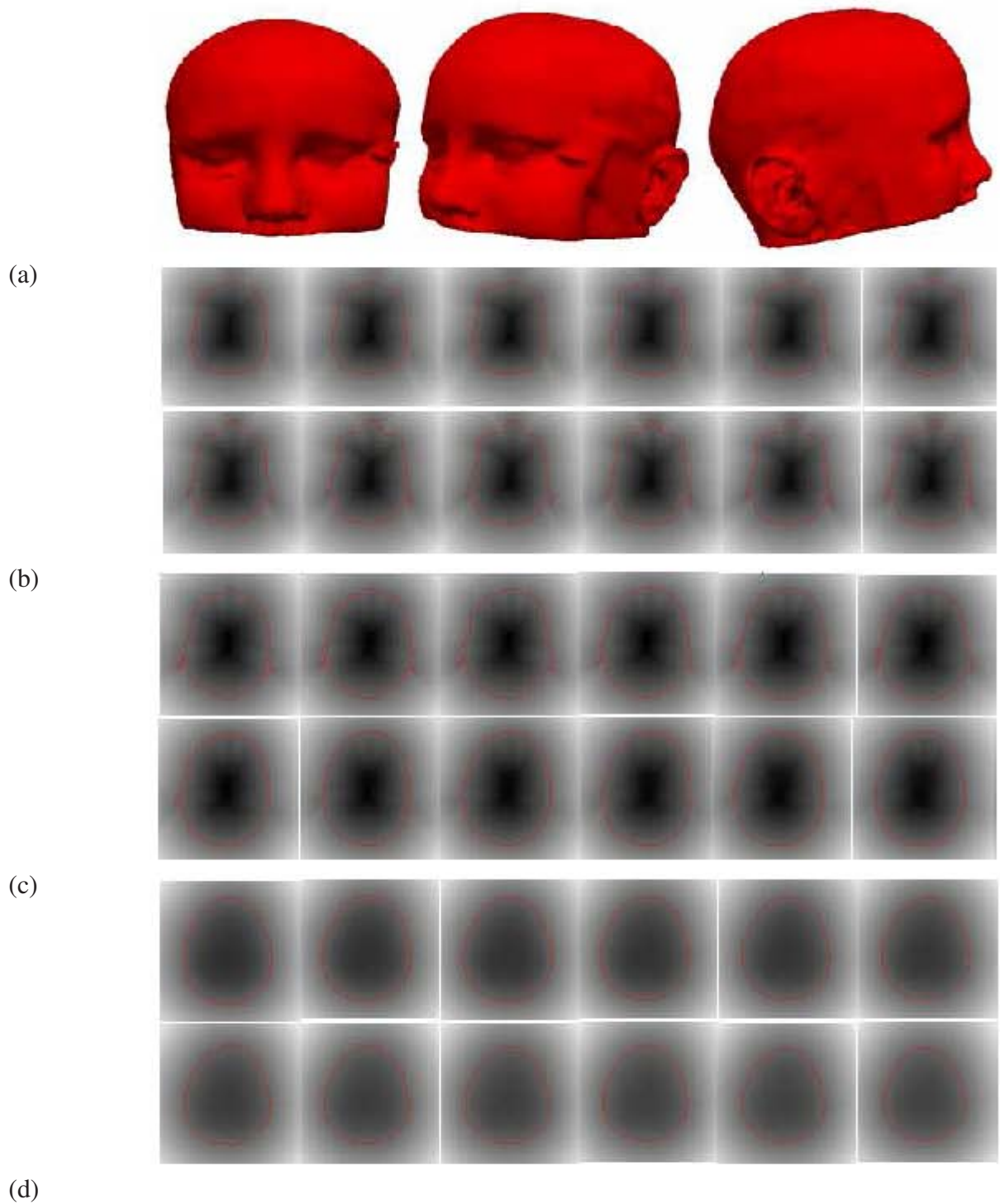
FIGURE 13 – Volumetric signed distance map of the human head by negating the distance inside the region occupied by the shape. The data correspond to an *MRI* scan of size $256 \times 256 \times 124$. (a) Three different views of the surface model. Distance transform slices corresponding to the beginning (b), middle (c), and end (d) of the scan with the zero-level contour in red.

sional shapes with moderate sizes, while, the distance maps of large 2D shapes and those of 3D shapes are approximated using the Fast Marching Method (*FMM*).

The implicit representation using distance transforms has been used previously in several shape registration techniques [5, 22]. In this work, the signed distance transform is chosen to represent shapes for different reasons. First and foremost, this representation provides a feature space in which the registration energy functionals that can be optimized using gradient descent can be conveniently and efficiently used. Indeed, Huang et al. [5] stated that this representation satisfies a sufficient condition for the convergence of gradient descent methods. Second, the signed distance representation is invariant to rotations and translations. Third, in the context of shape based segmentation, since this representation is set in an Eulerian framework, it does not require point correspondences during the phase of building a shape model from a set of training samples. In addition, it has the ability of handling topological changes, such as merging and breaking. This ability is of great value for segmenting medical images where some organs or lesions can present as one confluent object or as a union of disconnected islands.

The only concern of the implicit signed distance representation is that it has one dimension higher than the original shapes. This problem has been addressed thoroughly in the level set segmentation literature using a narrow band implementation. In the context of shape registration, one can reduce the sample domain for registration to a narrow band around the input shape in the embedding space.

B. Summary

In this chapter, several existing shape representation techniques were reviewed. These techniques are generally categorized as parametric and non-parametric. Different aspects of each of these representations, in the context of shape registration, are highlighted. The computation of each of these descriptors from gray scale or binary images are discussed. Finally, the choice of signed distance transform to implicitly represent shapes in this dissertation is justified.

CHAPTER III

GLOBAL REGISTRATION OF SHAPES IN IMPLICIT SPACES

A.   Introduction

As was seen in the previous chapter, shape representation plays a crucial role in many areas of computer vision, pattern recognition, contour matching for medical imaging, etc. This is a very vast and complex problem, which was addressed in Chapter II.

This chapter focuses on the specific implicit representation of shapes using signed distance transforms (see Fig. 14) and how this representation can be used for global shape alignment. The implicit representation of shapes using the signed distance map was employed in some existing works to achieve global alignment of shapes [5, 7]. This representation is proven to be invariant to rotations and translations, and can be efficiently used in the case of homogeneous scaling. In this chapter, a **new** cost function which measures the disparity between the implicit representations of the two input shapes is proposed. This measure leads to accurate results even when dealing with anisotropic scales. Comparisons with existing techniques will be presented to show the potential of the proposed measure.

FIGURE 14 – Implicit shape representation using the signed distance function.

B.   Global Registration of Shapes

Global transformation models are usually defined by a small set of parameters. These models include, among others, the rigid transformation (translations and rotations), the similarity transformation (translations, rotations, and isotropic scaling), the affine transformation, which in addition to translations and rotations, accounts for anisotropic scaling and/or shearing. Such a transformation can be used alone to efficiently align two shapes, or it can be used as a pre-step for a local matching algorithm. Several techniques have been proposed to achieve global alignment between shapes. Some of these techniques are feature-based [72]. Such a technique proceeds by extracting salient features and uses them to match a set of corresponding points. Finally, the matched points are used to recover the transformation parameters. Other methods, on the other hand, recover these parameters by directly optimizing a similarity/dissimilarity criterion between the two shape representations. For instance, in [5], the authors proposed to achieve global registration of shapes by maximizing the *MI* between the *SDF* representation of the input shapes.

In this work, a new *SSD* criterion expressed in the space of signed distance transforms is introduced to globally align shapes. As it will be shown, this new criterion can handle both rigid and affine transformations and leads to more accurate results when compared to other criteria. Two different types of transformations will be considered to achieve shape alignment.

C.   Similarity Alignment

To simplify the presentation, the discussion will be limited in this section to the two dimensional case. Consider two shapes, S and T, that are implicitly represented by their corresponding signed distance maps, Φ_S and Φ_T, respectively. Assume that the target shape, $\mathcal{T}$, is a deformed version of the source shape S, according to a similarity transfor-

mation $\mathcal{A} \doteq \mathcal{A}(s, \mathcal{R}, \mathcal{T})$, given by

$$
\begin{aligned}
\mathcal{A}\mathbf{x} &= s\mathcal{R}.\mathbf{x} + \mathcal{T}, \\
&= s \begin{pmatrix} \cos\theta & \sin\theta \\ -\sin\theta & \cos\theta \end{pmatrix} \cdot \begin{pmatrix} x \\ y \end{pmatrix} + \begin{pmatrix} \mathcal{T}_x \\ \mathcal{T}_y \end{pmatrix},
\end{aligned}
$$

where, s a scaling factor, $\mathcal{R} = \mathcal{R}(\theta)$ is a rotation matrix, and $\mathcal{T} = [\mathcal{T}_x, \mathcal{T}_y]^T$ a translation vector. The question is how to recover these parameters and then align the two given shapes?

First, note that if $\widehat{\Phi}_S$ denotes the transformed level set function Φ_S by $\mathcal{A}$, then one could show that the zero crossing of $\widehat{\Phi}_S$ gives a new shape, $\widehat{S}$, that corresponds, up to the scale s, to the transformation of the original shape S by $\mathcal{A}$. Indeed, let $\mathbf{x}$ be an image point, and let $\widehat{\mathbf{x}}$ denote its image by $\mathcal{A}$, i.e., $\widehat{\mathbf{x}} = \mathcal{A}\mathbf{x}$. Then, one has,

$$
\begin{aligned}
dist(\widehat{\mathbf{x}}, \widehat{S}) &= \min_{\widehat{\mathbf{y}} \in \widehat{S}} \|\widehat{\mathbf{x}} - \widehat{\mathbf{y}}\| = \min_{\mathbf{y} \in S} \|(s\mathcal{R}\mathbf{x} + \mathcal{T}) - (s\mathcal{R}\mathbf{y} + \mathcal{T})\| \\
&= \min_{\mathbf{y} \in S} s\|\mathbf{x} - \mathbf{y}\| = s.dist(\mathbf{x}, S).\square
\end{aligned}
$$

Considering this property of the signed distance function under similarity transformation, one way of recovering the parameters of the transformation $\mathcal{A}$, is by minimizing the following *SSD* similarity criterion as was proposed in [7]:

$$
\mathcal{D}(s, \mathcal{R}, \mathcal{T}) = \frac{1}{2} \int_\Omega (s\Phi_S(\mathbf{x}) - \Phi_T(\mathcal{A}\mathbf{x}))^2 d\mathbf{x}. \tag{16}
$$

This criterion measures the dissimilarity between the distance values of image points on one image and that of the transformed points by A on the other image.

Note that, in some cases, the two input shapes may not produce signed distance representations that are equally defined in a fixed image domain. In addition, the implicit representation has one dimension higher than the original shapes and then its efficiency in registration is of big concern. To cope with these two issues, one can consider a narrow band formed of points that are a distance ϵ away from the source shape and their projections on the target,

$$
\mathcal{D}(s, \mathcal{R}, \mathcal{T}) = \frac{1}{2} \int_\Omega \delta_\epsilon(\Phi_S(\mathbf{x}), \Phi_T(\mathcal{A}\mathbf{x})) \cdot [s\Phi_S(\mathbf{x}) - \Phi_T(\mathcal{A}\mathbf{x})]^2 d\mathbf{x}, \tag{17}
$$

where,

$$\delta_\epsilon(a, b) = \begin{cases} 0, & \text{if } \min(|a|, |b|) > \epsilon, \\ \\ 1, & \text{otherwise.} \end{cases}$$

The corresponding Euler-Lagrange equations to each transformation parameter are given by:

$$\frac{d}{dt}s = \int_\Omega \delta_\epsilon(\Phi_S, \Phi_T) \cdot [\Phi_S(\mathbf{x}) - \nabla\Phi_T^T(\mathcal{A}\mathbf{x}) \begin{pmatrix} x\cos\theta + y\sin\theta \\ -x\sin\theta + y\cos\theta \end{pmatrix}] \cdot \mathbf{r}d\mathbf{x}, \quad (18)$$

$$\frac{d}{dt}\theta = \int_\Omega \delta_\epsilon(\Phi_S, \Phi_T) \cdot [s\nabla\Phi_T^T(\mathcal{A}\mathbf{x}) \begin{pmatrix} -x\sin\theta + y\cos\theta \\ -x\cos\theta - y\sin\theta \end{pmatrix}] \cdot \mathbf{r}d\mathbf{x},$$

$$\frac{d}{dt}\mathcal{T}_x = \int_\Omega \delta_\epsilon(\Phi_S, \Phi_T)\frac{\partial\Phi_T}{\partial x}(A\mathbf{x}) \cdot \mathbf{r}d\mathbf{x},$$

$$\frac{d}{dt}\mathcal{T}_y = \int_\Omega \delta_\epsilon(\Phi_S, \Phi_T)\frac{\partial\Phi_T}{\partial y}(A\mathbf{x}) \cdot \mathbf{r}d\mathbf{x},$$

where $\mathbf{r}(\mathbf{x}) = s\Phi_S(\mathbf{x}) - \Phi_T(\mathcal{A}\mathbf{x})$. A gradient descent scheme can be used to solve these equations. Fig. 17(b) and 16(b) show few examples of global alignment of different shapes using this model.

D. Affine Alignment

Consider a more general transformation (to be recovered) $\mathcal{A} \doteq \mathcal{A}(\mathcal{S}, \mathcal{R}, \mathcal{T})$, defined by:

$$\mathcal{A}\mathbf{x} = \mathcal{S}.\mathcal{R}.\mathbf{x} + \mathcal{T} \qquad (19)$$

$$= \begin{pmatrix} s_x & 0 \\ 0 & s_y \end{pmatrix} \cdot \begin{pmatrix} \cos\theta & \sin\theta \\ -\sin\theta & \cos\theta \end{pmatrix} \cdot \begin{pmatrix} x \\ y \end{pmatrix} + \begin{pmatrix} \mathcal{T}_x \\ \mathcal{T}_y \end{pmatrix}. \qquad (20)$$

The minimization of the cost function given by Eq. (17) fails to produce accurate results in this case because of the anisotropic scales (different scales in the $x-$ and $y-$directions). One way of coping with this issue is to represent the input shapes using the *VDF* representation (see chapter II).

In this work, a different way of dealing with scale variations using the signed distance

35

representation is proposed. A **new** dissimilarity criterion is introduced and its potential is shown when compared to the homogeneous scale-based and the *VDF*-based criteria (see Eq. (17) and Eq. (24), respectively).

1. *VDF*-Based Dissimilarity Measure

Let V_S and V_T be the *VDF* representations of the shapes, S and T, respectively. First, it is clear that the *VDF* representation is invariant to translation. Now, let $\widehat{V}_S$ denote the *VDF* obtained after transforming V_S by $\mathcal{A}$. The set $\widehat{V}_S^{-1}(\mathbf{0})$ implicitly represents a shape $\widehat{S}$ which corresponds to the warped shape $\mathcal{A}(S)$, up to a rotation and some scale effects. Given an image point $\mathbf{x} \in \Omega_S$ on the source shape, let $\widehat{\mathbf{x}}$ be its transform by $\mathcal{A}$, i.e., $\widehat{\mathbf{x}} = \mathcal{A}\mathbf{x}$, and let $\mathbf{x}_0 = V_S(\mathbf{x})$ be the closet point to $\mathbf{x}$ on S. One can easily show that

$$V_T(\mathcal{A}(\mathbf{x})) = V_T(\widehat{\mathbf{x}}) = \widehat{\mathbf{x}} - \widehat{\mathbf{x}}_0 \tag{21}$$

$$= \mathcal{S}.\mathcal{R}(\mathbf{x} - \mathbf{x}_0) = \mathcal{S}.\mathcal{R}.V_S(\mathbf{x}). \tag{22}$$

Based on this property of the *VDF* representation under affine transformation, one can consider the following *SSD* criterion to achieve global alignment of the two input shapes:

$$\mathcal{D}(\mathcal{S},\mathcal{R},\mathcal{T}) = \frac{1}{2}\int_\Omega \|\, \mathcal{S}.\mathcal{R}.V_S(\mathbf{x}) - V_T(\mathcal{A}\mathbf{x})\,\|^2\, d\mathbf{x}. \tag{23}$$

To reduce the computational complexity of minimizing this criterion, one can limit the matching space to a narrow band around the two given shapes. This leads to

$$\mathcal{D}(\mathcal{S},\mathcal{R},\mathcal{T}) = \frac{1}{2}\int_\Omega \delta_\epsilon(V_S(\mathbf{x}), V_T(\mathcal{A}\mathbf{x}))\cdot \|\, \mathcal{S}.\mathcal{R}.V_S(\mathbf{x}) - V_T(\mathcal{A}\mathbf{x})\,\|^2\, d\mathbf{x}, \tag{24}$$

where δ_ϵ is given by

$$\delta_\epsilon(\mathbf{a}, \mathbf{b}) = \begin{cases} 0, & \text{if } \min(\|\mathbf{a}\|, \|\mathbf{b}\|) > \epsilon, \\ 1, & \text{if } \min(\|\mathbf{a}\|, \|\mathbf{b}\|) \leq \epsilon. \end{cases}$$

The corresponding Euler-Lagrange equations to each parameter of the transformation A are given by:

$$\frac{d}{dt}s = \int_\Omega \delta_\epsilon(V_S, V_T).\mathbf{r}^T \cdot [\nabla_s \mathcal{S}.\mathcal{R}.V_S(\mathbf{x}) - \nabla V_T^T(A\mathbf{x})\nabla_s(Ax)], \qquad (25)$$

$$\frac{d}{dt}\theta = \int_\Omega \delta_\epsilon(V_S, V_T).\mathbf{r}^T \cdot [\mathcal{S}\nabla_\theta \mathcal{R}V_S(\mathbf{x}) - \nabla V_T^T(A\mathbf{x})\nabla_\theta(Ax)],$$

$$\frac{d}{dt}t = \int_\Omega \delta_\epsilon(V_S, V_T).\mathbf{r}^T \cdot [\nabla V_T^T(A\mathbf{x})\nabla_t(Ax)],$$

where, $\mathbf{r}(\mathbf{x}) = \mathcal{S}.\mathcal{R}.V_S(\mathbf{x}) - V_T(A\mathbf{x})$, $s \in \{s_x, s_y\}$, and $t \in \{\mathcal{T}_x, \mathcal{T}_y\}$. Each of these equations is solved using the gradient method.

2. Proposed *SDF*-Based Dissimilarity Measure

Let Φ_S and Φ_T be the signed distance representations of the shapes, S and T, respectively. Let's denote by $\widehat{\Phi}_S$ the transformed level set function Φ_S by A, the zero crossing of $\widehat{\Phi}_S$ corresponds to a new shape that will be denoted $\widehat{S}$.

Now, let $\mathbf{x}$ be an image point, and let $\widehat{\mathbf{x}} = A\mathbf{x}$ denote its image by A. Then, one has,

$$\widehat{\Phi}_S(\widehat{\mathbf{x}}) = dist(\widehat{\mathbf{x}}, \widehat{S}) = \min_{\widehat{\mathbf{y}} \in \widehat{S}} \|\widehat{\mathbf{x}} - \widehat{\mathbf{y}}\| = \min_{\mathbf{y} \in S} \|\mathcal{S}\mathcal{R}(\mathbf{x} - \mathbf{y})\|,$$

$$\leq \min_{\mathbf{y} \in S} \|\mathcal{S}\|.\|\mathbf{x} - \mathbf{y}\| = \|\mathcal{S}\|.dist(\mathbf{x}, S),$$

where, $\|\mathcal{S}\| = \max(|s_x|, |s_y|)$ is the infinity norm of the diagonal matrix $\mathcal{S}$. Hence, we have the following inequality:

$$\widehat{\Phi}_S(\widehat{\mathbf{x}}) \leq \|\mathcal{S}\|.\Phi_S(\mathbf{x}). \qquad (26)$$

In order to align the two input shapes, one could seek a transformation A that minimizes the following cost function:

$$\widehat{\mathcal{D}}(\mathcal{S}, \mathcal{R}, \mathcal{T}) = \frac{1}{2}\int_\Omega (\widehat{\Phi}_S(A\mathbf{x}) - \Phi_T(A\mathbf{x}))^2 d\mathbf{x}.$$

Based on the inequality derived in (26), one can easily show that

$$\int_\Omega (\widehat{\Phi}_S(A\mathbf{x}) - \Phi_T(A\mathbf{x}))^2 d\mathbf{x} \leq \int_\Omega (\|\mathcal{S}\|\Phi_S(\mathbf{x}) - \Phi_T(A\mathbf{x}))^2 d\mathbf{x}.$$

Hence, we propose to minimize the following **new** cost function in order to recover the parameters of the transformation $\mathcal{A}$,

$$\mathcal{D}(\mathcal{S}, \mathcal{R}, \mathcal{T}) = \frac{1}{2}\int_\Omega (\|\mathcal{S}\|\Phi_S(\mathbf{x}) - \Phi_T(\mathcal{A}\mathbf{x}))^2 d\mathbf{x}, \tag{27}$$

Again, one can restrict the registration space to a narrow band formed of points that are a distance ϵ away from the source shape and their projections on the target shape,

$$\mathcal{D}(\mathcal{S}, \mathcal{R}, \mathcal{T}) = \frac{1}{2}\int_\Omega \delta_\epsilon(\Phi_S(\mathbf{x}), \Phi_T(\mathcal{A}\mathbf{x}))[\|\mathcal{S}\|\Phi_S(\mathbf{x}) - \Phi_T(\mathcal{A}\mathbf{x})]^2 d\mathbf{x}, \tag{28}$$

where,

$$\delta_\epsilon(a, b) = \begin{cases} 0, & \text{if } \min(|a|, |b|) > \epsilon, \\ 1, & \text{otherwise.} \end{cases}$$

Each parameter of the transformation $\mathcal{A}$ is recovered by solving its corresponding Euler-Lagrange equations using a gradient descent scheme:

$$\frac{ds_x}{dt} = \int_\Omega [\frac{d\|\mathcal{S}\|}{ds_x}\Phi_S(\mathbf{x}) - \nabla\Phi_T^T(A\mathbf{x})\begin{pmatrix} x\cos\theta + y\sin\theta \\ 0 \end{pmatrix}].r(\mathbf{x})d\mathbf{x}, \tag{29}$$

$$\frac{ds_y}{dt} = \int_\Omega [\frac{d\|\mathcal{S}\|}{ds_y}\Phi_S(\mathbf{x}) - \nabla\Phi_T^T(A\mathbf{x})\begin{pmatrix} 0 \\ -x\sin\theta + y\cos\theta \end{pmatrix}].r(\mathbf{x})d\mathbf{x},$$

$$\frac{d\theta}{dt} = \int_\Omega [\nabla\Phi_T^T.\begin{pmatrix} s_x(-x\sin\theta + y\cos\theta) \\ s_y(-x\cos\theta - y\sin\theta) \end{pmatrix}].r(\mathbf{x})d\mathbf{x},$$

$$\frac{d\mathcal{T}_x}{dt} = \int_\Omega \frac{\partial\Phi_T}{\partial x}(A\mathbf{x}).r(\mathbf{x})d\mathbf{x},$$

$$\frac{d\mathcal{T}_y}{dt} = \int_\Omega \frac{\partial\Phi_T}{\partial y}(A\mathbf{x}).r(\mathbf{x})d\mathbf{x},$$

where

$$r(\mathbf{x}) = \delta_\epsilon(\Phi_S(\mathbf{x}), \Phi_T(\mathbf{x}))(\|\mathcal{S}\|\Phi_S(\mathbf{x}) - \Phi_T(A\mathbf{x})),$$

and ∇ denotes the gradient operator. Note that, since only positive scale values are considered, the terms $\frac{d\|\mathcal{S}\|}{ds_{x;y}}$ equal either 0 or 1.

Three Dimensional Case   The proposed *SSD* criterion given by (28) is generalized in a straightforward manner to the three dimensional case. In this case, the similarity transform $\mathcal{A}$ is defined by:

$$\mathcal{A}\mathbf{x} = \mathcal{S}.\mathcal{R}.\mathbf{x} + \mathcal{T},$$

where,

$$\mathcal{S} = \begin{pmatrix} s_x & 0 & 0 \\ 0 & s_y & 0 \\ 0 & 0 & s_z \end{pmatrix}, \quad \mathcal{T} = \begin{pmatrix} \mathcal{T}_x \\ \mathcal{T}_y \\ \mathcal{T}_z \end{pmatrix}.$$

and

$$\mathcal{R} = \mathcal{R}(\theta_x, \theta_y, \theta_z) = \mathcal{R}_x \cdot \mathcal{R}_y \cdot \mathcal{R}_z,$$

with

$$\mathcal{R}_x = \begin{pmatrix} 1 & 0 & 0 \\ 0 & \cos\theta_x & \sin\theta_x \\ 0 & -\sin\theta_x & \cos\theta_x \end{pmatrix}, \mathcal{R}_y = \begin{pmatrix} \cos\theta_y & 0 & -\sin\theta_y \\ 0 & 1 & 0 \\ \sin\theta_y & 0 & \cos\theta_y \end{pmatrix}, \mathcal{R}_z = \begin{pmatrix} \cos\theta_z & \sin\theta_z & 0 \\ -\sin\theta_y & \cos\theta_z & 0 \\ 0 & 0 & 1 \end{pmatrix}.$$

In this case, the cost function, to be minimized in order to recover the nine parameters of the transformation $\mathcal{A}$, is given as in Eq. (28) by:

$$\mathcal{D}(\mathcal{S}, \mathcal{R}, \mathcal{T}) = \frac{1}{2} \int_{\Omega} (\|\mathcal{S}\| \Phi_S(\mathbf{x}) - \Phi_T(A\mathbf{x}))^2 d\mathbf{x},$$

where, $\|\mathcal{S}\| = \max(|s_x|, |s_y|, |s_y|)$ is the infinity norm of the matrix $\mathcal{S}$.

As was done in the 2D case, one can consider a narrow band formed of points that are a distance ϵ away from the source shape and their projections on the target shape (see Eq.(28)), and solve the following Euler-Lagrange equations for each of the nine parameters

of $\mathcal{A}$ using a gradient descent scheme:

$$\frac{ds_x}{dt} = \int_\Omega [\frac{d\|\mathcal{S}\|}{ds_x}\Phi_S(\mathbf{x}) - \nabla\Phi_T^T(A\mathbf{x})\begin{pmatrix} R_{11}x + R_{12}y + R_{13}z \\ 0 \\ 0 \end{pmatrix}].r(\mathbf{x})d\mathbf{x}, \quad (30)$$

$$\frac{ds_y}{dt} = \int_\Omega [\frac{d\|\mathcal{S}\|}{ds_y}\Phi_S(\mathbf{x}) - \nabla\Phi_T^T(A\mathbf{x})\begin{pmatrix} 0 \\ R_{21}x + R_{22}y + R_{23}z \\ 0 \end{pmatrix}].r(\mathbf{x})d\mathbf{x},$$

$$\frac{ds_z}{dt} = \int_\Omega [\frac{d\|\mathcal{S}\|}{ds_x}\Phi_S(\mathbf{x}) - \nabla\Phi_T^T(\mathcal{A}\mathbf{x})\begin{pmatrix} 0 \\ 0 \\ R_{31}x + R_{32}y + R_{33}z \end{pmatrix}].r(\mathbf{x})d\mathbf{x},$$

$$\frac{d\theta_x}{dt} = \int_\Omega [\nabla\Phi_T^T(\mathcal{A}\mathbf{x}).\mathcal{S}.\mathcal{R}_x'.\mathcal{R}_y.\mathcal{R}_z.\mathbf{x}].r(\mathbf{x})d\mathbf{x},$$

$$\frac{d\theta_y}{dt} = \int_\Omega [\nabla\Phi_T^T(\mathcal{A}\mathbf{x}).\mathcal{S}.\mathcal{R}_x.\mathcal{R}_y'.\mathcal{R}_z.\mathbf{x}].r(\mathbf{x})d\mathbf{x},$$

$$\frac{d\theta_z}{dt} = \int_\Omega [\nabla\Phi_T^T(\mathcal{A}\mathbf{x}).\mathcal{S}.\mathcal{R}_x.\mathcal{R}_y.\mathcal{R}_z'.\mathbf{x}].r(\mathbf{x})d\mathbf{x},$$

$$\frac{d\mathcal{T}_x}{dt} = \int_\Omega \frac{\partial\Phi_T}{\partial x}(\mathcal{A}\mathbf{x}).r(\mathbf{x})d\mathbf{x},$$

$$\frac{d\mathcal{T}_y}{dt} = \int_\Omega \frac{\partial\Phi_T}{\partial y}(\mathcal{A}\mathbf{x}).r(\mathbf{x})d\mathbf{x},$$

$$\frac{d\mathcal{T}_z}{dt} = \int_\Omega \frac{\partial\Phi_T}{\partial z}(\mathcal{A}\mathbf{x}).r(\mathbf{x})d\mathbf{x},$$

where $r(\mathbf{x}) = \delta_\epsilon(\Phi_S(\mathbf{x}), \Phi_T(\mathbf{x}))(\|\mathcal{S}\|\Phi_S(\mathbf{x}) - \Phi_T(A\mathbf{x}))$, ∇ denotes the gradient operator,

and

$$\mathcal{R}_x' = \begin{pmatrix} 0 & 0 & 0 \\ 0 & -\sin\theta_x & \cos\theta_x \\ 0 & -\cos\theta_x & -\sin\theta_x \end{pmatrix}, \mathcal{R}_y' = \begin{pmatrix} -\sin\theta_y & 0 & -\cos\theta_y \\ 0 & 0 & 0 \\ \cos\theta_y & 0 & -\sin\theta_y \end{pmatrix}, \mathcal{R}_z' = \begin{pmatrix} -\sin\theta_z & \cos\theta_z & 0 \\ -\cos\theta_y & -\sin\theta_z & 0 \\ 0 & 0 & 0 \end{pmatrix}.$$

Note that, since only positive scale values are allowed, the terms $\frac{d\|\mathcal{S}\|}{ds_{x;y;z}}$ equal either 0 or 1.

E. 2D Empirical Evaluation of the Proposed Global Alignment Model

As mentioned earlier, each parameter of the global transformation is recovered by solving its corresponding evolution equation (Eqn. 29) using a gradient descent scheme.

	Corpus Callosum				Fish #1				Bunny #3			
	GT	**M1**	**M2**	**M3**	**GT**	**M1**	**M2**	**M3**	**GT**	**M1**	**M2**	**M3**
s_x	1.5	1.50	1.42	0.99	0.6	0.60	0.61	0.71	1.0	1.01	0.90	0.622
s_y	0.9	0.90	0.89	—	1.0	1.00	1.0	—	0.45	0.45	0.51	—
θ°	10	10	10	22.75	60	60	60	52.03	-45	-44.69	-44.9	-16.47
t_x	2.5	1.61	-1.70	0.14	-3.5	-4.17	-4.62	-5.82	10	9.12	-2.28	-0.15
t_y	0.0	-0.6	-2.72	2.50	-5	-5.16	-4.42	-7.52	5	4.78	-2.80	0.01

This type of optimization methodology is very sensitive to initial conditions. The convexity of the proposed objective function (Eqn. 28) is not guaranteed and hard to prove in the space of the five parameters. However, we propose to analyze the characteristics of this function in the space of two parameters while the remaining parameters are fixed. To this end, we consider two instances of the "Hand" shape shown in the 3rd column of Fig. 14. The exact parameters that transform one instance towards the other are obviously unity scales, zero rotation, and zero translations. Once at a time, we fix three of these parameters and study the behavior of the registration criterion in terms of the remaining two parameters. Different combinations were tested, some of which are presented in Fig. 15. We have considered the following ranges for each parameter: $\theta \in [-\frac{\pi}{3}, \frac{\pi}{3}]$, s_x, $s_y \in [0.5, 2.0]$, and $\mathcal{T}_x$, $\mathcal{T}_y \in [-50, 50]$. For each test, the unknown parameter ranges were quantized using uniform sampling. The corresponding results (Fig. 15) show that, for each case, the proposed cost function exhibits nice smoothness and convexity properties. In addition, for each of the shown combinations, the energy is smooth and has a single global minimum that is attained at the optimal point in the space of the two unknown parameters. This gives a good indication on the well-behaved minimization criterion and its convergence properties.
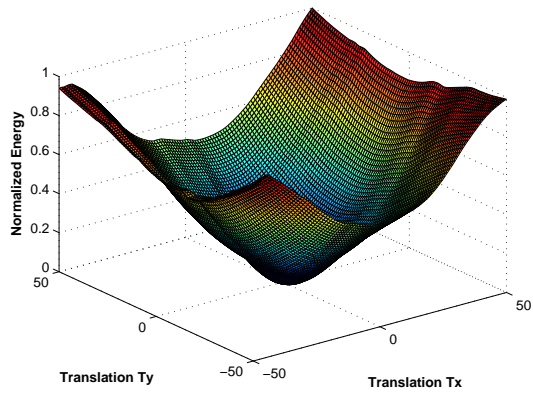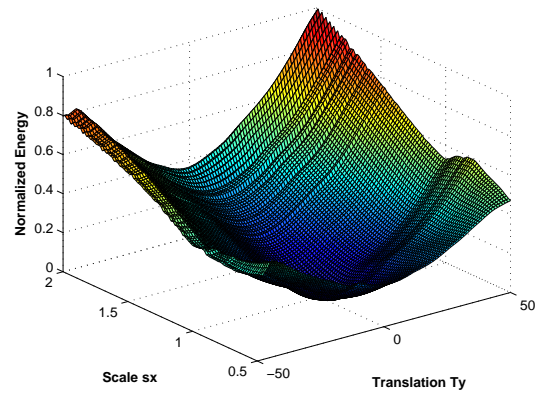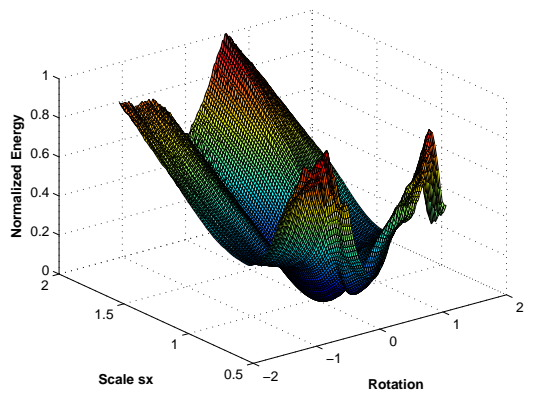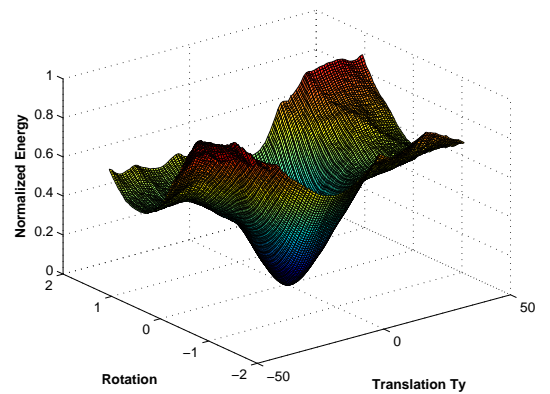
FIGURE 15 – Empirical evaluation of the proposed criterion (Eq. 28). Unknowns are: (a) T_x and T_y; (b) s_x and s_y; (c) θ and s_y; (d) θ and T_y.
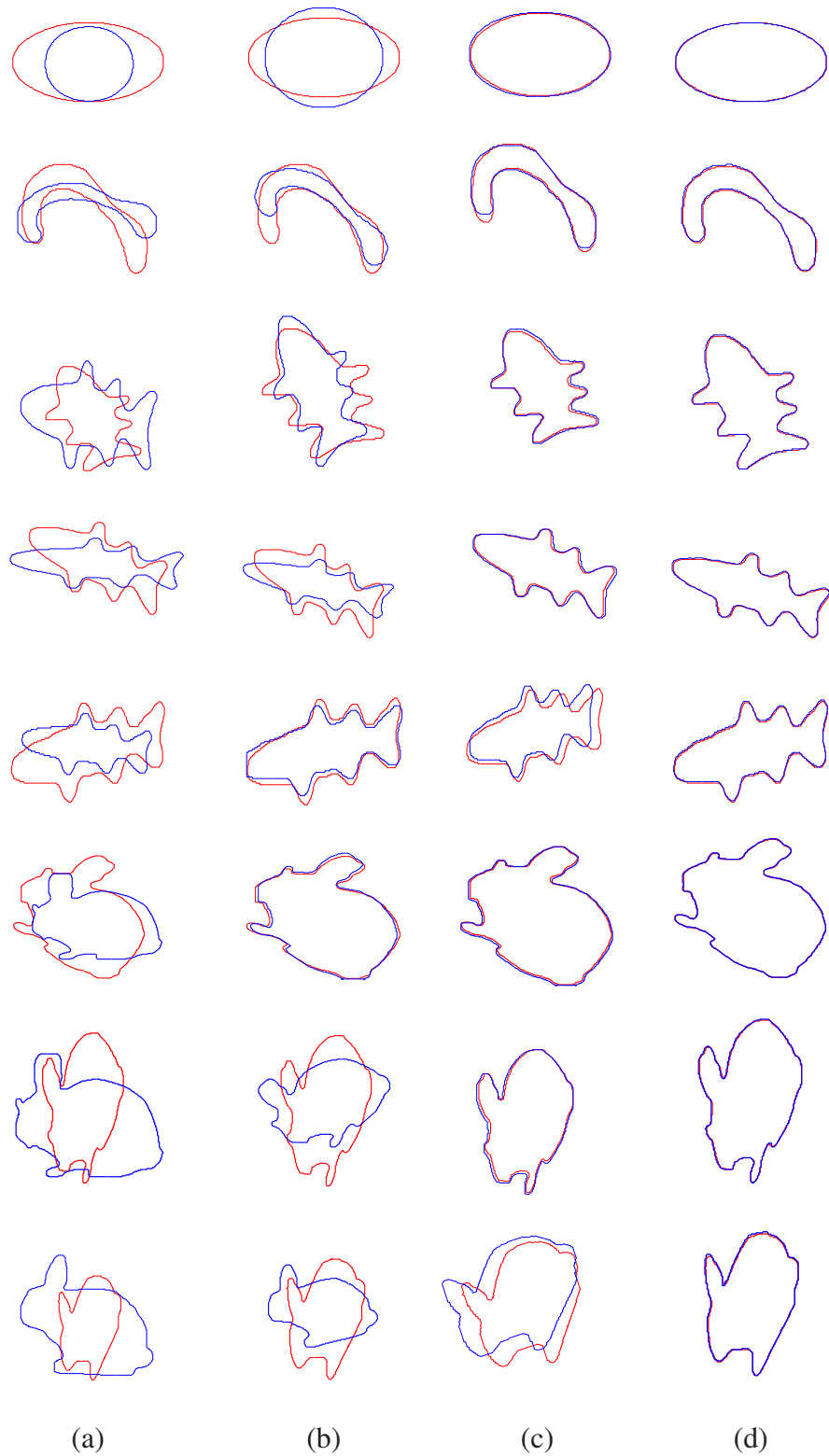
FIGURE 16 – Global registration. (a) Input Shapes (blue:source; red: target). (b) Registration results using the isotropic-scale based model 17. (c) Registration results using the *VDF*-based model (Eq. 24). (d) Registration using the proposed model (Eq. 28). Note how accurate the registration results are when using the proposed model; see Table. 1 for some comparisons of recovered vs. ground truth parameters using both criteria.

TABLE 2

EXECUTION TIME COMPARISONS BETWEEN THE PROPOSED ALIGNMENT MODEL AND THE *VDF*-BASED ALIGNMENT MODEL FOR THE REGISTRATION EXAMPLES PRESENTED IN FIG. 16. NOTE THAT, FOR EACH CASE, THE REPORTED TIMES CORRESPOND TO THE COMPUTATION OF THE IMPLICIT REPRESENTATION AND THE ITERATION PROCESS. THE TIMES ARE IN SECONDS.

	The proposed Alignment Model	The *VDF*-based Model
Circle	139.67	208.67
Corpus callosum	206.82	300.57
Fish #1	102.23	141.26
Fish #2	180.68	221.35
Fish #3	169.77	263.69
Bunny #1	147.20	271.57
Bunny #2	157.76	219.87
Bunny #3	296.67	538.67

F. Experimental Results

To quantitatively validate the proposed model (Eq. 28), several 2D registration experiments were performed. For each trial, the source shape is fixed and the target shape is generated by deforming the source using a known transformation $\mathcal{A} = \mathcal{A}(\mathcal{S}, \mathcal{R}, \mathcal{T})$ which will be considered as the Ground Truth (*GT*). Then, the proposed model is used to recover the optimal alignment parameters. The recovered parameters are then compared to the *GT* and to those obtained when using the homogeneous scale-based measure (17) [7] and to those obtained using the *VDF*-based model (24).   In each case, the proposed algorithm leads to more accurate results and one can see that the isotropic scale-based criterion completely fails when the difference between s_x and s_y is large (see e.g., first and last two rows of Fig. 16). In addition, even though the *VDF*-based model did lead to relatively good results in some of the considered cases, this model executes slower compared to the the proposed model (28) as reported in table 2. For some of the presented examples, such as the examples on the 5th and that on the last rows of Fig. 16, the *VDF*-based criterion failed
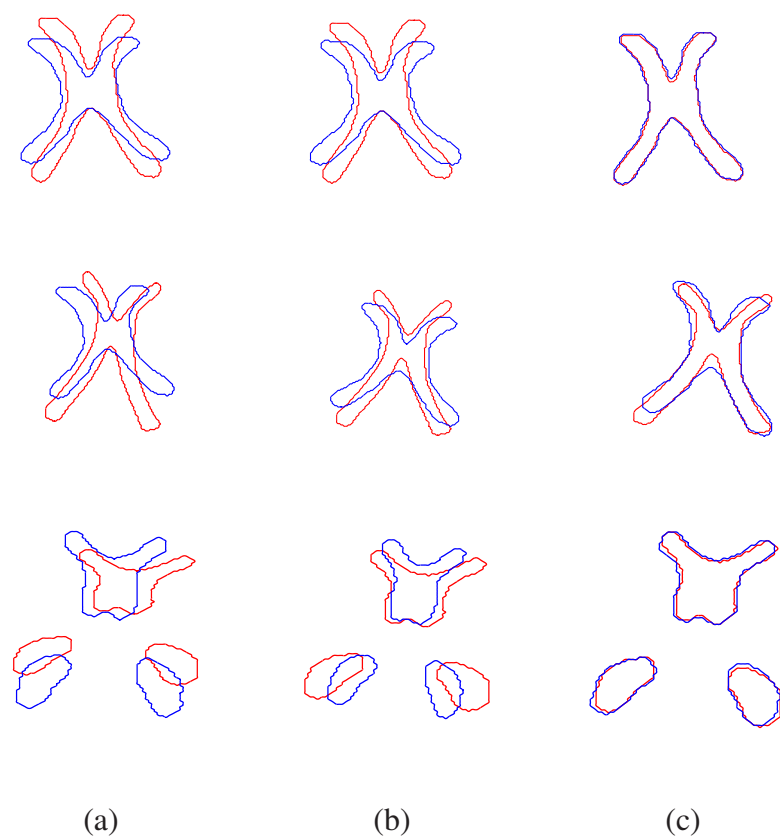
FIGURE 17 – More global registration results. (a) Input Shapes. (b) Registration using homogeneous scale-based measure. (c) Registration using the proposed registration model (Eq. 28).
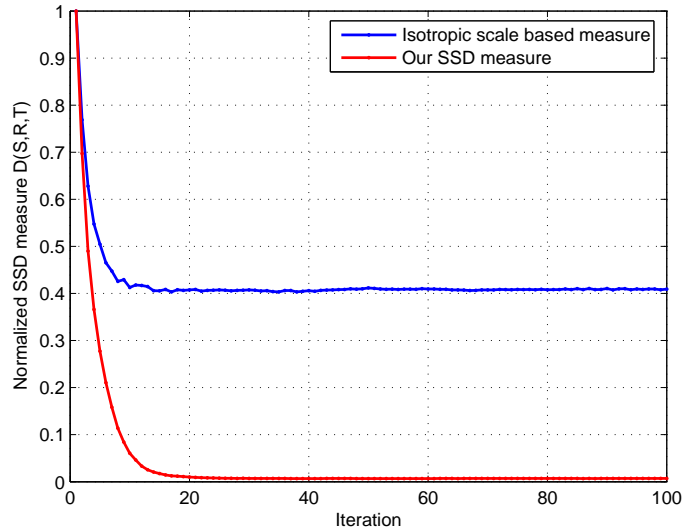
FIGURE 18 – Convergence of the new *SSD* measure (Eq. 28) and comparison to rigid matching case for the examples shown on the 1st row of Fig. 17. History of $\mathcal{D}(\mathcal{S}, R, T)$ for both cases: the proposed measure (red) and isotropic scale-based measure (blue).

to accurately align the two shapes. For these specific cases, many trials were ran for the *VDF* representation, but none did lead to better result. Comparisons between the recovered parameters when using these three registration models are summarized on table 1.

Another set of experiments was carried out to compare the registration performance of the proposed criterion with the other two criteria by registering pairs of arbitrary shapes that belong to the same class. Some of these results are presented on Fig. 17 and Fig. 19 respectively. On can easily notice from these figures that the proposed method outperforms the other two models.

Figure 18 stresses the out-performance of the proposed criterion over the isotropic scale-based one. This figure shows the history of the proposed *SSD* measure and that of the isotropic scale-based measure vs. iteration for the example shown on the 1st row of Fig. 17. One can clearly see that the value of the proposed distance functional drops faster at each iteration step. In addition, contrary to the proposed *SSD* measure, the isotropic scale-based measure stops decreasing at a value far from the ideal minimum leading to less accurate results when compared to ours.

Finally, several three dimensional experiments were carried out to test the proposed

46
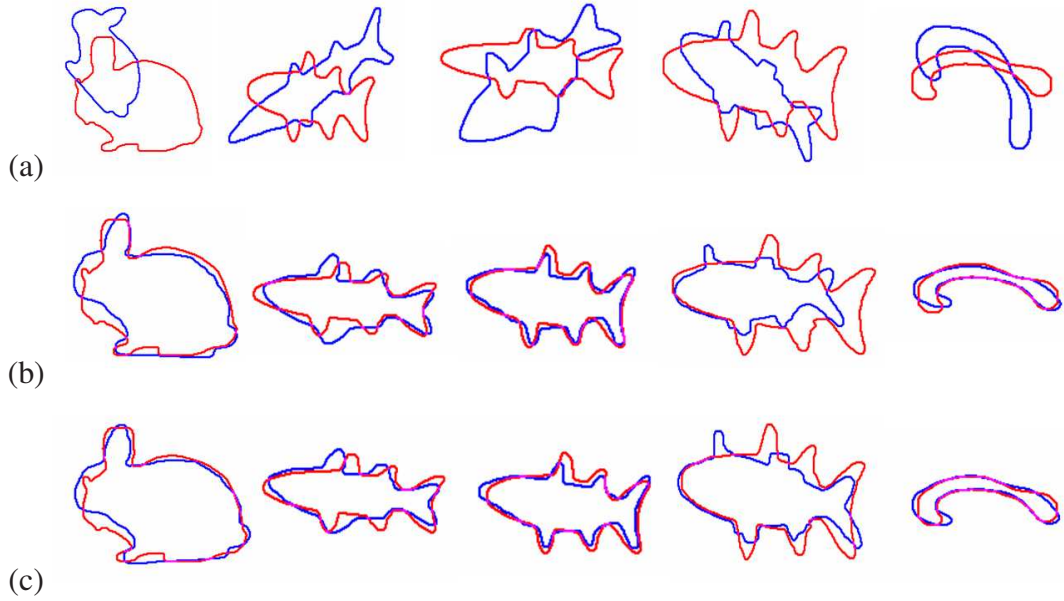
FIGURE 19 – Global registration: Proposed Signed Distance-based vs. *VDF*-based affine registrations. (a) Input Shapes. (b) Affine Registration using the *VDF* representation (Eq. 24). (c) Affine Registration using the new *SSD* criterion (Eq. 28).

global alignment algorithm. A 3D tooth shape of size $117 \times 117 \times 125$ is used as the target shape. This shape is used to generate various deformed instances by randomly assigning different values to the transformation parameters (s_x, s_y, s_z, θ_x, θ_y, θ_z, t_x, t_y, and t_z). For each trial, the generated deformed shape is used as the source and is registered to the target shape using the proposed algorithm. Some of the corresponding results are shown in Fig. 20. For each trial, one can notice the high accuracy of the registration results.

G. Application: Statistical Modelling of Shapes

A major application that may greatly benefit from the proposed registration model consists of building compact representations of anatomical structures from a set of training samples using the Principal Component Analysis (*PCA*) [73]. This application is a critical component of various medical image analyzes including statistical modelling of anatomical structures, and shape prior learning which can be used to devise robust segmentation algorithms (e.g., see [39]).

The alignment process allows one to capture shape variations in the databases without
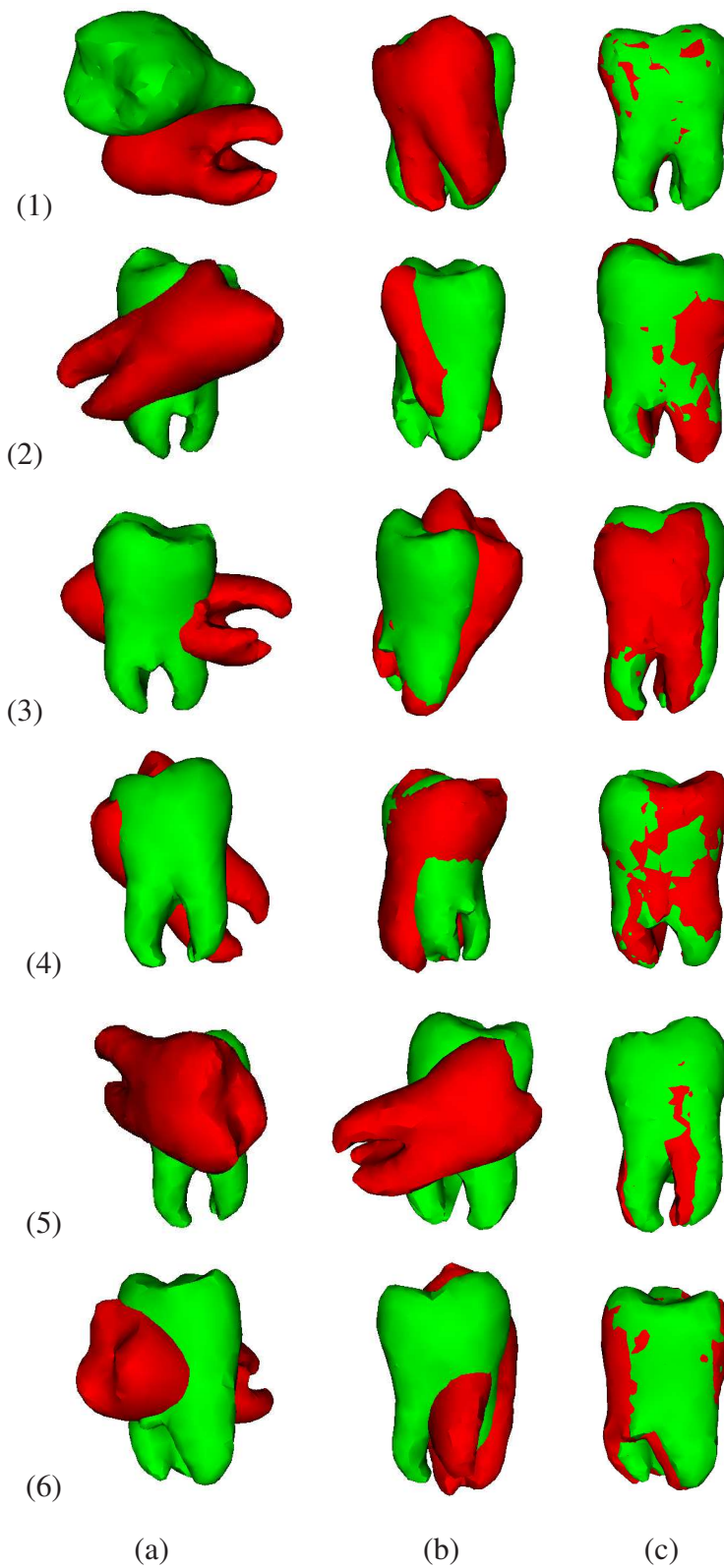
FIGURE 20 – Global registration of 3D shapes of five tooth shapes. (a) Input Shapes. (b) An intermediate state. (c) Final registration result using the proposed registration model (Eq. 28).
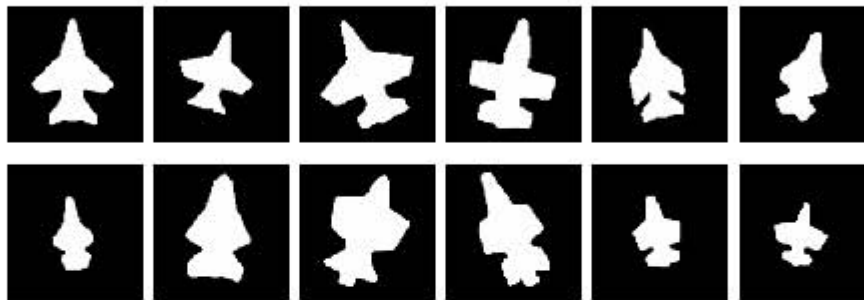
FIGURE 21 – Training data. Twelve 2D shape models of the fighter jet before alignment.
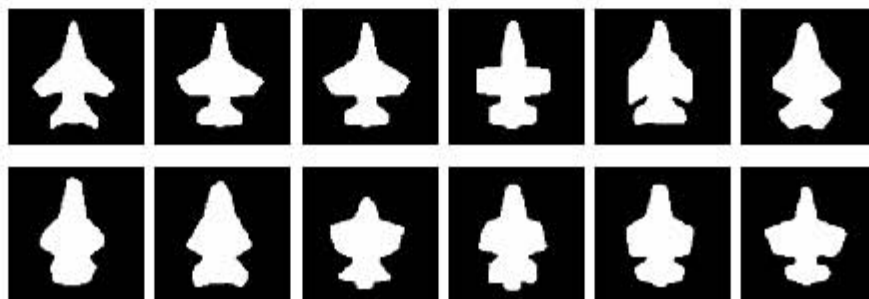
FIGURE 22 – Training data. Twelve 2D shape models of the fighter jet after alignment.

(a)   (b)
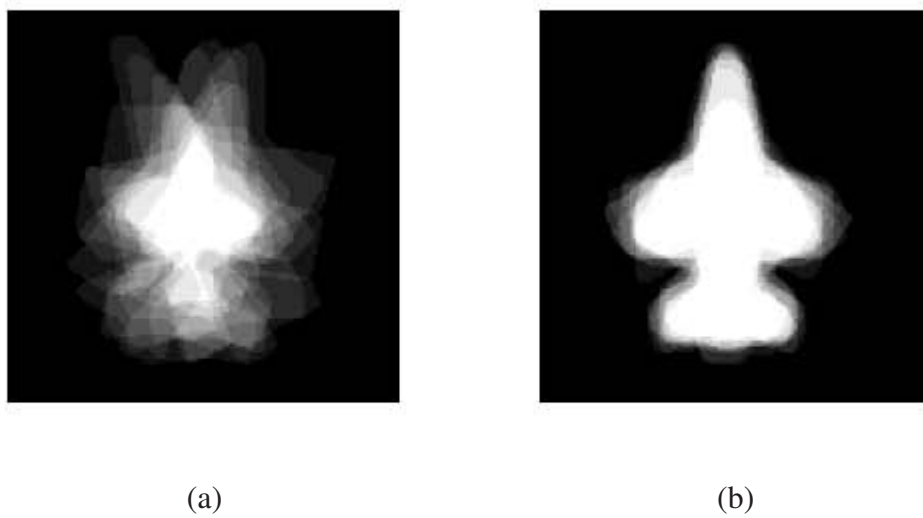
FIGURE 23 – Shape overlap before (a) and after (b) alignment in the fighter data base.

FIGURE 24 – Training data. Twelve 2D shape models of the digit four before alignment.

FIGURE 25 – Training data. Twelve 2D shape models of the digit four after alignment using the proposed alignment process (28).

(a)   (b)
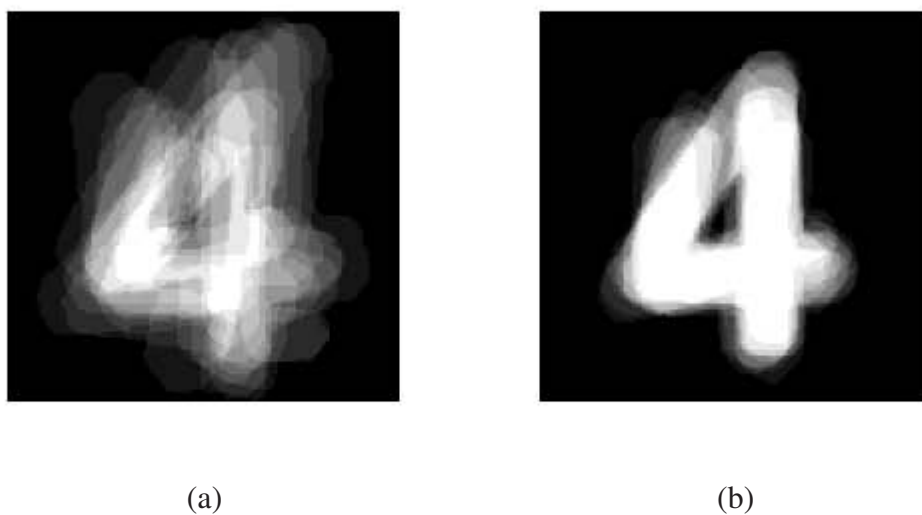
FIGURE 26 – Shape overlap before (a) and after (b) alignments in the digit four data base.
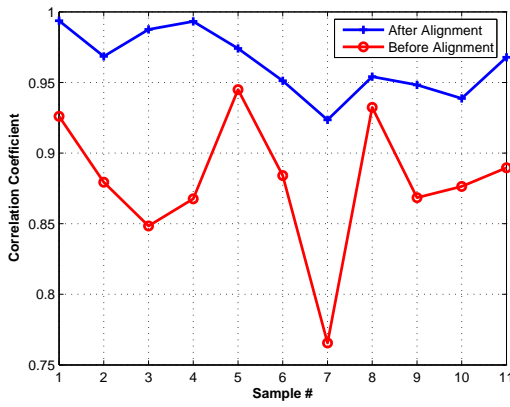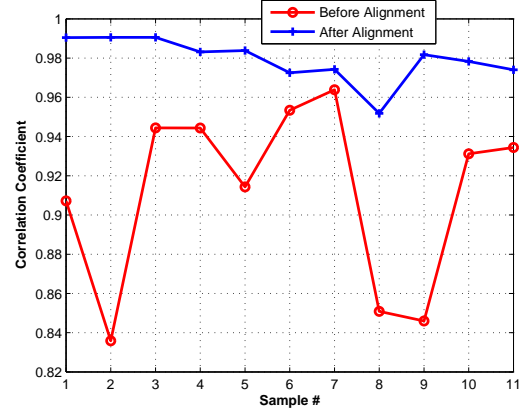
FIGURE 27 – Correlation coefficients before and after alignments for (a) the fighter jet data base and (b) the number four data base. Note that the sample number starts from 2 to 12 for each data base.

interference from pose variations. This problem is addressed using the proposed global registration model. As an example, the statistical modelling of two different shapes: a fighter jet shape and the digit four shape are presented. A training set consisting of twelve binary representation of each of these two shapes are presented in Fig. 21 and Fig. 24 respectively. The proposed global registration approach is first applied to align the shapes in each of these training sets. To this end, the first shape, within each data base, is chosen as reference. The alignment results are shown on Fig. 22 and Fig. 25 for both training data sets.

To qualitatively assess the accuracy of the alignment results, the overlap images before and after alignments for each of these shapes are shown in Fig. 23 and Fig. 26 respectively. These overlap images are generated by stacking together all the binary images within each group and adding them together in a pixel wise fashion. The clear increase in the amount of overlap between the after and before alignment images illustrates the effectiveness of the proposed alignment process. Quantitatively, the correlation coefficient is computed as a measure of similarity between these shapes before and after alignments. This measure is given by

$$\gamma = \frac{E[(\Phi_1 - \mu_1)(\Phi_2 - \mu_2)]}{\sigma_1 \sigma_2}, \tag{31}$$

where, Φ_1 and Φ_2 are the implicit representations of the input shapes to be compared and μ_i and σ_i denote the mean and standard deviations of each of these representations over the image domain occupied by the shapes. Finally, $E(\cdot)$ stands for the mathematical expectation. The closet the correlation coefficient is to one, the more accurate is the alignment result.

For each data base, the correlation coefficients before and after alignments are plotted and shown on Fig. 27(a-b). Note how the proposed registration algorithm leads to accurate alignments.

1. Modelling Shape Variations

For each training data set, let $\Psi_1, \Psi_2, \ldots, \Psi_N$ denote the signed distance representations of the N aligned shapes. These representation form a distribution in the Nd dimensional space in which they reside, where $d = r \times c$ is the size of the image domain occupied by each shape. Modelling this distribution allows one to generate new and plausible shapes "similar" to those in the original training set. To this end, the Principal Component Analysis (*PCA*)[3] plays a major role. The *PCA* reduces the dimensionality of the data by computing the main axes of the cloud of points represented by each point in the training set. By convention, the first principal component accounts for as much of the variability in the data as possible. The *PCA* approach can be summarized in the following steps:

1. Compute the mean of the data

$$\overline{\Phi} = \frac{1}{N} \sum_{i=1}^{N} \Psi_i. \tag{32}$$

2. Compute the mean-offsets, $\widetilde{\Psi}_i$'s, to capture the shape variabilities

$$\widetilde{\Psi} = \Psi_i - \overline{\Phi}. \tag{33}$$

---

[3]Principal component analysis also known as Karhunen-Loéve Transform (*KLT*) was originally introduced in 1933 by Harold Hotelling [74] as a method of dealing with redundancy in multivariate data.

3. Represent each mean-offset, $\widetilde{\Psi}_i$, as a column vector, $\widetilde{\psi}_i$, by stocking its column vectors on top of one another (recall that $\widetilde{\Psi}_i$ are 2D matrices of size $d = r \times c$). Then, form the shape variability matrix as follows:

$$S = [\widetilde{\psi}_1 \widetilde{\psi}_2 \cdots \widetilde{\psi}_N]. \tag{34}$$

Note that S is of size $d \times N$.

4. Perform an eigenvalue decomposition to factor the following covariance matrix of the data

$$\frac{1}{N} S S^T = U.\Sigma.U^T, \tag{35}$$

where, U is an $d \times N$ matrix whose columns are the d orthogonal modes of variations in the shape and Σ is an $d \times d$ diagonal matrix whose entries are the corresponding eigenvalues.

The ith principal mode, also known as the ith eigenshape, and denoted by Υ_i, can be determined by rearranging the column vectors of the matrix U back into the structure of a r-by-c rectangular grid. A maximum of N such eigenshapes are then generated, and will be denoted $\Phi_1, \Phi_2, \cdots, \Phi_N$

From a computational view point, the eigenvalues and eigenvectors of the covariance matrix, $\frac{1}{N} S S^T$, can be efficiently computed from the following smaller matrix of size $N \times N$

$$T = \frac{1}{N} S^T S. \tag{36}$$

One can easily show that if X_i is an eigenvector of T corresponding to the eigenvalue λ_i, then $Y_i = S.X_i$ is an eigenvector of $\frac{1}{N} S S^T$ associated with the same eigenvalue λ_i. Indeed,

$$
\begin{aligned}
\frac{1}{N} S S^T.Y_i &= \frac{1}{N} S S^T.(S.X_i) \tag{37}\\
&= S(\frac{1}{N} S^T S.X_i)\\
&= S(\lambda_i.X_i) = \lambda_i.S.X_i\\
&= \lambda.Y_i \quad \blacksquare
\end{aligned}
$$

Remarks:

- The eigenvector associated with the largest eigenvalue has the same direction as the first principal component; the eigenvector associated with the second largest eigenvalue determines the direction of the second principal component and so forth [75].

- Each eigenvalue λ_i reflects the amount of variance of shape variability associated with the corresponding eignenshape.

- The number of models, k, to be used to capture the prominent shape variations present in the training set can be chosen in different ways, but there is no universal number k that can be set in advance. The most common way of choosing k is as follows: Let $\vartheta_T = \sum_i \lambda_i$ denote the total variance of the data about the mean shape in the direction of the corresponding eigenshapes. Then, if one wishes to retain a proportion, p_v, of the total variance ϑ_T, the number k can be chosen such that

$$\sum_i^k \lambda_i \geq p_v . \vartheta_T. \tag{38}$$

- Once the number of modes to be retained for the shape representation, new shapes can be generated. The signed distance representation of such a shape is expressed as:

$$\Phi(\mathbf{x}) = \overline{\Phi}(\mathbf{x}) + \sum_{i=1}^k \omega_i \Phi_i(\mathbf{x}), \tag{39}$$

where $\mathbf{w} = (\omega_i)_i$ is the weight vector. By varying the elements of $\mathbf{w}$, various instances of the model represented by the training shapes can be generated. This can be seen on figures 28 and 29, where three modes are shown with a variation from $-2\lambda_i$ to $2\lambda_i$.

To illustrate the encoding of the shape variability for both data sets, Fig. 28 and Fig. 29 show the mean shape and its shape variations based on varying the first four principal modes from $-2\sqrt{\lambda_i}$ to $-2\sqrt{\lambda_i}$ for $i = 1, \cdots, 4$ for the fighter jet and the number four data sets respectively. One can see that the model captures the variations in each training set very well and new plausible shapes similar to the ones in the training sets are generated. This is due mainly to the effectiveness of the proposed registration model.

$-2\sqrt{\lambda_i}$ $-1\sqrt{\lambda_i}$ $0\sqrt{\lambda_i}$ $1\sqrt{\lambda_i}$ $2\sqrt{\lambda_i}$

(a) (b) (c) (d) (e)
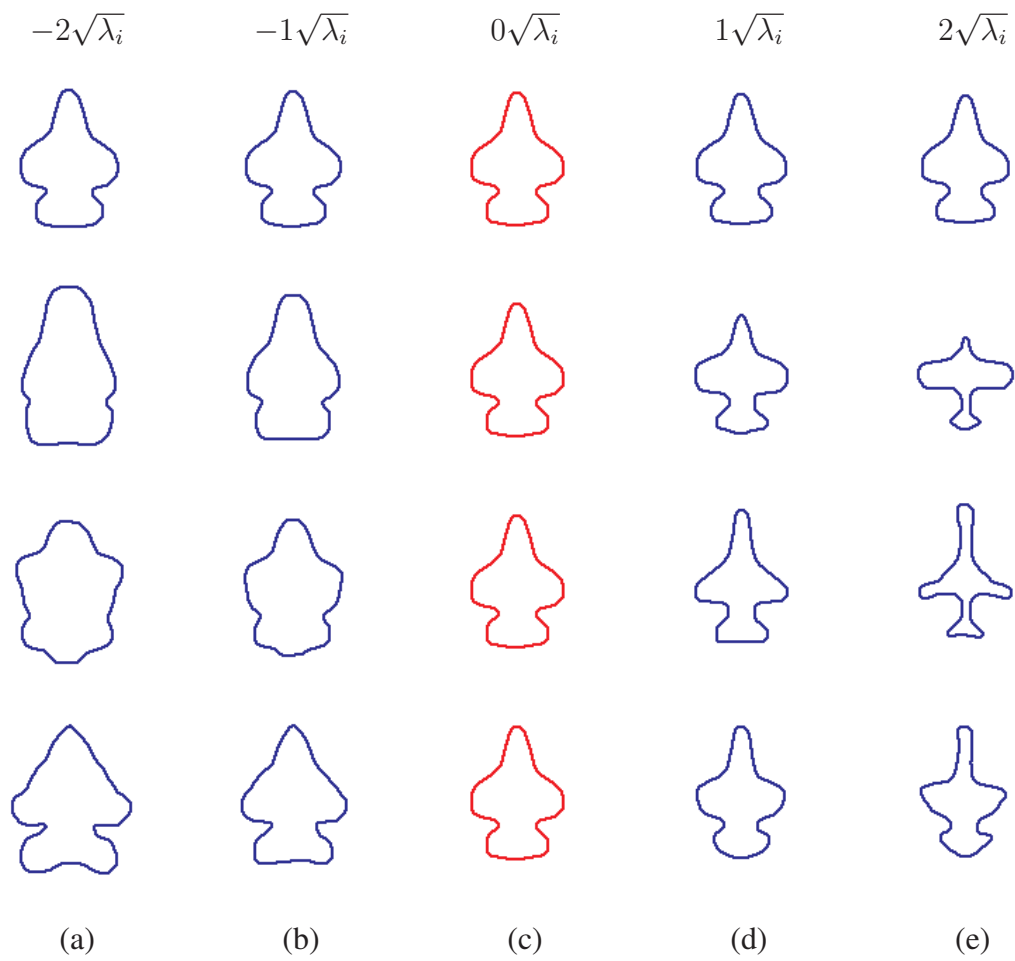
FIGURE 28 – Illustration of the shape variabilities in the fighter jet data base. The first four modes are shown from top to bottom w.r.t. to the average shape shown in red. For each mode, from left to right shows the mode changing from $-2\sqrt{\lambda_i}$ to $-2\sqrt{\lambda_i}$.
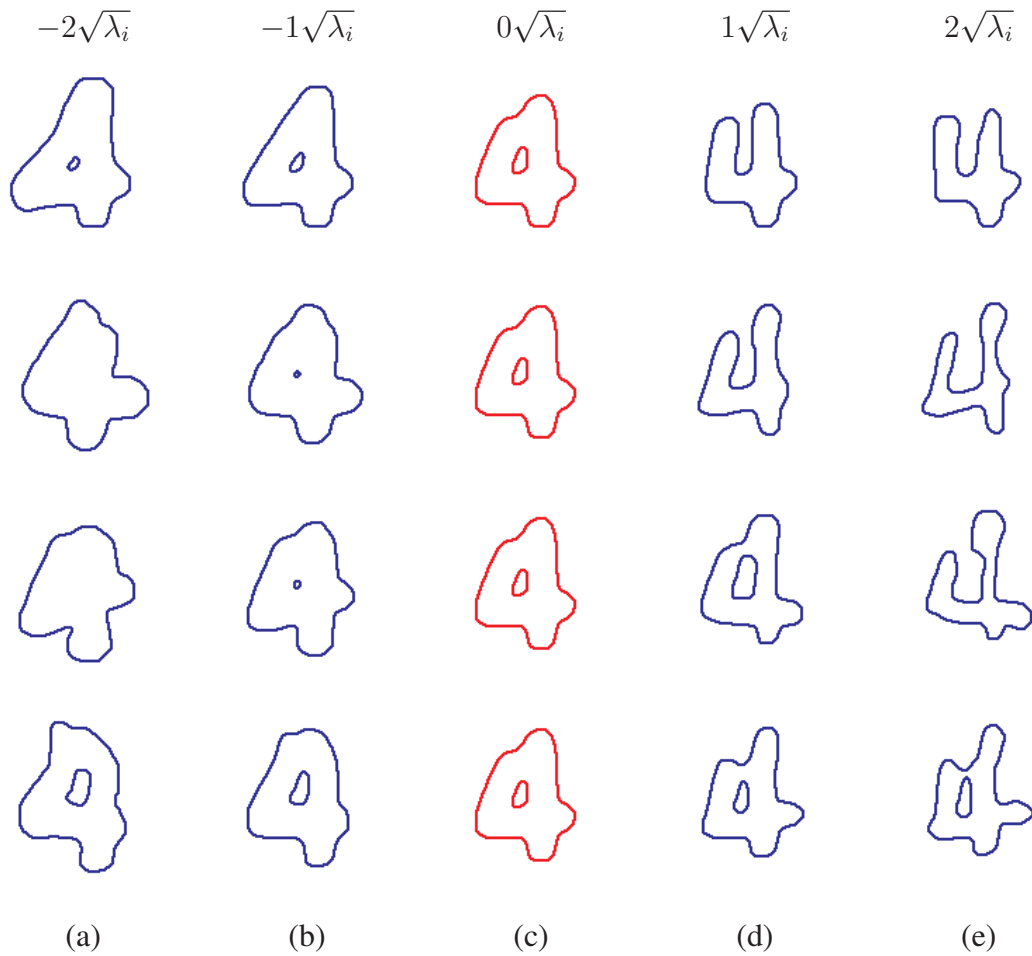
FIGURE 29 – Illustration of the shape variabilities in the number four data base. The first four modes are shown from top to bottom w.r.t. to the average shape shown in red. For each mode, from left to right shows the mode changing from $-2\sqrt{\lambda_i}$ to $-2\sqrt{\lambda_i}$.

H.   Conclusion

In this chapter, a new global registration technique of shapes was presented. The shapes are implicitly represented in higher dimensional space through their sign distance maps. This representation is either computed directly for moderate size shape or approximated using the *FMM* for large and 3D shapes. A new criterion, measuring the disparity between the two representations, was proposed and optimized using a gradient descent scheme to globally align the input shapes. This criterion supports both rigid/similarity and affine transformations. Various experiments were presented to show the effectiveness of the proposed criterion, and comparisons with the isotropic-based alignment proposed in [7] and the *VDF*-based alignment used in [22, 40] were performed showing the out-performance of the proposed model.

The three dimensional version of the proposed registration technique was implemented in C/C++ language and a graphical user interface was designed for an interactive use of the proposed approach.

CHAPTER IV

LOCAL SHAPE REGISTRATION

A.   Introduction

In many applications, the global matching has to be completed by dense one-to-one displacement field in the presence of local deformations [76]. Explicitly determining the displacement field plays a key role in various medical applications. For instance, the statistics of such a field over a set of subjects can help in classifying normals versus abnormal subjects as was done in a research work dedicated to classifying autistic vs. typically developing brains [77]. Complementary to the global registration field, the local coordinate transformation between the two globally aligned shapes is explicitly estimated by minimizing a **new** energy functional. This functional consists of three terms, the first of which is a discrepancy measure between the two shape representations. The second term penalizes the deviation of the distance map representation of the globally warped source shape from a signed distance function, while the local displacement field, which aims at aligning it with the target shape, is being updated. The last term is a regularization term that enforces the smoothness of the recovered deformations. This leads to a set of coupled equations that are simultaneously minimized through a gradient descent scheme.

B.   Local Alignment

Various applications may benefit from explicitly establishing dense point correspondences between two or more shapes. For instance, given a training set of anatomical shapes, the established point correspondences can be used to build a Point Distribution Model (*PDM*) [78] to capture the statistics of the corresponding elements across the training data.

Many techniques have also been published using shape-priors for the segmentation of medical imagery. A major component in learning such priors is the alignment of the training shapes (see for instance [38, 39, 78]).

In this section, a new variational framework to recover a dense local displacement field between two globally aligned shapes is proposed.

1. Proposed Variational Formulation

Given are two shapes, a source S and a target T, and assume that these two shapes are globally aligned according to an affine transformation model $\mathcal{A}$ recovered as explained in chapter IV. Let $\widehat{S} = \mathcal{A}(S)$ denote the corresponding transformed source shape. To complement the global matching model, one should recover a pixel-wise displacement field $\mathbf{u} = [u_1, \cdots, u_n]^T : \mathbb{R}^n \rightarrow \mathbb{R}^n$, with $n = 2, 3$ in practice, in such a way that the transformed representation $\Phi_T \circ g$ matches $\Phi_{\widehat{S}}$, where $\Phi_{\widehat{S}}$ and Φ_T are the implicit distance map representations of $\widehat{S}$ and T, respectively, and where $g(\mathbf{x}) = \mathbf{x} + \mathbf{u}(\mathbf{x})$ is the geometric deformation. The most common way of solving this problem is through the minimization of the following functional with respect to $\mathbf{u}$:

$$E_1(\mathbf{u}) = \int_\Omega (\Phi_{\widehat{S}}(\mathbf{x}) - \Phi_T(g(\mathbf{x})))^2 d\mathbf{x}. \tag{40}$$

This measure, known as the Sum of Squared Differences (*SSD*) or the L_2 measure has been extensively used for image and shape matching. Its limitations are well established, especially when dealing with images with different modalities and other criteria have been proposed to cope with this issue. When dealing with shapes, the registration in presence of scale variations is analogous to aligning different modality images [5]. However, it was already shown that the proposed global alignment model (see chapter IV) yields accurate results in the presence of scale variations. Hence, in order to recover the local displacement field, the *SSD* criterion (40) is adopted in this work, but in a different setting. Instead of directly minimizing the functional $E_1(.)$ with respect to $\mathbf{u}$, a function $\Phi(.)$ is initialized to be the signed distance representation of the globally aligned source shape, $\widehat{S}$, when there is no displacement (i.e., when $\mathbf{u} = \mathbf{0}$). Then, once $\mathbf{u}$ starts being updated $\mathbf{u}$, we propose to

simultaneously penalize the deviation of the corresponding deformed shape representation, $\Phi(g(.))$, from a signed distance function.

2. Re-initialization of a Signed Distance Function

In most scenarios of moving interface-based methods, it is impossible to maintain the level set function as a signed distance function to the moving front. As the interface moves, flat and/or step regions develop which introduces computational inaccuracies. For this practical reason, as well as for theoretical reasons (see [79]), one needs to keep the level set function close to a signed distance function (i.e., $|\nabla\Phi| \approx 1)^4$ from time to time during the course of its evolution. This process is known as the distance reinitialization of the level set function. Note that it remains theoretically unclear when and how to apply the reinitialization [79, 81].

The standard reinitialization method is to compute the embedding function, $\Phi(\cdot)$, as the steady state of the following *PDE* equation:

$$\begin{cases} \Phi_t = sign(\Phi_0)(1 - |\nabla\Phi|), \\ \Phi(\mathbf{x}, 0) = \Phi_0(\mathbf{x}), \end{cases} \tag{41}$$

where Φ_0 is the function to be reinitialized and $sign(\cdot)$ is the sign function. The idea of using this equation is that at steady state, the solution will correspond to a signed distance function (i.e., $|\nabla\Phi| = 1$) with the same zero-level set as the initial function Φ_0. Hence, every few steps of the evolution process, the embedding function Φ is rebuilt with the above equation. However, as was reported in various works, such as [81–83], if the initial condition Φ_0 is not smooth or if it is much steeper on one side of the embedded interface, the resulting function, Φ, can be moved incorrectly from that of the original function. In addition, this reinitialization may fail if the level set function is initially far from a signed distance function. Several other reinitialization approaches have been proposed (see for instance [81, 84, 85]). Most of these approaches are variants of the equation (41). Practically,

---

[4]A signed distance function satisfies the desirable property $|\nabla\Phi| = 1$. Conversely, any function Φ satisfying $|\nabla\Phi| = 1$ is a signed distance function plus a constant [80].

the reinitialization process can be very complicated, expensive and have subtle side effects.

Recently, Li et al. [83] have proposed a new variational level set formulation that forces the level set function to be close to a signed distance and hence eliminates the need of the reinitialization process. This was done in the context of level set based segmentation, by incorporating the following internal energy term into their segmentation energy,

$$\mathcal{I}(\Phi) = \frac{1}{2} \int_{\Omega} (|\nabla\Phi(\mathbf{x})| - 1)^2 d\mathbf{x}. \tag{42}$$

Due to this energy, the level set function is automatically kept close to a signed distance function during the evolution process. The numerical advantages of this new reinitialization technique were highlighted in [83].

In this work, this same reinitialization approach is chosen and a new variational formulation for non-rigid registration of shapes is proposed.

3. Energy Formulation

Instead of directly minimizing the functional $E_1(.)$ (see Eq. (40)) with respect to the unknown displacement field $\mathbf{u}$, a function $\Phi(.)$ is initialized as the signed distance representation of the globally aligned source shape, $\widehat{S}$, when there is no displacement (i.e., when $\mathbf{u} = \mathbf{0}$). Then, once $\mathbf{u}$ starts being updated, the deviation of the corresponding deformed shape representation, $\Phi(g(.))$ is simultaneously penalized from a signed distance function following the same idea proposed in [83] and expressed by Eq. (42). To this end, it is proposed to add the following energy term into the functional E_1:

$$E_2(\Phi, \mathbf{u}) = \int_{\Omega} (|\nabla\Phi(g(\mathbf{x}))| - 1)^2 d\mathbf{x}. \tag{43}$$

This new term is simultaneously minimized w.r.t. both Φ and $\mathbf{u}$. This will ensure that the source shape is kept implicitly represented by a signed distance function while it is being warped by the updated displacement field $\mathbf{u}$. One of the advantages of this new energy term is illustrated in Fig. 30. It is clear from these examples that adding the penalizing term helps guide the transformed shape towards the right direction even in the presence of large deformations.

With the aforementioned two functionals, E_1 and E_2, the following data-driven energy is minimized in order to explicitly determine the geometric transformation between the two shapes,

$$
\begin{aligned}
E_{data}(\Phi, \mathbf{u}) &= E_1(\Phi, \mathbf{u}) + \alpha E_2(\Phi, \mathbf{u}), \\
&\doteq \int_\Omega (\Phi(\mathbf{x}) - \Phi_T(g(\mathbf{x})))^2 d\mathbf{x} + \alpha \int_\Omega (|\nabla \Phi(g(\mathbf{x}))| - 1)^2 d\mathbf{x},
\end{aligned}
$$

where $\alpha > 0$ is a real parameter controlling the effect of the penalizing term (43).

To further measure and constrain the "irregularity" of $\mathbf{u}$, a regularization term inspired from the equilibrium equations of linearized elasticity is added (the interested reader is referred to [18] for a formal study of three dimensional elasticity theory). Indeed, if one assumes that the geometric deformation $g(\mathbf{x}) = \mathbf{x} + \mathbf{u}(\mathbf{x})$ corresponds to the strain of an elastic and isotropic material, then the strain energy is given by:

$$
E_{smoothness}(\mathbf{u}) = \int_\Omega \{\frac{\lambda}{2}(div\mathbf{u})^2 + \mu \sum_{i,j=1}^{n} (\varepsilon_{ij}(\mathbf{u}))^2\} d\mathbf{x},
$$

where μ, λ are the Lamé coefficients [18] of the material, and

$$
\varepsilon_{ij}(\mathbf{u}) = \frac{1}{2}(\frac{\partial u_i}{\partial x_j} + \frac{\partial u_j}{\partial x_i})
$$

is the deformation tensor. Such a regularization term is chosen over others for the flexibility gained by the relative weight which one can give to the operators $\Delta \mathbf{u}$ and $\nabla(\nabla \mathbf{u})$ (divergence of Jacobian of $\mathbf{u}$) (see e.g., [16] for in depth studies of this and other regularization operators).

The integration of all the above defined energy functionals lead to minimizing the following total energy in order to recover $\mathbf{u}$:

$$
E_{total}(\Phi, \mathbf{u}) = E_{data}(\Phi, \mathbf{u}) + \beta E_{smoothness}(\mathbf{u}), \tag{44}
$$

where β is a constant controlling the contribution of the smoothness term. In our experiments, β was chosen equal to one.

C. Gradient Descent Flows and Numerical Implementation

In order to recover the displacement field $\mathbf{u}$, the total energy E_{total} (see Eq. 44) is simultaneously minimized with respect to $\mathbf{u}$ and Φ. The standard gradient descent (or steepest descent) method is used to minimize this energy.

By calculus of variations, the Gâteaux derivatives of the functional E_{total} w.r.t. Φ and to the displacement field $\mathbf{u}$ can be found as detailed below.

1. Gradient Flow w.r.t. Φ

Finding a minimizer Φ of E_{total} is equivalent to numerically solving the following *PDE*:

$$\Phi_t = -\frac{\partial E_{total}}{\partial \Phi},$$

with a given initial data Φ_0.

The derivatives of the total energy w.r.t. Φ, $\frac{\partial E_{total}}{\partial \Phi}$, can be written as follows:

$$\frac{\partial E_{total}}{\partial \Phi} = \frac{\partial E_1}{\partial \Phi} + \alpha \frac{\partial E_2}{\partial \Phi} + \beta \frac{\partial E_{smoothness}}{\partial \Phi}, \tag{45}$$

where,

$$\begin{aligned}
\frac{\partial E_1}{\partial \Phi} &= 2(\Phi(\mathbf{x}) - \Phi_T(g(\mathbf{x}))), \\
\frac{\partial E_2}{\partial \Phi} &= 2[\Delta\Phi(g(\mathbf{x})) - div(\frac{\nabla\Phi(g(\mathbf{x}))}{|\Phi(g(\mathbf{x}))|})], \\
\frac{\partial E_{smoothness}}{\partial \Phi} &= 0.
\end{aligned}$$

2. Gradient Flow w.r.t. $\mathbf{u}$

Similarly, finding a minimizer $\mathbf{u}$ of E_{total} is equivalent to numerically solving the following *PDE*:

$$\mathbf{u}_t = -\frac{\partial E_{total}}{\partial \mathbf{u}},$$

with a given initial data $\mathbf{u}_0$.

The derivatives of the total energy w.r.t. $\mathbf{u}$, $\frac{\partial E_{total}}{\partial \mathbf{u}}$, can be written as follows

$$\frac{\partial E_{total}}{\partial \mathbf{u}} = \frac{\partial E_1}{\partial \mathbf{u}} + \alpha \frac{\partial E_2}{\partial \mathbf{u}} + \beta \frac{\partial E_{smoothness}}{\partial \mathbf{u}}. \tag{46}$$

each of these terms will be derived separately.

First,

$$\frac{\partial E_1}{\partial \mathbf{u}} = 2(\Phi(\mathbf{x}) - \Phi_T(g(\mathbf{x}))) \cdot \nabla \Phi_T(g(\mathbf{x})). \tag{47}$$

Second,

$$\frac{\partial E_2}{\partial \mathbf{u}} = 2(|\nabla \Phi(g(\mathbf{x}))| - 1) \cdot \frac{\partial}{\partial \mathbf{u}}(|\nabla \Phi(g(\mathbf{x}))|). \tag{48}$$

The term

$$\frac{\partial}{\partial \mathbf{u}}|\nabla \Phi(g(\mathbf{x}))| = [\frac{\partial}{\partial u_1}(|\nabla \Phi(g(\mathbf{x}))|) \cdots \frac{\partial}{\partial u_n}(|\nabla \Phi(g(\mathbf{x}))|)]^T,$$

in the last equation can be evaluated as follows.

Let $\mathbf{x} = (x_1, \cdots, x_n)$, $\mathbf{u}(\mathbf{x}) = (u_1(\mathbf{x}), \cdots, u_n(\mathbf{x}))$, and let

$$\nabla \Phi(g(\mathbf{x})) = [\frac{\partial}{\partial x_1}\Phi(\mathbf{x} + \mathbf{u}(\mathbf{x})), \cdots, \frac{\partial}{\partial x_n}\Phi(\mathbf{x} + \mathbf{u}(\mathbf{x}))]^T.$$

With these notations, one has

$$|\nabla \Phi(g(\mathbf{x}))| = \sqrt{\sum_{i=1}^{n}(\frac{\partial}{\partial x_i}\Phi(\mathbf{x} + \mathbf{u}(\mathbf{x})))^2}$$

Hence, the derivative of $|\nabla \Phi(g(\mathbf{x}))|$ with respect to the jth component, u_j, of the displacement field $\mathbf{u}$, is given by

$$\frac{\partial}{\partial u_j}|\nabla \Phi(g(\mathbf{x}))| = \frac{1}{2}|\nabla \Phi(g(\mathbf{x}))|^{-1}\sum_{i=1}^{n}2\frac{\partial}{\partial x_i}\Phi(\mathbf{x} + \mathbf{u}(\mathbf{x})) \cdot \frac{\partial}{\partial u_j}(\frac{\partial}{\partial x_i}\Phi(\mathbf{x} + \mathbf{u}(\mathbf{x})))$$

$$= |\nabla \Phi(g(\mathbf{x}))|^{-1}\sum_{i=1}^{n}\frac{\partial}{\partial x_i}\Phi(\mathbf{x} + \mathbf{u}(\mathbf{x})) \cdot \frac{\partial}{\partial x_i}(\frac{\partial}{\partial u_j}\Phi(\mathbf{x} + \mathbf{u}(\mathbf{x}))).$$

If one notes that $\frac{\partial}{\partial u_j}\Phi(\mathbf{x} + \mathbf{u}(\mathbf{x}))) = \frac{\partial}{\partial x_j}\Phi(\mathbf{x} + \mathbf{u}(\mathbf{x})))$, then

$$\frac{\partial}{\partial u_j}(|\nabla \Phi(g(\mathbf{x}))|) = |\nabla \Phi(g(\mathbf{x}))|^{-1}\sum_{i=1}^{n}\frac{\partial}{\partial x_i}\Phi(\mathbf{x} + \mathbf{u}(\mathbf{x})) \cdot \frac{\partial}{\partial x_i}(\frac{\partial}{\partial x_j}\Phi(\mathbf{x} + \mathbf{u}(\mathbf{x})))$$

$$= |\nabla \Phi(g(\mathbf{x}))|^{-1}\sum_{i=1}^{n}\frac{\partial}{\partial x_i}\Phi(g(\mathbf{x})) \cdot \frac{\partial^2}{\partial x_i \partial x_j}\Phi(g(\mathbf{x})). \tag{49}$$

The equations (Eq. 49) can be put together in a matrix form as

$$
\frac{\partial}{\partial \mathbf{u}}|\nabla\Phi(g(\mathbf{x}))| = [\frac{\partial}{\partial u_i}|\nabla\Phi(g(\mathbf{x}))|, \cdots \frac{\partial}{\partial u_n}|\nabla\Phi(g(\mathbf{x}))|)]^T,
$$

$$
= |\nabla\Phi(g(\mathbf{x}))|^{-1}
\begin{bmatrix}
\frac{\partial^2\Phi\circ g}{\partial x_1\partial x_1}(\mathbf{x}) & \cdots & \frac{\partial^2\Phi\circ g}{\partial x_1\partial x_n}(\mathbf{x}) \\
\vdots & \ddots & \vdots \\
\frac{\partial^2 v}{\partial x_n\partial x_1}(\mathbf{x}) & \cdots & \frac{\partial^2\Phi\circ g}{\partial x_n\partial x_n}(\mathbf{x})
\end{bmatrix}
\cdot
\begin{pmatrix}
\frac{\partial\Phi\circ g}{\partial x_1}(\mathbf{x}) \\
\vdots \\
\frac{\partial\Phi\circ g}{\partial x_n}(\mathbf{x})
\end{pmatrix}
$$

$$
= |\nabla\Phi(g(\mathbf{x}))|^{-1}\mathcal{H}(\Phi\circ g)(\mathbf{x})\cdot\nabla\Phi(g(\mathbf{x})). \tag{50}
$$

Then, the derivative of the energy term E_2 w.r.t. $\mathbf{u}$ (see Eq. 48) can be written as

$$
\begin{aligned}
\frac{\partial E_2}{\partial \mathbf{u}} &= 2(|\nabla\Phi(g(\mathbf{x}))| - 1)|\nabla\Phi(g(\mathbf{x}))|^{-1}\mathcal{H}(\Phi\circ g)(\mathbf{x})\cdot\nabla\Phi(g(\mathbf{x})) \\
&= 2(1 - \frac{1}{|\nabla\Phi(g(\mathbf{x}))|})\mathcal{H}(\Phi\circ g)(\mathbf{x})\cdot\nabla\Phi(g(\mathbf{x})),
\end{aligned} \tag{51}
$$

where, $\mathcal{H}(\Phi\circ g)(\mathbf{x})$ is the Hessian matrix of $\Phi\circ g$ as defined in equation (50).

Finally, the derivative of the smoothness energy, $E_{smoothness}$, w.r.t. $\mathbf{u}$ lead to the following operator

$$
\frac{\partial}{\partial \mathbf{u}}E_{smoothness} \doteq \mathcal{R}(\mathbf{u}) = 2.
\begin{pmatrix}
\mu\Delta u_1(\mathbf{x}) + (\lambda+\mu)\sum_{i=1}^n \frac{\partial^2}{\partial x_1\partial x_i}u_i(\mathbf{x}) \\
\vdots \\
\mu\Delta u_n(\mathbf{x}) + (\lambda+\mu)\sum_{i=1}^n \frac{\partial^2}{\partial x_n\partial x_i}u_i(\mathbf{x})
\end{pmatrix}, \tag{52}
$$

where, $\Delta = \sum_{i=1}^n \frac{\partial^2}{\partial x_i^2}$ denotes the Laplace operator.

Assembling equations (45) and (46) results in the following set of $(n+1)$ coupled evolution equations:

$$
\begin{cases}
\frac{\partial\Phi}{\partial t} = -\frac{\partial E_{total}}{\partial\Phi} = -2[(\Phi(\mathbf{x}) - \Phi_T(g(\mathbf{x})) + \alpha(\Delta\Phi(g(\mathbf{x})) - div(\frac{\nabla\Phi(g(\mathbf{x}))}{|\nabla\Phi(g(\mathbf{x}))|})))], \\[2mm]
\frac{\partial\mathbf{u}}{\partial t} = -\frac{\partial E_{total}}{\partial\mathbf{u}} = -2[(\Phi(\mathbf{x}) - \Phi_T(g(\mathbf{x})))\cdot\nabla\Phi_T(g(\mathbf{x}) \\[2mm]
\qquad\qquad - \alpha(1 - \frac{1}{|\nabla\Phi(g(\mathbf{x}))|})\cdot H(\Phi\circ g)(\mathbf{x})\cdot\nabla\Phi(g(\mathbf{x})) + \beta\mathcal{R}(\mathbf{u})], \\[2mm]
\Phi(\mathbf{x},0) = \Phi_{\widehat{S}}(\mathbf{x}), \\[2mm]
\mathbf{u}(\mathbf{x},0) = \mathbf{0}.
\end{cases} \tag{53}
$$

3. Numerical Implementation

The following finite difference schemes were used to discretize the continuous non-rigid matching equations (53) (more details can be found in the Appendix II):

- The gradient terms are approximated using central differences.

- Standard second-order approximations are used to compute $\frac{\partial^2 u}{\partial x_i^2}$.

- The 4-point approximation with truncation order of δ^2 is used to approximate $\frac{\partial^2 u}{\partial x_i \partial x_j}$, with δ being the isotropic grid spacing in each direction.

- Bilinear interpolation schemes(for 2D cases) and trilinear interpolation schemes (for 3D cases) are used to estimate data values (such as distance maps of transformed shapes) at positions other than grid points.

Finally, the Lamé constants were set to $\mu = \frac{1}{2}$ and $\lambda = 0$ for all experiments.

D. Two Dimensional Experiments

First, several experiments were carried out to analyze the effect of energy term in Eq. (44) on the registration performance. If only the dissimilarity measure between the representations of the two input shapes is minimized. That is, if only the energy term $E_1(\cdot)$ is minimized, which is equivalent to choosing $\alpha = 1$, $\beta = 0$, and dropping the smoothness energy $E_{smoothness}(\cdot)$ in equation (44), then as one would expect numerical instabilies are encountered and the algorithm diverges. This is because no constraints are imposed on the displacement field $\mathbf{u}$ which makes the registration problem ill-posed. Second, the effect of the penalizing term, $E_2(\cdot)$, is studied. In this case, it was noticed on most examples, especially when local deformations between the two input shapes are high, that the registration accuracy is better when $E_2(\cdot)$ is used. Indeed, this penalizing energy $E_2(\cdot)$ guides the deformed shape towards right directions even where the deformations are large and it allowed for larger time steps and then faster convergence. This effect is qualitatively illustrated in Figs. 30 (2). In contrary, more iterations were used with less accurate results for the results

66
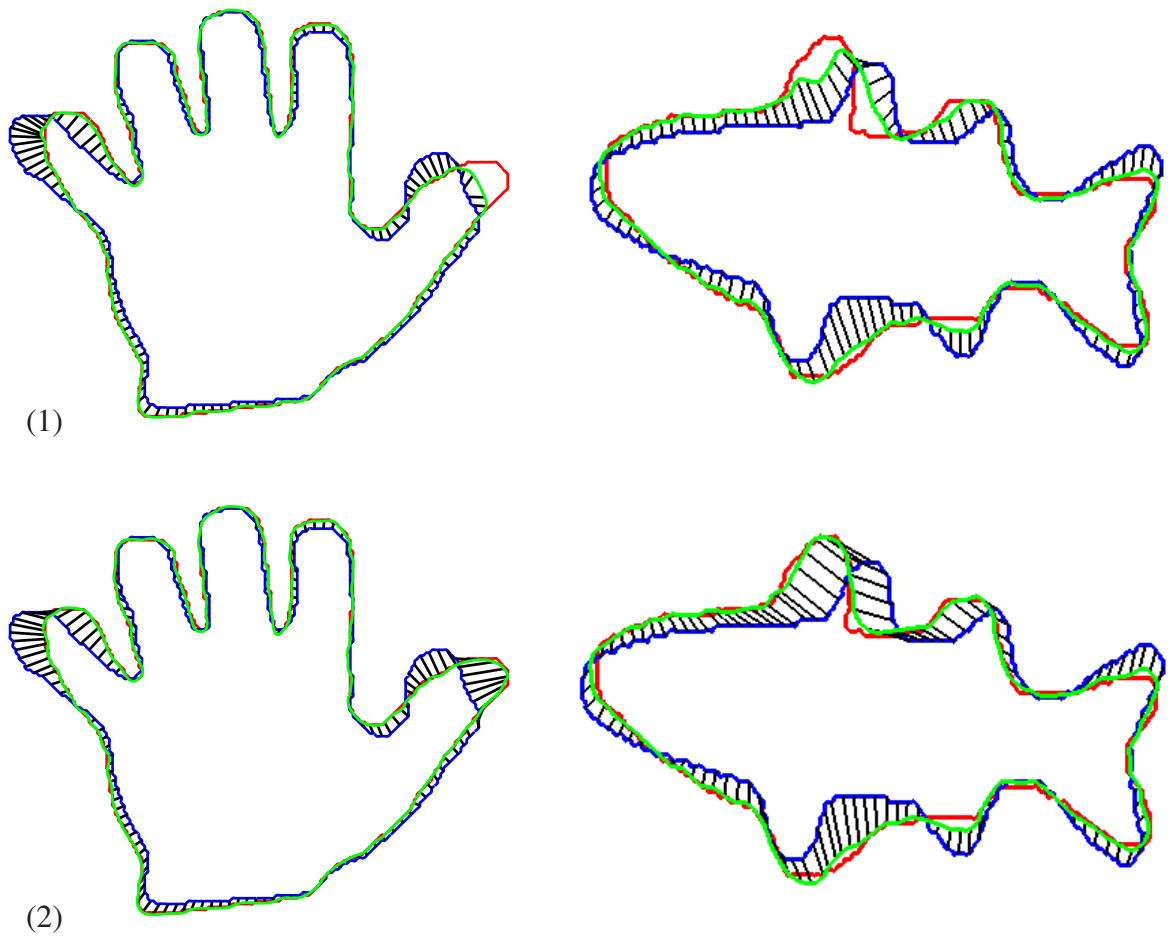
FIGURE 30 – Established point-wise correspondences after local registration: source shape (blue); Locally deformed source (green) and target (red). (1) Without penalizing energy $E_2(.)$. (2) Using the new model (Eq. 53).
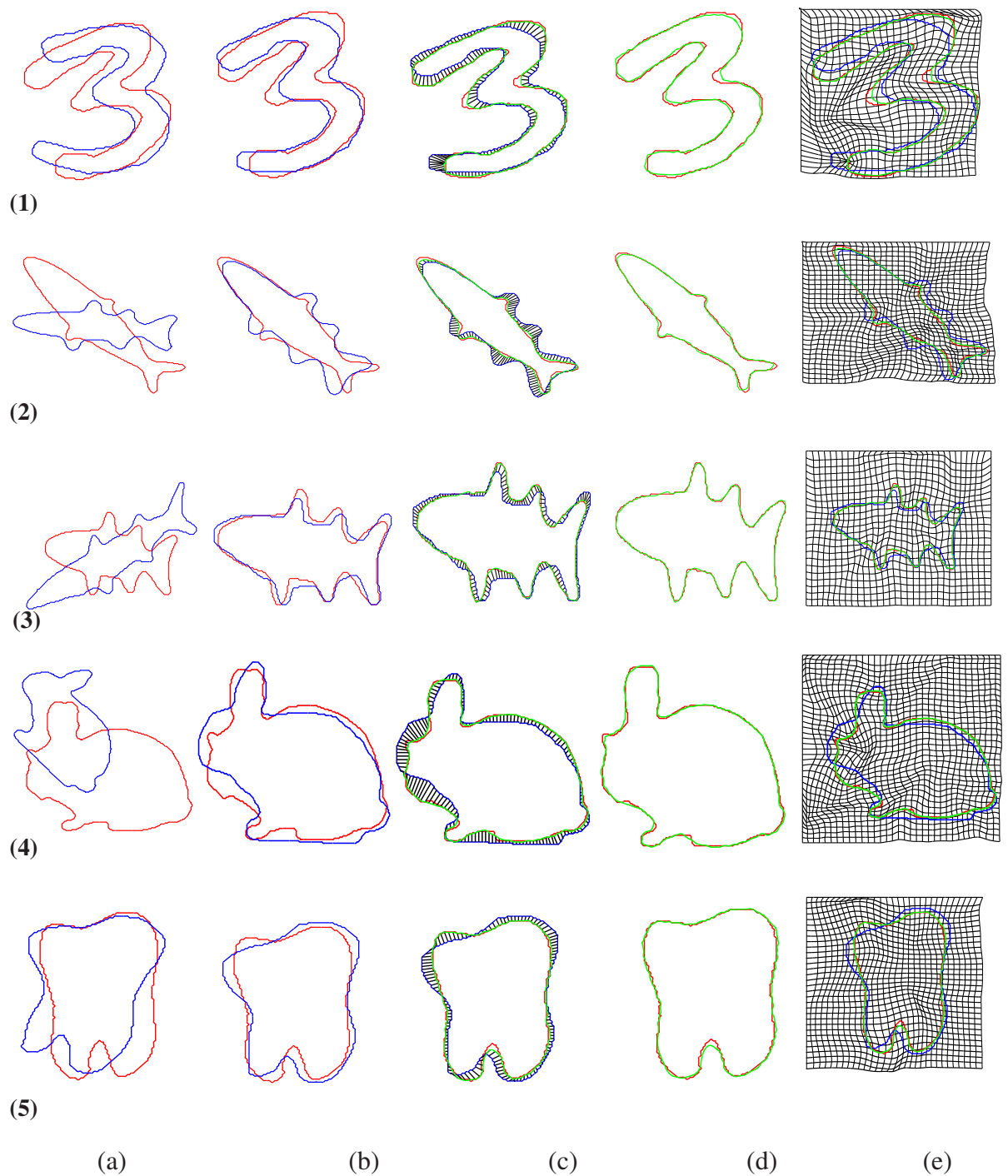
FIGURE 31 – Proposed Registration Framework. (1) Digit 3, (2-3) Fish, (4) Rabbit, (5) Tooth. (a) Initial positions of the source shape (blue) and target (red); (b) Global alignment using our new global matching model. (c) Established shape correspondences after local matching. (d) Locally deformed source (green) overlaid on target (red). (e) Space warping with globally deformed source (blue), locally deformed source (green), and target (red).
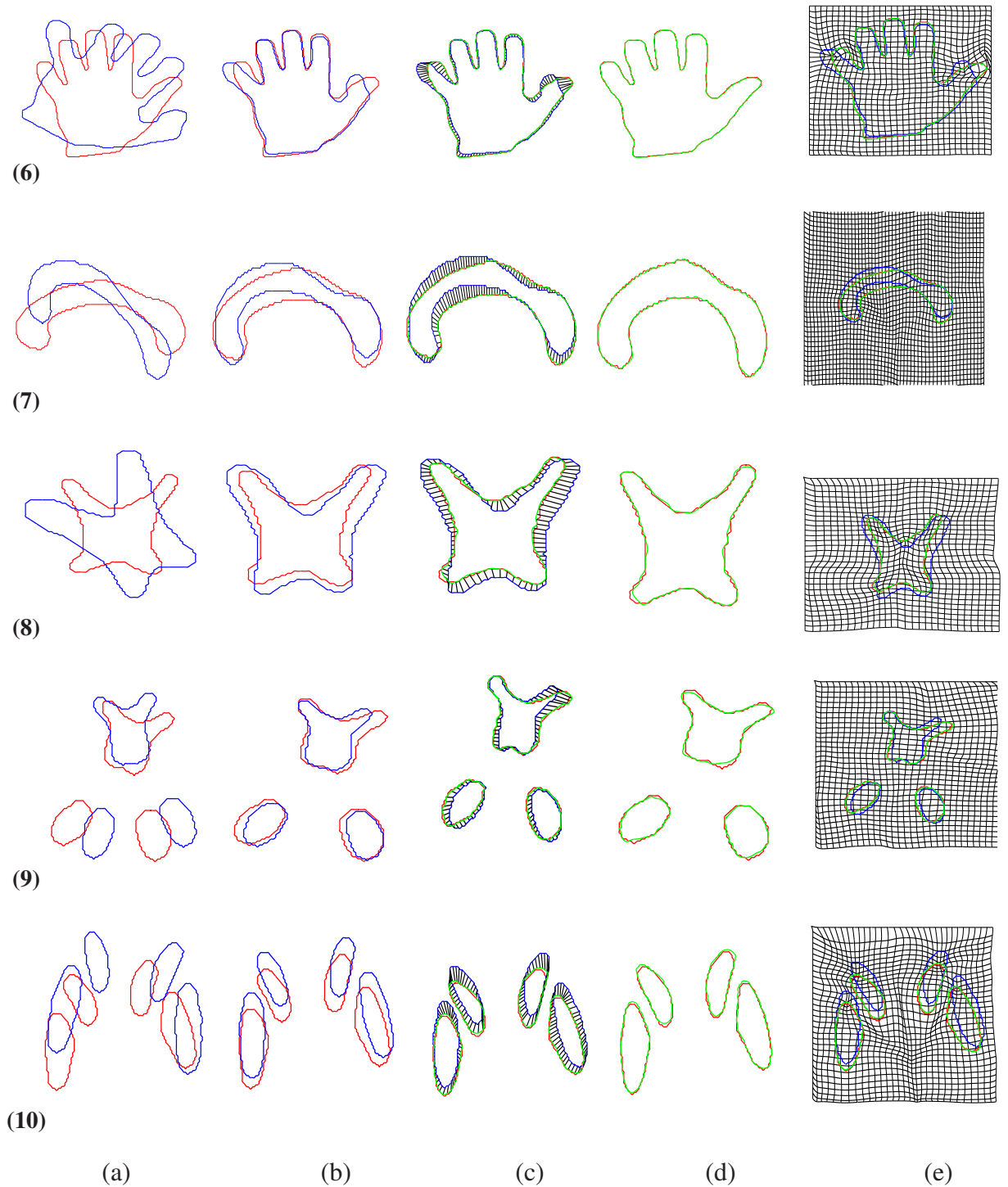
FIGURE 32 – More elastic registration. (6) Hand, (7-10) Brain Structures. (a) Initial positions of the source shape (blue) and target (red). (b) Global alignment using our new global matching model. (c) Established shape correspondences after local matching; (d) Locally deformed source (green) overlaid on target (red). (e) Space warping with globally deformed source (blue), locally deformed source (green), and target (red).
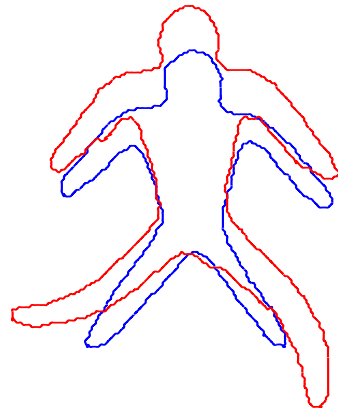
(a)
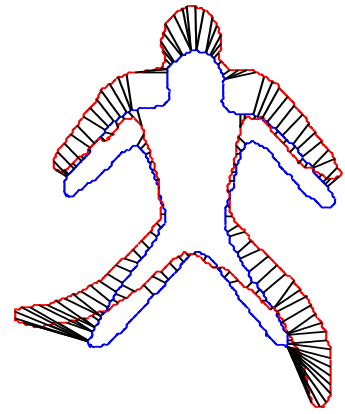
(b)
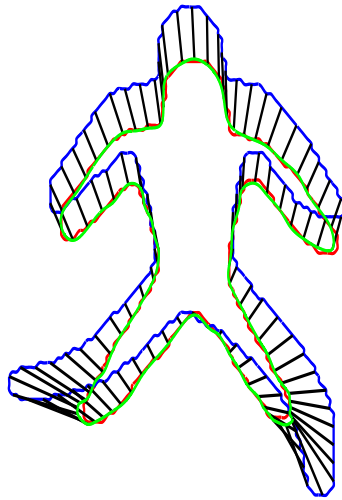
(c)
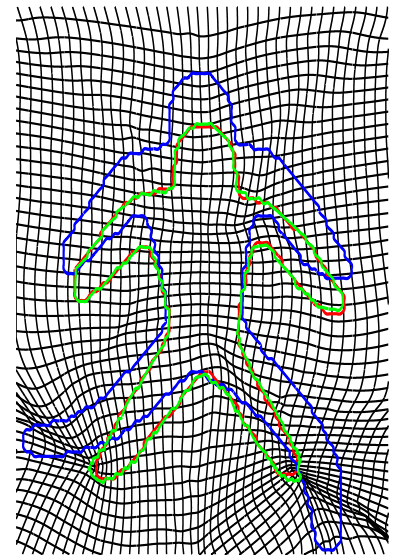
(d)

FIGURE 33 – Example of registration in presence of large deformations. (a) Initial pose of source relative to target shape. (b) Point correspondences using the *ICP* algorithm. (c) Point correspondences using the proposed registration method. (d) Deformation field corresponding to results in (c).
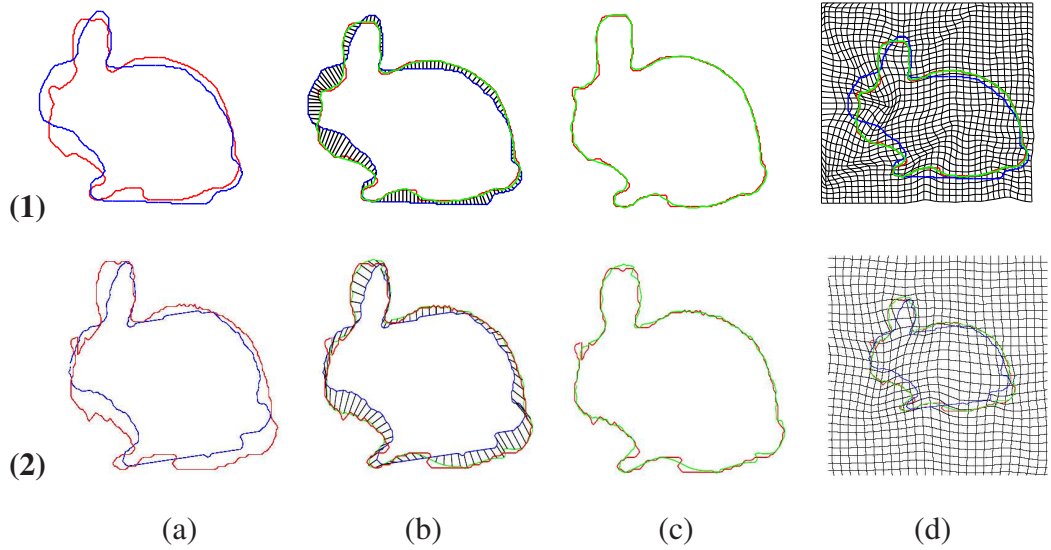
FIGURE 34 – Comparison with the Iterative Free Form Deformation (*IFFD*) algorithm proposed in [5]. (1) Results obtained using the proposed method. (2) Results reported in [5]. Initial shapes are shown on Fig. 17(4-a). (1-a) Results after global alignment using our the proposed new *SSD* measure (see Chap. III), and (2-a) using *MI*-based measure in [5]. (b) Established shape correspondences; (c) Locally deformed source shape (green) overlaid on the target (green). (d) Displacement vector field depicting the space warping, with source shape after global alignment (blue), source shape after local deformation (green), and target (red).

shown in Fig. 30(1), when the penalization term $E_2(\cdot)$ is dropped.

More 2D examples are shown in Fig. 32 to demonstrate the overall performance of the proposed non-rigid registration framework.

Finally, Fig. 33 shows how accurate are the registration results even in the presence of very large deformations. The shown results are compared to those obtained using the Iterative Closet Point (*ICP*) method [86, 87]. A multi-resolution B-spline model is used to recover the non-rigid deformations based on correspondences established by the *ICP* algorithm. The proposed approach clearly outperforms the *ICP*. Finally, the accuracy of our algorithm is compared to that presented in [5], which also uses the signed distance-based implicit representation for shape registration. The first row in Fig. (34) corresponds to the results obtained using the proposed registration model (44), while the results from the method in [5] are shown in the second row of the same figure. It is clear from this figure that, for this specific case, both methods lead to favorably comparable results with subtle dif-

ferences. These differences are in part due to the difference between the global alignment models used in each work. In [5], the authors maximize the mutual information between the two implicit representations, where the probability density functions are approximated using non-parametric Gaussian kernels with empirical width value. Regarding the local deformation (Fig. 34(d)), the method used in [5] recovers the registration field by iteratively minimizing a regularized energy with respect to each component of each control point, using the gradient descent method.

E.   Three Dimensional Experiments

Several elastic registration experiments are conducted on face range scans of two subjects. These data are acquired using the the 3D laser scanner *"CyberWare3030"*[5] at the Computer Vision and Image Processing Lab (more details about this type of data and image acquisition and preprocessing will be given in the next chapter).

For each subject, data for three different facial expressions were collected: a neutral expression, a smiling expression, and cheeks inflation expression. Example of the generated 3D facial surfaces of two subjects are shown on Fig. 35. Finally, the distance maps of each data set is approximated using the fast marching method (see Appendix III..3).

1.   Experiments

A set of intra-subject alignments are carried out to show the potential of the proposed registration framework in accurately aligning 3D surfaces. Qualitatively, three different views of both, the initial pose of the target face relative to the source, the global and the local registration results are shown (see Fig. 36, and Fig. 38 for subject#1 and Fig. 40, and Fig. 41 for subject#2).

As a quantitative evaluation of both the global and the local registration models on these data sets, the root-mean-square error (*RMS*) is computed between the implicit representations of the two input shapes before and after global and local alignments. The *RMS* error

---

[5]http://cyberware.com
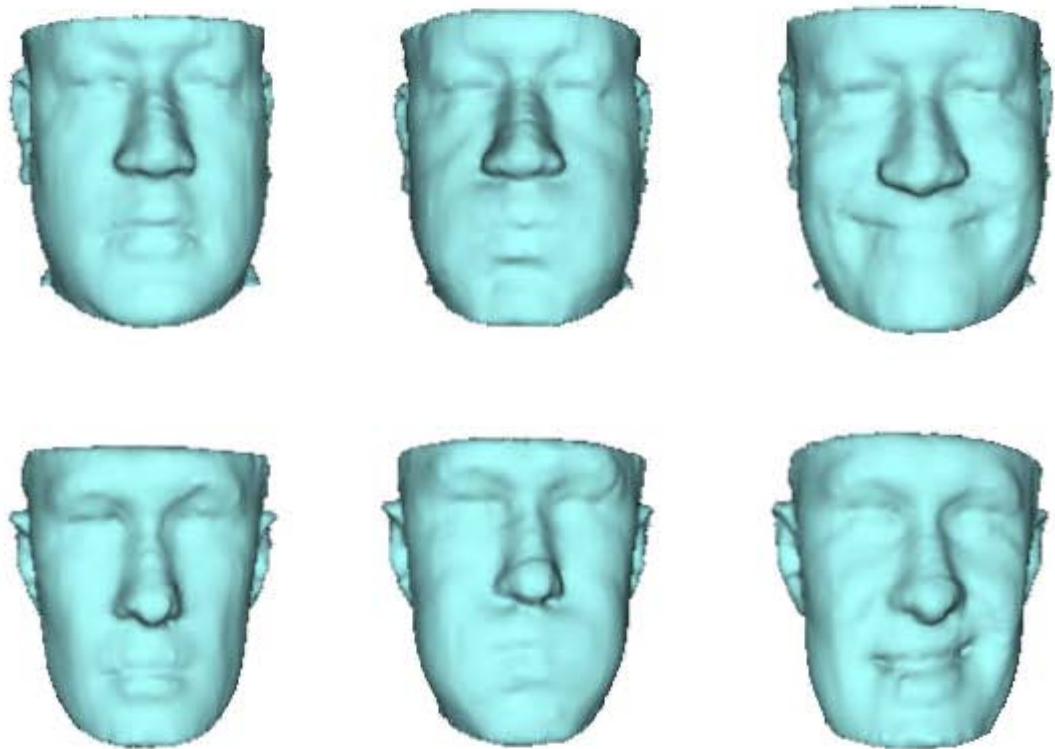
FIGURE 35 – Examples of the generated face surfaces corresponding to two different subjects. First row: subject#1 with neutral, inflate and smile expressions. Second row: subject#2 with neutral, inflate, and smile expressions.
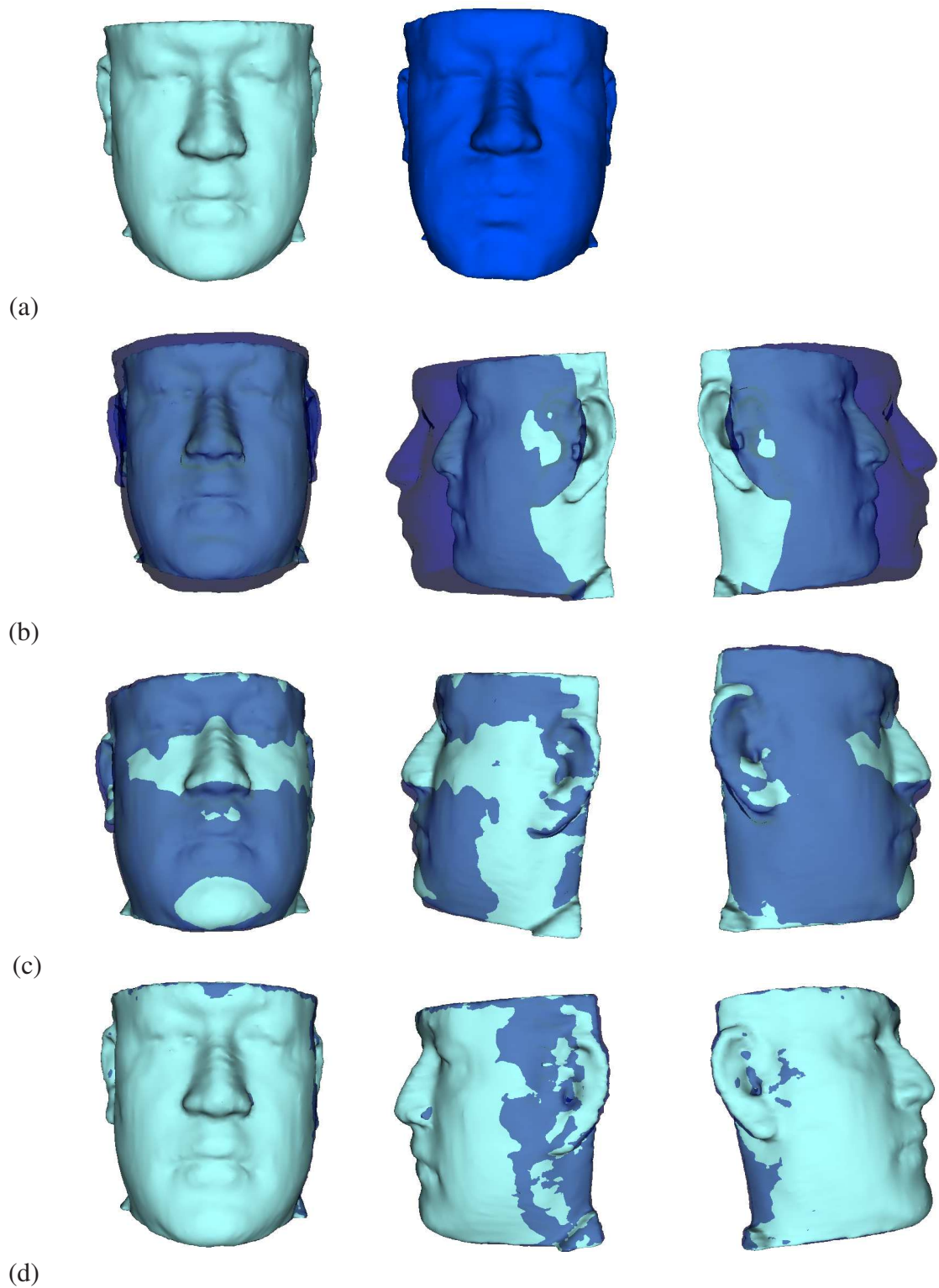
FIGURE 36 – 1st Experiment: Global-to-local registration Inflate-to-Neutral face of subject#1. (a) The 2 input faces: neutral face (light blue) and inflate face (dark blue). Shown are 3 different views of **(b)** initial pose of the source shape relative to the target, **(c)** the globally registered source overlaid on the target, and **(d)** the locally deformed source shape overlaid on the target.
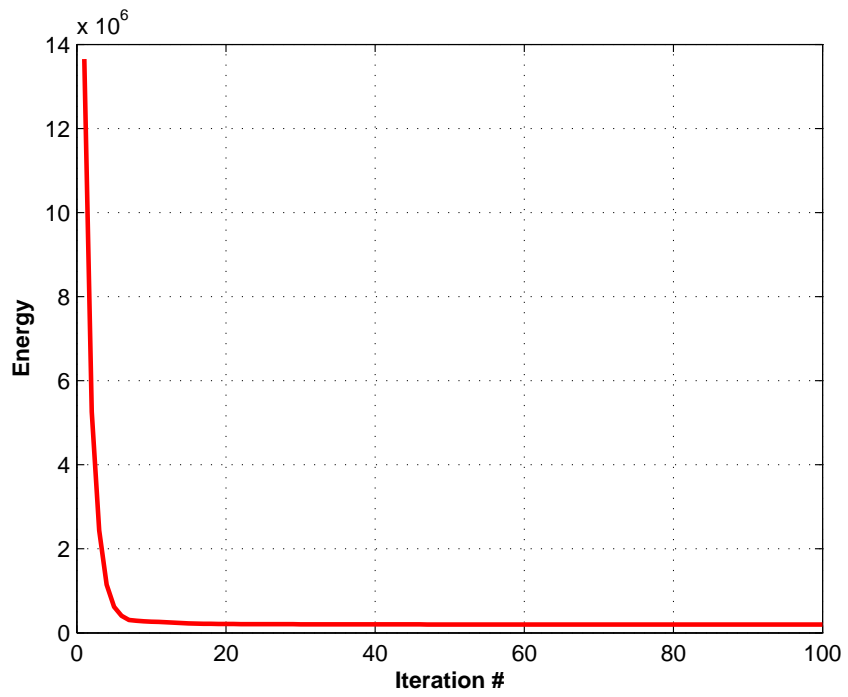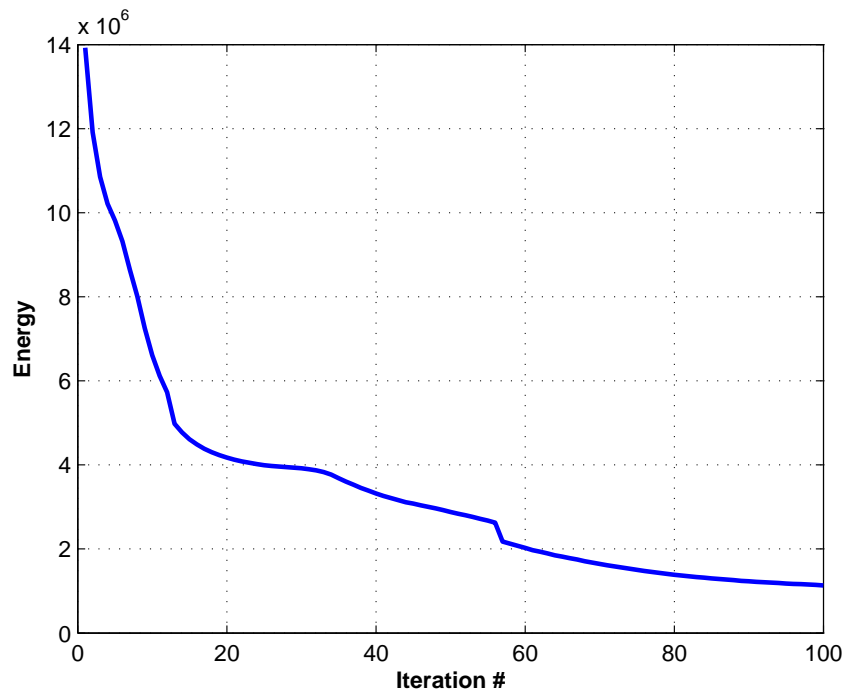
FIGURE 37 – Registration energies vs. iteration corresponding to the experiments shown on Fig. 36. (a) Global registration energy. (b) Local registration energy.

is denoted as ζ and is given by:

$$\zeta = \sqrt{\frac{\sum(\Phi_1^2(\mathbf{x}_i) - \Phi_2^2(\mathbf{x}_i))}{N}}, \tag{54}$$

where Φ_i, $i = 1, 2$, refer to the implicit representation of the two shape being registered, $\mathbf{x}_i$ are the image voxels, and N is the total number of voxels.

For the first subject, this error was equal to $\zeta = 8.0285$ between the original inflate face model and the neutral face model, and reduces to $\zeta = 1.5432$ after performing global alignment. After local registration, the matching error was reduced to $\zeta = 0.8952$. For the second experiment (see Fig. 38), this error dropped from $\zeta = 2.0416$ before alignment to $\zeta = 1.7813$ after global registration, and then was reduced to $\zeta = 1.1432$ after local alignment.

For the second subject, where only local registration was performed between the original neutral face and the two non-neutral face surfaces, this error was equal to $\zeta = 1.5347$ between the original inflate face model and the neutral face model, and reduces to $\zeta = 1.0235$ after performing local registration. For the second experiment (see Fig. 41), this error dropped from $\zeta = 2.6392$ before alignment to $\zeta = 1.1976$ local alignment.

These errors are summarized in table. 4 as well as those corresponding to the registration cases for the first subject.

The registration energies corresponding to the global and local alignments performed for the first subject (see Fig. 36 and 38)) are shown in Fig. 37 and Fig. 39. Note how these energies drop versus iterations. The registration energies corresponding to the alignments performed for the second subject (see Fig. 40 and 41)) are plotted in Fig. 42. Note how these energies drop after each iteration.
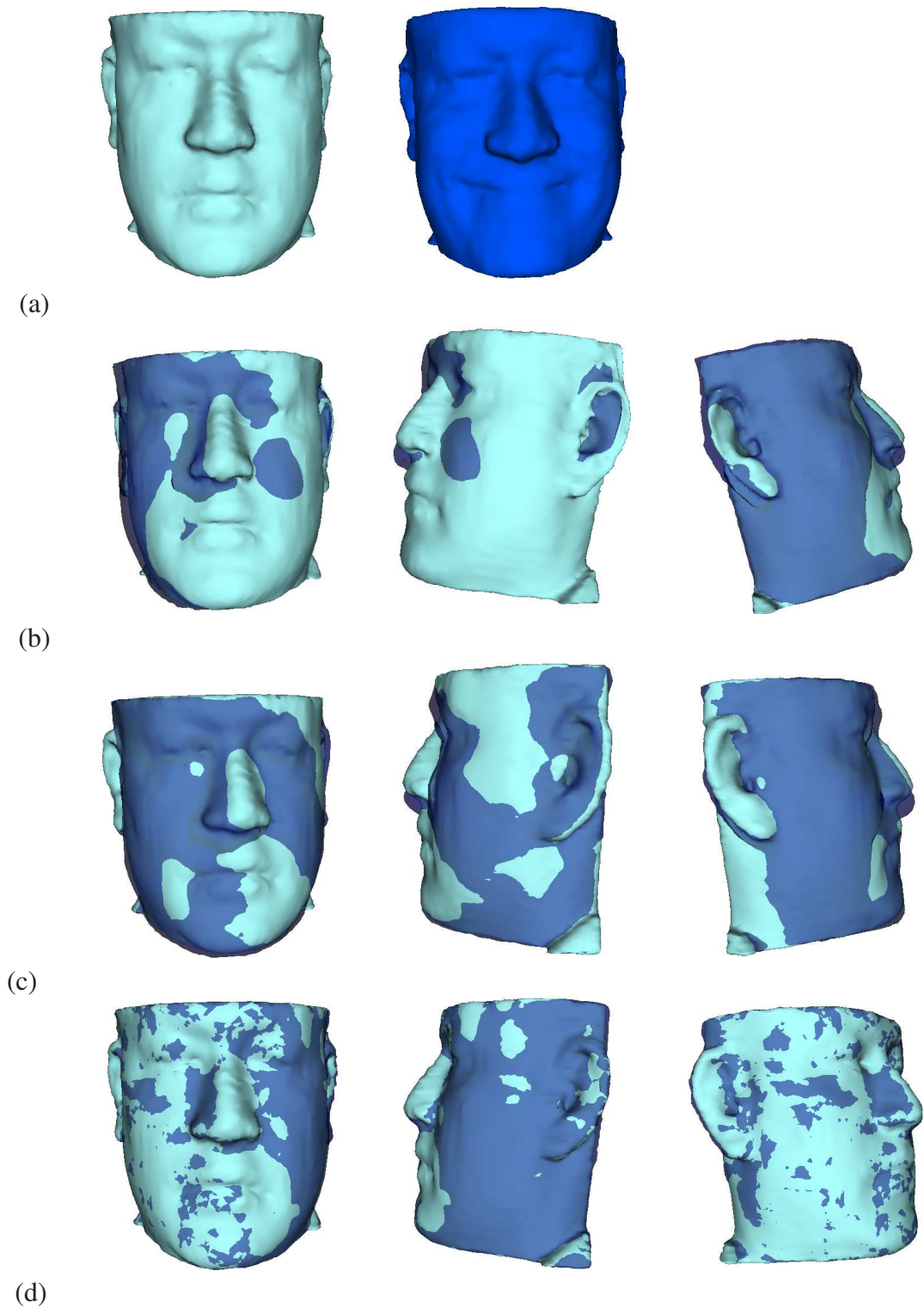
FIGURE 38 – 2nd Experiment: Global-to-local registration of Smile-to-Neutral face of subject#1. (a) The 2 input faces: neutral face (dark blue) and smile face (light blue). Shown are 3 different views of **(b)** initial pose of the source shape relative to the target, **(c)** the globally registered source overlaid on the target, and **(d)** the locally deformed source shape overlaid on the target.
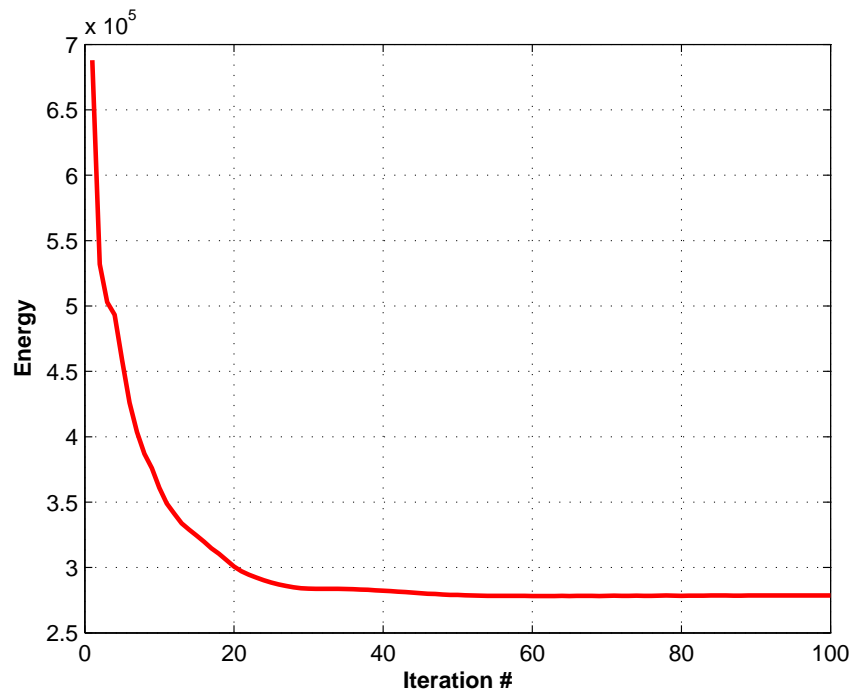
(a)
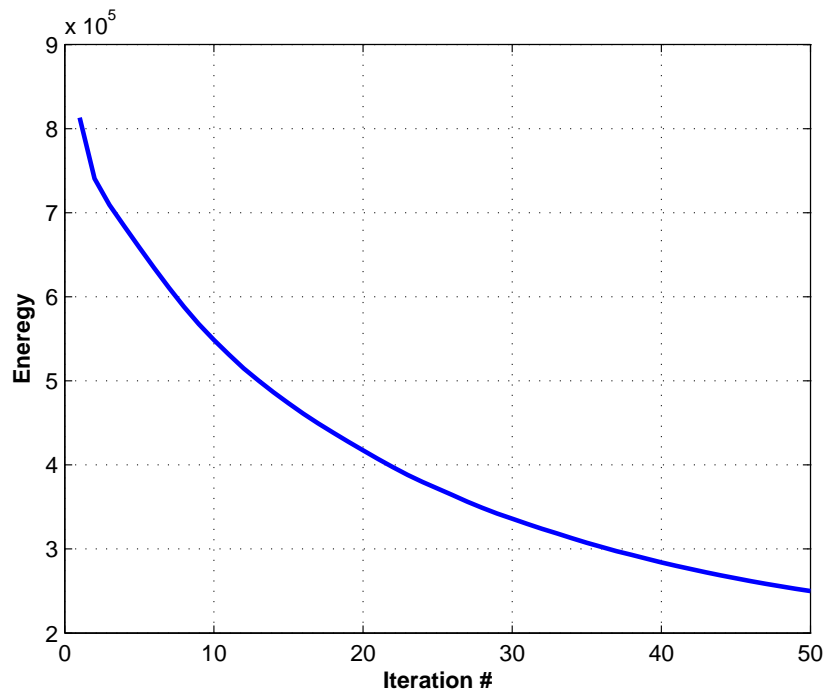
(b)

FIGURE 39 – Registration energies vs. iteration corresponding to the experiments shown on Fig. 38. (a) Global registration energy. (b) Local registration energy.
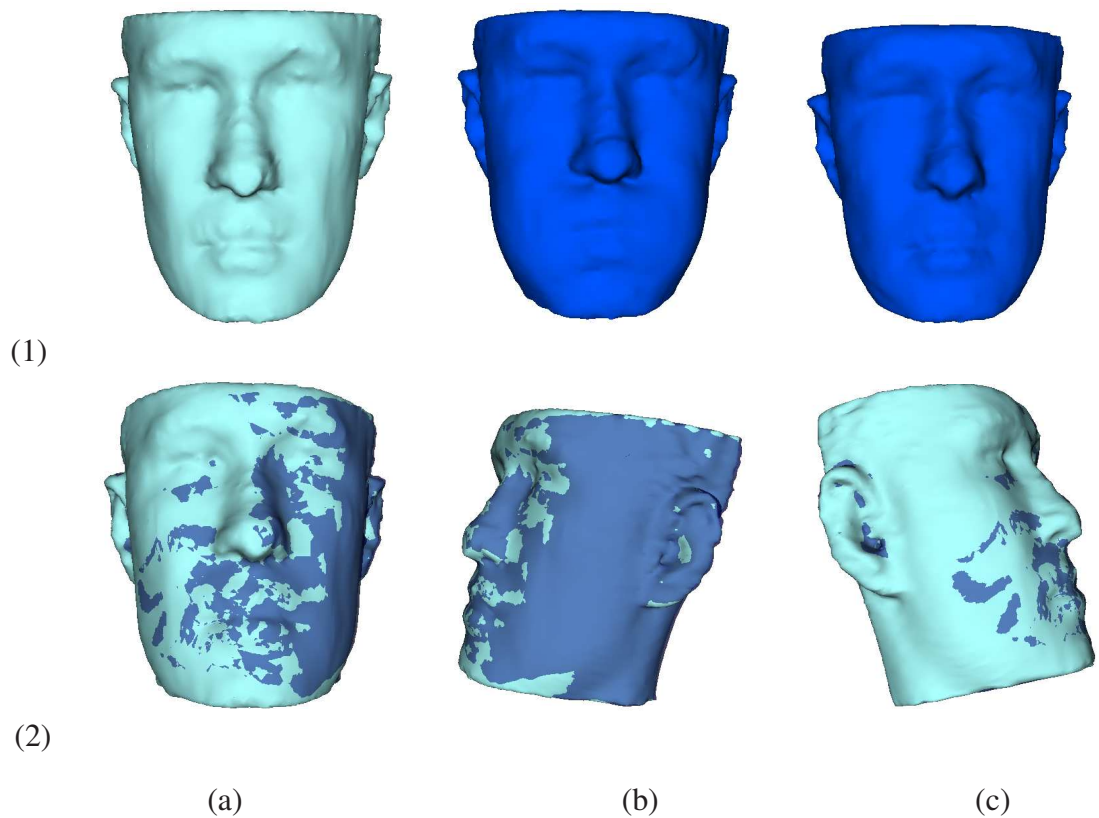
FIGURE 40 – Local registration of 3D face shapes generated from face range scans. Non-rigid registration of face with inflated expression to neutral face of the subject#2. (1-a) Target shape (neutral expression). (1-b) Original source shape (inflate expression). (1-c) Deformed source shape. (2-a,b,c) Three different views of the locally deformed source shape overlaid on the target shape.

2nd Experiment: Smile-to-Neutral
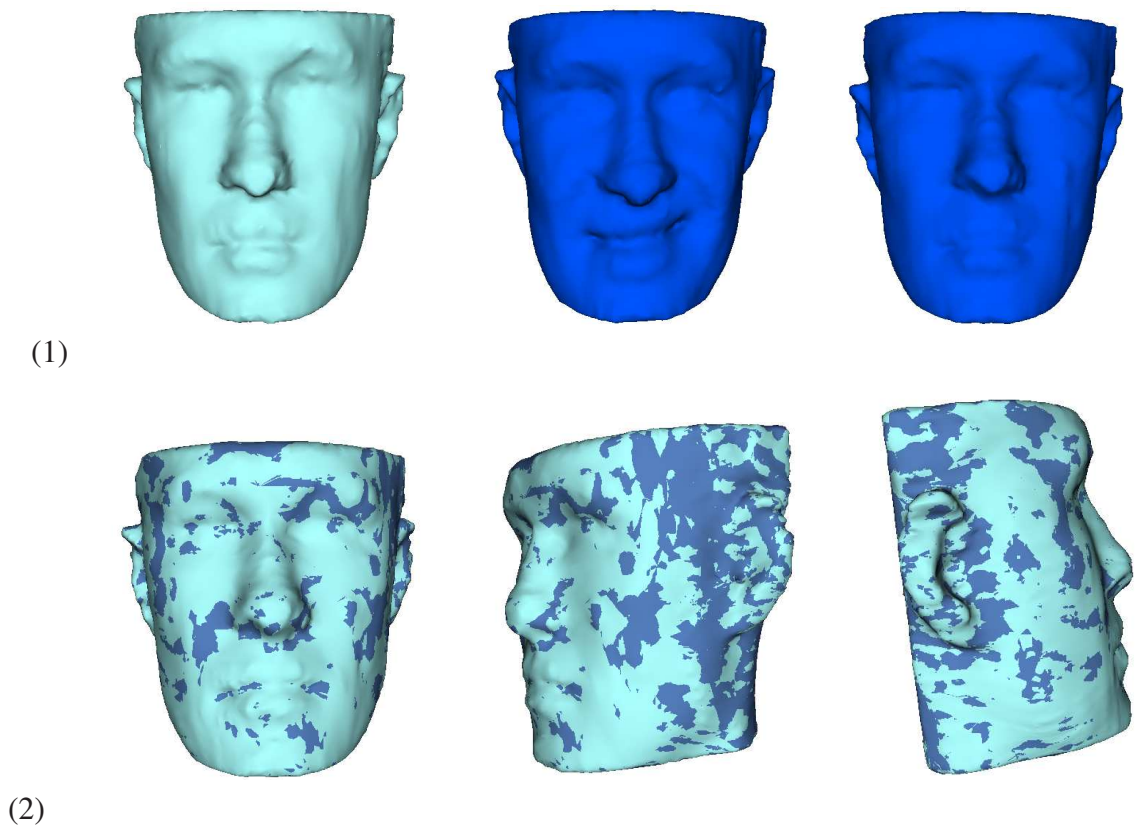
FIGURE 41 – Local registration of 3D face shapes generated from face range scans. Non-rigid registration of inflate face to neutral face of subject#2. (1-a) Target shape (neutral expression). (1-b) Original source shape (smile expression). (1-c) Deformed source shape. (2-a,b,c) Three different views of the locally deformed source shape overlaid on the target shape.
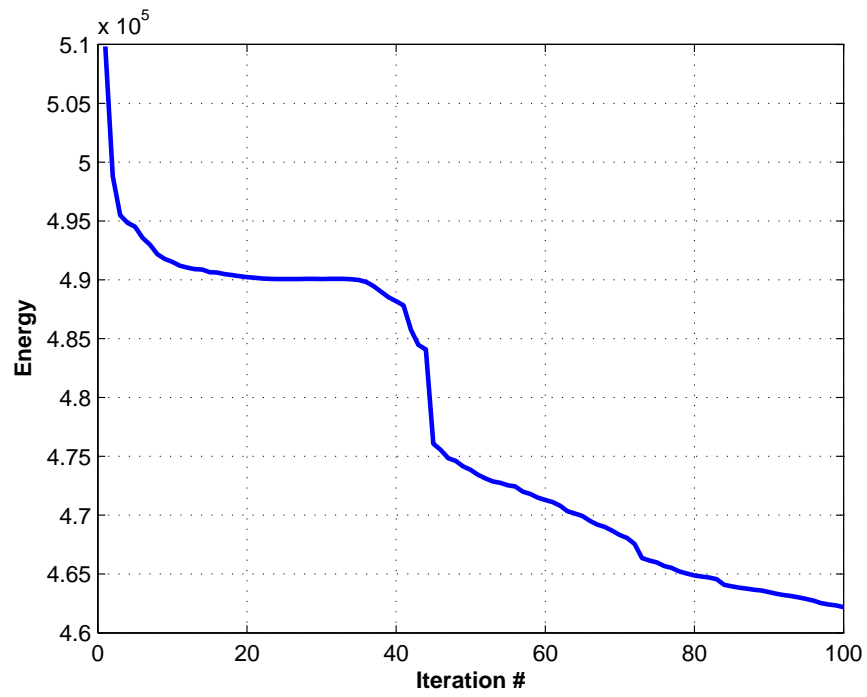
(a)
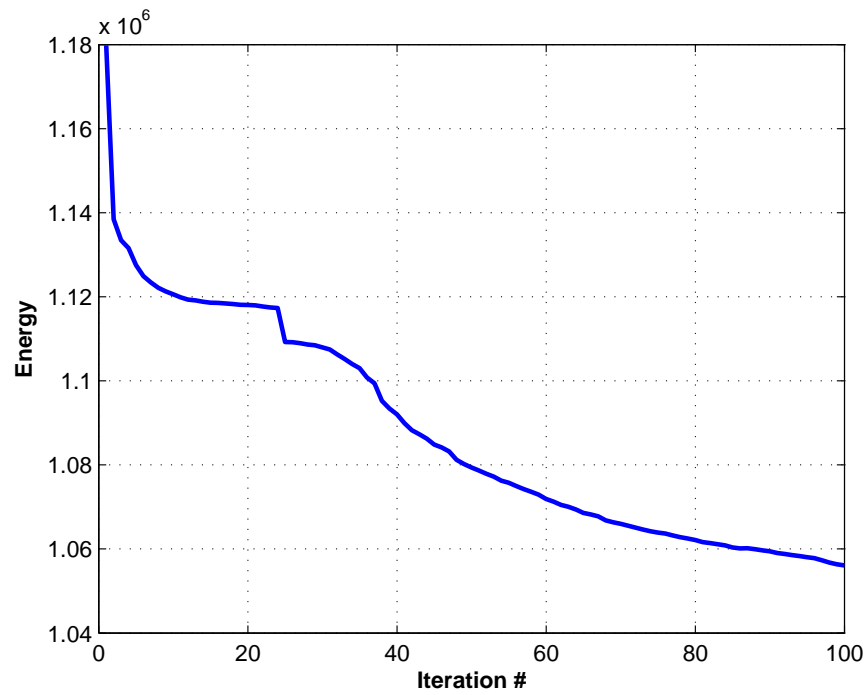
(b)

FIGURE 42 – Registration energies vs. iteration corresponding to the experiments shown in Fig. 40 and Fig. 41 respectively.

81

TABLE 3
ROOT-MEAN-SQUARE ERROR BETWEEN THE SIGNED DISTANCE MAPS OF
THE REGISTERED NON-NEUTRAL FACE MODELS WITH THE NEUTRAL FACE
MODELS FOR THE TWO SUBJECTS. FOR EACH SUBJECT, THE NON-NEUTRAL
FACE ARE THE SOURCES AND ARE REGISTERED WITH THE NEUTRAL FACE
OF THE SAME SUBJECT. **S** STANDS FOR SMILE AND **I** FOR INFLATE
EXPRESSIONS. NOTICE HOW THE *RMS* ERROR IS DROPPING AFTER EACH
ALIGNMENT STEP.

	Subject1		Subject2	
	I	**S**	**I**	**S**
Initial	8.0284	2.0446	1.5347	2.6392
After global registration	1.5433	1.7813	$\cdots$	$\cdots$
After local registration	0.8952	1.1432	1.0235	1.1976

F. Conclusion

In this chapter, a new variational framework for local registration of shapes is proposed. The shapes are implicitly represented through their signed distance maps. The local deformation field is explicitly established between the two globally aligned shapes, by minimizing a new energy functional that incrementally and simultaneously update the displacement field while keeping the corresponding distance map representation of the globally warped source shape as close to a signed distance function as possible. Various experiments were presented to show the effectiveness of the proposed framework.

Both the 2D and the 3D versions of the proposed non-rigid registration technique was implemented in C/C++ language and a graphical user interface was designed for an interactive use of the proposed approach.

CHAPTER V

3D FACE REGISTRATION:
AN ATTEMPT TO SOLVING THE FACE RECOGNITION PROBLEM

In this chapter, some insight is given as to how the proposed global-to-local shape registration framework can be employed to solve the problem of three dimensional face recognition in the presence of facial expressions. A data base of twenty one face scans of seven different subjects is acquired using the 3D laser scanner at the *CVIP* Lab.. Each subject is scanned with a neutral and two non-neutral facial expressions. The neutral face models will be used as gallery faces (enrollment), while the non-neutral face models will be used as probe faces (test against gallery). The goal is to devise a way to be able to recognize a non-neutral face by registering it to the existing neutral face models in the gallery.

A. 3D Face Registration and Face Recognition

The face recognition problem has received significant attention over the past decade for its wide range of commercial and law enforcement applications. Three dimensional registration of faces can serve greatly in solving this problem and can be employed as well to tackle the problems of facial expression tracking and face modelling.

Earlier efforts in this area of research were dedicated to solving the face recognition problem in two dimensional space. However, recent technological advances in 3D digitizing techniques have made the acquisition of 3D human face data much easier and cheaper. This type of data offers more clues and makes recognition using 3D models feasible. The recognition problem becomes more challenging in the presence of facial expressions, which cause shape distortions and hence weaken the performance of any rigid matching approach. Several methods have been developed to solve the 3D facial recognition problem using rigid matching approaches. The basic idea is to align the input facial surfaces and measure the

similarity between the aligned surfaces using, for example, the Hausdorff distance [88, 89], or the root-of-mean-squared (*RMS*) distance [90]. However, these methods lead to inaccurate results in the presence of facial expressions which introduce non-rigid distortions. Hence, 3D face recognition should be approached as a non-rigid surface matching problem. Few approaches have already been proposed to tackle this problem. Most of these approaches extract rigid parts of facial surfaces and use them for matching [91, 92].

This chapter aims at showing the potential of the proposed surface registration framework in addressing the 3D face recognition in the presence of facial expressions. It will be shown how the proposed registration approach can be used to reduce the local shape distortions induced by the expressions and that it can also be employed to tackle the problem of facial expression tracking.

Following is a description of how the 3D face recognition problem can be solved using the proposed shape registration approach. Assume that the gallery contains a neutral face model for each subject (which is the case for the available data sets). Given a probe face to be recognized, it is registered to every neutral face model in the gallery and then the amount of deformation undergone by the probe is estimated for each registration case and then a match score is returned. The probe face is recognized as the gallery subject whose neutral face corresponds to the smallest amount of deformation when registered with the probe.

B.   Data Acquisition and Preprocessing

The presented experiments are conducted on face scans of seven subjects. These data are acquired using the 3D laser scanner *"CyberWare3030"*[6] at the Computer Vision and Image Processing Lab (see Fig 43). This scanner provides head structure data in a cylindrical representation, with radii of surface points sampled at 512 equally-spaced angles, and at 450 equally spaced vertical distances. Figure 44 shows a sample cyclograph image of the scanned face and a 3D view of the corresponding scan respectively. For each

---

[6]http://cyberware.com

(a)   (b)

FIGURE 43 – (a) Laser scanner *"CyberWare3030"*. (b) Scanning set up.

(a)   (b)

FIGURE 44 – (a) Cyclograph image of a scanned face. (b) Corresponding 3D view.

subject, data corresponding to three different facial expressions were collected: a neutral expression, a smiling expression, and cheeks inflation expression (see Fig 45 for some examples of facial expressions). A total of 21 face data sets are generated by the scanner. These data contain large missing regions and holes, in particular on the hairy areas (see Fig. 44-b). Various techniques have been proposed to fill holes by interpolation between the borders (see e.g., [93]). In these experiments, the scanned faces undergo a series of preprocessing steps. First, a preliminary cropping is performed to separate the background from the facial region. The facial region is defined by a binary mask image whose computation involves thresholding the histogram of the depth coordinates. Morphological operations are then applied to the mask in order to remove non-connected regions and isolate the facial region as a single object. Holes inside the facial contour are closed by morphological closing. The final masked face regions are used to build 3D closed surfaces enclosing the facial region of interest. Examples of the these generated surfaces are shown on Fig. 45. Finally, the distance maps of each data set is approximated using the fast marching method (see Appendix I).

C. Experiments

A set of inter- and intra-subject alignments are carried out. For each subject, the non-neutral face models (i.e., faces with smile and inflate expressions) are registered, using the proposed surface registration technique, to every gallery face. That is, the probe faces are registered to every face model with neutral expression. A total of seven registration cases are performed for each probe face: one intra-subject registration and six inter-subject registrations.

The basic idea for the recognition process is to *"measure"* the amount of deformation undergone by the probe face during each of these registration cases. The probe is then recognized as the subject whose gallery face corresponds to the smallest measure of deformation. It is assumed that the gallery contains a neutral face model for each subject to be recognized. The following section summarizes the inter- and intra-subject registration

FIGURE 45 – Examples of generated face surfaces. Top row: examples of face models with non-neutral expressions. Bottom row: example of face models with neutral expression.

performances.

1. Some Registration Results

This section illustrates the inter and intra-subject registration results. For each subject, the face models with smiling and inflated expressions are locally registered with the neutral face model.

Qualitatively, some of the within-subject registration results can be seen in Figs. 46-52. The overlap between the input face models before and after registration are shown to visually highlight the registration accuracy. Moreover, for each registration case, the probe face is shown before registration and after being warped to match the gallery face. Note how accurate the results are.

Figure 53 and Fig. 54 illustrate couple of examples of the inter-subject registrations. Recall that the probe faces (faces with non-neutral expressions) of each subject are locally registered to the neutral faces of all other subjects. For instance, in Fig. 53, the face with

Inflate Expression
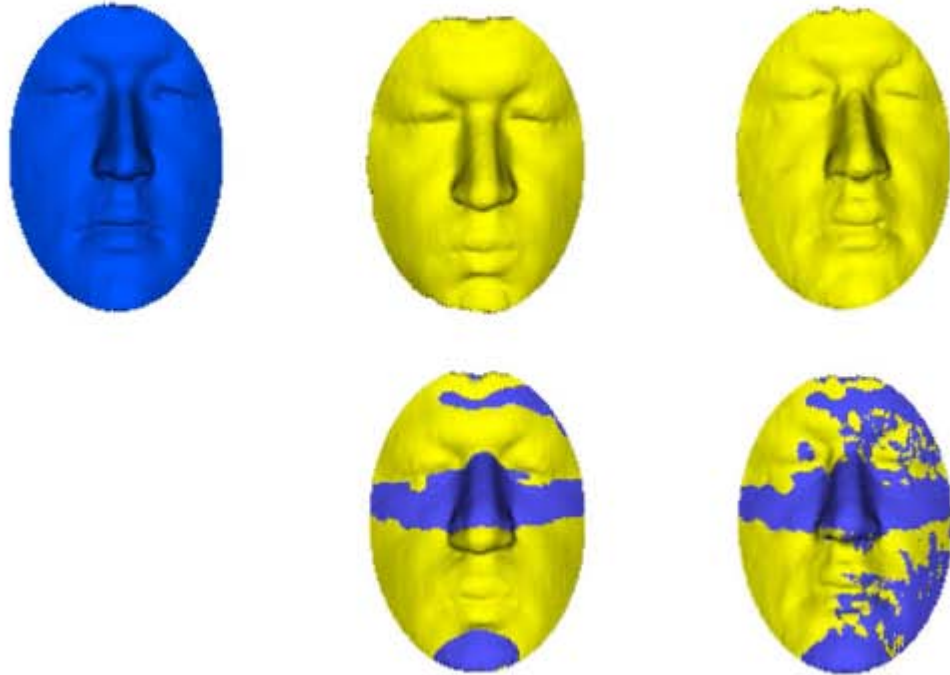
Smile Expression
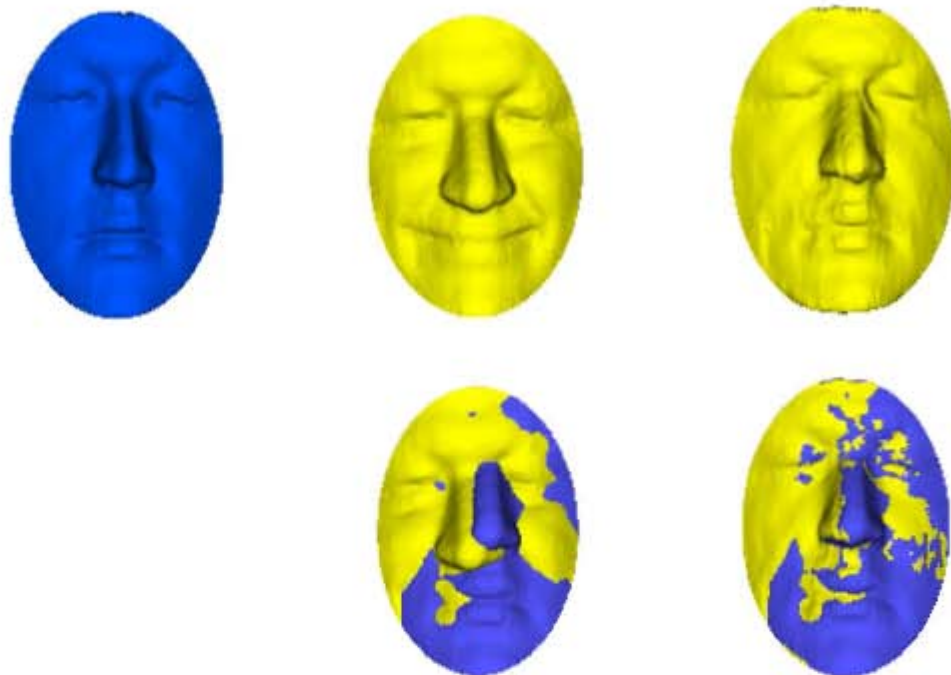
FIGURE 46 – Intra-subject registrations for subject#1. For each non-neutral expression are shown: Top: the original neutral face (blue), the original non-neutral face (yellow) and the locally deformed probe (yellow). Bottom: the overlap between original faces before and after registrations respectively.

Inflate Expression
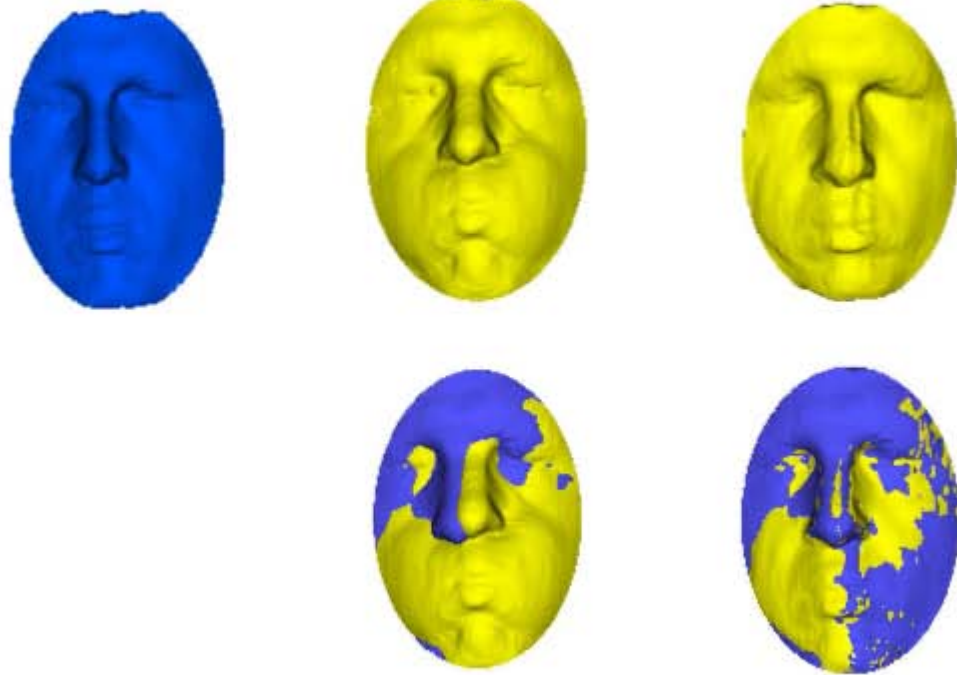
Smile Expression
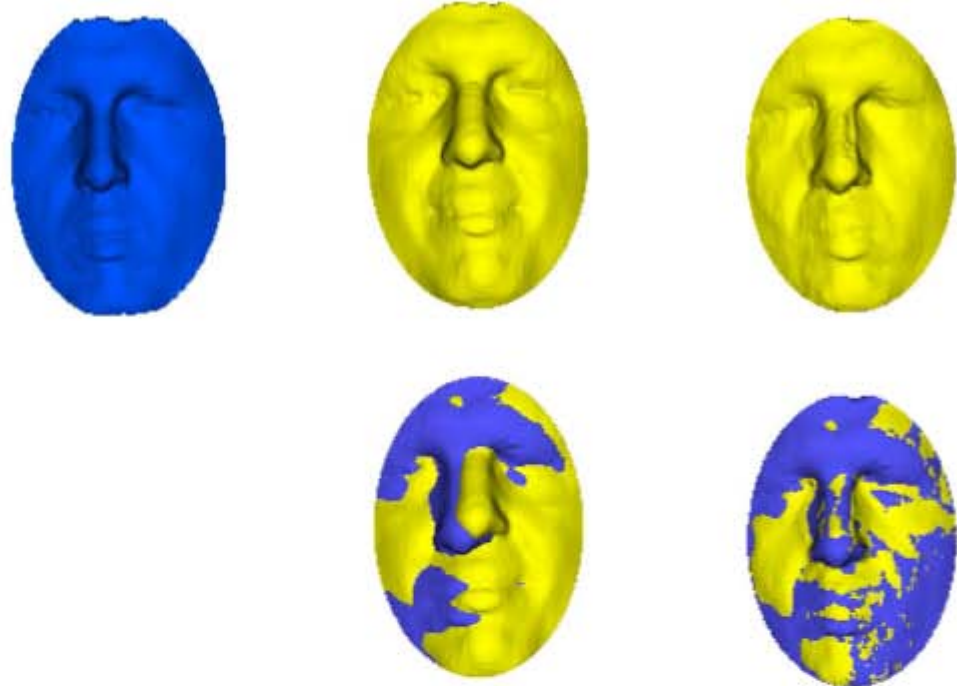
FIGURE 47 – Intra-subject registrations for subject#2. For each non-neutral expression are shown: Top: the original neutral face (blue), the original non-neutral face (yellow) and the locally deformed probe (yellow). Bottom: the overlap between original faces before and after registrations respectively.

Inflate Expression
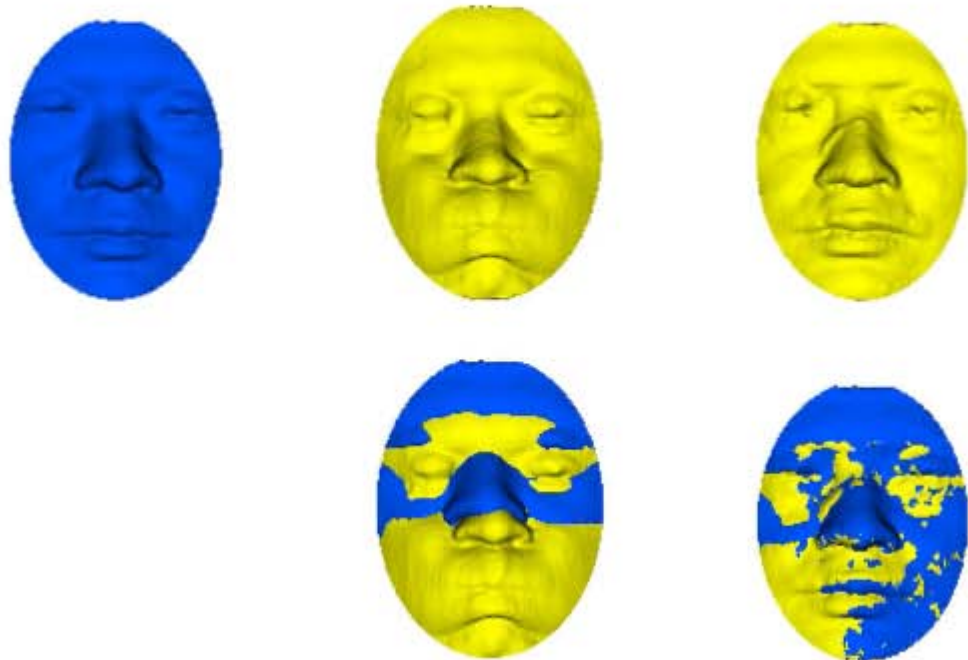
Smile Expression
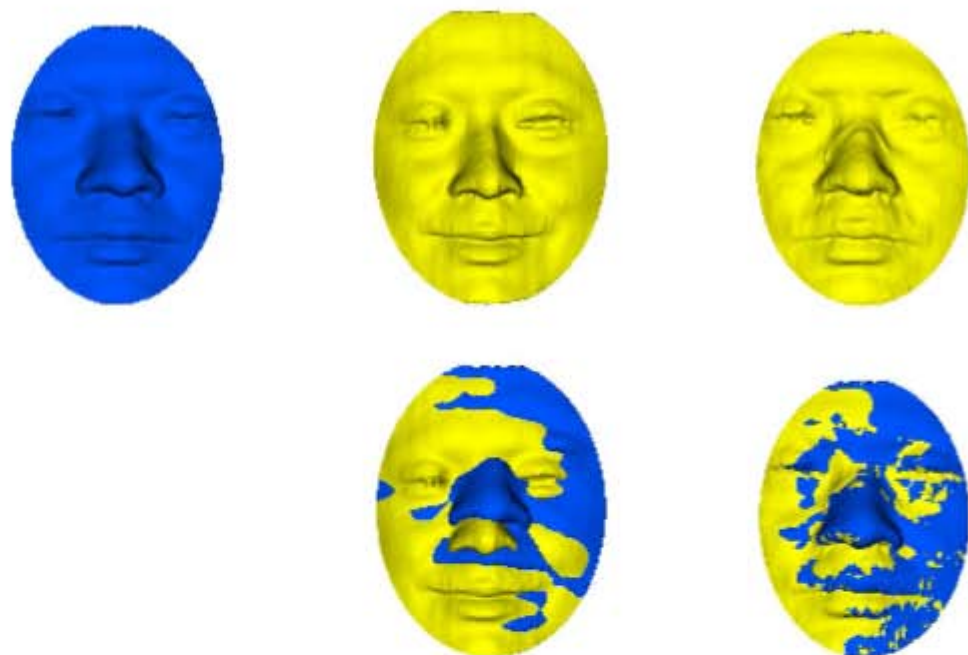
FIGURE 48 – Intra-subject registrations for subject#3. For each non-neutral expression are shown: Top: the original neutral face (blue), the original non-neutral face (yellow) and the locally deformed probe (yellow). Bottom: the overlap between original faces before and after registrations respectively.

Inflate Expression
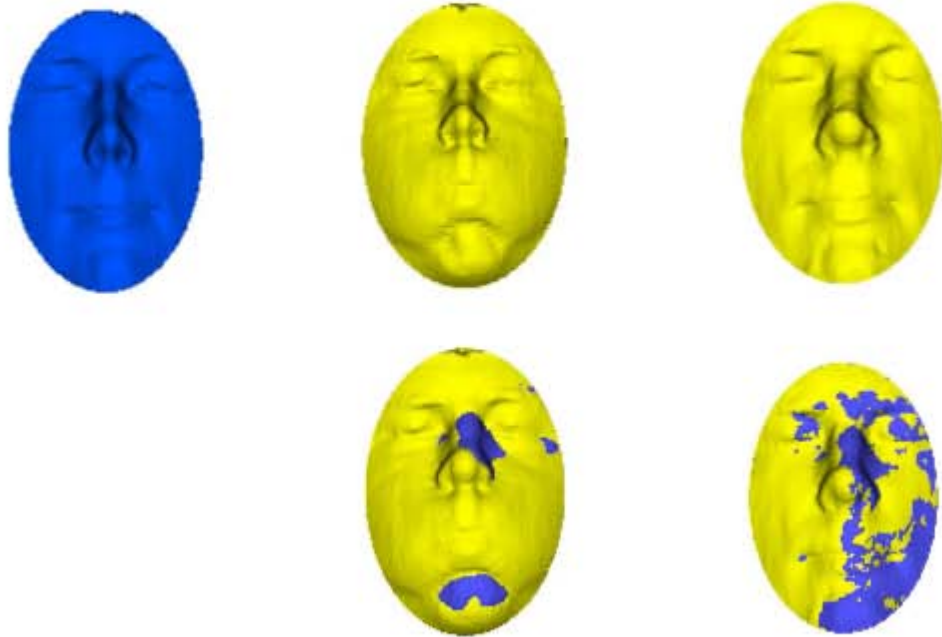
Smile Expression
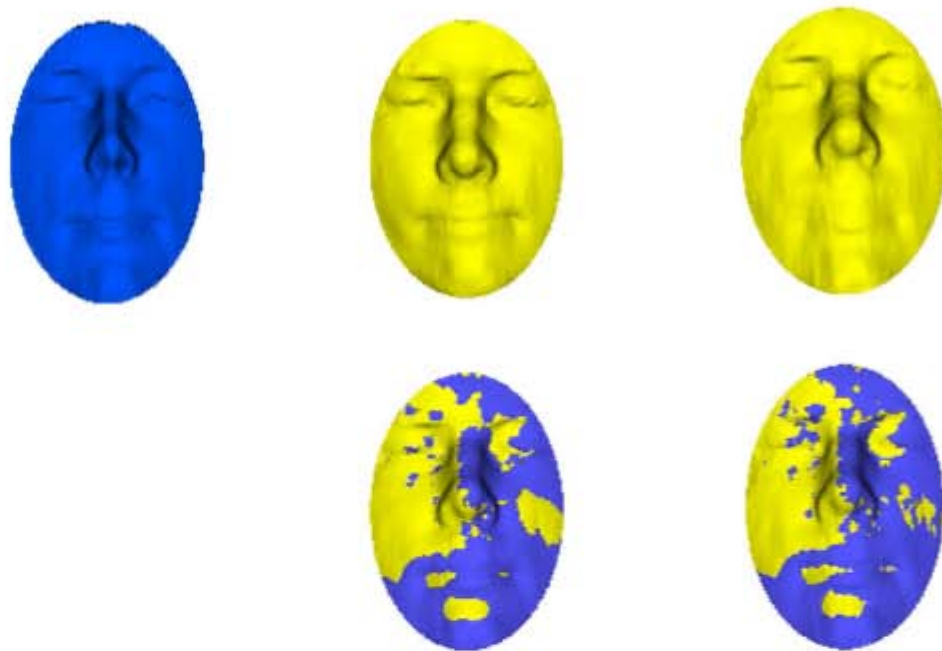
FIGURE 49 – Intra-subject registrations for subject#4. For each non-neutral expression are shown: Top: the original neutral face (blue), the original non-neutral face (yellow) and the locally deformed probe (yellow). Bottom: the overlap between original faces before and after registrations respectively.

Inflate Expression
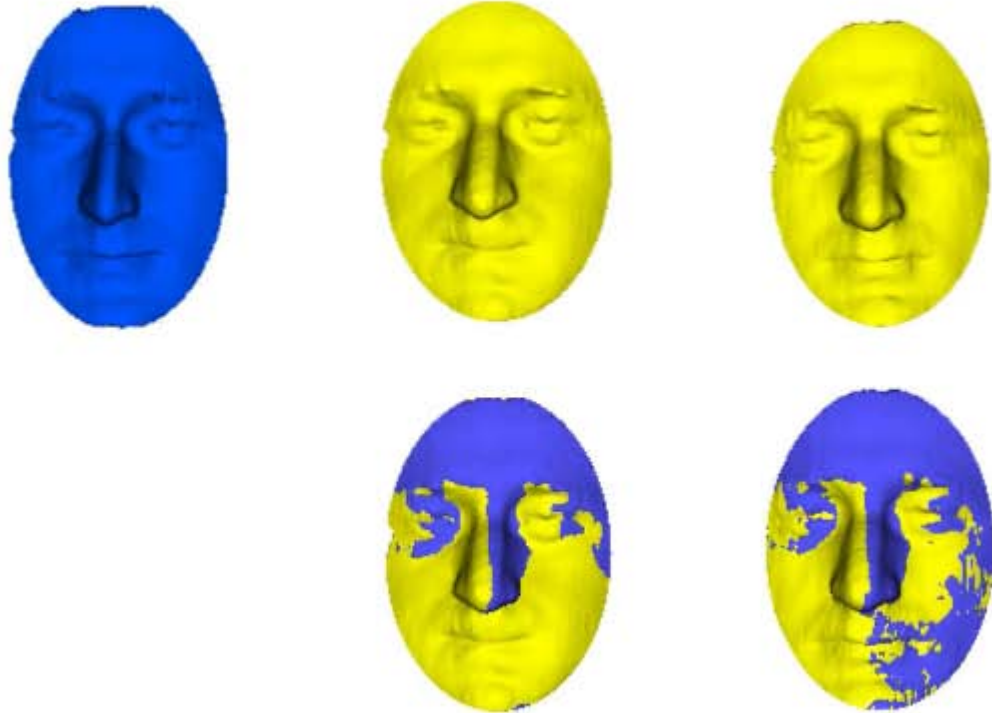
Smile Expression
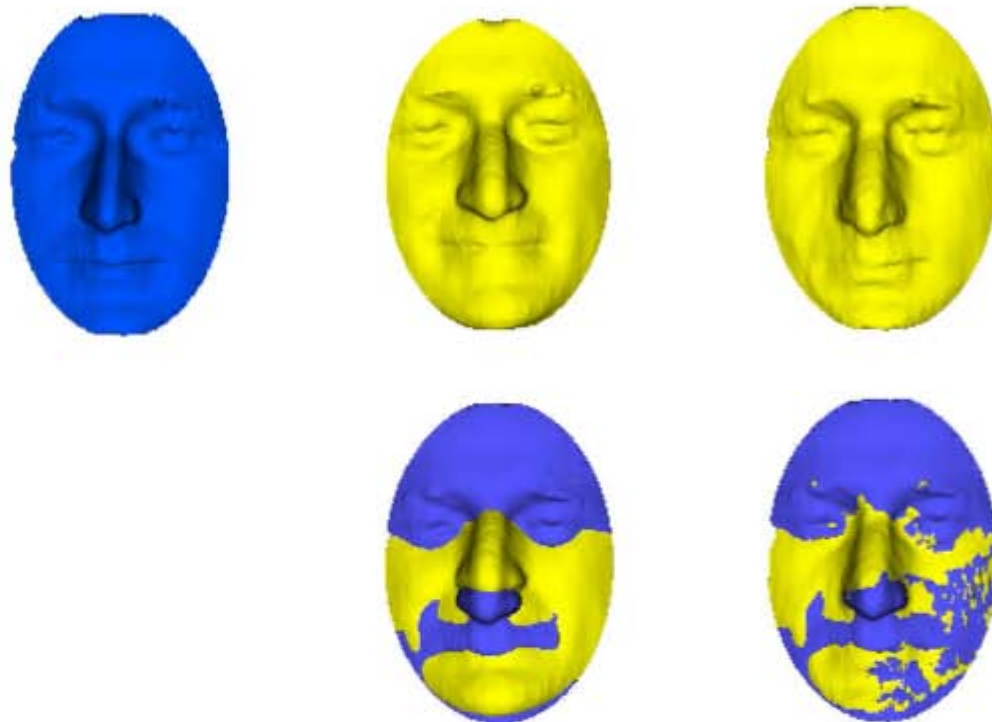
FIGURE 50 – Intra-subject registrations for subject#5. For each non-neutral expression are shown: Top: the original neutral face (blue), the original non-neutral face (yellow) and the locally deformed probe (yellow). Bottom: the overlap between original faces before and after registrations respectively.

Inflate Expression
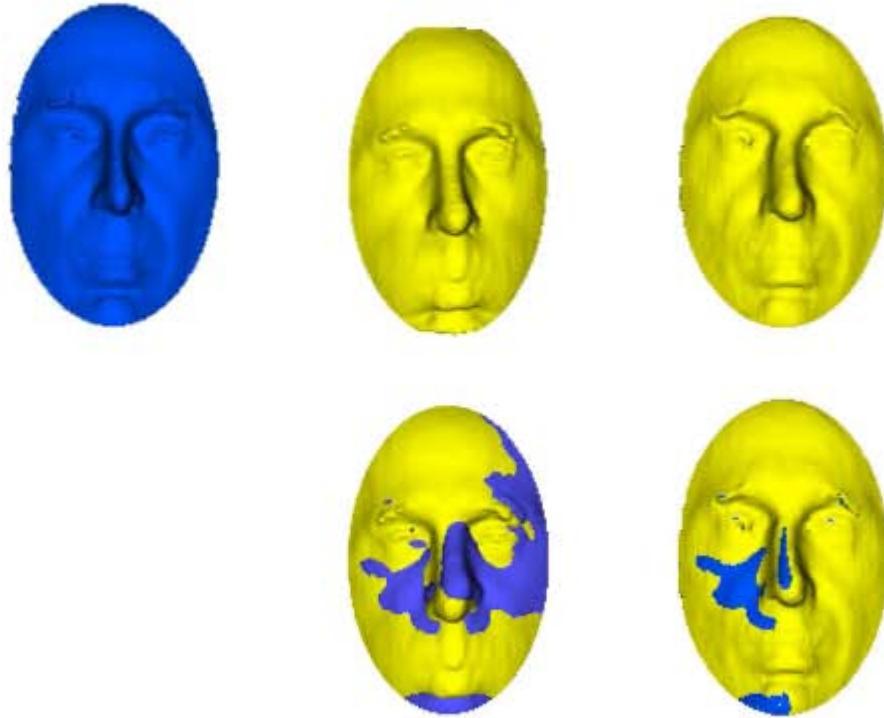
Smile Expression
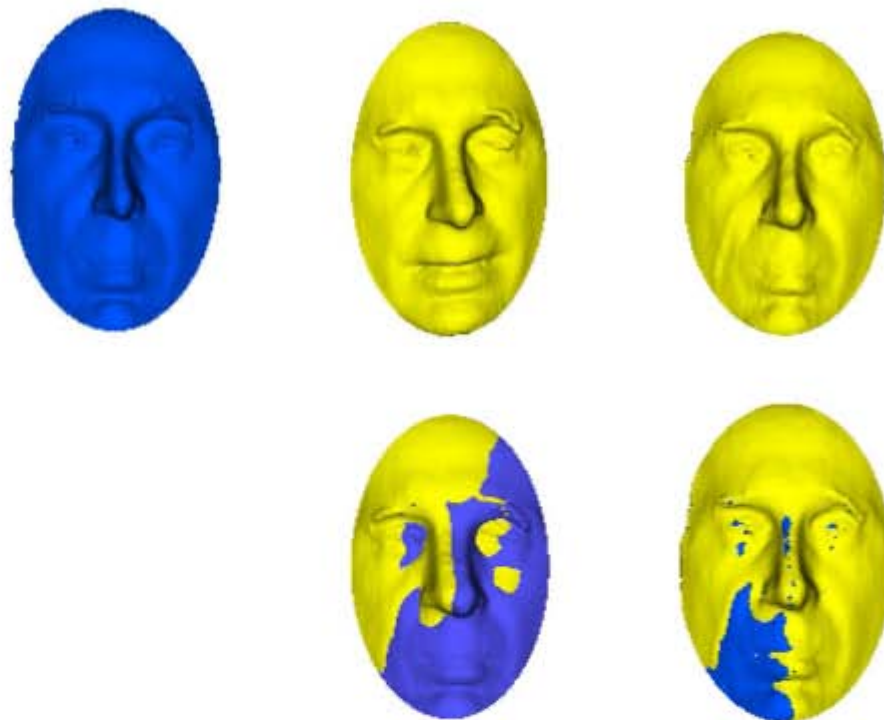
FIGURE 51 – Intra-subject registrations for subject#6. For each non-neutral expression are shown: Top: the original neutral face (blue), the original non-neutral face (yellow) and the locally deformed probe (yellow). Bottom: the overlap between original faces before and after registrations respectively.

Inflate Expression
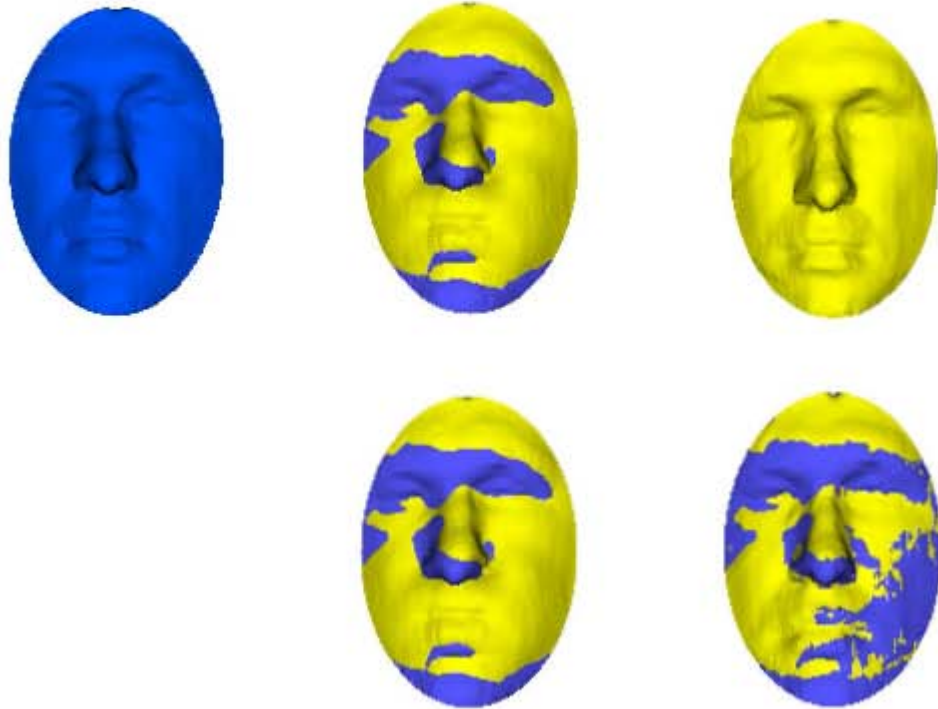
Smile Expression
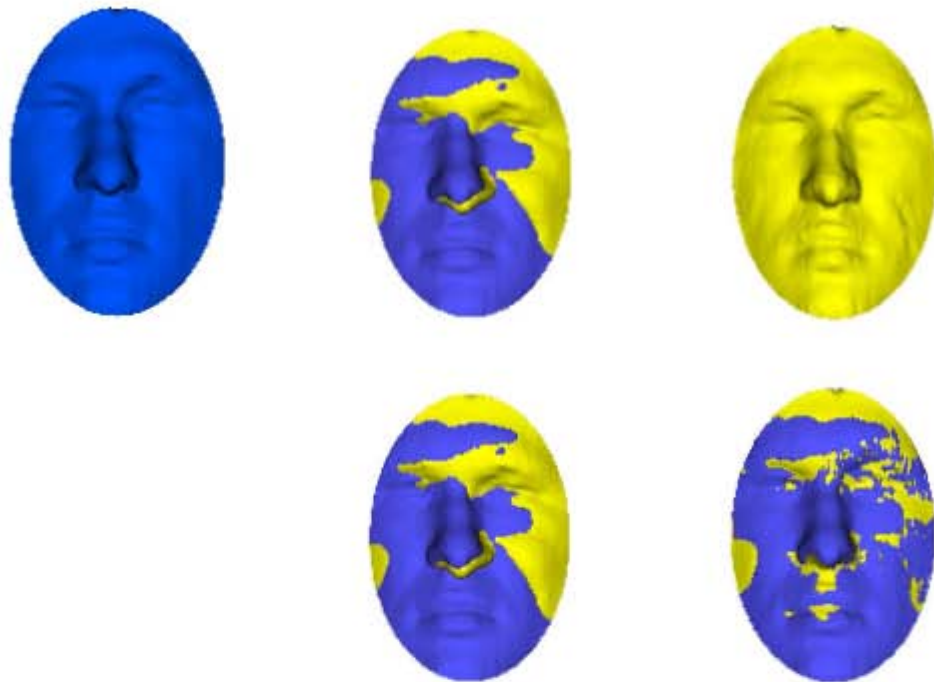
FIGURE 52 – Intra-subject registrations for subject#7. For each non-neutral expression are shown: Top: the original neutral face (blue), the original non-neutral face (yellow) and the locally deformed probe (yellow). Bottom: the overlap between original faces before and after registrations respectively.
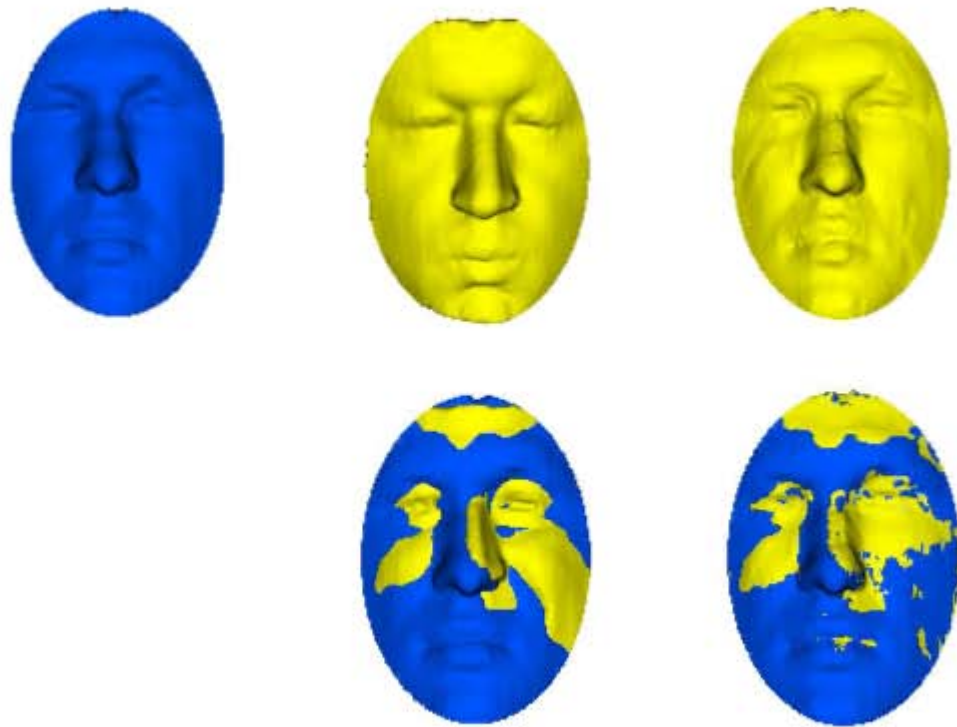
FIGURE 53 – Example of inter-subject registration. The smile face corresponding to subject#1 (probe) is locally registered to the neutral face of subject#7 (gallery). Top: the original neutral face (blue), the original non-neutral face (yellow) and the locally deformed probe (yellow). Bottom: the overlap between original faces before and after registrations respectively.

the smile expression of subject#1 is registered to the neutral face of subject#7. while in Fig. 54, the inflate face of subject#2 is locally registered to the neutral face of subject#1. The warped faces as well as the overlap between the input faces before and after registration are shown to appreciate the registration performance.

2. Face Recognition Results

To be able to recognize a probe face, a quantitative measure of the amount of deformation undergone by the probe after being registered to each and every galley face, is computed. The root of-mean-squared distance *RMS* is chosen for this purpose. More precisely, the *RMS* is computed between the established pairs of correspondences after reg-
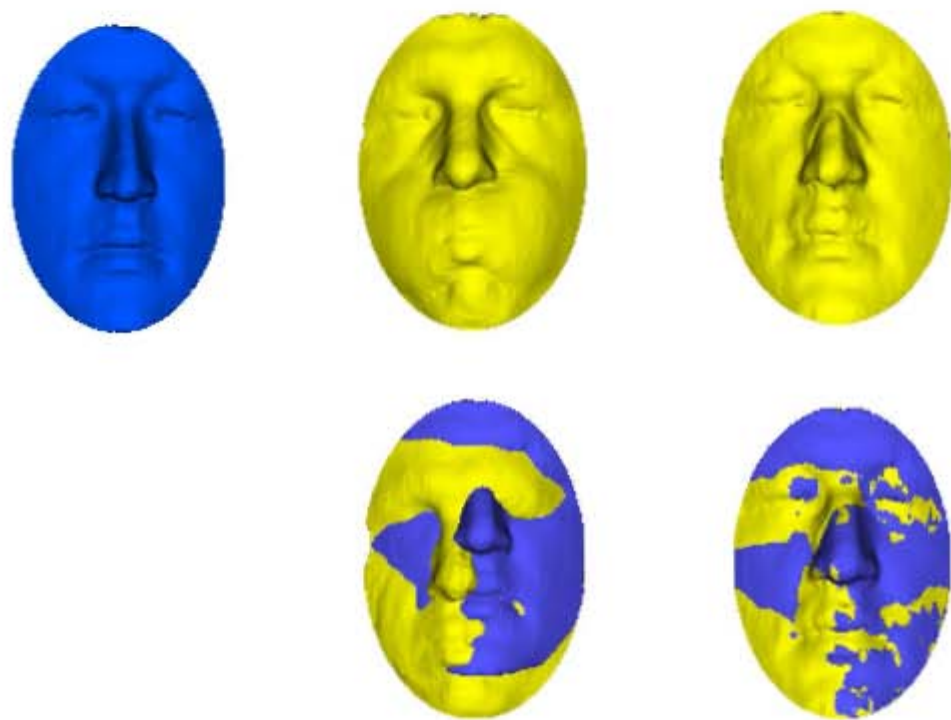
FIGURE 54 – Example of inter-subject registration. The inflate face corresponding to subject#2 (probe) is locally registered to the neutral face of subject#1 (gallery). Top: the original neutral face (blue), the original non-neutral face (yellow) and the locally deformed probe (yellow). Bottom: the overlap between original faces before and after registrations respectively.

TABLE 4

RECOGNITION RESULTS. GIVEN ARE THE *RMS* ERRORS BETWEEN THE PROBE FACES ((S):SMILE AND (I):INFLATE) AND THEIR REGISTERED VERSIONS WITH THE GALLERY FACES (NEUTRAL FACE MODELS). GREEN MEANS THAT THE PROBE IS SUCCESSFULLY IDENTIFIED AND RED MEANS OPPOSITE.

		Subj#1	Subj#2	Subj#3	Subj#4	Subj#5	Subj#6	Subj#7
Subj#1	I	**0.019842**	0.047931	0.038348	0.030126	0.051036	0.063783	0.035250
	S	**0.024153**	0.045304	0.029947	0.027911	0.045726	0.025520	0.023644
Subj#2	I	0.058390	**0.030468**	0.059906	0.047755	0.044904	0.079048	0.04707
	S	0.052777	**0.019161**	0.051331	0.040372	0.038069	0.131241	0.039805
Subj#3	I	0.065677	0.055352	**0.056455**	0.174547	0.057972	0.064426	0.049933
	S	0.061880	0.047181	**0.037325**	0.045390	0.047848	0.048107	0.038857
Subj#4	I	0.056424	0.044011	0.050895	**0.037237**	0.058062	0.048336	0.042773
	S	0.032214	0.033183	0.029455	**0.003868**	0.046452	0.082621	0.026098
Subj#5	I	0.059639	0.030813	0.050174	0.049932	**0.023717**	0.046663	0.041166
	S	0.054103	0.027181	0.04552	0.045998	**0.021597**	0.043586	0.037639
Subj#6	I	0.041413	0.052403	0.039734	0.043313	0.045754	**0.220750**	0.023194
	S	0.044355	0.060526	0.037331	0.127140	0.050012	**0.021756**	0.022223
Subj#7	I	0.038112	0.053220	0.033626	0.037286	0.052911	0.034526	**0.020590**
	S	0.039640	0.053394	0.032698	0.142636	0.043597	0.027711	**0.021188**

istering the given probe expression model with each neutral face models. The *RMS* distance is computed as follows:

$$\zeta = \sqrt{\frac{\sum_i^N \|\mathbf{x}_i - \overline{\mathbf{x}}_i\|^2}{N}}, \tag{55}$$

where N corresponds to the number of voxels on the non-neutral face surface. Note that this error (Eq. 55) corresponds to the root-mean-square of the displacement field magnitude over the probe surface. Indeed, for each given voxel $\mathbf{x}_i$ on the probe surface, its corresponding voxel after registration is given by $\overline{\mathbf{x}}_i = \mathbf{x}_i + \mathbf{u}(\mathbf{x}_i)$, with $\mathbf{u}$ being the displacement field. Ideally, this error is smaller when the probe is registered to the galley face corresponding to the same subject.

The *RMS* values corresponding to the two probe faces of each subject (smile and inflate) are summarized on Tables 4 where the green color means that a successful *"rank-1"* recognition and the red color means that the rank-1 match is incorrect. The probe is said to be rank-1 successfully recognized if the *RMS* distance obtained when registering it with its corresponding neutral model is the smallest compared to that obtained when it is registered to the remaining neutral models in the gallery.

Seven subjects were tested, each of which has two non-neutral expression models that needs to be recognized (total of 14 probes). If the recognition performance is only based on the smallest *RMS* value, which is known as the *"rank-1"* match, eleven out of the fourteen probes were successfully recognized, which corresponds to 78.6% success rate. However, results of facial identification or recognition are usually displayed using a Cumulative Rank Curve (*CRC*). Such a curve gives the recognition probability if the top K match results are returned. In this study, these match results correspond to the top K smallest *RMS* distances. The *CRC* gives an indication of how close one may get the correct match if the rank-1 match is not correct. The *CRC* corresponding to the presented experiments is illustrated in Fig. 55. One can notice that the proposed face recognition idea using the proposed surface registration has a rank-2 recognition rate of 93%.

D. Remarks and Possible Improvements

This chapter showed the potential of the proposed shape registration framework in registering three dimensional face data acquired from range scanners. Several inter and intra-subject registration cases were performed and the accuracy of the results was highlighted. These results showed that the proposed registration models are capable of handling the local distortions caused by facial expressions. This motivated this first attempt in applying the proposed surface registration technique for 3D face recognition. The root-mean-squared distance was used as a matching measure and a way of recognizing a probe face. Fourteen models were tested and eleven of them were successfully rank-1 recognized. Measures, other than the *RMS*, such as the surface interpenetration measure [94] are to be
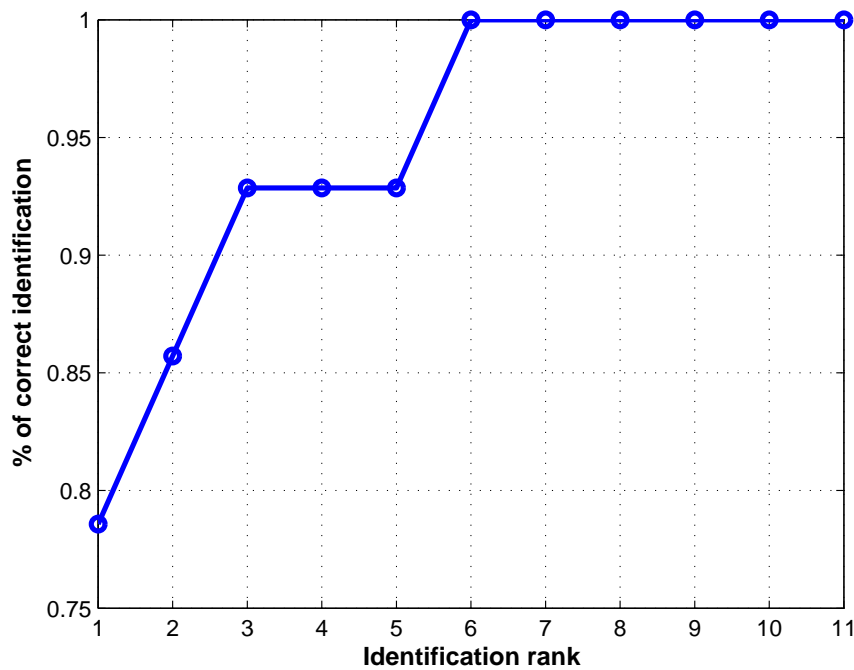
FIGURE 55 – Cumulative Rank Curve (*CRC*) corresponding to the recognition experiments summarized in table 4.

tested. Currently, the displacement fields generated from each of the intra- and inter-subject registrations are analyzed to improve the recognition accuracy.

The results obtained on the available small data base are encouraging and show that the proposed shape registration approach can be integrated in a face verification system. Such system manages the access control scenario where an authorized subject presents his or her identity to gain access to a secure facility. In such a scenario, an immediate acquisition of the subject face is performed and matched to its corresponding enrollment face (gallery face). Access is then granted if the matching score exceeds a certain threshold that is set through statistical examination of the probability of correct verification, or false reject rate, against false accept rate. Such threshold is set to guarantee that unauthorized individuals cannot get access to the facility.

The accuracy of the proposed idea for face recognition can be improved if a technique can be devised to deform the probe face in such a way that the within-class discriminative information is preserved. Following the ideas by Wang et al. [92], this can be done

by introducing some constraints while performing inter-subject registrations. The authors proposed to identify some face regions that nearly do not undergo any or small deformations when performing intra-subject alignments. They referred to these regions as *"nearly rigid"* components. A learning process is employed on a set of 60 training samples to build a rigid template that denotes the nearly rigid components. The Poisson-based mesh deformation technique is finally used to guide the deformation so that the nearly rigid components of the probe remain unchanged during registrations. This will guarantee that these registrations will make face models from the same subject more similar while maintaining the discrimination between different subjects which would improve the recognition scores.

CHAPTER VI

MULTI-REGION LEVEL SET SEGMENTATION WITH SELECTIVE SHAPE PRIORS AND POSE INVARIANCE

A.   Introduction

Segmenting an image into its semantically significant parts plays a fundamental role in various computer vision and medical imaging applications. Yet, the segmentation process presents several challenges that are mainly related to image noise, poor contrast, weak or missing boundaries between imaged objects, and inhomogeneities, etc. Consequently, segmentation approaches that primarily rely on low level image cues, such as color information and/or texture may not output accurate results. One way to overcome this difficulty is to exploit the prior knowledge of shapes and other properties of the imaged structures in order to constrain the segmentation process. The incorporation of such priors into the segmentation framework becomes even more necessary in the presence of occlusion, corruption, shadows, etc.

The integration of shape priors into level set based segmentation approaches has become a major focus in the field of medical imaging as well as other computer vision applications. In this chapter, the particular piece-wise constant Chan and Vese segmentation models with shape priors are addressed, and a fast algorithm to solve the 2-phase Chan-Vese model with shape prior is first proposed. This algorithm is motivated, in part, by the work of Song and Chan [6]. Instead of directly solving the underlying *PDE*'s, the segmentation energy is calculated and its changes are checked when image points are moved from inside the region enclosed by the evolving interface to the outside region and vice-versa. This algorithm is then generalized to the multi-phase Vese-Chan model with multiple selective shape priors and a corresponding labelling function for each prior. This makes the

proposed algorithm different from that in [34] and other similar works in different aspects. On one hand, the proposed algorithm is not restricted to two regions, but allows segmentation into several regions. On the other hand, more than one shape prior can be taken into account by this algorithm. In addition, the proposed algorithm improves dramatically the computational speed. Finally, the new dissimilarity measure introduced in chapter (III.C) is used to address the pose invariance problem and to recover the registration parameters between the shape prior(s) and the evolving interface(s). Experimental results, on both synthetic and real images, demonstrate the performance of the proposed algorithm and the computational improvements it offers.

B. Chan and Vese Segmentation Models

Chan and Vese first proposed a two-region active contour model without edges for image segmentation as a generalization of the Mumford-Shah functional [95]. The same authors extended their formalism to deal with multiple regions. This extension enforces an efficient domain partition up to 2^m regions with no gaps and overlaps, using m level-set functions (see [1]). In this chapter, only the piece-wise constant versions of these models are considered.

1. Two-Phase Model

Given are an image $f : \Omega \rightarrow \mathbb{R}$ with two gray level values f_+ and f_-, a curve $\mathcal{C} = \partial\omega$, with $\omega \subseteq \Omega$, and two unknown constants c_1 and c_2. Chan and Vese used a level set function ϕ to represent the curve $\mathcal{C}$, i.e., $\mathcal{C} = \{\mathbf{x} \in \Omega / \phi(\mathbf{x}) = 0\}$ and proposed to minimize the following energy with respect to ϕ, c_1 and c_2 in order to segment f into object and background [1]:

$$E_{2CV}(\phi, c_1, c_2) = \int_\Omega [(f - c_1)^2 H(\phi) + (f - c_2)^2 H(-\phi)] d\mathbf{x} + \nu \int_\Omega |\nabla H(\phi)| d\mathbf{x}, \quad (56)$$

where $H(a)$ denotes the Heaviside function which equals 1 if $a \geq 0$ and vanishes elsewhere. The scalars c_1 and c_2 are iteratively updated with ϕ and take on the average gray

values in the regions $A = \{\mathbf{x} \in \Omega / \phi(\mathbf{x}) > 0\}$ and $B = \{\mathbf{x} \in \Omega / \phi(\mathbf{x}) < 0\}$ respectively,

$$c_1 = \frac{\int_\Omega f(\mathbf{x}) H(\phi(\mathbf{x})) d\mathbf{x}}{\int_\Omega H(\phi(\mathbf{x})) d\mathbf{x}}, \quad c_2 = \frac{\int_\Omega f(\mathbf{x}) H(-\phi(\mathbf{x})) d\mathbf{x}}{\int_\Omega H(-\phi(\mathbf{x})) d\mathbf{x}}.$$

Minimizing (56) leads to a 2-phase segmentation of the image given by $\widetilde{f}(\mathbf{x}) = c_1 H(\phi(\mathbf{x})) + c_2(H(-\phi(\mathbf{x})))$.

2. Multi-Phase Model

Within the multi-phase model proposed by Vese and Chan [1], m level set functions, $\phi_1, \ldots, \phi_m$, are used to segment the domain Ω up to $n = 2^m$ regions or phases with no vacuums or overlaps between them. Each phase is defined as the set of image points $\mathbf{x}$ such that the vector function $\mathbf{H}(\Phi(\mathbf{x})) \doteq (H(\phi_1(\mathbf{x})), \ldots, H(\phi_m(\mathbf{x})))$ is constant. In the particular case of using two level set functions (i.e., $n = 2^2 = 4$), the piece-wise constant energy, E_{4CV}, can be written as:

$$E_{4CV} = \int_\Omega [(f - c_{11})^2 H(\phi_1) H(\phi_2) + (f - c_{10})^2 H(\phi_1) H(-\phi_2) + (f - c_{01})^2 H(-\phi_1) H(\phi_2) +$$
$$(f - c_{00})^2 H(-\phi_1) H(-\phi_2)] d\mathbf{x} + \nu \int_\Omega [|\nabla H(\phi_1)| d\mathbf{x} + |\nabla H(\phi_2)|] d\mathbf{x},$$

$$(57)$$

where the constants c_{ij} are updated at each iteration as the mean gray values of the sets $A = \{\phi_1 > 0, \phi_2 > 0\}$, $B = \{\phi_1 > 0, \phi_2 < 0\}$, $C = \{\phi_1 < 0, \phi_2 > 0\}$, and $D = \{\phi_1 < 0, \phi_2 < 0\}$.

To minimize the energies given by (56) or (57), the classical way of proceeding is to use a gradient descent scheme to implement the corresponding Euler-Lagrange equations. Adequate smooth approximations of the Heaviside function and its derivative are to be used for such implementation. Such minimization procedure requires the energy functional to be differentiable with respect to the level set functions, which may not be always the case. Moreover, this algorithm is computationally expensive given the nonlinear parabolic nature of the underlying *PDE*s. To overcome this difficulties, Song and Chan [6] proposed a new algorithm which does not necessitate to solve the Euler-Lagrange equations, but instead it directly computes the segmentation energy and checks if it decreases or not when a point

is moved from one region to another. A different algorithm was proposed by Gibou and Fedkiw [41] to reduce the computational effort required to solve the Chan-Vese segmentation model. Both of these techniques exploit the fact that one only needs to know the sign of the level set function and not its value in order to evolve the segmenting contour. The technique proposed in [41] differs from that in [6] in the sense that the former solves a simplified Euler-Lagrange version of the Chan-Vese model by dropping the length term and allowing for large time steps. The regularization length term is re-introduced through a separate non-linear diffusion process. In [6], the length term is generally ignored. However, this term can be easily considered when checking the change of energy as needed to regularize the contour evolution.

C.   Segmentation Using Shape Priors and Labelling Functions

Incorporating shape priors into the Chan-Vese model was considered in several previous works. A single training prior (or an inferred statistical model from a set of training shapes) is embedded by its signed distance function, $\widetilde{\phi}$, and a shape energy term, measuring the distance between the evolving level set ϕ and $\widetilde{\phi}$, is added for instance to the functional (56):

$$E = E_{2CV} + \alpha \int_{\Omega} (\phi(\mathbf{x}) - \widetilde{\phi}(\mathbf{x}))^2 d\mathbf{x}, \tag{58}$$

where $\alpha \geq 0$ determines the weight of the prior. The pose invariance of the prior with respect to the evolving shape can be incorporated into this energy as will be seen in a subsequent section. However, at this point, the discussion is limited to the case where each object of interest and its corresponding shape prior share the same pose and same orientation. Note that for large values of α, only the image object with a shape form similar to the prior shape will be segmented and all unfamiliar structures will be suppressed when minimizing (58). This is illustrated in Fig. 56(c). In order to segment the known object, or any of its corrupted versions, without affecting the segmentation of the unknown objects, Cremers et al. [34] proposed to add a labeling function $L : \Omega \rightarrow \mathbb{R}$ which takes on the value ± 1 to indicate the image regions where the shape prior should be active. The shape

energy is then changed to the following form:

$$E_{shape} = \int_\Omega (\phi(\mathbf{x}) - \widetilde{\phi}(\mathbf{x}))^2 (L(\mathbf{x}) + 1)^2 d\mathbf{x}.$$

Figs. 56(d) show some results when using the labelling function. Note that only the case of static labelling is considered by assuming the localization of the learned object to be known.

In this chapter, these ideas are also extended to the multi-phase Chan and Vese model, and one shape prior and one labelling function is used for each level set. The labelling functions indicate where to enforce which prior. For the purpose of simplicity, the presentation is limited to the 4-phase case with two level set functions.

Let $\widetilde{\phi}_1$ and $\widetilde{\phi}_2$ denote the implicit representation of two different shape priors, and let L_1 and L_2 be their corresponding labeling functions. The proposed functional to be minimized is,

$$E = E_{4CV} + \alpha_1 \int_\Omega (\phi_1(\mathbf{x}) - \widetilde{\phi}_1(\mathbf{x}))^2 (L_1(\mathbf{x}) + 1)^2 d\mathbf{x} + \alpha_2 \int_\Omega (\phi_2(\mathbf{x}) - \widetilde{\phi}_2(\mathbf{x}))^2 (L_2(\mathbf{x}) + 1)^2 d\mathbf{x},$$

(59)

where E_{4CV} is given by (57),

D.   Proposed Algorithm

Instead of minimizing the functional given by (Eq. 58) or (Eq. 59) by directly solving the corresponding Euler-Lagrange equations which is computationally expensive, the work of Song et al. [6] is followed and the following algorithms are proposed. The length terms are left out and only the sign of the level set functions counts.

1.   2-Phase Model

(1) Initialize ϕ by partitioning the image into two regions: $A = \{\mathbf{x} \in \Omega / \phi(\mathbf{x}) = 1\}$ and $B = \{\mathbf{x} \in \Omega / \phi(\mathbf{x}) = -1\}$.

(2) Let $a = |A|$ and $b = |B|$ denote the number of pixels in each region, and c_1 and c_2 the average gray values in A and B resp.. Let $\mathbf{x}_0$ be the current pixel, if $\mathbf{x}_0 \in A$ (resp. $\mathbf{x}_0 \in B$),

then compute the change in energy if the point $\mathbf{x}_0$ is moved to B (resp. to A), as:

- $\Delta E_{AB} = (f(\mathbf{x}_0) - c_2)^2 \dfrac{b}{b+1} - (f(\mathbf{x}_0) - c_1)^2 \dfrac{a}{a+1} + 4\alpha \widetilde{\phi}(\mathbf{x}_0)(L(\mathbf{x}_0) + 1)^2,$

- $\Delta E_{BA} = (f(\mathbf{x}_0) - c_1)^2 \dfrac{a}{a+1} - (f(\mathbf{x}_0) - c_2)^2 \dfrac{b}{b-1} - 4\alpha \widetilde{\phi}(\mathbf{x}_0)(L(\mathbf{x}_0) + 1)^2. \quad (60)$

If $\Delta E_{AB} < 0$ (resp. $\Delta E_{BA} < 0$) then move $\mathbf{x}_0$ to B (resp. to A).

(3) Repeat step 2 until the energy E remains unchanged.

2. 4-Phase Model

(1) Initialize ϕ_1 and ϕ_2 by partitioning the image into 4 regions: $A = \{\phi_1 = 1, \phi_2 = 1\}$, $B = \{\phi_1 = 1, \phi_2 = -1\}$, $C = \{\phi_1 = -1, \phi_2 = 1\}$, and $D = \{\phi_1 = -1, \phi_2 = -1\}$.
(2) Let $a = |A|$, $b = |B|$, $c = |C|$, and $d = |D|$ denote the number of pixels in each region, and let c_{11}, c_{10}, c_{01}, and c_{00} be the average gray values in A, B, C, and D, resp.. For each pixel $\mathbf{x}_0$, check how the energy changes when moving $\mathbf{x}_0$ from its current region to each one of the other three regions, and then update $\mathbf{x}_0$ by assigning it to the region that corresponds to the largest decrease of energy. For instance, if $\mathbf{x}_0 \in B$, then move it one at a time to the remaining three regions and compute the corresponding energy changes as follows:

- $\Delta E_{BA} = (f(\mathbf{x}_0) - c_{11})^2 \dfrac{a}{a+1} - (f(\mathbf{x}_0) - c_{10})^2 \dfrac{b}{b-1} - 4\alpha_2 \widetilde{\phi}_2(\mathbf{x}_0)(L_2(\mathbf{x}_0) + 1)^2,$

- $\Delta E_{BC} = (f(\mathbf{x}_0) - c_{01})^2 \dfrac{c}{c+1} - (f(\mathbf{x}_0) - c_{10})^2 \dfrac{b}{b-1} + 4\alpha_1 \widetilde{\phi}_1(\mathbf{x}_0)(L_1(\mathbf{x}_0) + 1)^2$
$$- 4\alpha_2 \widetilde{\phi}_2(\mathbf{x}_0)(L_2(\mathbf{x}_0) + 1)^2,$$

- $\Delta E_{BD} = (f(\mathbf{x}_0) - c_{00})^2 \dfrac{d}{d+1} - (f(\mathbf{x}_0) - c_{10})^2 \dfrac{b}{b-1} + 4\alpha_1 \widetilde{\phi}_1(\mathbf{x}_0)(L_1(\mathbf{x}_0) + 1)^2.$

$$(61)$$

Move $\mathbf{x}_0$ to the region corresponding to the smallest negative difference in energy.
(3) Repeat step 2 until the energy remains unchanged.

3. Remarks

⋆ The derivation of the equations giving the difference of energies ($\Delta E_{??}$) can be found in the appendix IV.

⋆ In order to segment only the familiar objects, one can drop the terms $(L_i + 1)^2$, $i = 1, 2$, in the expressions given by (60) and (61).

⋆ The sign of the prior terms in (60) and (61) depends on whether the prior function $\widetilde{\phi}(\mathbf{x}_0)$ is changing from $+1$ to -1 or vice-versa when moving $\mathbf{x}_0$ between phases.

⋆ In steps **(2)**, one can sweep the pixels row by row, using either the Jacobi or Gauss-Seidel iteration in each sweep.

E. Experimental Results

All of the presented experiments were run on a $2.99GHz$ Pentium4 PC with 2GB RAM. First, the proposed algorithms are tested on several 2-phase images of size 150×150 as shown in Fig. 56. The proposed algorithm is applied on these images without using shape prior (Fig. 56(b)), with shape prior (Fig. 56(c)), and with prior and a static labelling function (Fig. 56(d)). In each case, Jacobi iteration is used and the algorithm converges in one quick sweep ($\leq 0.1sec$). In Figs. 56(c-d), the used shape prior, $\widetilde{\phi}$, encodes the shape of the corrupted object in the image scene.

In order to demonstrate the speed and robustness of the proposed algorithm, two synthetic images with synthetic noise are used and the standard Chan-Vese model with prior is applied by solving the underlying *PDE* (see [1, 34]) and compared the results (see Figs. 57(b)) to those obtained when using the proposed algorithm (see Fig. 57(c)). For the top image, which is of size 100×100, the introduced algorithm converges in 4 sweeps ($0.125sec$) to the exact solution without using the length term, while after 200 iterations ($6.36sec$), the standard Chan-Vese implementation leads to less satisfactory results. The bottom image is of size 176×176. For this image, convergence of the proposed algorithm is achieved in 6 sweeps ($0.21sec$) compared to 140 iterations and $25.85sec$ for the standard CV implementation with less accurate results. The normalized energy is plotted vs. the

iteration for both implementations as shown in Figs. 57(d). Note how fast the introcuded algorithm executes.

In Fig. 58, multi-phase cases are considered. For these experiments, only the results corresponding to the fast implementation are presented. The input images are all 4-phase images with two familiar objects being corrupted. For the top two images (Figs. 58(1-2)), which are of size 176×176, the two corrupted objects are the Lenticular Nucleus (*LN*) and Ventricle, and the Caudate Nucleus and the *LN*, respectively. For the bottom two images (Figs. 58(3-4)), which are of size 200×200, the two corrupted objects are the left and right dudes, and the plus sign and the triangle, respectively. Figs. 58(a) show the purely intensity-based segmentations. The use of two shape priors, encoding the shapes of the corrupted familiar objects, allows the recovery of these objects and suppressed the unfamiliar ones as shown on Figs. 58(c). Finally, a labelling function is assigned to each prior (as shown on Figs. 58(b)), in order to segment both familiar and unfamiliar objects as shown on Figs. 58(d). Four sweeps ($0.25sec$) were needed for the results on Figs. 58(1,2-d) while only one sweep ($0.125sec$) was sufficient for the results shown on Figs. 58(1,2-a,b,c). For the bottom images, the results on Figs. 58(3,4-d) took $\approx 0.5sec$ in 4 sweeps, and only one sweep ($0.23sec$) was enough for the results shown on Figs. 58(3,4-a,b,c). The proposed algorithm was also tested on real images with only shape priors and no labelling functions. Figure 59 and Fig. 60 show the results on two multi-phase images with and without partial occlusion. In both cases, the proposed algorithm converges to the exact solution (recovery of the two known objects: Rabbit and Mug for Fig. 59 and ventricle and gray matter for Fig. 60) in one sweep. For the MR brain image, which is of size 256×256, the shape-based segmentation result was obtained in $0.234sec$ (Fig. 60(c)) and $0.984sec$ for the fast purely intensity based segmentation (Fig. 60(b)). Note that when using the standard implementation, about 200 iterations ($35.45sec$) were required to duplicate the segmentation result shown on Figs. 59(b). More experiments on real images are shown on Fig. 61 to illustrate how fast and robust the proposed method is to noise and partial occlusion. Note that the length term was not considered in neither of these experiments.
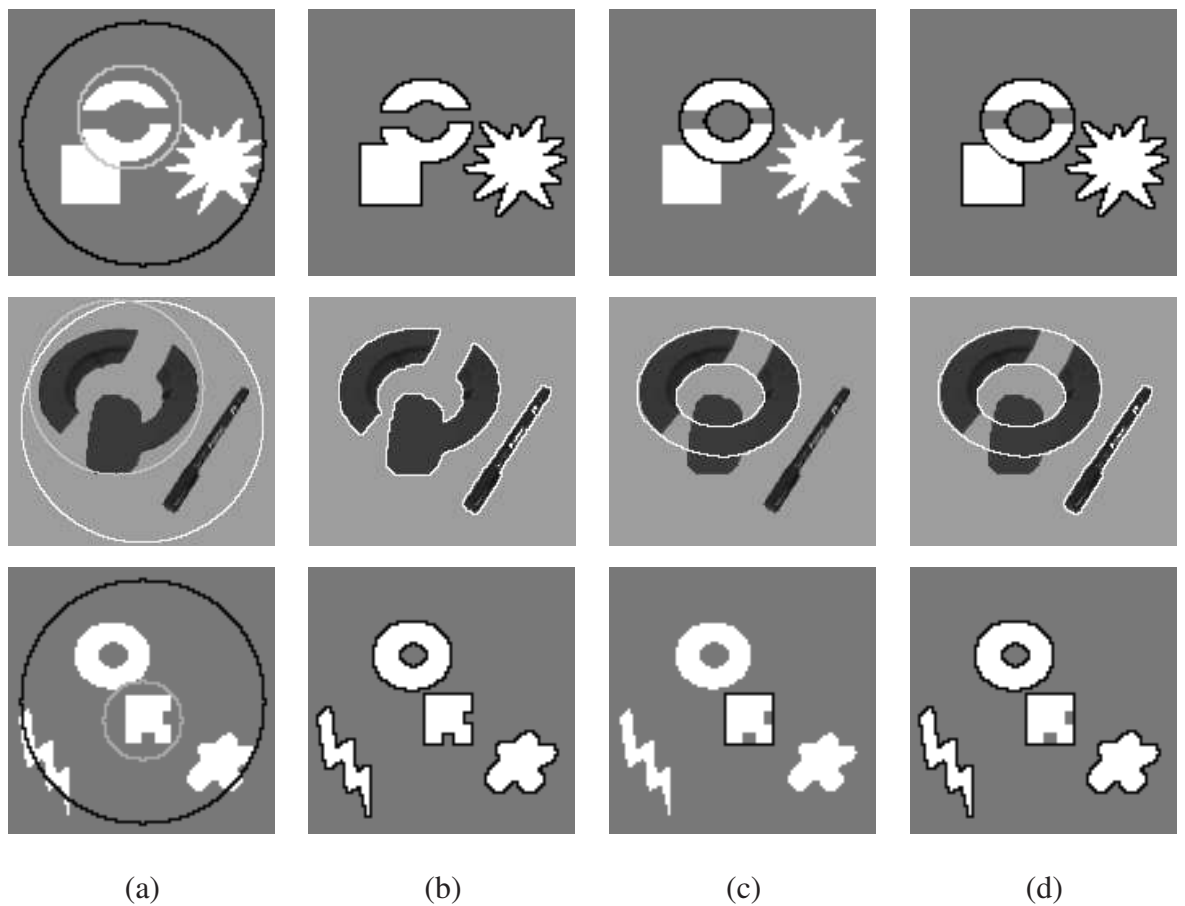
FIGURE 56 – The 2-phase segmentation results. (a) Input images with initial level set and labeling function around the corrupted object. (b) Results when using pure fast Chan-Vese model [6]. (c) Results when adding shape prior. Only the familiar object is recovered while other objects are suppressed. (d) Results when using shape prior with labeling function, in this case the segmentation of unfamiliar objects is not affected.

(a)	(b)	(c)	(d)
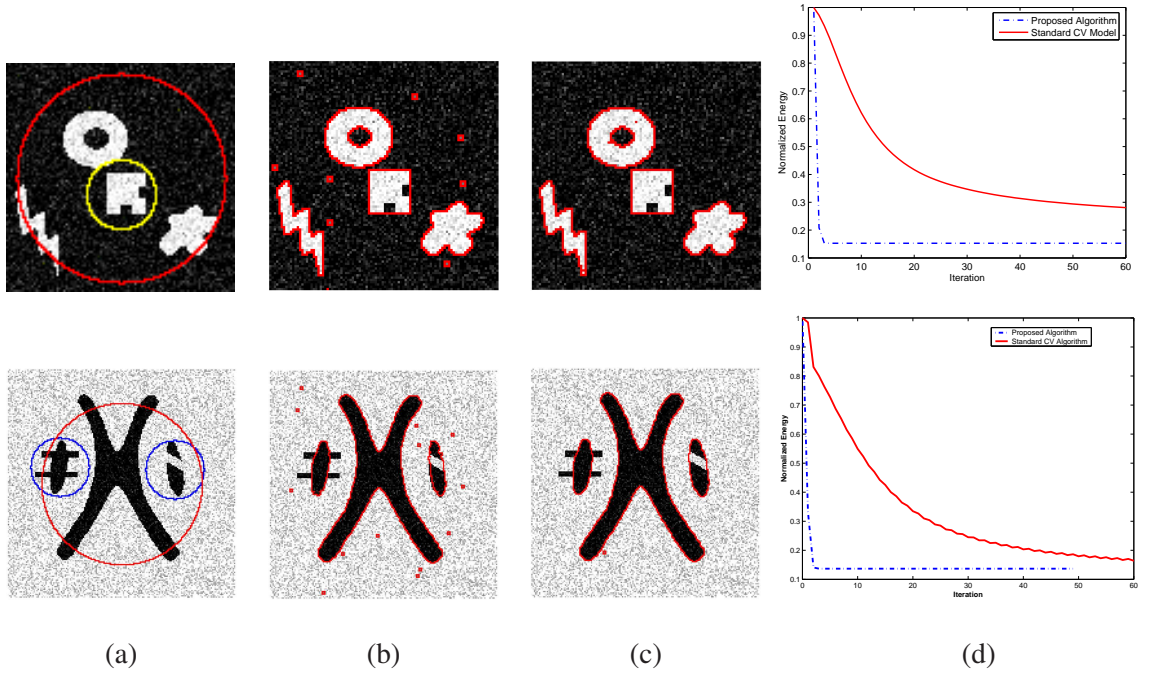
FIGURE 57 – (a) Initial conditions of the level set function ϕ (big circles), and a static labelling function around the corrupted objects (small circles). (b) Standard Chan-Vese model (some noise is kept at steady state). (c) Result using the proposed algorithm. (d) Normalized energy vs. iteration for both cases.

F. An Affine Invariant Formulation

Up to this point, the pose and orientation of the object(s) of interest are supposed known and in accordance with the pose of the shape prior(s). However, this is not the case in a realistic segmentation problem. If an object of interest is no longer located with the same scale and orientation on the image scene as the shape prior $\widetilde{\phi}$, the segmentation formalism presented in Sec. VI.E will fail. To solve this problem, the proposed global alignment model (see Chap.III) is used to recover the transformation, $\mathcal{A} = \mathcal{A}(\mathcal{S}, \mathcal{R}, \mathcal{T})$, between the evolving level set function ϕ and the prior $\widetilde{\phi}$, where $\mathcal{S} = diag(s_x, s_y)$ is a diagonal matrix whose entries are the scale factors in each direction, $\mathcal{R} = \mathcal{R}(\theta)$ is a 2D rotation matrix, and $\mathcal{T} = [\mathcal{T}_x, \mathcal{T}_y]^T$ is a translation vector. The following shape energy is proposed

$$E_{shape} = \int_{\Omega} (\|\mathcal{S}\|\phi(\mathbf{x}) - \widetilde{\phi}(\mathcal{A}\mathbf{x}))^2 d\mathbf{x}, \tag{62}$$

and is simultaneously minimized with respect to ϕ and the transformation parameters, with

111
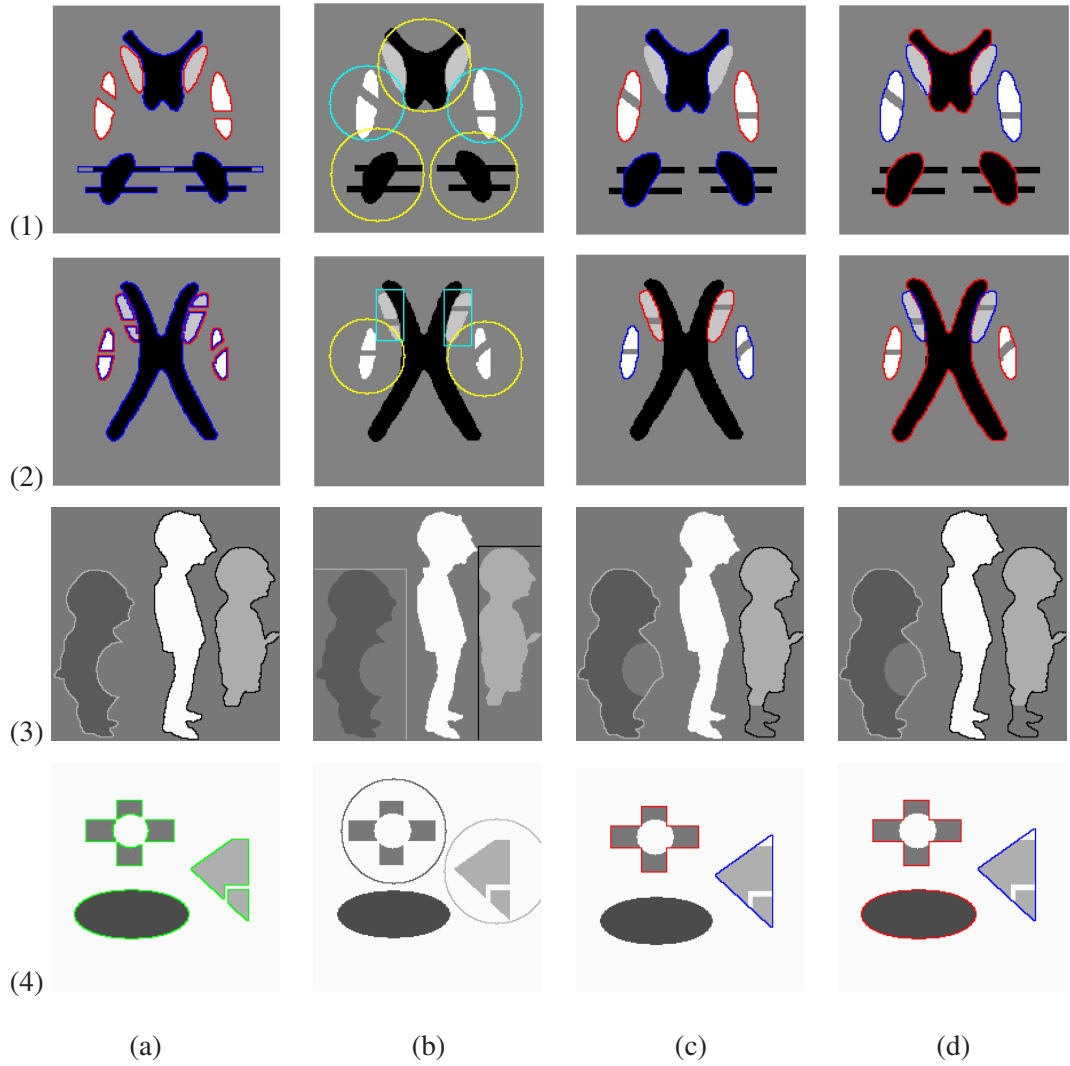
FIGURE 58 – Multi-phase segmentation results with 2 shape priors. (a) Data-driven segmentation. (b) Labelling functions around the familiar corrupted objects that are to be recovered. (c) Results using shape priors; the familiar objects are successfully reconstructed but the unfamiliar ones are suppressed. (d) Results when adding the labelling functions; in this case the correct segmentation of the unfamiliar objects is not affected (see text for details).

(a) (b)

(c) (d)
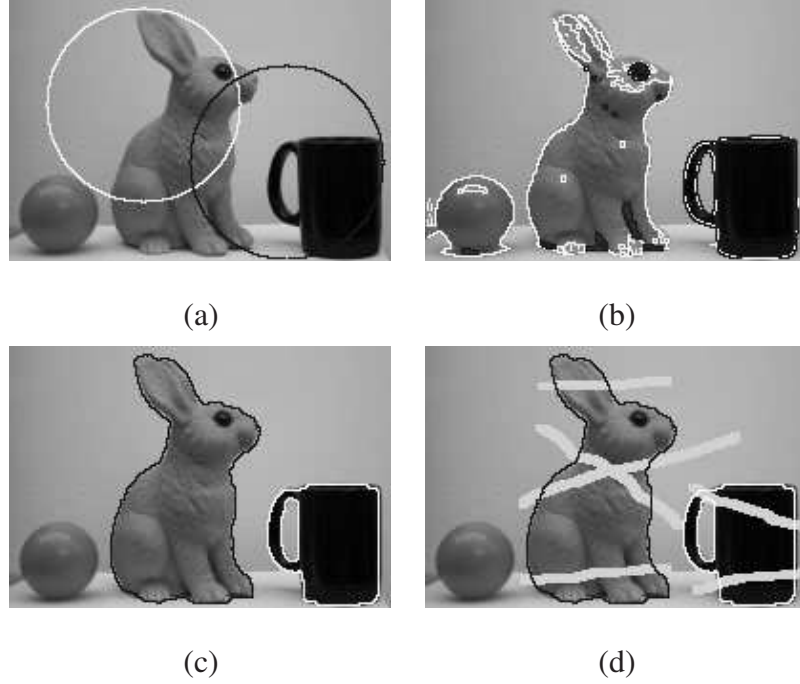
FIGURE 59 – Application to real images. (a) Initial level sets. (b) Purely intensity-based segmentation. (c) Integration of shape priors which allows to recover the 2 objects of interest (Rabbit and Mug). (d) The object of interest are successfully segmented even in the presence of partial occlusion using the same initial conditions as in (a).

$\|\mathcal{S}\| = max(|s_x|, |s_y|)$ denoting the infinity norm of the diagonal matrix $\mathcal{S}$. As was shown in Chapter III, the proposed *SSD* handles accurately the case of anisotropic scales. For computational considerations and better performance, the functional given by Eq. (62) is minimized within a narrow band around the zero-crossing of the level set function. The calculus of variations leads to the following evolution equations for each parameter of the transformation $\mathcal{A}$:

$$\frac{ds}{dt} = 2 \int_{\Omega} \mathbf{r}(\mathbf{x}) \cdot [\frac{d\|\mathcal{S}\|}{ds_x} \phi(\mathbf{x}) - \nabla \widetilde{\phi}(\mathcal{A}\mathbf{x})^T \cdot \nabla_s \mathcal{A}\mathbf{x}],$$

$$\frac{da}{dt} = 2 \int_{\Omega} \mathbf{r}(\mathbf{x}) \cdot \nabla \widetilde{\phi}(\mathcal{A}\mathbf{x})^T \cdot \nabla_a \mathcal{A}\mathbf{x},$$

where $s \in \{s_x, \ s_y\}$, $a \in \{\theta, \ \mathcal{T}_x, \ \mathcal{T}_x\}$ and $\mathbf{r}(\mathbf{x}) = \delta(\phi(\mathbf{x}))(\|\mathcal{S}\|\phi(\mathbf{x}) - \widetilde{\phi}(\mathcal{A}\mathbf{x}))$, with $\delta(.)$ being the derivative of $H(.)$, and ∇ denotes the gradient operator.

The shape energy (62) is combined with the 2-phase and the 4-phase Chan and Vese segmentation models (see Eqs. 63, and 64-65 resp.). In this case, each evolving interface, ϕ, is updated through a gradient descent scheme using its *"actual"* value not only its sign:

(a)　　　　　　　　　　　　(b)

(c)　　　　　　　　　　　　(d)
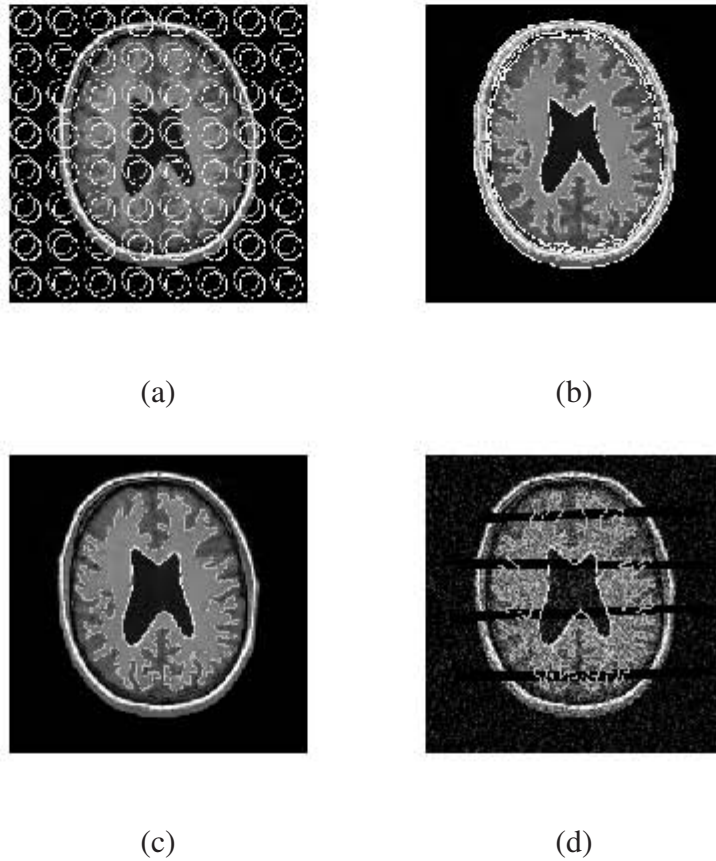
FIGURE 60 – Application to real images. (a) Initial level sets. (b) Purely intensity-based segmentation. (c) Integration of shape priors which allows to recover the 2 objects of interest (Gray matter and ventricle). (d) The object of interest are successfully segmented even in the presence of partial occlusion using the same initial conditions as in (a).
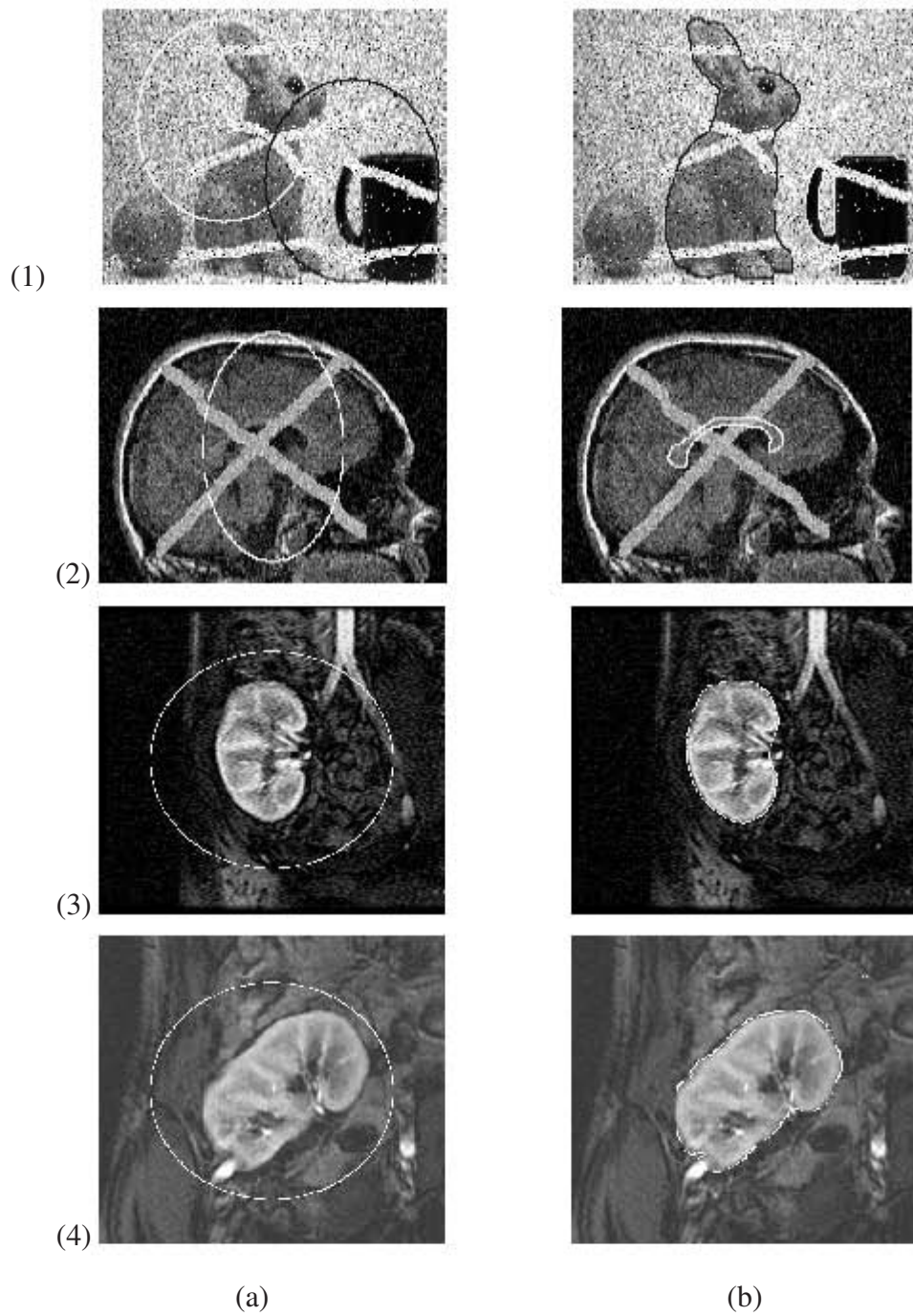
FIGURE 61 – Robustness to noise and partial occlusion. (a) Initial Level set(s). (b) Segmentation results using the proposed algorithm with no labelling functions. (1-a): 2 shape priors are used, one for the Rabbit and one for the Mug; The algorithm converges in 3 sweeps. (2,3,4-a) one shape prior is used to recover the corpus callosum, and kidneys in one sweep, resp.
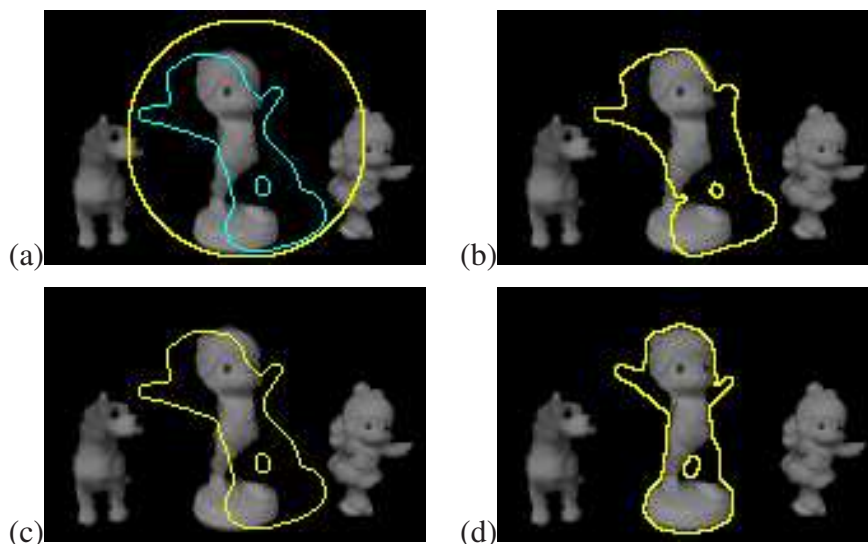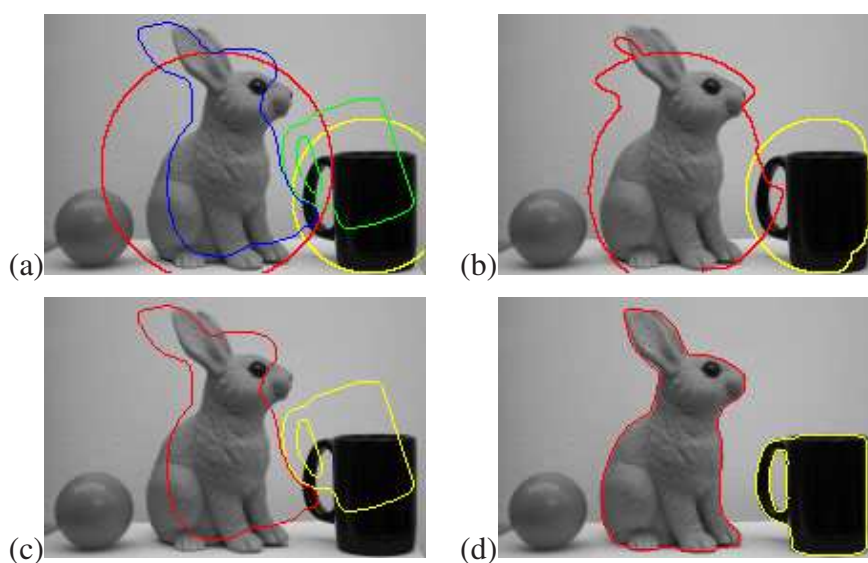
FIGURE 62 – Pose Invariance Formulation for the 2-phase (Top) and 4-phase (Bottom) cases. (a) Initial level set(s) (Top: yellow; Bottom: yellow & red) considering displaced shape priors (Top: light blue; Bottom: green & blue). (b) Intermediate step. (c) Result without simultaneous pose optimization; the familiar objects appear at the wrong location. (d) Result with simultaneous optimization of the pose parameters; the familiar objects and the priors correspond.

116

2-PHASE CASE:

Only one shape prior is used and one transformation matrix is to be recovered:

$$\bullet \frac{\partial \phi}{\partial t} = \delta(\phi)[\nu div \frac{\nabla \phi}{|\nabla \phi|} - (f - c_1)^2 + (f - c_2)^2 - 2\alpha(\|\mathcal{S}\|\phi(\mathbf{x}) - \widetilde{\phi}(\mathcal{A}\mathbf{x}))], \qquad (63)$$

4-PHASE CASE:

Two shape priors are used and two transformation matrices are to be recovered:

$$\bullet \frac{\partial \phi_1}{\partial t} = \delta(\phi_1)\{\nu div(\frac{\nabla \phi_1}{|\nabla \phi_1|}) - [((f - c_{11})^2 - (f - c_{01})^2)H(\phi_2) + ((f - c_{10})^2 - \qquad (64)$$
$$(f - c_{00})^2)H(-\phi_2)] - 2\alpha_1(\|\mathcal{S}_1\|\phi_1(\mathbf{x}) - \widetilde{\phi}_1(\mathcal{A}_1\mathbf{x}))\},$$

$$\bullet \frac{\partial \phi_2}{\partial t} = \delta(\phi_2)\{\nu div(\frac{\nabla \phi_2}{|\nabla \phi_2|}) - [((f - c_{11})^2 - (f - c_{10})^2)H(\phi_1) + ((f - c_{01})^2 - \qquad (65)$$
$$(f - c_{00})^2)H(-\phi_1)] - 2\alpha_2(\|\mathcal{S}_2\|\phi_2(\mathbf{x}) - \widetilde{\phi}_2(\mathcal{A}_2\mathbf{x}))\}.$$

The pose parameters as well as the scalars c_i ($i \in \{1, 2\}$), and c_{ij} ($i, j \in \{0, 1\}$) are simultaneously updated during the course of evolution of the level set functions ϕ_i's.

Figure 62 shows the resulting segmentation of familiar objects with and without the pose invariance formulation for the 2-phase and the 4-phase case. Figure 62(Top-d) corresponds to the recovery of a single familiar object by solving equation (63), while in Fig. 62(Bottom-d) two familiar objects are recovered using the multi-phase segmentation model with two shape priors and simultaneous pose estimations (see Eqs. (64) & 65). Without simultaneous pose parameters optimization, the familiar objects are forced to appear at wrong locations as shown on Fig. 62(c).

Finally, when the shape prior is statistically learned from a set of aligned training shapes using the *PCA* method (see section F of chapter III), then the shape prior, denoted above by $\widetilde{\phi}$ and now called active shape model (*ASM*) [39], could be implicitly expressed as

$$\Phi[\mathbf{w}] = \overline{\Phi} + \sum_{i=1}^{k} w_i \Phi_i, \qquad (66)$$

where, Φ_i, $i = 1, \cdots, k$, are the first k principal modes of variations or eignenshapes, and $\overline{\Phi}$ is the average of the aligned training shapes.

To address the pose variations in the context of shape-based segmentation, the *ASM* is

(1)

(2)

(a)   (b)   (c)
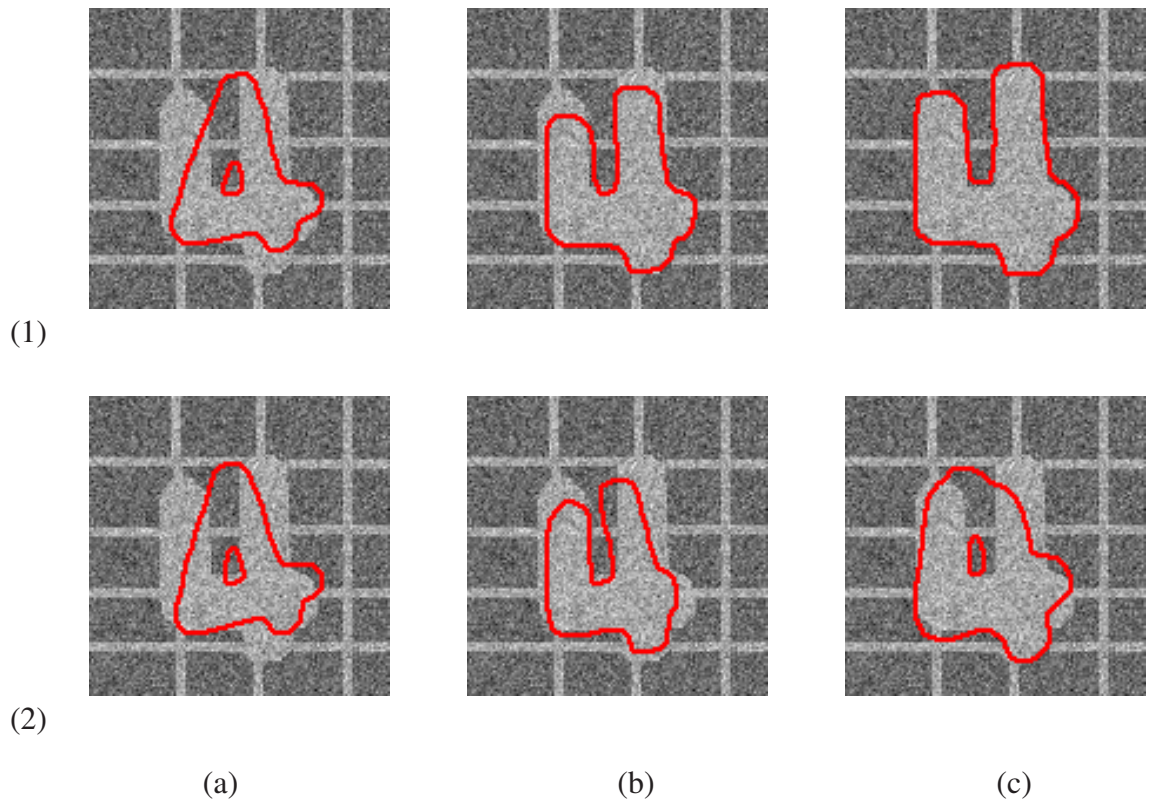
FIGURE 63 – Example of shape-based segmentation using a statistical shape model. Comparison between the proposed shape alignment model with the scale-based one [7] in the context of shape-based segmentation. model. (1) The results corresponding to the proposed alignment model. (2) The results when using the model in [7]. (a) Initial positions of the evolving contour. This corresponds to initializing the parameters $\mathbf{w}$ and $\mathbf{p}$ (see text). (b) An intermediate evolution step. (c) Final segmentation result.
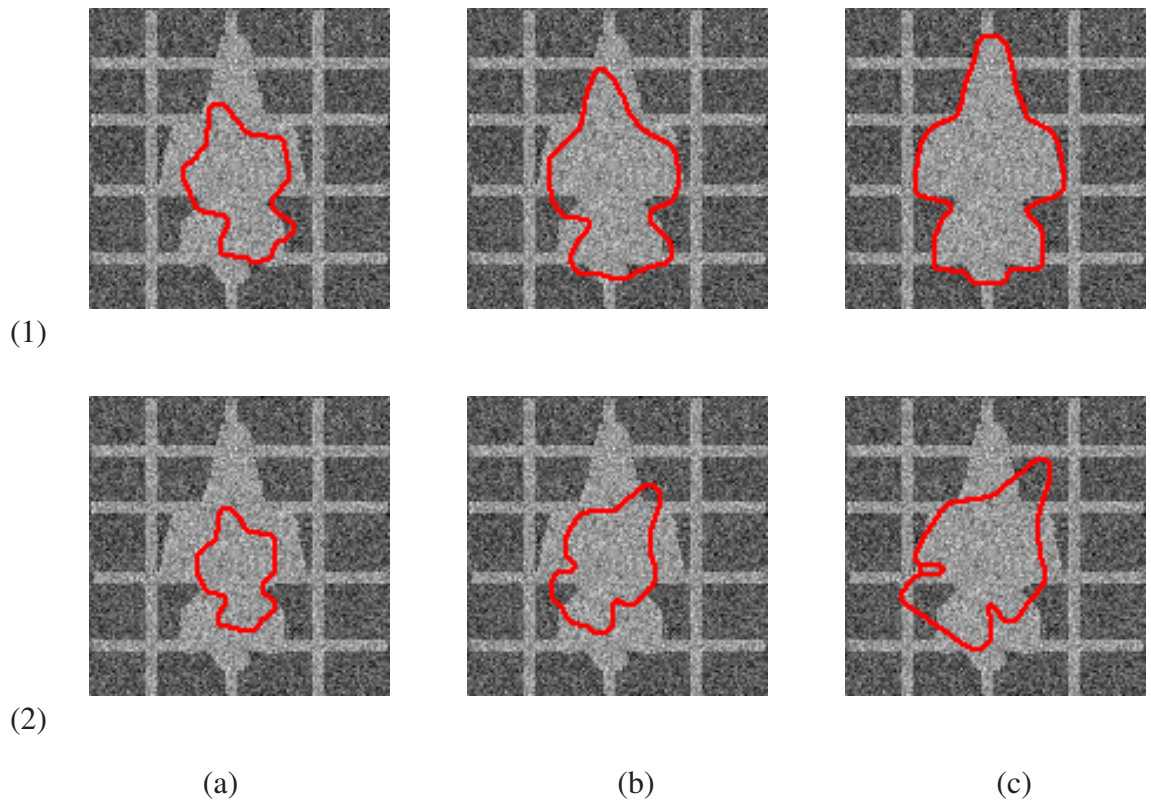
FIGURE 64 – Example of shape-based segmentation using a statistical shape model. Comparison between the proposed shape alignment model with the scale-based one [7] in the context of shape-based segmentation. model. (1) The results corresponding to the proposed alignment model. (2) The results when using the model in [7]. (a) Initial positions of the evolving contour. This corresponds to initializing the parameters $\mathbf{w}$ and $\mathbf{p}$ (see text). (b) An intermediate evolution step. (c) Final segmentation result.

changed to account for the pose parameters, $\mathbf{p}$,

$$\Phi[\mathbf{w}, \mathbf{p}](\mathbf{x}) = \overline{\Phi}(\overline{\mathbf{x}}) + \sum_{i=1}^{k} w_i \Phi_i(\overline{\mathbf{x}}), \tag{67}$$

with $\overline{\mathbf{x}} = \mathcal{A}[\mathbf{p}](\mathbf{x})$ and $\mathbf{p}$ refers to the transformation parameters $\mathcal{S}$, $\mathcal{R}$, $\mathcal{T}$.

The shape-based segmentation using the *ASM* given by Eq. (67) is performed by calculating the parameters $\mathbf{w}$ and $\mathbf{p}$ that optimize the segmentation energy functional. Several experiments were carried out to extract objects in noisy and cluttered images using the *ASM*. Few of the corresponding results are shown in Fig. 63 and Fig. 64. Also are shown in these figures the results obtained when the isotropic scale-based alignment model [7] is used to build the statistical shape model and to perform simultaneous segmentation and registration. It is clear from these figures that the proposed shape alignment model leads to more accurate results.

G.   Conclusion

This chapter addressed several aspects of the level set segmentation problem with shape priors, with a particular focus on the piece-wise constant Chan and Vese models. First a new and fast method to solve the 2-phase model with a selective shape prior was proposed. The key idea is inspired by the works presented in [6] [41]. The computational cost is decreased dramatically by directly computing the energy and checking how it changes when a pixel is moved from one phase to another instead of solving the corresponding Euler-Lagrange equations. The speed and robustness to noise of this algorithm was first shown on 2-phase images.

Secondly, these ideas were extended to the multi-phase model which allows the integration of multiple selective shape priors and can handle the segmentation into multiple regions. The power and effectiveness of the resulting paradigm are demonstrated on several synthetic and real images with/without noise and with/without partial occlusions. Note that in the multi-phase case, the results depend on an appropriate choice of the initial conditions.

Finally, a new pose invariance formulation was introduced. The transformation parameters that align the evolving level set function and the shape prior are dynamically

updated by minimizing a new dissimilarity measure expressed in the space of distance functions. Contrary to previous works, e.g., [37], the proposed pose invariance formulation allows the integration of multiple selective prior shapes using more than one level set function. Note that attempts were made to solve the pose invariance problem using the proposed fast algorithm, but the results were not very convincing. This problem will be solved in future works.

In this chapter, the labelling functions, which indicate where to enforce the shape priors, were specified beforehand. To overcome this limitation one can consider dynamic labelling functions as in [34, 37]. An extension to statistical shape priors is also conceivable.

CHAPTER VII

IMAGE REGISTRATION USING SCALE SPACE AND LEVEL SET THEORIES

A.   Introduction

Image registration is a major component in many medical image analysis applications. In particular, it is used in motion correction, spatial normalization of functional images, multi-modal fusion, etc. Image-guided neurosurgery is certainly one of the medical areas where deformable registration plays a vital role by offering the surgeon a better visualization. This helps, for instance, in removing a tumor without damaging the nearby healthy tissues. Many registration techniques have therefore been developed to tackle each one of these issues. These techniques can be categorized into two main families: feature-based and area-based techniques. The feature-based methods rely on extracting and matching salient anatomical structures from images (closed-boundary regions, edges, contours, line intersections, corners, etc.). The area-based methods, also known as correlation-like methods, are used directly to match image intensities without any attempt to detect distinctive objects. A major disadvantage of such methods is their sensitivity to intensity changes introduced by noise, illumination variations, etc. Another limitation of area-based methods is their inability to directly solve the problem of anatomical correspondences, as image similarity does not necessarily imply accurate registration of the underlying anatomy. This may be the case when registering brain images where large areas (e.g. gray matter) have practically uniform intensity which makes it hard to define correspondence and then results in false alignment. To cope with this issue, Shen and Davatzikos [96] proposed a new deformable registration for brain images, known as *"HAMMER"*. This method utilizes an attribute vector, which reflects the geometric characteristics of the underlying anatomical structures, as a signature for each point instead of using only the image intensity. Part of

each attribute vector is a number of geometric moment invariants (*GMI*s) calculated locally around each point. Considering all brain voxels for descriptor buildings using identical neighborhood size may fail in obtaining distinctive GMIs [96]. Another elastic registration technique, applicable to brain images, was introduced by Vemuri et al. [20]. This techniques is based on evolution of level sets moving along their respective normals to achieve image intensity morphing.

In the context of preoperative planning and enhanced visualization in support of image-guided neurosurgery, Warfield et al. [97] proposed an elastic registration technique based on an active surface model to match the segmented regions in both brain volumes. The corresponding surface displacements serve as boundary conditions for the 3D finite element (*FE*) model to estimate the volumetric deformation field. The obtained field is finally applied to preoperative data sets for intraoperative visualization. The accuracy of this technique relies strongly on the segmentation quality and on the bio-mechanical model adopted for the brain tissues.

In this chapter, a new approach for two and three dimensional image registration is presented. The global motion of the imaged object is modelled by an affine transformation, while equi-spaced closed surfaces (iso-surfaces) are evolved to handle the local deformations. These iso-surfaces are generated using fast marching level sets. Local invariant feature descriptors are used as a signature for each point. A novel approach for building robust and efficient 3D local invariant feature descriptors is used [98]. The obtained results are compared to those obtained using our own implementation of the B-spline based free deformation approach [8]. This shows the potential of the proposed method over the spline-based deformation technique. To validate the proposed approach, this study proposes to simulate a 2D kidney deformation case and three 3D physically plausible brain deformation cases using the *FE* method. The registration accuracy with respect to the *FE* simulations is assessed by co-registering the deformed images with the original ones and comparing the recovered displacement fields with the bio-mechanically simulated ones. The obtained results are very promising and show that the proposed method outperforms the spline-based deformation technique.

The following sections present a description of the main components of the proposed non-rigid registration technique.

B.   Local Invariant Features for Voxel-Based Similarity Measure

Building a good invariant feature descriptor starts from the selection of the points that are less affected by geometrical variations. Hence, distinct characteristics, which also should be invariant to different imaging changes, are carefully collected to build the feature descriptor. Finally, matching these feature descriptors is performed to find the correspondent pairs of control points. The following sections introduce a brief overview of the scale space theory and how it is used to build stable feature descriptors. The presentation is made in the general three dimensional case (one can see for example [98, 99] for more details).

1.   Interest Point Detection

Interest points are usually selected in highly informative locations such as edges, corners, or textured regions. In the context of feature invariance, interest points should be selected so that they achieve the maximum possible repeatability under different imaging conditions.

The most challenging point is the invariance w.r.t. scale changes. Scale-space theory offers the main tools for selecting the most robust feature locations, or the interest points, against scale variations.

Indeed, given a signal $f : \mathbb{R}^N \to \mathbb{R}$, $N = 3$ in the case of volumetric data, the scale-space representation $L : \mathbb{R}^N \times \mathbb{R}^+ \to \mathbb{R}$ is defined as the following convolution:

$$L(\vec{x}, t) = g(\vec{x}, t) * f(\vec{x}), \tag{68}$$

where $L(\vec{x}, 0) = f(\vec{x}) \; \forall \vec{x} \in \mathbb{R}^N$, and $g(\vec{x}, t)$ denotes the scale-space kernel which is proven to be Gaussian with $t = \sigma^2$ [100]. Note that as t increases, the scale-space representation $L(\vec{x}, t)$ of the signal tends to coarser scales [100].

The normalization of the Laplacian of Gaussian, $\nabla^2 g$, with factor $\sigma^2 = t$ is nec-

essary for true scale invariance, as proven by Lindeberg [100]. Later, Mikolajczyk and Schmid [99] proved experimentally that the extrema (maxima and minima) of $\sigma^2 \nabla^2 g$ produces the most stable image features. In other words, the locations of the extrema in the difference-of-Gaussian (DoG) hyper pyramid, i.e. scale-space levels, correspond to the most stable features with respect to scale changes.

In this work, the scale-space representation of an input 3D signal f is generated as follows. First, let's define

$$L_0 = g(\vec{x}, t_0) * f(\vec{x}), \text{ and } L_1 = g(\vec{x}, t_1) * f(\vec{x}), \ t_1 = C.t_0, \quad (69)$$

where $C > 1$ is a real number, and $g(\vec{x}, t) = \frac{1}{(2\pi t)^{\frac{3}{2}}} e^{\frac{-\vec{x}^T \vec{x}}{2t}}$. The first level of the DoG hyper pyramid is obtained by subtracting L_0 from L_1. Then, L_1 is sub-sampled to a smaller scale ($\frac{1}{2}$ of L_1 is used). The convolution and subtraction process is repeated for L_1 to generate the second level of the hyper pyramid. The whole procedure is repeated recursively to generated the consecutive levels.

The interest points are detected at the local extrema of the DoG hyper pyramid. This is performed by checking every voxel in the current level. If the checked voxel is a local extremum, then it is compared with its neighbors in the upper and the lower levels. The location of the voxel is selected as an interest point if it is also an extremum w.r.t. its local neighborhood in the upper and the lower levels of the DoG hyper pyramid.

2. Descriptor Building and Matching

According to [98], the feature descriptor in 3D space is built using gradient orientations histograms with 2D polar-coordinate bins for neighboring cells which consist of voxels in the current level-neighborhood of every interest point. This method was previously used in [98] for 2D medical applications and was proven to be efficient with respect to rotation and affine transformations in other applications [101, 102]. The gradient magnitude of each voxel in the neighborhood of an interest point is calculated as

$$r = \sqrt{G_x^2 + G_y^2 + G_z^2}, \quad (70)$$

where G_x, G_y and G_z are the gradient components in x, y and z directions, respectively. The gradient orientations in the polar coordinate system are given by

$$\theta = \tan^{-1}\frac{G_y}{G_x}, \text{ and } \phi = \sin^{-1}\frac{\sqrt{G_x^2 + G_y^2}}{r} = \cos^{-1}\frac{G_z}{r}. \tag{71}$$

To successfully describe the neighborhood of an interest point, the closer voxel should have a larger influence on the descriptor's entries. Therefore, Gaussian weights are assigned to every voxel in the neighborhood of the interest point, and are used with mean at the interest point itself to guarantee a distance-weighted contribution to the gradient orientation histogram. Moreover, this gives the built descriptor a robustness with respect to skew distortions [100].

According to [100, 101], one way to achieve rotation invariance is to describe all the descriptor entries relative to a canonical orientation. This orientation can be set to the dominant gradient orientation in the interest point neighborhood, which corresponds to the histogram bin with the maximum value. Therefore, the 2D histogram bin (ϕ_i, θ_i) for the ith feature is updated by adding the term $r(\mathbf{x}_i) \cdot g(\mathbf{x}_i, \sigma^2)$. The considered bin for update is calculated as $\theta_r = \theta - \theta_c$, and $\phi_r = \phi - \phi_c$, where θ_c, ϕ_c are the components of the canonical orientation of the interest point, and θ, ϕ are the components of the gradient orientation referred to the zero-axes of the coordinate system, as calculated above. The final descriptor is built as shown in Fig. 65. This vector is normalized to reduce the effect of linear intensity changes [101]. In this work, neighborhoods of $8 \times 8 \times 8$ for both canonical gradient orientation and descriptor's entries and cells of $4 \times 4 \times 4$ are used which means that eight cells are used for building the entries of the descriptor. For each cell, eight and four histogram bins for ϕ and θ, respectively are used. Hence, the descriptor is of size $8 \times 8 \times 4 = 256$ and after adding the overhead of the original location, pyramid level, and the canonical orientation, the total descriptor size becomes $256 + 6 = 262$.

Finally, given a descriptor feature F_1 in the first image, its match, F_2, in the second image is found when the following condition is satisfied:

$$\frac{D(F_1, F_2)}{\min(D(F_1, F_2'))} < Threshold < 1, \ \forall F_2' \neq F_1, \text{and } F_2' \neq F_2, \tag{72}$$

where, $D(\cdot, \cdot)$ is the Euclidean distance. Other distances may be used as well.
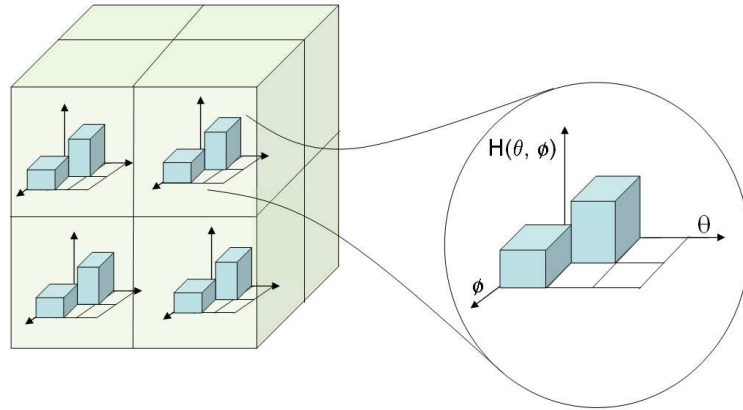
FIGURE 65 – The structure of the 3D feature descriptor. Only eight samples of neighboring cells and six histogram bins are shown in the figure for illustration purposes. Image is courtesy of Dr. Alaa E. Abdel-Hakim

3. Global Registration

To model the global motion between the two images $I_t(\cdot)$ and $I_s(\cdot)$, the feature descriptors are built as described in Section VII.B, and then the features of the reference image are matched with those of the target image. The matched pairs are used to estimate a global transformation through the gradient descent minimization of the mean squared positional error between the corresponding points. In this dissertation, a 5-parameter transformation in 2D cases and a 9-parameter transformation matrix in 3D cases are adopted. That is, the estimated transformation parameters include scales in each direction, rotations, and translations.

4. Local Registration

To handle local deformations undergone by the imaged organ, a new approach is proposed. This approach is based on deforming the organ over evolving closed and equi-spaced surfaces (iso-surfaces) to closely match the prototype. The evolution of the iso-surfaces is guided by an exponential speed function in the directions minimizing distances between corresponding voxel pairs on the iso-surfaces on both images.

The first step of the introduced approach is to generate the distance map inside the

$$\phi_{m_{iso}}^{I_s}(X_c)$$

$$\phi_{n_{iso}}^{I_t}(X,\upsilon)$$

$$S(X,X_c)$$

$$V = e^{\beta.S} - 1$$
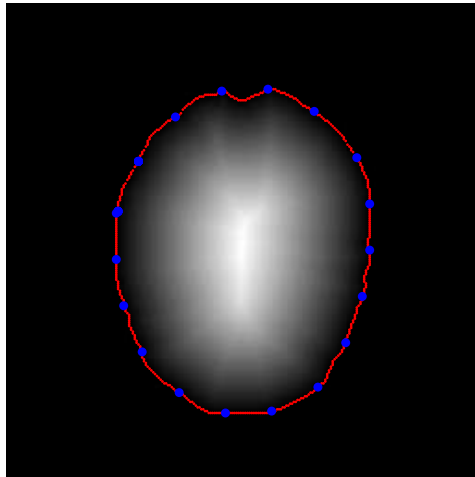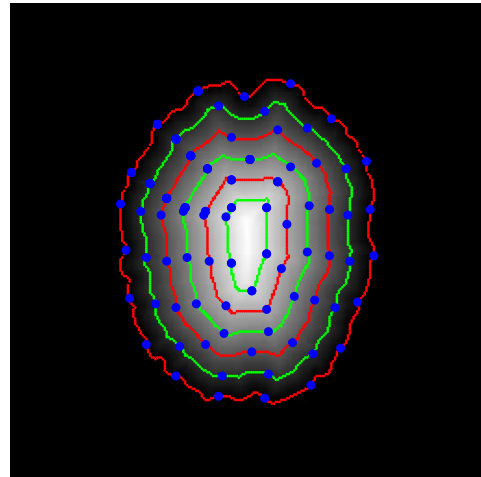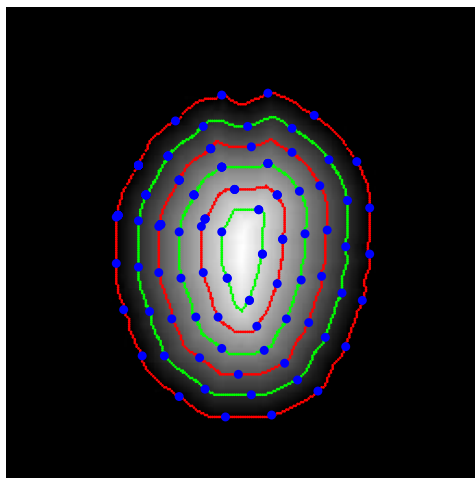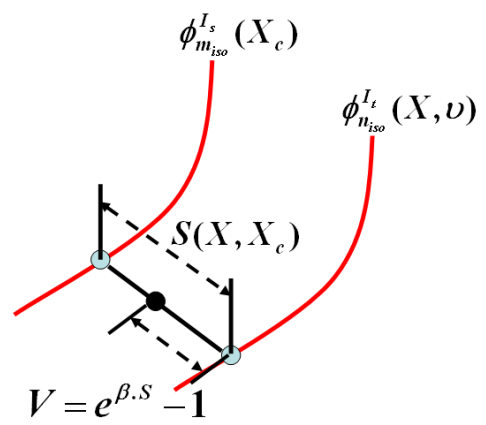
FIGURE 66 – Cross sectional views of generated distance map and iso-surfaces before (a) and after (b,c) deformation. (d) The evolution scenario.

imaged object as shown in Fig. 66(a). The second step is to use this distance map to generate and sample iso-contours/surfaces as shown in Fig. 66(b-c). Note that the number of iso-surfaces, which is not necessarily the same for both input images, depends on the accuracy and the speed required by the user. The third step consists in finding the correspondences between the iso-surfaces. The final step is the evolution of the iso-surfaces. Here, the goal is to deform the iso-surfaces in the first data set (target image $I_t(\cdot)$) to match the iso-surfaces in the second data set (source image $I_s(\cdot)$). Before stating the evolution equation, let us define the following:

1. $\phi_{n_{iso}}^{I_t}(\cdot, \nu)$ are the iso-surfaces on the target image $I_t(\cdot)$, with $n_{iso} = 1, \ldots, N_{iso}$ the index of the iso-surfaces, and ν the iteration step.

2. $\phi_{m_{iso}}^{I_s}(\cdot)$ are the iso-surfaces on the source image $I_s(\cdot)$, where $m_{iso} = 1, \ldots, M_{iso}$ is the index of the iso-surfaces.

3. $S(\mathbf{x}, \mathbf{x}_c)$ denotes the Euclidean distance between a iso-surface voxel $\mathbf{x}$ on $I_t(\cdot)$ and its corresponding iso-surface voxel $\mathbf{x}_c$ on $I_s(\cdot)$. The point $\mathbf{x}_c$ is searched for within a local window, $\mathcal{W}$, centered at $\mathbf{x}$'s position in $I_s(\cdot)$ by minimizing the normalized cross correlation between the center of $\mathcal{W}$ and all the iso-surface points that lie within $\mathcal{W}$. Note that $\mathbf{x}_c$ may be the same for different $\mathbf{x}$'s.

4. $S_{n_{iso},n_{iso}-1}^{I_t}(\mathbf{x})$ is the Euclidian distance between $\phi_{n_{iso}}^{I_t}(\mathbf{x}, \nu)$ and $\phi_{n_{iso}-1}^{I_t}(\mathbf{x}, \nu)$ at each iteration ν.

5. $V(\cdot)$ is the propagation speed function.

One major step in the propagation model is the selection of the propagation speed function V. This selection must satisfy the following conditions:

$$V(\mathbf{x}) = 0, \text{ if } S(\mathbf{x}, \mathbf{x}_c) = 0, \tag{73}$$

$$V(\mathbf{x}) \leq \min(S(\mathbf{x}, \mathbf{x}_c), S_{n_{iso},n_{iso}-1}^{I_t}(\mathbf{x}), S_{n_{iso},n_{iso}+1}^{I_t}(\mathbf{x})), \text{ if } S(\mathbf{x}, \mathbf{x}_c) \neq 0. \tag{74}$$

The latter condition, known as the smoothness constraint, prevents the current point from

cross-passing the closest neighbor surfaces as shown in Fig. 66(d). Note that the function

$$V(\mathbf{x}) = \exp(\beta(\mathbf{x}) \cdot S(\mathbf{x}, \mathbf{x}_c)) - 1, \tag{75}$$

satisfies the above conditions, where $\beta(\mathbf{x})$ is the propagation term such that, at each iso-surface point $\mathbf{x} \in I_t$,

$$\beta(\mathbf{x}) \preceq \frac{\ln[\min(S(\mathbf{x}, \mathbf{x}_c), S_{n_{iso},n_{iso}-1}^{I_t}(\mathbf{x}), S_{n_{iso},n_{iso}+1}^{I_t}(\mathbf{x})) + 1]}{S(\mathbf{x}, \mathbf{x}_c)}. \tag{76}$$

Finally, when the corresponding point, $\mathbf{x}_c$, of the current voxel $\mathbf{x}$ is determined as explained in the step#3 above, and based on the speed function given by Eq. 75, the current point is moved along the ray that connects it with its corresponding point. This evolution process is governed by following equation:

$$\phi_{n_{iso}}^{I_t}(\mathbf{x}, \nu + 1) = \frac{V(\mathbf{x})}{S(\mathbf{x}, \mathbf{x}_c)} \phi_{m_{iso}}^{I_s}(\mathbf{x}_c) + \frac{S(\mathbf{x}, \mathbf{x}_c) - V(h)}{S(\mathbf{x}, \mathbf{x}_c)} \phi_{n_{iso}}^{I_t}(\mathbf{x}, \nu), \tag{77}$$

where $\mathbf{x}$ denotes a sample iso-surface point on image $I_t(\cdot)$, and $\mathbf{x}_c$ its corresponding iso-surface point on $I_s(\cdot)$.

C.   Experimental Results

The proposed deformable registration technique is tested on various 2D and 3D medical images (e.g., kidney, lung, brain, etc). In this section, some results corresponding to the application of the proposed registration technique on two T1-weighted brain *MRI*s of the same patient acquired at different times ($\approx$ one year apart) are presented. Each of the two data sets is of size $256 \times 256 \times 200$ with a voxel size of $1 \times 1 \times 1 \ mm^3$.

The performance of the proposed approach was assessed qualitatively and compared to our own implementation of the free form deformation technique [8]. To visually assess the quality of the introduced approach, the two registered volumes are fused in a checkerboard visualization as shown in Fig. 67. One can clearly see that when applying the proposed registration approach, the connectivity between the two volumes is smoother both at the edges as well as inside the brain region.

For a quantitative assessment of accuracy of the introduced image registration method, a
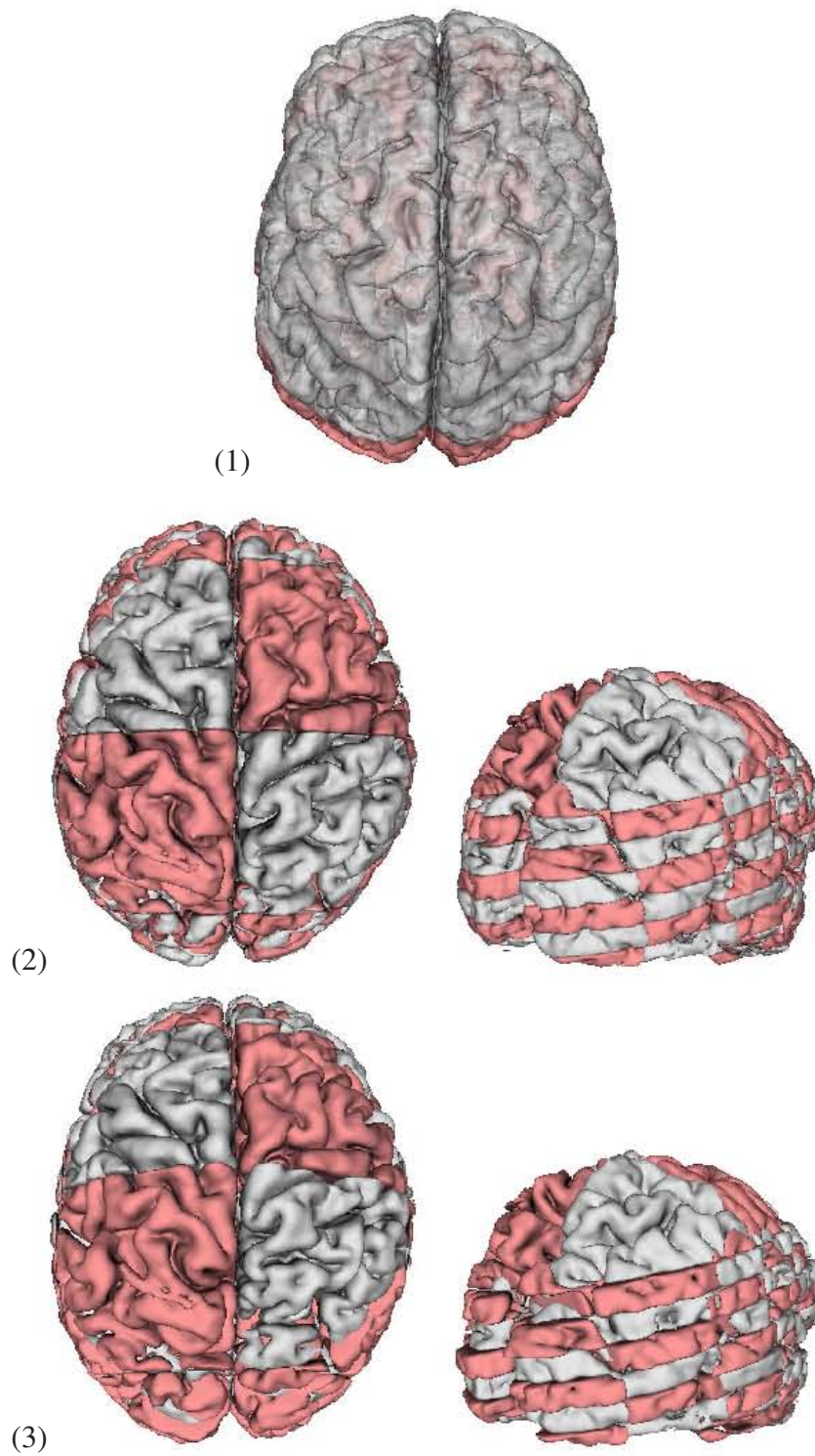
FIGURE 67 – Rigid and non-rigid registration results. (1) Proposed rigid alignment. (2) Proposed non-rigid registration. (3) Non-rigid registration using the free form technique [8].

novel framework using the finite element methods [72] is proposed as will be shown in the next section.

D.   Validation Using the Finite Element Method

In this section, a novel method using the *FEM* is proposed to validate the proposed non-rigid registration approach . Both 2D and 3D validation results are presented on medical data.

1.   2D Case: Kidney Images

Given a 2D image of the kidney, a deformation is simulated using a biomechanical model of the kidney tissue. The pair of images (deformed and non deformed ones) is used to test the proposed elastic registration method. The Abaqus/CAE (Ver. 6.5) [7] environment was used to generate a cubic spline fit to the points representing the outer contour of the kidney object and then a 2D *FE* model was built from it. Fig. 68(a) and (b) show the 2D mesh before and after deformation, and the overlay of these two meshes, respectively. For the sake of generating a deformed shape only, the kidney tissue is assumed to be isotropic and homogeneous elastic material with a Young Modulus $E = 2500Pa$ and a Poisson Ratio $\nu = 0.4$. Note that this model does not reflect the results of any rheological experiments conducted on the kidney tissue. A uniformly distributed pressure $P = 100N$ was applied normal to the boundary of the kidney. The points on this boundary are allowed to move freely in the x and y directions, but are constrained to rotate around the z direction. The mesh consists of 1253 3-node linear plane stress angular elements. The average displacement of the induced deformation is $4.75mm$, the minimum is $1.19mm$, and the maximum is $6.9mm$. The accuracy of the registration method is assessed by registering the simulated deformed image to the original one and comparing the recovered point displacements with the bio-mechanically simulated ones. The average registration error is about $1.54mm$, with a maximum of $2.7458mm$, a minimum of $0.0221mm$, and a standard deviation of 0.5517.

_____

[7] www.abaqus.com
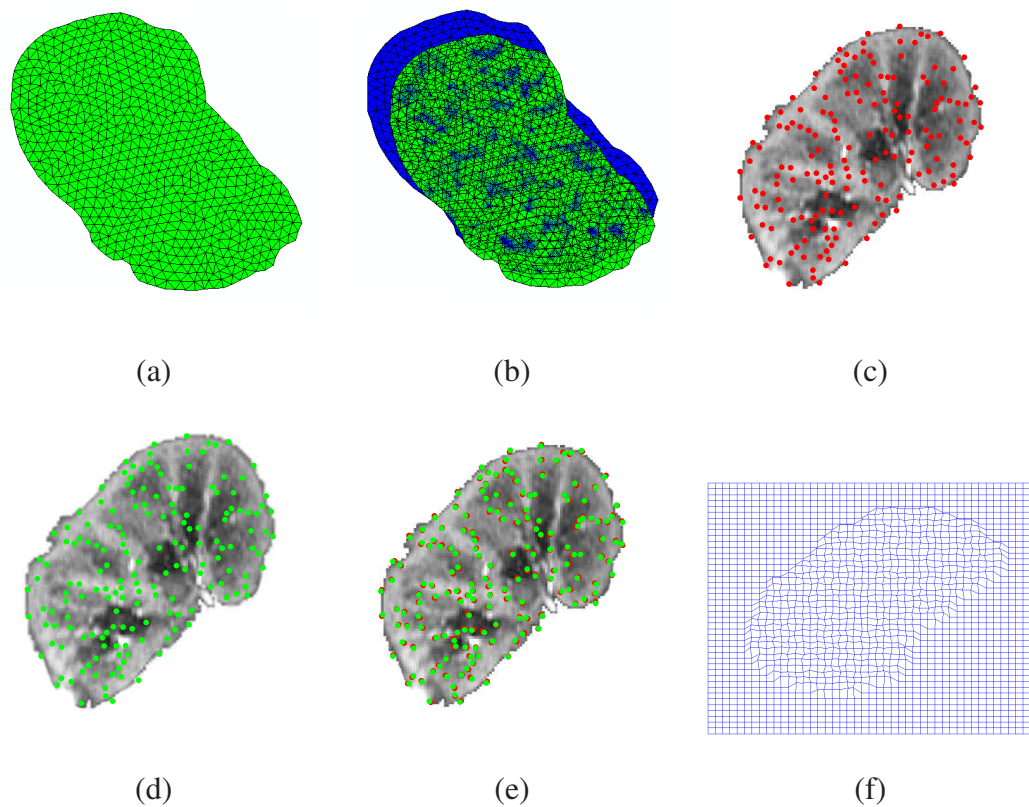
FIGURE 68 – Validation of the proposed non-rigid registration technique in 2D case. (a) Mesh before deformation. (b) Overlay of deformed and non-deformed (green) meshes. (c) New locations of some mesh nodes as simulated by the *FEM* software and (d) their locations after applying the proposed registration approach and (e) their Overlay. (f) Deformation field showing the smoothness of the results.

To illustrate these results, Fig. 68 shows a set of ground truth locations (Abaqus simulated)(c), the corresponding recovered ones using the proposed technique (d), and their overlay (e). The corresponding displacement field (see Fig. 68(f) shows the smoothness of the registration results. This proves the accuracy of the proposed non-rigid registration technique in 2D cases.

2. 3D Case: Validation on Brain *MRI*s

In this section, the performance of the proposed non-rigid registration approach on real 3D brain *MR* data using the *FEM*. Two deformation types, characteristics for real patient-specific acquisitions, are simulated: gravity-induced deformation and ventricles contraction. For the first type of deformations, two biomechanical models for the brain

tissues are used separately: the linear elastic model (*case 1*) and the hyperelastic model (*case 2*). The latter model is also chosen for the ventricle contraction case (*case 3*). The choice to simulate these deformation types is motivated by the findings in the literature. Indeed, it has been reported in various studies (e.g., [103]) that the gravity-induced deformation is one of the primary sources of intraoperative movements. In addition, the change of volume of the lateral ventricles was pointed out as a consequence of tumor mass-effect simulations [104]. These deformations compromise the registration between the pre- and intraoperative position of important brain structures. Taking into consideration such deformations results in more accurate alignment between pre- and intraoperative images.

Model Construction: For the construction of the *FE* models for the three cases, the same T1-weighted MRIs of a normal brain of size $256 \times 256 \times 198$ and a voxel size of $1 \times 1 \times 1mm^3$ is used as input data. Firstly, the brain volume is skull-stripped (i.e., non brain tissue removed) and segmented into white matter (WM), gray matter (GM), and CSF ventricles using the FSL package[8]. Secondly, the segmented images are input into the TetSplit [105] program to generate 3D tetrahedral meshes. The quality of the output meshes conforms to the quality measure used by the *FE* commercial package Abaqus. The built meshes consist of $102,301$ linear tetrahedra (Fig. 69(a, b)) each of which is labelled corresponding to the underlying tissue type. Then, material properties for different tissue types were carefully chosen from the literature. Several rheological experiments have been performed on the brain tissue (e.g., see [106–108]). In the simulations that use the hyperelastic model (cases 2 and 3), the isotropic and homogeneous hyperelastic model proposed by Miller and Chinzei [106] is adopted. This models neglects viscous effects. Such a material model can be described in terms of a strain energy potential W defined as a function of the strain at each point. Several forms of the energy W are available in Abaqus, among which the Ogden model was chosen (see [109]):

$$W = \frac{2\mu_1}{\alpha^2}(\overline{\lambda}_1^\alpha + \overline{\lambda}_2^\alpha + \overline{\lambda}_3^\alpha - 3) + \frac{1}{D_1}(\frac{J}{J^t} - 1)^2 \qquad (78)$$

---

[8]Free package at http://www.fmrib.ox.ac.uk/fsl/
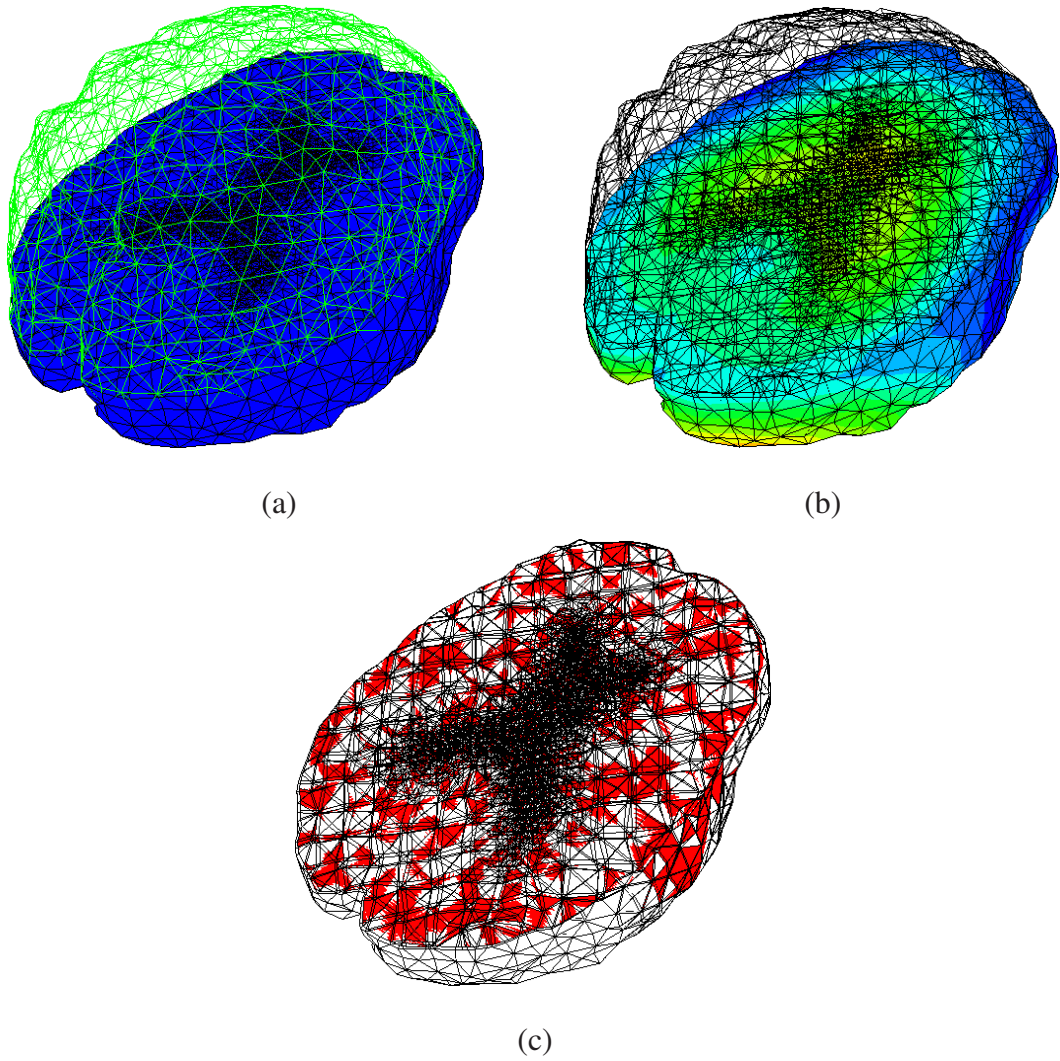
FIGURE 69 – (a) 3D finite element mesh. (b) Deformed mesh. (c) Z-plane cut of overlayed meshes before (red) and after (white) deformation.

TABLE 5
MATERIAL PARAMETERS FOR OGDEN AND FOAM MODELS. VALUES TAKEN
FROM [3]

	α	$\mu_1(Pa)$	$D_1(Pa)$
Brain	-4.7	842	7.2×10^{-5}
Ventricles	2.5	150	0.0

where, $\overline{\lambda}_i = J^{-\frac{1}{3}} \cdot \lambda_i$, with λ_i, $i = 1, 2, 3$ are the principal stretches and J is the total defor-mation ratio; μ_1 and D_1 are temperature-dependent material parameters, and $J^t = (1 + \epsilon^t)$ denotes the thermal volume ratio with ϵ^t being the linear thermal expansion strain. For the linear elastic model (case 2), the Young modulus and Poisson ratio were set to $E = 1200Pa$ and $\nu = 0.45$ [110] for the white matter and the gray matter [111]. A density $\rho = 1000.0\frac{kg}{m^3}$ was set for the entire brain in the two gravity-induced deformation cases (cases 1 & 2) [110].

As boundary conditions and according to Miga [107] and Warfield et al. [97], the points of the brain where the falx meets the skull are fixed and the falx is considered to have the same material parameters as those assigned to the brain. The remaining points on the brain outer surface were allowed to slide freely in the direction tangent to the brain surface only. According to [112], these types of boundary conditions produce more realistic deforma-tions. Finally, to anticipate the contact between the ventricle walls during the simulations, the ventricles are modelled with hyperfoam material [109]. Such a material differs, in part, from hyperelastic materials in that it is highly compressible. The following values were chosen from the literature [106]: $\mu_1 = 842Pa$, $D_1 = 7.2 \times 10^{-5}Pa$, $\alpha = -4.7$ for the Ogden model, and $\mu_1 = 150Pa$, $D_1 = 0.0Pa$, $\alpha = 2.5$ for the hyperfoam model. These pa-rameters are summarized in Tab. 5. An example of simulated deformation (case 2) is shown in Fig. 69(c) as a z-plane cut of the overlapped meshes before and after deformation.

Generation of Gray-Scale Deformed Images: To be used in the registration process, the original images are deformed using the dense displacement field obtained from each

simulation. Within the *FE* framework, the displacement $\vec{u}$ of any voxel $\vec{x}$ lying within an element el in the model, is defined as a weighted interpolation of the node displacements

$$u(x) = \sum_{j=1}^{4} h_j^{el}(x) u_j^{el},$$ (79)

where $h_j^{el}(.)$, $j = 1, \cdots, 4$, are the element shape functions [113]. Using this interpolator to generate deformed images overcomes the problem of residual errors at the *FE* node locations that may appear when using, for example, B-spline based interpolation [114]. The simulated deformed images are used as the target images for the registration process, while the original images are the source.

Validation Results: For each one of the simulated deformation cases, both the proposed registration method and our independent implementation of the registration method proposed in [8] have been tested. The accuracy of the proposed technique has been quantitatively assessed at the finite element node positions by comparing the recovered voxel displacements with the simulated ones. Table 6 summarizes the error statistics for the three cases using the two registration techniques. One can see that the proposed algorithm outperforms the other one in all of the three cases, with an average accuracy almost five times higher. Moreover, the proposed approach converges faster than the other method for all considered cases with an average speed 3 to 4 times higher. Both algorithms were implemented using Matlab, and were run on the same PIII-PC. To highlight this difference, Fig. 70 shows a typical comparison between a set of 100 randomly selected finite element nodes positions (case 3) and their corresponding recovered positions using both the proposed method and the one presented in [8].

E.   Conclusion

This chapter introduced a novel registration approach for 2D and 3D images. The proposed approach uses fast marching level sets method to generate and sample iso-surfaces. These iso-surfaces are evolved to handle the local deformations. A new approach was introduced to build 3D local invariant feature descriptors using scale-space theory. These
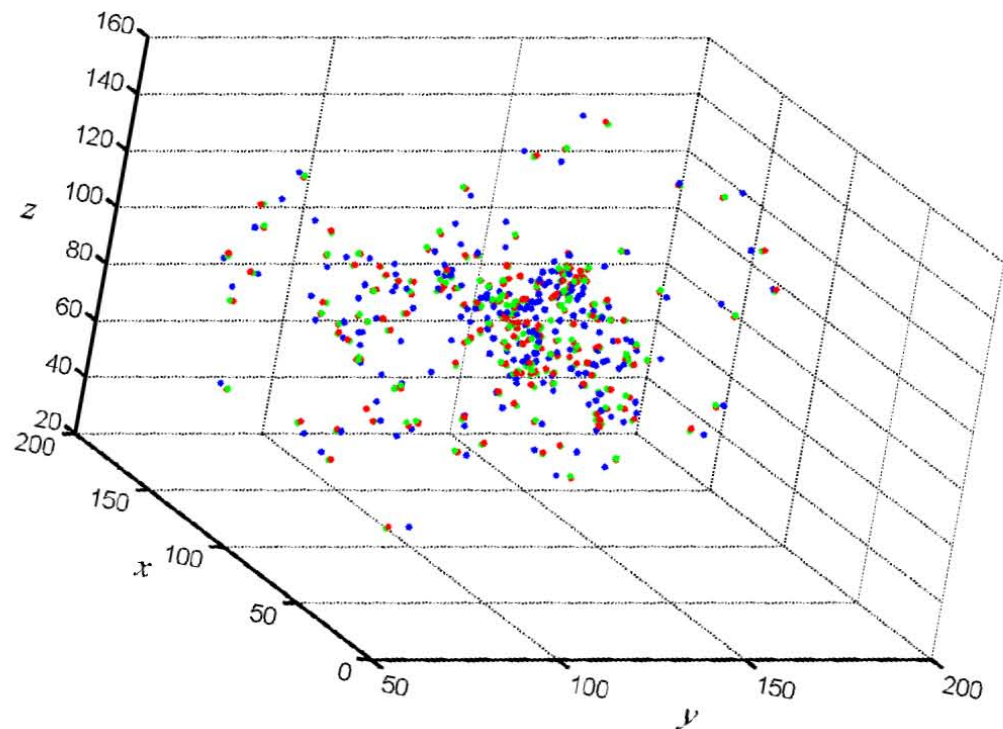
FIGURE 70 – Comparison between 100 randomly selected finite element node positions corresponding to deformation case#3. (Red) Ground truth (Abaqus simulated positions). (Green) Corresponding positions using the proposed method and (Blue) the ones obtained with our own implementation of the *FFD* [8]. Note the closeness of the results obtained using the proposed method to the ground truth.

TABLE 6
QUANTITATIVE ASSESSMENT OF THE REGISTRATION ACCURACY.
COMPARISON WITH OUR OWN IMPLEMENTATION OF THE FREE-FORM
DEFORMATION (OWN_FFD) METHOD. DISPLACEMENTS CORRESPOND TO
THE SIMULATED ONES. ALL UNITS ARE IN (**MM**).

		Case 1	Case 2	Case 3
Max. Displacement		9.88	4.76	1.68
Mean Displacement $\pm$ std. dev.		6.08 ± 1.06	2.25 ± 0.68	0.55 ± 0.38
Max Error	Ours	2.08	2.36	0.63
	Own_FFD	9.18	7.46	4.03
Mean Error $\pm$ std. dev.	Ours	1.20 ± 1.58	1.32 ± 0.38	0.36 ± 0.31
	Own_FFD	5.15 ± 1.50	4.20 ± 1.26	2.29 ± 0.67

descriptors are used in the estimation of the global transformation parameters. The use of these descriptors provides a robust matching under different geometrical and intensity variations, which enhances the registration accuracy. The evaluation results show the high accuracy of the proposed approach over free form deformation approaches. The performance of the proposed non-rigid registration method was validated using a novel *FE*-based approach. Both 2D and 3D deformation cases were simulated for quantitative assessment of the registration accuracy. In all of these cases, the proposed method was faster and more accurate than our independent implementation of the *FFD* method.

CHAPTER VIII

SUMMARY

This dissertation introduced several contributions on shape and image registrations. A novel global-to-local shape registration framework in implicit space was presented. The potential of applying this framework to address the challenging problem of three dimensional face recognition in the presence of facial expressions is demonstrated on real data base of 3D face scans. The dissertation also presented a new image/volume registration technique which was validated using a novel finite element-based method.

A. Conclusions and Future directions

In this work, a new variational framework for dense global-to-local registration of shapes was presented. Implicit shape representation through signed distance function was considered to represent the input shapes. A new *SSD* criterion, measuring the disparity between the representations of the two input shapes, was proposed to globally align the input shapes. This criterion supports both rigid and affine transformations. Various experiments were presented to show the effectiveness of this new measure. Comparisons with the isotropic scale-based *SSD* criterion and with the *VDF*-based criterion showed the outperformance of the proposed dissimilarity measure.

The local deformation field is explicitly established between the two globally aligned shapes by minimizing a new energy functional that incrementally and simultaneously updates the displacement field while keeping the corresponding distance map representation of the globally warped source shape as close to a signed distance function as possible. Various experiments were presented to show the potential of the proposed framework, and comparisons with the latest published results were presented. The potential of the proposed surface registration to tackle the problem of 3D face recognition problem in presence of fa-

cial expressions was demonstrated. Facial expressions are among the most critical factors limiting face recognition performance, and this point was best addressed in this work with 3D models. It was shown how the proposed registration model reduces the local shape distortions induced by facial expressions. The amount of deformation undergone by a probe face when registered to the gallery faces was estimated in order to recognize the probe. The results are very encouraging.

Tracking facial expressions is another interesting area of research that may greatly benefit from the proposed surface registration framework. Starting from a dynamic sequence of range scan faces, the basic idea of tracking is to register a generic face mesh model with the sequence frames in an ordered fashion. This will generate dense intraframe correspondences between points that register with the same vertex on the common mesh model. This would then help tracking and identifying the locations of important face landmarks, such as mouth corners and cheeks, when an expression is performed.

Another possible direction of the proposed shape registration framework is its extension to image/volume registration. One way of achieving this goal is by looking at the possibility of using contrast invariant features (e.g., the *MI*) in the intensity space and combine it with the matching of shapes to achieve multi-modal image registration.

The use of the Gaussian curvature-based regularization model proposed in [15] is being investigated. This regularization model is proven not to penalize affine-linear displacements, which may allow, if used, to do away with the global as a pre-alignment step for non-rigid registrations.

As an application of the proposed global shape registration approach, the problem of level set-based segmentation with shape priors was addressed. The shape prior is either represented by a fixed template or learned from a set of training samples, and it is associated with a set of pose parameters allowing for anisotropic scaling, rotation, and translation. When a fixed template is used to represent the shape prior, a fast implementation of the Chan-Vese level set based segmentation with shape priors is designed and implemented. Both the two phase and the multi-phase cases were considered. Currently, the generalization of this fast implementation to the case of statistical shape priors (learned by *PCA*) is

being investigated. In addition, the labelling functions were specified beforehand. This may be overcome by considering dynamic labelling functions as in [37].

This dissertation has also contributed to the problem of image/volume registration. The proposed approach uses fast marching level sets method to generate iso-surfaces. These iso-surfaces are evolved to handle the local deformations. A new approach was introduced to build 3D local invariant feature descriptors using scale-space theory. These descriptors are used in the estimation of the global transformation parameters. A novel finite element (*FE*)-based technique was proposed to validate the introduced non-registration method. Given an image, a *FE* deformation is simulated for the imaged organ and used the generated deformed image as the target image. The simulated displacement field is used as ground truth. The accuracy of the proposed non-rigid registration method is assessed by registering the simulated deformed image with the original one, and comparing the recovered displacement field with the bio-mechanically simulated one.

A possible extension of the proposed image registration approach is to build descriptors for each sample point on the iso-contours, using scale space theory, and use them to deform iso-contours on one image to match those on the other image.

REFERENCES

[1] Luminita A. Vese and Tony F. Chan. A multiphase level set framework for image segmentation using the mumford and shah model. *Int. J. of Computer Vision*, 50(3):271–293, 2002.

[2] M. B. Stegmann and D. D. Gomez. *A Brief Introduction to Statistical Shape Analysis*. Informatics and Mathematical Modelling, Technical University of Denmark, DTU, March 2002.

[3] M. K. Chung, K. M. Dalton, and R. J. Davidson. Encoding neuroanatomical information using weighted spherical harmonic representation. In *IEEE Statistical Signal Processing (SSP) Workshop*, 2007.

[4] M. K. Chung, K. M. Dalton, L. L. Shen, A. C. Evans, and R. J. Davidson. Weighted fourier series representation and its application to quantifying the amount of gray matter. *Special Issue of IEEE Transactions on Medical Imaging, on Computational Neuroanatomy*, 26, 2007.

[5] Xiaolei Huang, Nikos Paragios, and Dimitris N. Metaxas. Shape registration in implicit spaces using information theory and free form deformations. *IEEE Transactions on Pattern Analysis and Machine Intelligence*, 28(8):1303–1318, 2006.

[6] B. Song and T. Chan. Fast algorithm for level set based optimization. In *UCLA CAM Report, 02(68)*, 2002.

[7] Nikos Paragios, Mikael Rousson, and Visvanathan Ramesh. Non-rigid registration using distance functions. *Comput. Vis. Image Underst.*, 89(2-3):142–165, 2003.

[8] Daniel Rueckert, LI Sonoda, C Hayes, DLG Hill, M Leach, and DJ Hawkes. Non-rigid registration using free-form deformations: Application to breast MR images. *IEEE Transactions on Medical Imaging*, 18(8):712–721, 1999.

[9] James A. Sethian. *Level Set Methods and Fast Marching Methods: Evolving Interfaces in Computational Geometry, Fluid Mechanics, Computer Vision, and Materials Science*. Cambridge University Press, 2nd Edition., New York, 1999.

[10] Paul A. Viola. Alignment by maximization of mutual information. Technical Report AITR-1548, 1995.

[11] Paul Viola, William, and M. Wells III. Alignement by maximization of mutual information. *The International Journal of Computer Vision*, 24(2):137–154, 1997.

[12] A. Roche, G. Malandain, X. Pennec, and N. Ayache. The correlation ratio as new similarity metric for multimodal image registration. In *Proc. of International Conference on Medical Image Computing and Computer-Assisted Intervention (MICCAI'98)*, October 1998, 1998.

[13] A.N. Tikhonov and V.Y. Arsenin. Solutions of ill-posed problems. *Winston and Sons*, 1977.

[14] Yali Amit. A nonlinear variational problem for image matching. *SIAM Journal on Scientific Computing*, 15(1):207–224, 1994.

[15] Stephen Henn and Kristian Witsch. Image registration based on multiscale energy information. *Society for Industrial and Applied Mathematics, SIAM*, 4(2):584–609, 2005.

[16] G. Hermosillo Valadez. *Variational Methods for Multimodal Image Matching*. PhD thesis, Ph.D., Thesis at Université de Nice - Sophia Antipolis, 2002.

[17] Christophe Chefd'Hotel, Gerardo Hermosillo, and Olivier Faugeras. A variational approach to multi-modal image matching. volume 00, pages 21–28, Los Alamitos, CA, USA, 2001. IEEE Computer Society.

[18] Philippe G. Ciarlet. Mathematical elasticity: Volume i: Three dimensional elasticity. *Elsevier, North Holland*, 1988.

[19] Marcelo Bertalmío, Guillermo Sapiro, and Gregory Randall. Morphing active contours. *IEEE Transactions on Pattern Analysis and Machine Intelligence*, 22(7):733–737, 2000.

[20] B. Vemuri, J. Ye, Y. Chen, and C. Leonard. Image registration via level-set motion: Applications to atlas-based segmentation. *Medical Image Analysis*, 7, 2003.

[21] Stanley Osher and James A. Sethian. Fronts propagating with curvature-dependent speed: Algorithms based on Hamilton-Jacobi formulations. *Journal of Computational Physics*, 79:12–49, 1988.

[22] Rachid Fahmi and Aly A. Farag. A global-to-local 2d shape registration in implicit spaces using level sets. In *Proc. IEEE International conference on Image Processing (ICIP'07)*, pages 237–240, San Antonio, TX, USA, September 16-19, 2007.

[23] Byung-Woo Hong, Emmanuel Prados, Stefano Soatto, and Luminita Vese. Shape representation based on integral kernels: Application to image matching and segmentation. In *CVPR '06: Proceedings of the 2006 IEEE Computer Society Conference on Computer Vision and Pattern Recognition*, pages 833–840, Washington, DC, USA, 2006. IEEE Computer Society.

[24] Hossam AbdEl-Munim and Aly A. Farag. A variational approach for shapes registration using vector maps. In *Proc. of the 2006 IEEE International conference on Image Processing*, pages –, Washington, DC, USA, October 8-11, 2006.

[25] H. Guo, A. Rangarajan, S. Joshi, and L. Younes. Non-rigid registration of shapes via diffeomorphic point-matching. In *IEEE International Symposium on Biomedical Imaging*, pages 924–927, 2004.

[26] S. Belongie, J. Malik, and J. Puzicha. Shape matching and object recognition using shape contexts. *IEEE Transactions on Pattern Analysis and Machine Intelligence*, 24(24):509–522, 2002.

[27] Thomas B. Sebastian, Philip N. Klein, and Benjamin B. Kimia. Recognition of shapes by editing their shock graphs. *IEEE Transactions on Pattern Analysis and Machine Intelligence*, 26(5):550–571, 2004.

[28] Lawrence H. Staib and James S. Duncan. Boundary finding with parametrically deformable models. *IEEE Trans. Pattern Anal. Mach. Intell.*, 14(11):1061–1075, 1992.

[29] Yefeng Zheng and David Doermann. Robust point matching for two-dimensional nonrigid shapes. In *ICCV '05: Proceedings of the Tenth IEEE International Conference on Computer Vision*, pages 1561–1566, Washington, DC, USA, 2005. IEEE Computer Society.

[30] Hui Chen and Bir Bhanu. Global-to-local non-rigid shape registration. In *Proc. of the 18th International Conference on Pattern Recognition (ICPR'06)*, pages 57–60, Washington, DC, USA, 2006. IEEE Computer Society.

[31] H. Chui and A. Rangarajan. A new algorithm for non-rigid point matching. In *Proc. IEEE Conf. Computer Vision and Patern Recognition (CVPR'00)*, pages 44–51, 2000.

[32] M. Rousson and N. Paragios. Shape priors for level set representations. In *Proceedings of European Conference On Computer Vision (ECCCV'02)*, pages 78–29, 2002.

[33] T. Riklin-Raviv, N. Kiryati, and N.A. Sochen. Unlevel-sets: Geometry and prior-based segmentation. In *Proccedings of ECCV'04*, pages 50–61, 2004.

[34] D. Cremers, N. Sochen, and C. Schorr. Towards recognition-based variational segmentation using shape priors and dynamic labeling. In *Int. Conf. on Scale Space Theories in Computer Vision, vol. 2695 of LNCS*, pages 388–400, 2003.

[35] M. Fussenegger, R. Deriche, and A. Pinz. A multiphase level set based segmentation framework with pose invariant shape priors. In *Proc. of Asian Conference on Computer Vision (ACCV'06)*, pages 395–404, 2006.

[36] T. Brox and J. Weickert. Level set based image segmentation with multiple regions. In *Proc. of 26th DAGM*, pages 415–423, 2004.

[37] D. Cremers, N. Sochen, and C. Schnorr. Multiphase dynamic labeling for variational recognition-driven image segmentation. *Int. J. of Computer Vision*, 66(1):67–81, 2005.

[38] M.E. Leventon, W.E.L. Grimson, and O. Faugeras. Statistical shape influence in geodesic active contour. In *Proc. of CVPR'00*, volume 1, pages 316–323, 2000.

[39] A. Tsai, A. Yezzi Jr., W. Wells, C. Tempany, D. Tucker, A. Fan, W.E. Grimson, and A. Willsky. A shape-based approach to the segmentation of medical imagery using level sets. *IEEE Trans. Med. Imag.*, 22(2):137–154, 2003.

[40] Hossam AbdEl-Munim and Aly A. Farag. Shape representation and registration using vector distance functions. In *IEEE Conference on Computer Vision and Pattern Recognition (CVPR'07)*, pages 1–8, Minneapolis, MN, USA, June 18-23, 2007.

[41] F. Gibou and R. Fedkiw. A fast hybrid k-means level set algorithm for segmentation. In *4th Annual Hawaii Int. Conf. on Statistics and Mathematics*, volume 14, pages 281–291, 2002.

[42] Colin Goodall. Procrustes methods in the statistical analysis of shape. *Journal of Royal Statistical Society*, 53(2):285–339, 1991.

[43] Ming-Kuei Hu. Visual pattern recognition by moment invariants. *IRE Transactions on Information Theory*, 49(8):179–189, 1962.

[44] H. Dirilten and T. G. Newman. Pattern matching under affine transformations. *IEEE Transactions on Computers*, C-26(3):314–317, March 1977.

[45] R. Wong and E.L. Hall. Scene matching with invariant moments. *Comput. Vision, Graphics Image Process.*, 8(1):16–24, 1978.

[46] A. Foulonneau, P. Charbonnier, and F. Heitz. Affine-invariant geometric shape priors for region-based active contours. *IEEE Transactions on Pattern Analysis and Machine Intelligence*, 28(8):1352–57, August 2006.

[47] C. Brechbühler, G. Gerig, and O. Kübler. Surface parametrization and shape description. *Computer Vision and Image Understanding*, 61(2):154–170, 1995.

[48] M. Kazhdan, T. Funkhouser, and S. Rusinkiewicz. Rotation invariant spherical harmonic representation of 3d shape descriptors. In H. Hoppe L. Kobbelt, P. Schrder, editor, *Eurographics Symposium on Geometry Processing'03*, 2003.

[49] M. K. Chung, L. Shen, K. M. Dalton, and R. J. Davidson. Multi-scale voxel-based morphometry via weighed spherical harmonic representation. In *International Workshop on Medical Imaging and Augmented Reality (MIAR)*, 2006.

[50] M. K. Chung, S. Robbins, K. M. Dalton, S. Wang, A. C. Evans, and R. J. Davidson. Tensor-based cortical morphometry via weighted spherical harmonic representation. In *IEEE Computer Society Workshop on Mathematical Methods in Biomedical Image Analysis (MMBIA)*, 2006.

[51] X. Pennec, N. Ayache, and J. P. Thirion. Landmark-based registration using features identified through differential geometry. pages 499–513, 2000.

[52] P. Laskov and C. Kambhamettu. Curvature-based algorithms for nonrigid motion and correspondence estimation. *IEEE TPAMI*, 25(10):1349–54, 2003.

[53] S. Belongie, J. Malik, and J. Puzicha. Matching shapes. In 8th *IEEE International Conference on Computer Vision (ICCV'01)*, pages 456–461, July 2001.

[54] Nicolae Duta, Milan Sonka, and Anil K. Jain. Learning shape models from examples using automatic shape clustering and procrustes analysis. In *In Proc. of Information Processing in Medical Imaging (IPMI'99)*, pages 370–375, 1999.

[55] Harry Blum. A Transformation for Extracting New Descriptors of Shape. In Weiant Wathen-Dunn, editor, *Models for the Perception of Speech and Visual Form*, pages 362–380. MIT Press, Cambridge, 1967.

[56] N. Cornea, M. Demirci, D. Silver, A. Shokoufandeh, S. Dickinson, and P. Kantor. 3d object retrieval using many-to-many matching of curve skeletons. In *IEEE International Conference on Shape Modeling and Applications*, MIT, Boston, MA. June 15-17, 2005.

[57] A. Brennecke and T. Isenberg. 3D shape matching using skeleton graphs. In *Simulation and Visualization*, pages 299–310, 2004.

[58] Masaki Hilaga, Y. Shinagawa, T. Kohmura, and T. L. Kunii. Topology matching for fully automatic similarity estimation of 3D shapes. In *SIGGRAPH 01: Proceedings of the 28th annual conference on Computer graphics and interactive techniques*, pages 203–212, 2001.

[59] H. Sundar, D. Silver, N. Gagvani, and S. Dickinson. Skeleton based shape matching and retrieval. In *Proceedings of the Shape Modeling International (SMI03)*, pages 130–139, 2003.

[60] R. Fahmi, A. Jerebko, M. Wolf, and A. A. Farag. Robust segmentation of tubular structures in medical images. In *Proc. of SPIE08*, San Diego, CA, 2008.

[61] M. Sabry Hassouna and A. A. Farag. PDE-based three dimensional path planning for virtual endoscopy. In *Proc. of Information Processing in Medical Imaging (IPMI05)*, pages 529–540, Glenwood springs, CO, USA, July 2005.

[62] Daniel S. Fritsch, Stephen M. Pizer, Bryan S. Morse, David H. Eberly, and Alan Liu. The multiscale medial axis and its applications in image registration. *Pattern Recogn. Lett.*, 15(5):445–452, 1994.

[63] S. M. Pizer, D. S. Fritsch, V. E. Johnson, and E. L. Chaney. Segmentation, registration, and measurement of shape variation via image object shape. *IEEE Transactions om Medical Imaging*, 18(10):851–865, October 1999.

[64] W. Gong and G. Bertrand. A simple parallel 3d thinning algorithm. In *International Conference on Pattern Recognition (ICPR'90)*, pages 188–190, 1990.

[65] Olivier D. Faugeras and José Gomes. Dynamic shapes of arbitrary dimension: The vector distance functions. In *Proceedings of the 9th IMA Conference on the Mathematics of Surfaces*, pages 227–262, London, UK, 2000. Springer-Verlag.

[66] José Gomes and Olivier D. Faugeras. Using the vector distance functions to evolve manifolds of arbitrary codimension. In *Proc. of the 3rd Int. Conf. on Scale-Space and Morphology in Computer Vision*, pages 1–13, London, UK, 2001. Springer-Verlag.

[67] Polina Golland and W. Eric. L. Grimson. Fixed topology skeletons. In *Proceedings of IEEE Conference on Computer Vision and Pattern Recognition (CVPR'00)*, pages 10–17, 2000.

[68] I. Bitter, A. E. Kaufman, and M. Sato. Penalized-distance volumetric skeleton algorithm. *IEEE Transactions on Visualization and Computer Graphics*, 7(3):195–206, 2001.

[69] T. Deschamps and L. D. Cohen. Fast extraction of minimal paths in 3d images and applications to virtual endoscopy. *Medical Image Analysis*, 5(4):281–299, 2001.

[70] Per-Erik Danielsson. Euclidean distance mapping. *Computer Graphics and Image Processing*, 14:277–248, 1980.

[71] G. Borgefors. Distance transformations in digital images. *Computer Vision, Graphics and Image Processing*, 34:344–371, 1986.

[72] R. Fahmi, A. Abdel-Hakim Aly, A. El-Baz, and A. Farag. New deformable registration technique using scale space and curve evolution theory and a finite element based validation framework. In *28th Annual Int. Conf. of the IEEE Engineering in Medicine and Biology Society*, pages 3041–3044, New York, NY, Aug-Sep 2006.

[73] R. A. Johnson and D. W. Wichern. *Multivariate statistics, a practical approach.* Chapman & Hall, London/New York, 1988.

[74] Harold Hotelling. Analysis of a complex of statistical variables into principal components. *Journal of Educational Psychology*, 24(7):498–520, 1933.

[75] Andy Tsai. *Coupled Multi-Shape Model for Medical Image Segmentation: An Approach Utilizing Region Statistics, Edge Information, and Information-Theoretic Criteria.* PhD thesis, Harvard Medical School M.D. Thesis, February 2003.

[76] Jacques Feldmar and Nicholas Ayache. Rigid, affine and locally affine registration of free-form surfaces. *Int. J. Comput. Vision*, 18(2):99–119, 1996.

[77] Rachid Fahmi, Ayman Elbaz, Hassan Abdel-Munim, Alaa E. Abdel-Hakim, Aly A. Farag, and Manuel F. Casanova. Robust neuroimaging-based classification techniques of autistic vs. typically developing brain. In J. S. Suri and A. Farag, editors, *Parametric and Geometric Deformable Models: An application in Biomaterials and Medical Imagery*. Springer Verlag, May 2007.

[78] T. Cootes, C. Taylor, D. Cooper, and J. Graham. Active shape models-Their training and application. *Computer Vision and Image Understanding*, 61(1):38–59, 1995.

[79] J. Gomes and O. Faugeras. Reconciling distance functions and level sets. *J. Visiual Communication and Image Representation*, 11:209–223, 2000.

[80] V. I. Arnold. *Geometrical Methods in The theory of ordinary Differential Equations.* Springer-Verlag, New York, 1983.

[81] D. Peng, B. Merriman, S. Osher, H. Zhao, and M. Kang. A pde-based fast local level set method. *Journal of Computational Physics*, 155:410–438, 1999.

[82] S. Osher and R. Fedkiw. Level set methods and dynamic implicit surfaces. *Springer-Verlag, New York*, 2002.

[83] C. Li, C. Xu, C. Gui, and M. D. Fox. Level set evolution without re-initialization: A new variational formulation. In *Proc. of IEEE Computer Vision and Pattern Recognition (CVPR'2005)*, volume 1, pages 430–436, 2005.

[84] M. Sussman and E. Fatemi. An efficient, interfacepreserving level set redistancing algorithm and its application to interfacial incompressible fluid flow. *SIAM J. Sci. Comp.*, 20:1165–91, 1999.

[85] M. Sussman, P Smerka, and S. Osher. A level set method for computing solutions of incompressible two phase flows. *Journal of Computational Physics*, 114:146–159, 1994.

[86] Paul J. Besl and Neil D. McKay. A method for registration of 3-d shapes. *IEEE Trans. Pattern Anal. Mach. Intell.*, 14(2):239–256, 1992.

[87] Zhengyou Zhang. Iterative point matching for registration of free-form curves and surfaces. *Int. J. Comput. Vision*, 13(2):119–152, 1994.

[88] G. Pan, Z. Wu, and Y. Pan. Automatic 3d face verification from range data. In *Proc. of Acoustics, Speech, and Signal Processing (ICASSP'03)*, pages 193–196, 6-10 April 2003.

[89] Trina D. Russ, Mark W. Koch, and Charles Q. Little. A 2d range hausdorff approach for 3d face recognition. In *Proc. of the IEEE Conference on Computer Vision and Pattern Recognition (CVPR'05) - Workshops*, pages 169–176, Washington, DC, USA, 2005.

[90] Kyong J. Chang, Kevin W. Bowyer, and Patrick J. Flynn. Effects on facial expression in 3d face recognition. In *Proc. of SPIE Conf. on Biometric Tech. for Human Identification*, pages 132–143, March 2005.

[91] Y. Wang, G. Pan, Z. Wu, and Y. Wang. 3d face recognition in the presence of expression: A guidance-based constraint deformation approach. In *Proc. of Asian Conference on Computer Vision (ACCV'06)*, pages 581–590, 2006.

[92] Y. Wang, G. Pan, and Z. Wu. Exploring facial expression effects in 3d face recognition using partial ICP. In *Proc. of Computer Vision and Pattern Recognition (CVPR'07)*, pages 1–7, 17-22 June 2007.

[93] J. Davis, S. R. Marschner, M. Garr, and M. Levoy. Filling holes in complex surfaces using volumetric diffusion. In *Proceedings of the First International Symposium on 3D Data Processing Visualization and Transmission (3DPVT'02)*, pages 858–868, 2002.

[94] L. Silva, O. R. Bellon, and K.L. Boyer. Multiview range image registration using the surface interpenetration measure. *Image and Vision Computing*, 25(1):114–125, January 2007.

[95] D. Mumford and J. Shah. Optimal approximations by piecewise smooth functions and associated variational problems. *Comm. Pure Appl. Math.*, 42.

[96] Dinggang Shen and Christos Davatzikos. Hammer: Hierarchical attribute matching mechanism for elastic registration. *IEEE Trans. on Medical Imaging*, 21(11):1421–39, 2002.

[97] S. Warfield, S. Haker, I. Talos, C. Kemper, N. Weisenfeld, A. Mewes, D. Zimring, K. Zou, C. Westin, W. Wells, C. Tempany, A. Golby, P. Black, F. Jolesz, and R. Kikinis. Capturing intraoperative deformations: research experience at brigham and women's hospital. *Medical Image Analysis*, 9(2), 2005.

[98] Alaa E. Abdel-Hakim and Aly A. Farag. Colored local invariant features for object description. In *ICGST International Conference on Graphics, Vision and Image Processing (GVIP-05)*, pages 19–21, Cairo, Egypt, December 2005 2005.

[99] K. Mikolajczyk and C. Schmid. An affne invariant interest point detector. In *Proc. of the European Conference on Computer Vision (ECCV'02)*, pages 128–142, Copenhagen, Denmark, May-June 2002.

[100] Tony Lindeberg. *Scale-Space Theory in Computer Vision.* Kluwer Academic Publishers, Norwell, MA, USA, 1994.

[101] David G. Lowe. Distinctive image features from scale-invariant keypoints. *Int. J. Comput. Vision*, 60(2):91–110, 2004.

[102] Krystian Mikolajczyk and Cordelia Schmid. A performance evaluation of local descriptors. *IEEE Transactions on Pattern Analysis and Machine Intelligence*, 27(10):1615–1630, 2005.

[103] M. Miga, K. Paulsen, J. Lemery, S. Eisner, A. Hartov, and F. Kennedy. Model-updated image-guided: Initial clinical experiences with gravity-induced brain deformation. *IEEE Transaction On Medical Imaging*, 18(10), Oct. 1999.

[104] O. Clatz, M. Sermesant, P. Bondiau, H. Delingette, S. Warfield, G. Malandain, and N. Ayache. Realistic simulation of the 3d growth of brain tumors in mr images coupling diffusion with mass effect. *IEEE Transactions on Medical Imaging*, 24(10), 2005.

[105] A. Mohamed and C. Davatzikos. Finite element mesh generation and remeshing from segmented medical images. In *Proc. of Int. Symp. Biom. Imag. (ISBI'04), From Nano to Macro, Arlington, VA*, 2004.

[106] K. Miller and K. Chinzei. Mechanical properties of brain tissue in tension. *J. Of Biomechanics*, 35, 2002.

[107] M. I. Miga, K. D. Paulsen, F.E. Kennedy, A. Hartov, and D. W. Roberts. Model-updated image-guided neurosurgery using finite element method: Incorporation of the falx cerebri. In *proc. of MICCAI'99, Lecture Notes in Computer Science, Cambridge, UK*, 1999.

[108] M. T. Prange and S.S. Margulies. Regional, directional, and age-dependent properties of the brain undergoing large deformation. *J. Of Biomechanical Engineering*, 124(2), 2002.

[109] *Abaqus Version 6.5*, 2005.

[110] M. Miga, D. Roberts, F. Kennedy, L. Platenik, A. Hartov, K. Lunn, and K. Paulsen. Modeling of retraction and resection for intraoperative updating of images. *Neurosurgery*, 49(1), July 2001.

[111] O. Clatz, H. Delingette, I. Talos, A. Golby, R. Kikinis, F. Jolesz, N. Ayache, and S. Warfield. Robust non-rigid registration to capture brain shift form intra-operative MRI. In *Proceedings of MICCAI'05*, Oct., 2005.

[112] R. Wasserman and R. Acharya. A patient-specific in vivo tumor model. (review). *Mathematical Biosciences*, 136(2), 1996.

[113] O. C. Zienkiewicz and R. L. Taylor. *The Finite Element Method*, volume Vol II. 2000.

[114] J. Schnabel, C. Tanner, A. Castellano-Smith, A. Degenhard, M. Leach, D. Hose, D. Hill, and D. Hawkes. Validation of non-rigid image registration using finite-element methods: Application to breast MR images. *IEEE Transactions on Medical Imaging*, 22(2), Feb., 2003.

[115] J.E. Vidale. Finite-difference calculation of traveltimes in three dimensions. *Journal of Geophysics*, 55:521–526, 1990.

[116] D. Adalsteinsson and J. Sethian. A fast level set method for propagating interfaces. *Journal of Computational Physics*, 118:269–277, 1995.

[117] S. Kim. Eno-dno-ps: a stable, second-order accuracy eikonal solver. *Society of Exploration Geophysicists*, pages 1747–1750, 1999.

[118] R. Kimmel and J. Sethian. Fast marching methods on triangulated domains. *PNAS*, 95(11):8341–8435, 1998.

[119] J. Sethian and A. Vladimirsky. Fast methods for the eikonal and related hamilton-jacobi equations on unstructured meshes. *Proceedings of the National Academy of Science*, 97(11):5699–5703, 2000.

APPENDICES I
NOMENCLATURE

The following convention is used throughout the document.

$\mathbf{x}$	Point in 2D or 3D Cartesian space
$\mathbb{R}$	Set of real numbers
$\mathbb{N}$	Set of non-negative integers
Ω	Open bounded subset of $\mathbb{R}$
$\Omega \setminus \Omega_0$	Complement of Ω_0 in Ω
$\subseteq$	Subset of
$\|\cdot\|$	Absolute value in $\mathbb{R}$
$\|\cdot\|$	Euclidean norm in a vector space
$\mathcal{C}$	Curve or family of curves in $\mathbb{R}^2$
$\phi,\ \Phi,\ \Psi$	Level set functions
Φ_S	Signed distance representation of a shape S
V_S	Vector distance function of a shape S
$\widetilde{\phi}$	implicit representation of a shape prior
$L(.)$	Labelling function
$\mathcal{A}$	Rigid or affine transformation in $\mathbb{R}^n$
$\mathcal{S}$	Scale matrix
$\mathcal{R}, \theta,\ \theta_x,\ \theta_y,\ \theta_z$	Rotation matrix and rotation angles in different directions
$\mathcal{T}$	Translation vector
$\mathbf{u} = (u_i)_{1 \leq i \leq n}$	Displacement field in $\mathbb{R}^n$
F	Speed function
∇	Gradient operator
Δ	Laplace operator
$D(\mathbf{u})$	Jacobian of $\mathbf{u}$

$div(.)$	Divergence of a vector field
$\mathcal{H}(f)$	Hessian matrix of a function f
$\circ$	Composition operator between functions
$\mathcal{D}(.)$	Dissimilarity measure
$\mathcal{D}^{MI}(.)$	Mutual information dissimilarity measure
$\mathcal{D}^{SSD}(.)$	Sum of squared differences dissimilarity measure
$\mathcal{R}(.)$	Regularization term
$\mathcal{M}$	Manifold in $\mathbb{R}^n$
$\delta(\mathbf{x})$	Distance from $\mathbf{x} \in \mathbb{R}^n$ to a manifold $\mathcal{M}$
$\delta_\epsilon(a,b)$	Indicator function to determine narrow band
$\eta(\mathbf{x})$	Squared distance from $\mathbf{x} \in \mathbb{R}^n$ to a manifold $\mathcal{M}$
$\delta(.)$	Dirac function
$H(.)$	Heaviside function
α_i's	Weight of shape energy
$\mathbf{w}_i$'s	Weight of active shape model
$\mu,\ \lambda$	Lamé coefficients of a material
ϵ_{ij}	Deformation tensor

This chapter describes some of the numerical schemes employed in discretizing the continuous evolution equations (see chapter IV). These evolution equations are given by:

$$
\begin{cases}
\Phi_t = -\frac{\partial E_{total}}{\partial \Phi} = -2[(\Phi(\mathbf{x}) - \Phi_T(g(\mathbf{x})) + \alpha(\Delta\Phi(g(\mathbf{x})) - div(\frac{\nabla\Phi(g(\mathbf{x}))}{|\nabla\Phi(g(\mathbf{x}))|}))], \\[2mm]
\mathbf{u}_t = -\frac{\partial E_{total}}{\partial \mathbf{u}} = -2[(\Phi(\mathbf{x}) - \Phi_T(g(\mathbf{x}))) \cdot \nabla\Phi_T(g(\mathbf{x})) \\[2mm]
\qquad\qquad - \alpha(1 - \frac{1}{|\nabla\Phi(g(\mathbf{x}))|}) \cdot \mathcal{H}(\Phi \circ g)(\mathbf{x}) \cdot \nabla\Phi(g(\mathbf{x})) + \beta\mathcal{R}(\mathbf{u})], \\[2mm]
\Phi(\mathbf{x}, 0) = \Phi_{\widehat{S}}(\mathbf{x}), \\[2mm]
\mathbf{u}(\mathbf{x}, 0) = \mathbf{0}.
\end{cases}
\qquad (80)
$$

First, the terms of the form $\Phi(g(\mathbf{x})) = \Phi(\mathbf{x} + \mathbf{u}(\mathbf{x}))$ are numerically approximated using the following interpolation schemes:

- **2D Case:**

  The value of a function $f(\cdot)$ at a point (x, y) (not necessarily a grid point) is computed using a bilinear interpolation scheme as follows. Four neighboring points are explored to lead to

  $$
  f(x, y) \approx (1-a)(1-b)f(i, j) + a(1-b)f(i+1, j) + (1-a)bf(i, j+1) + abf(i+1, j+1),
  $$

  $$(81)$$

  where,

  $$
  \begin{aligned}
  i &= floor(x), \quad a = x - i, \\
  j &= floor(y), \quad b = y - j.
  \end{aligned}
  $$

- **3D case:**

  The value of $f(\cdot)$ at a point (x, y, z) is approximated using trilinear interpolation as

follows. First, let:

$$i = floor(x), \quad a = x - i,$$

$$j = floor(y), \quad b = y - j,$$

$$k = floor(z), \quad c = z - k,$$

and

$$V_1 = f(i, j, k), \qquad V_2 = f(i+1, j, k),$$

$$V_3 = f(i+1, j+1, k), \qquad V_4 = f(i, j+1, k),$$

$$V_5 = f(i, j, k+1), \qquad V_6 = f(i+1, j, k+1),$$

$$V_7 = f(i+1, j+1, k+1), \quad V_8 = f(i, j+1, k+1).$$

Then, the value $f(x, y, z)$ is estimated as

$$f(x, y, z) \approx V_1(1-a)(1-b)(1-c) + V_2 a(1-b)(1-c) +$$
$$V_3 ab(1-c) + V_4(1-a)b(1-c) +$$
$$V_5(1-a)(1-b)c + V_6 a(1-b)c +$$
$$V_7 abc + V_8(1-a)bc.$$

Now, all the finite difference schemes necessary to implement the different terms in equation (80) are introduced.

To begin with, if $h(\cdot)$ denotes the scalar function whose derivatives are to be approximated, and if the same grid spacing is assumed in all directions, i.e., $\Delta x = \Delta y = \Delta z = \delta$, then all the first derivatives at a grid point (i, j, k) are implemented using central differences as follows (equations are given in the general case of a 3D space):

$$\partial_x h_{i,j,k} = \frac{h_{i+1,j,k} - h_{i-1,j,k}}{2\delta},$$
$$\partial_y h_{i,j,k} = \frac{h_{i,j+1,k} - h_{i,j-1,k}}{2\delta},$$
$$\partial_z h_{i,j,k} = \frac{h_{i,j,k+1} - h_{i,j,k-1}}{2\delta}.$$

These schemes serve in implementing the gradient terms $\nabla h_{i,j,k} = \begin{pmatrix} \partial_x h_{i,j,k} \\ \partial_y h^y_{i,j,k} \\ \partial_z h_{i,j,k} \end{pmatrix}$.

The second derivatives are approximated as follows:

- Standard second order approximation of $\partial^2_{\alpha\alpha} h_{i,j,k} \doteq (\frac{\partial^2 h}{\partial \alpha^2})_{i,j,k}$, with $\alpha = x, y,\ z$

$$
\begin{aligned}
\partial^2_{xx} h_{i,j,k} &= \frac{h_{i+1,j,k} - 2h_{i,j,k} + h_{i-1,j,k}}{\delta^2}, \\
\partial^2_{yy} h_{i,j,k} &= \frac{h_{i+1,j,k} - 2h_{i,j,k} + h_{i-1,j,k}}{\delta^2}, \\
\partial^2_{zz} h_{i,j,k} &= \frac{h_{i+1,j,k} - 2h_{i,j,k} + h_{i-1,j,k}}{\delta^2}.
\end{aligned}
\tag{82}
$$

- The 4-point schemes are used to approximate cross derivatives, such as $\frac{\partial^2 h}{\partial\alpha\partial\beta}$:

$$
\begin{aligned}
\partial^2_{xy} h_{i,j,k} &= \frac{h_{i+1,j-1,k} - h_{i+1,j-1,k} - h_{i-1,j+1,k} + h_{i-1,j-1,k}}{4\delta^2}, \\
\partial^2_{xz} h_{i,j,k} &= \frac{h_{i+1,j,k-1} - h_{i+1,j,k-1} - h_{i-1,j,k+1} + h_{i-1,j,k-1}}{4\delta^2}, \\
\partial^2_{yz} h_{i,j,k} &= \frac{h_{i,j+1,k-1} - h_{i,j+1,k-1} - h_{i,j-1,k+1} + h_{i,j-1,k-1}}{4\delta^2}.
\end{aligned}
\tag{83}
$$

Note that These approximations do not change if we change the order of derivation, i.e., $\frac{\partial^2 h}{\partial x \partial y} = \frac{\partial^2 h}{\partial y \partial x}$.

The above second order derivatives are used to implement the Laplacian term $\Delta\Phi()$, the Hessian matrix, $\mathcal{H}$, as well as the curvature term $\kappa = div(\frac{\nabla\Phi}{|\nabla\Phi|})$, where in general, given the level set representation of a given shape, $\phi(\cdot)$, then

In 2D: $\qquad \kappa = \frac{\phi_{xx}\phi_y^2 - 2\phi_x\phi_y\phi_{xy} + \phi_{yy}\phi_x^2}{(\phi_x^2 + \phi_y^2)^{\frac{3}{2}}},$

In 3D: $\quad \kappa = \frac{(\phi_{yy}+\phi_{zz})\phi_x^2 + (\phi_{xx}+\phi_{zz})\phi_y^2 + (\phi_{xx}+\phi_{yy})\phi_z^2 - 2\phi_x\phi_y\phi_{xy} - 2\phi_x\phi_z\phi_{xz} - 2\phi_y\phi_z\phi_{yz}}{(\phi_x^2 + \phi_y^2 + \phi_z^2)^{\frac{3}{2}}}$

Note that in the 3D case, the above expression of κ corresponds to the *"mean curvture"*.

Finally, the regularization operator

$$\textbf{In 2D:} \quad \mathcal{R}(\mathbf{u}) = \begin{pmatrix} \mathcal{R}_u \\ \mathcal{R}_v \end{pmatrix} = \begin{pmatrix} \mu\Delta u + (\lambda+\mu)(\partial_{xx}u(\mathbf{x}) + \partial_{xy}v(\mathbf{x})) \\ \mu\Delta v + (\lambda+\mu)(\partial_{yx}u(\mathbf{x}) + \partial_{yy}v(\mathbf{x})) \end{pmatrix}$$

$$\textbf{In 3D:} \quad \mathcal{R}(\mathbf{u}) = \begin{pmatrix} \mathcal{R}_u \\ \mathcal{R}_v \\ \mathcal{R}_w \end{pmatrix} = \begin{pmatrix} \mu\Delta u(\mathbf{x}) + (\lambda+\mu)(\partial_{xx}u(\mathbf{x}) + \partial_{xy}v(\mathbf{x}) + \partial_{xz}w(\mathbf{x})) \\ \mu\Delta v(\mathbf{x}) + (\lambda+\mu)(\partial_{yx}u(\mathbf{x}) + \partial_{yy}v(\mathbf{x}) + \partial_{yz}w(\mathbf{x})) \\ \mu\Delta w(\mathbf{x}) + (\lambda+\mu)(\partial_{zx}u(\mathbf{x}) + \partial_{zy}v(\mathbf{x}) + \partial_{zz}w(\mathbf{x})) \end{pmatrix},$$

was approximated using the above second derivatives (see Eqs. 82 and Eqs. 83). This lead to the following schematic expressions, where the tables represent the discrete grid and contain the weights associated with each image point (pixel/voxel) with zero weight if the voxel is empty. At the bottom of each table is written the function to which the grid corresponds together with the corresponding global weight (for instance: μw means that the grid corresponds to w weighted globally by μ). In each table, the index i is assumed to increase from left to right and the index j increases from top to bottom. In the 3D case, each of the three stacked tables corresponds to a different index k, increasing from bottom to top. Note that each center voxel corresponds to the grid point (i,j) or (i,j,k).

- **2D case:**

$\mathcal{R}_u^{i,j} \approx$

	1	
1	-4	1
	1	

μu

$+$

1	-2	1

$(\lambda+\mu)u$

$+$

1		-1
-1		1

$\frac{1}{4}(\lambda+\mu)v$

$\mathcal{R}_v^{i,j} \approx$

	1	
1	-4	1
	1	

μv

$+$

	1	
	-2	
	1	

$(\lambda+\mu)v$

$+$

1		-1
-1		1

$\frac{1}{4}(\lambda+\mu)u$

- **3D case:**

$$\mathcal{R}_u^{i,j,k} \approx [\mu u] + [(\lambda+\mu)u] + [\tfrac{1}{4}(\lambda+\mu)v] + [\tfrac{1}{4}(\lambda+\mu)w]$$

$$\mathcal{R}_v^{i,j,k} \approx [\mu v] + [(\lambda+\mu)v] + [\tfrac{1}{4}(\lambda+\mu)u] + [\tfrac{1}{4}(\lambda+\mu)w]$$

$$\mathcal{R}_w^{i,j,k} \approx [\mu w] + [(\lambda+\mu)w] + [\tfrac{1}{4}(\lambda+\mu)u] + [\tfrac{1}{4}(\lambda+\mu)v]$$

Note that in order to control the behavior of the regularization operator $\mathcal{R}(\mathbf{u})$, one can use a single parameter ν with $\frac{1}{2} < \nu \leq 1$ as:

$$\mathcal{R}(\mathbf{u}) = \nu \Delta \mathbf{u} + (1 - \nu)\nabla(\nabla \cdot \mathbf{u}).$$

To make the Laplacian operator dominant, one can chose ν close to 1, whereas the operator $\nabla(\nabla \cdot \mathbf{u})$ becomes dominant for ν close to zero.

In most of the presented experiments, an equal weight was given to each of these two operators, i.e., ν was chosen as $\nu = \frac{1}{2}$.

APPENDICES III

FAST MARCHING METHOD

This appendix describes the numerical technique used to approximate the distance map of a given shape. As was explained in Chap. III.H, the distance transform computes at each voxel its minimum distance from the shape boundary. This function can be discretely approximated using the Chamfer metric [71], or continuously computed using the Fast Marching Methods (*FMM*).

Continuously approximating the distance transform, which we will denote by $\phi(\mathbf{x})$, can be done by solving the following Eikonal [9] equation:

$$
\begin{cases}
|\nabla \phi(\mathbf{x})| = \frac{1}{F(\mathbf{x})} \text{ in } \Omega, \\
\phi = 0 \text{ on } \Gamma = \partial\Omega,
\end{cases}
\tag{84}
$$

where, ∇ is the gradient operator, and Γ is the shape boundary (a curve in 2D or a surface in 3D). In this equation, the value of ϕ at each point $\mathbf{x}$ can be interpreted as the minimum arrival time of a wave as it crosses the point $\mathbf{x}$ with a speed $F = 1$.

Several methods have been proposed to solve the Eikonal equation [115–117], the most stable and consistent of which is the fast marching method (*FMM*), which is applicable to both Cartesian [9, 116] and triangulated surfaces [118, 119]. The *FMM* combines entropy satisfying upwind schemes and fast sorting techniques to find the solution in one pass algorithm. The *FMM* was introduced by Sethian [116] as a way to solve equation (84). This method is based on the upwinding nature of equation (84) and uses a fast sorting technique, in particular a heap-based sorting technique, to exploit the fact that the solution at each point depends only on points closer to the interface, and finds the overall solution to

---

[9]The Eikonal equation is a non-linear *PDE* which was derived about 150 years ago by William R. Hamilton. The word Eikonal comes from the Greek word for image, $\epsilon\iota\kappa\omega\nu$. Such an equation can be derived from *Maxwell*'s equations.

equation 84 in linear time [10].

In order to get a feel of upwind schemes, consider the following standard finite difference schemes in the x-direction, used to approximate the first derivatives of the unknown function ϕ, on a grid with a spacing Δx in the x-direction.

$$D_{i,j,k}^{+x}\phi = \frac{\phi_{i+1,j,k} - \phi_{i,j,k}}{\Delta x}, \tag{85}$$

$$D_{i,j,k}^{-x}\phi = \frac{\phi_{i,j,k} - \phi_{i-1,j,k}}{\Delta x}. \tag{86}$$

The first expression, known as the *forward* difference scheme computes the solution at the grid point (i, j, k) using the information at (i, j, k) and $(i + 1, j, k)$. Therefore, the information for the solution is propagating, say, from left to right, while in the second equation, known as *backward* difference scheme, the information propagates in the opposite direction (right to left). Choosing the correct finite difference scheme, also called the *upwind* scheme depends on the information propagation, and there must be a specific criterion that allows the switching from one finite difference scheme to another based on the correct direction of information propagation.

1. Implementation of the *FMM*

The presentation is made for the general 3D case. The gradient $\nabla\phi$ in the Eikonal equation (84) is discretized such that the physically correct vanishing viscosity weak solution (see [21]). This leads to

$$\begin{bmatrix} \max(D_{i,j,k}^{-x}\phi, 0)^2 + \min(D_{i,j,k}^{+x}\phi, 0)^2 + \\ \max(D_{i,j,k}^{-y}\phi, 0)^2 + \min(D_{i,j,k}^{+y}\phi, 0)^2 + \\ \max(D_{i,j,k}^{-z}\phi, 0)^2 + \min(D_{i,j,k}^{+z}\phi, 0)^2 \end{bmatrix} = 1. \tag{87}$$

A more convenient upwind scheme was suggested by Sethian [116], namely,

$$\begin{bmatrix} \max(D_{i,j,k}^{-x}\phi, -D_{i,j,k}^{+x}\phi, 0)^2 + \\ \max(D_{i,j,k}^{-y}\phi, -D_{i,j,k}^{+y}\phi, 0)^2 + \\ \max(D_{i,j,k}^{-z}\phi, D_{i,j,k}^{+z}\phi, 0)^2 \end{bmatrix} = 1. \tag{88}$$

---

[10]Linear in number of visits to grid cells.

161

where, the forward and backward finite differences in each direction, $D^{\pm \alpha}_{i,j,k} \phi$ with $\alpha = x, y, z$ can be computed as shown on equation (85).Substuting these difference into equation (88) leads to

$$
\begin{bmatrix}
\max(\frac{\phi_{i,j,k}-\phi_{i-1,j,k}}{\Delta x}, \frac{\phi_{i,j,k}-\phi_{i+1,j,k}}{\Delta x}, 0)^2 + \\
\max(\frac{\phi_{i,j,k}-\phi_{i,j-1,k}}{\Delta y}, \frac{\phi_{i,j,k}-\phi_{i,j+1,k}}{\Delta y}, 0)^2 + \\
\max(\frac{\phi_{i,j,k}-\phi_{i,j,k-1}}{\Delta z}, \frac{\phi_{i,j,k}-\phi_{i,j,k+1}}{\Delta z}, 0)^2
\end{bmatrix} = 1, \tag{89}
$$

which can be re-arranged as follows:

$$
\begin{bmatrix}
\max(\frac{\phi_{i,j,k}-\min(\phi_{i-1,j,k},\phi_{i+1,j,k})}{\Delta x}, 0)^2 + \\
\max(\frac{\phi_{i,j,k}-\min(\phi_{i,j-1,k},\phi_{i,j+1,k})}{\Delta y}, 0)^2 + \\
\max(\frac{\phi_{i,j,k}-\min(\phi_{i,j,k-1},\phi_{i,j,k+1})}{\Delta z}, 0)^2
\end{bmatrix} = 1. \tag{90}
$$

Now, if one lets

$$
A = \phi_{i,j,k}, \tag{91}
$$

$$
A_1 = \min(\phi_{i-1,j,k}, \phi_{i+1,j,k}),
$$

$$
A_2 = \min(\phi_{i,j-1,k}, \phi_{i,j+1,k}),
$$

$$
A_3 = \min(\phi_{i,j,k-1}, \phi_{i,j,k+1}), \tag{92}
$$

then, one gets the following second order equation

$$
\max(\frac{A - A_1}{\Delta x}, 0)^2 + \max(\frac{A - A_2}{\Delta y}, 0)^2 + \max(\frac{A - A_3}{\Delta z}, 0)^2 = 1. \tag{93}
$$

To solve this equation, the following cases must be considered:

- $A > \max(A_1, A_2, A_3)$:

  in this case, equation (93) cab be written as

$$
(\frac{A - A_1}{\Delta x})^2 + (\frac{A - A_2}{\Delta y})^2 + (\frac{A - A_3}{\Delta z})^2 = 1, \tag{94}
$$

  which is a second order equation in A of the form $aA^2 + bA + c = 1$, with

$$
a = [\frac{1}{(\Delta x)^2} + \frac{1}{(\Delta y)^2} + \frac{1}{(\Delta z)^2}],
$$

$$
b = -2[\frac{A_1}{(\Delta x)^2} + \frac{A_2}{(\Delta y)^2} + \frac{A_3}{(\Delta z)^2}],
$$

$$
c = [\frac{A_1^2}{(\Delta x)^2} + \frac{A_2^2}{(\Delta y)^2} + \frac{A_3^2}{(\Delta z)^2}] - 1. \tag{95}
$$

162

If there are two different roots, the largest one is picked as the solution.

- $A < A_a$ and $A > \max(A_b, A_c$, with $a, b, c \in 1, 2, 3$:

  In this case, the addend corresponding to the index α in equation (93) is dropped and one has

  $$(\frac{A - A_b}{\Delta x_b})^2 + (\frac{A - A_c}{\Delta x_c})^2 = 1, \tag{96}$$

  where, Δx_b and Δx_c denote the grid spacing in the b and c directions. If there are two different roots, the largest one is picked as the solution.

- $A > A_a$ and $A < \min(A_b, A_c)$:

  In this case, the addends that correspond the indices b and c in equation (93) are dropped and

  $$A = 1 + \frac{\Delta x_a}{A_a}. \tag{97}$$

The idea behind the *FMM* to solve the equation (93) is based on *causality* criteria which states that the solution at any point depends only on the neighbors that have smaller values (i.e, the information is propagated from smaller values of ϕ to larger values). The *FMM* rests on building the solution of Eq. 93 outward from the smallest value, stepping away from the boundary condition in a downwind direction.

The following summarizes how the *FMM* algorithm works. A thin zone, or a *narrow band* of candidate points around the existing front is constructed. This zone is moved froward by sweeping its points and freezing those points whose values can not be altered and bringing new candidate points into the narrow band structure. Consider the 2D case illustrated by Fig. 72 where the algorithm will start from the known value at the origin point which is shown as dark black sphere, and is tagged as *frozen*. The light gray spheres represent the points where the solution is still *unknown*. The solution at four of these points (4 neighbors of the dark black sphere) is computed by solving equation (93). These points are then tagged as *trial* and are shown as dark gray spheres in Fig. (72-b). These points are inserted into the narrow band structure. Then, one of these neighboring points with the smallest ϕ
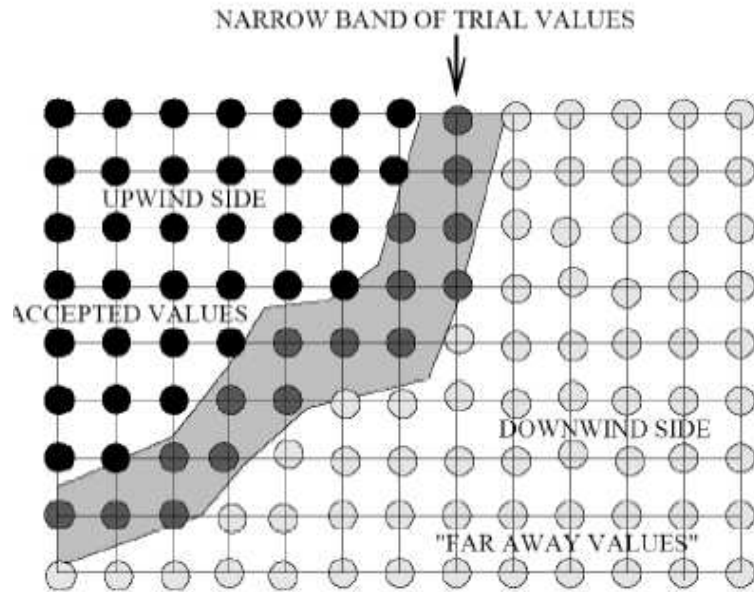
FIGURE 71 – Progress of *FMM* (image taken from [9]).

value is frozen [11] and proceed with the algorithm as shown on the rest of Fig. 72. Hence, the solution is marched outwards, always transforming the dark gray grid point with minimum trial value for ϕ into a known value, and readjusting downwind neighbors as shown in Fig. 71. Consequently, a point with a known value will never be revisited and its value remains unchanged by all later calculations.

2. The Update Procedure for the *FMM*

The following steps summarize the *FMM* algorithm. Initially, all the boundary points are tagged as *frozen* and the remaining points are tagged as *unknown*.

- Determine the neighboring points of the existing frozen points.

- Solve equation (88) at those neighbor points, tag them as *trial*, and insert them into the narrow band.

- **LOOP:** From the narrow band, pick the trial point A with the smallest arrival time.

- Remove A from the narrow band and tag it as *frozen*.

---

[11]That is, we represent it with a black sphere and consider its value known.

164
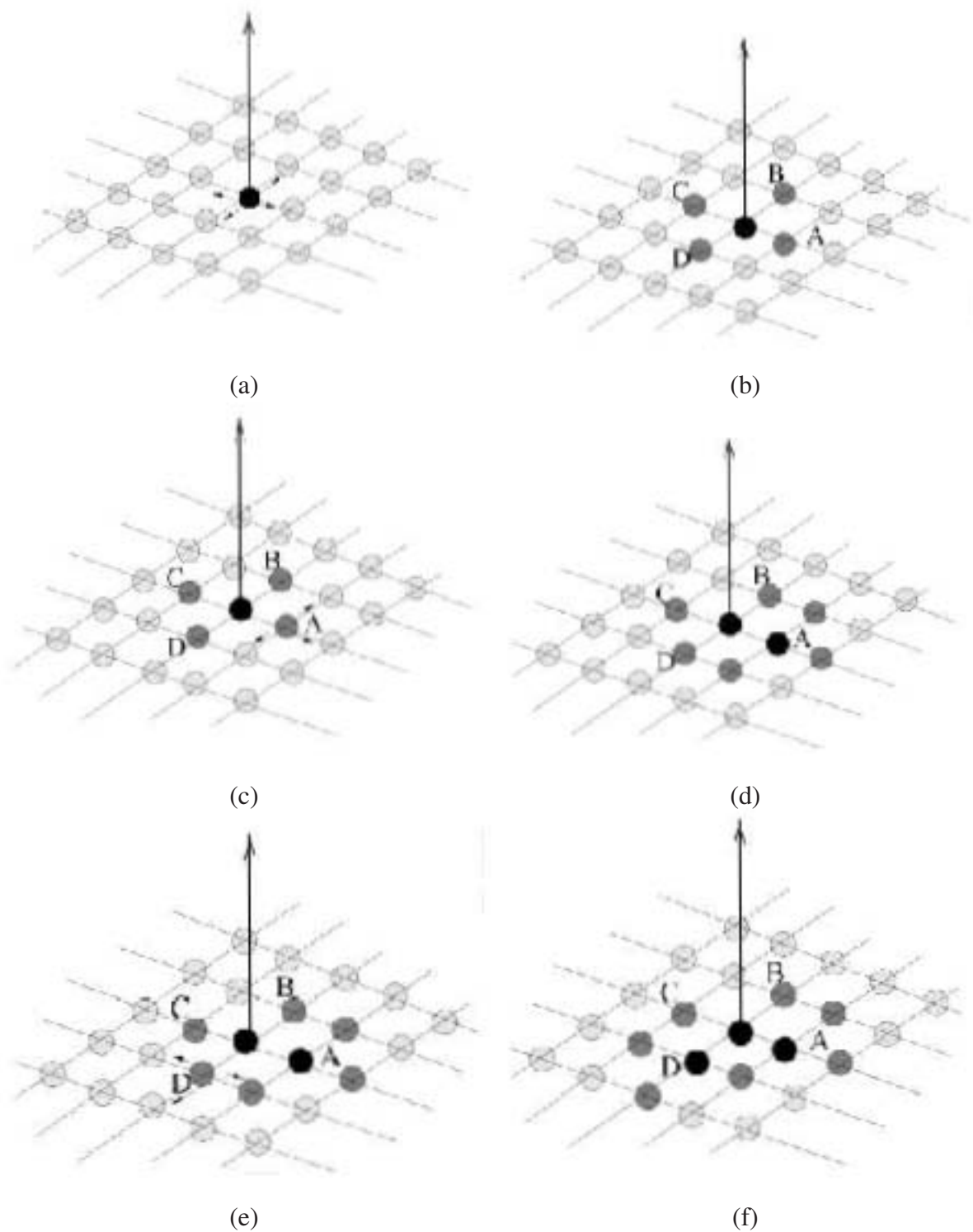
FIGURE 72 – Update procedure for *FMM*. (a) Find the four neighbors of the origin. (b) Compute the arrival of the neighbors. (c) Chose the point with smallest value (for example A). (d) Freeze value at A and update values at its neighboring points. (e) Chose the point with smallest value (for example D). (f) Freeze value at A and update values at its neighboring points. Images taken from [9]

- Find the neighbors of A that are either *narrow-band* or *unknown*.

- Solve equation (88) at those neighbor points, tag them as *trial*, and insert them into the narrow band.

- Go back to LOOP.

Note that in the fourth step of this process, either an *unknown* point is tagged as *narrow-band* or a *narrow-band* point is assigned a new value smaller than its previous value.

3. Data Structure in *FMM*

The *FMM* uses a sorted *min-heap* [12] data structure to store the ϕ values in the narrow band structure. These values are stored together with the indices which give the point locations in the grid structure, with the root node having the smallest value in the narrow band.

The marching algorithm proceeds as follows:

- Extract the top (smallest) element in the heap and freeze its value.

- Update and (possibly) insert its neighbors.

- Continue until heap is empty.

If a heap with M elements is assumed, the worst computational complexity of the *FMM* algorithm is $O(\log M)$. For more details about the *FMM* and its implementation, the interested reader is referred to [9].

In this work, the *FMM* was implemented as described above using *Multimap* data structure which is part of the Standard Template Library (*STL*).

---

[12]In an abstract sense, a min-heap is a complete binary tree with the property that the value at any given node is less or equal to values at its children.

APPENDICES IV

THE CHANGE OF ENERGY

In this appendix, the equations expressing the change of the segmentation energy with shape prior are when moving point from one region to another are derived. For simplicity, only the 2-phase Chan-Vese model with one shape prior is considered. Recall that the functional to be minimized in this case is given by:

$$E = \int_{\Omega} [(f - c_1)^2 H(\phi) + (f - c_2)^2 H(-\phi)] d\mathbf{x} + \nu \int_{\Omega} |\nabla H(\phi)| d\mathbf{x} + \alpha \int_{\Omega} (\phi(\mathbf{x}) - \widetilde{\phi}(\mathbf{x}))^2 d\mathbf{x}. \tag{98}$$

The length term can be ignored, i.e., $\nu = 0$. Let $A = \{\mathbf{x} \in \Omega / \phi(\mathbf{x}) = 1\}$ and $B = \{\mathbf{x} \in \Omega / \phi(\mathbf{x}) = -1\}$.

In a discrete form, the energy functional (98) can be written as:

$$E = E_A + E_B, \tag{99}$$

where,

$$E_A = \sum_{\mathbf{x} \in A} [(f - c_1)^2 + \alpha(\phi(\mathbf{x}) - \widetilde{\phi}(\mathbf{x}))^2],$$

$$E_B = \sum_{\mathbf{x} \in B} [(f - c_2)^2 + \alpha(\phi(\mathbf{x}) - \widetilde{\phi}(\mathbf{x}))^2].$$

Now, let $\mathbf{x}_0$ be the current point during the sweeping process, if assume that $\mathbf{x}_0$ is moved from A to B. The new grey level averages for each region become:

$$\widetilde{c}_1 = c_1 + \frac{c_1 - f(\mathbf{x}_0)}{a - 1},$$

$$\widetilde{c}_2 = c_2 - \frac{c_2 - f(\mathbf{x}_0)}{b + 1}.$$

where, $a = |A|$ and $b = |B|$ before moving the point $\mathbf{x}_0$ from A to B.

One can then easily show that the new energies (for each region) are given by:

$$\widetilde{E}_A = E_A - ((f(\mathbf{x}_0) - c_1)^2 \frac{a}{a-1} + \alpha(1 - \widetilde{\phi}(\mathbf{x}_0))^2),$$

$$\widetilde{E}_B = E_B + ((f(\mathbf{x}_0) - c_2)^2 \frac{b}{b+1} + \alpha(1 + \widetilde{\phi}(\mathbf{x}_0))^2).$$

The difference of energy corresponding to this move is

$$
\begin{aligned}
\Delta E_{AB} &= (\widetilde{E}_A + \widetilde{E}_B) - (E_A + E_B) \\
&= ((f(\mathbf{x}_0) - c_2)^2 \frac{b}{b+1} + \alpha(1 + \widetilde{\phi}(\mathbf{x}_0))^2) - ((f(\mathbf{x}_0) - c_1)^2 \frac{a}{a-1} + \alpha(1 - \widetilde{\phi}(\mathbf{x}_0))^2) \\
&= (f(\mathbf{x}_0) - c_2)^2 \frac{b}{b+1} - (f(\mathbf{x}_0) - c_1)^2 \frac{a}{a-1} + 4\alpha\widetilde{\phi}(\mathbf{x}_0). \square
\end{aligned}
$$

Similarly, we can derive the change of energy when moving a point from B to A. The use of the labeling function does not introduce any change in the way these equations are derived.

The generalization to the multi-phase case, when more than one prior shape is used is straightforward.

CURRICULUM VITAE

A.   BIOSKETCH

Rachid Fahmi
February, 16th, 1971 in Casablanca
American/Moroccan

4109 Stony Ridge Rd. #48
Louisville, Kentucky, 40299 USA
1-502-671-2009 (Home)
1-502-445-3502 (Cell)
1-502-852-6130/2789 (Office)
rachidf@cvip.uofl.edu

B.   RESEARCH INTERESTS

PDE-based Image Analysis, Level Set Methods and Numerical Analysis, Shape Registration, Shape-Based Segmentation, Medeling of Soft Tissue Deformation using *F.E.M.*, Neuroimaging Study of Dyslexia and Autism.

C.   EDUCATION

ECE-University of Louisville, Louisville, Kentucky USA

Ph.D., Electrical & Computer Engineering, May 2008

- Dissertation Title: "Variational Methods For Shape and Image Registration"
- GPA: 3.89
- Advisor: Prof. Aly A. Farag

LPMM-University of Metz, Metz, France

Ph.D., Applied Mathematics (option: Mechanical Engineering), $11/1998$

- Dissertation Topic: "Mathematical and Numerical Study of Vibration of Cyclic or Partially Cyclic Structures."
- Advisor: Prof. Michel Potier-Ferry.
- Graduated with distinction: "***Très Honorable***".

LMMAS-University of Metz, Metz, France

M.Sc., Applied Mathematics, 08/1994
- Dissertation Topic: "Shear Thermo-viscoplastic Instability"
- Advisor: Prof. Michel Chipot

Hassan II University, Casablanca, Morocco

B.Sc., Applied Mathematics, 06/1993
- Very Good With Honor.
- Grade: Distinction.

D. SOME TRAINING, RESEARCH AND WORK EXPERIENCE

- **Internship at Siemens Medical Solutions, Inc., Malvern, PA,** June'07 to Sep'07:
  Worked with Siemens staff scientists and other interns to develop a generic image segmentation technique for medical images.
  Also, worked and developed a new semi-automatic technique for segmentation of tubular-like structures. This work resulted on the acceptance of a paper at the SPIE'08 conference, and the filing of an invention disclosure with Siemens Medical Solutions, Inc,.

- **Attended the UCLA Advanced Neuroimaging Summer School (Admission Rate** $< 20\%$**)** August 13-24, 2007 at UCLA:
  This two-week summer course offered lectures from both UCLA faculty and a distinguished international group of lecturers, covering all aspects of neuroimaging data acquisition, experimental design, and data analysis, as well as hands-on laboratory exercises with advanced topics in functional and structural neuroimaging.

E. JOURNAL PUBLICATIONS

❑ Manuel F. Casanova, Aly Farag, Ayman EL-Baz, Meghan Mott, Hossam Hassan, **Rachid Fahmi**, Andrew E. Switala, "Abnormalities of the Gyral Window in Autism: A Macroscopic Correlate to a Putative Minicolumnopathy". *Journal of Special Education and Rehabilitation 2006, 1-2: pp. 85-101*.

❑ Hongjian Shi, Aly Farag, **Rachid Fahmi**, Dongqing Chen, "Validation of Finite Element Models using Micro-CT". *IEEE Transaction on Biomedical Engineering 2007, Vol 55-3: pp. 978-994*.

❑ Manuel F. Casanova, Ayman EL-Baz, Meghan Mott, Mannheim Glenn, Hossam Hassan, **Rachid Fahmi**, Jay Giedd , Judith Rumsey, Andrew Switala, Aly Farag, "Reduced Gyral

Window and Corpus Callosum Size in Autism: Possible Macroscopic Correlates of a Minicolumnopathy". *Submitted to BRAIN, Manuscript ID: BRAIN-2007-00744.*

F. CONFERENCE PUBLICATIONS

❑ **Rachid Fahmi** and Michel Potier-Ferry, "The Group Representation Theory and Vibration of Cyclic Structures", *Pitman Research Notes in Math. Series, Progress in Partial Differential Equations, Vol1, pp. 88-98, 1997.*

❑ **Rachid Fahmi** and Michel Potier-Ferry, "The Group Representation Theory and Vibration of Cyclic Structures", *The Tenth Int. Conf. on Domain Decomposition Methods, Boulder, CO, USA, August 1997.* **Oral Presentation**.

❑ **Rachid Fahmi** and Michel Potier-Ferry, "Cyclic Symmetry, Groups and Eigenvalue Problems", *The Third European Conf. on Elliptic and Parabolic Problems, Pont-À-Mousson, France, June 1997.* **Oral Presentation**.

❑ Hongjian Shi and **Rachid Fahmi**, "Energy Minimization within the F.E. Framework to Predict Liver Tissue Deformation", *Proc. of Int. Conf. Graphics, Vision and Image Processing, **GVIP'05***, Cairo, Egypt.

❑ Noha El-Zehiry and **Rachid Fahmi**, "Level Set Methods in Medical Imaging: An Overview", *Proc. of Int. Conf. Graphics, Vision and Image Processing, **GVIP'05***, Cairo, Egypt.

❑ Hongjian Shi, **Rachid Fahmi**, and Aly A. Farag, "Validation Framework of the Finite Element Modeling of Liver Tissue", *Proc. Of 8th International Conference on Medical Image Computing and Computer-Assisted Intervention - **MICCAI'05***, Palm Springs, CA, USA.

❑ Ayman El-Baz, Aly Farag, **Rachid Fahmi**, Seniha Yuksel, Mohamed A. El-Ghar, and Tarek Eldiasty "Image Analysis of Renal DCE-MRI for the Detection of Acute Renal Rejection", *Proc. of The 18th IEEE Int. Conf.on Pattern Recognition **(ICPR'06)**.*

❑ **Rachid Fahmi**, Alaa Aly, Ayman Elbaz, and Aly A. Farag, "New Deformable Registration Technique Using Scale Space and Curve Evolution Theory and a Finite Element Based Validation Framework", *Proc. of the 28th IEEE EMBS Annual International Conference*, New York City, USA, Aug 30-Sept 3, 2006.

❑ Ayman El-Baz, **Rachid Fahmi**, Seniha Yuksel, Aly A. Farag, William Miller, Mohamed A. El-Ghar, and Tarek Eldiasty, "A New CAD System for the Evaluation of Kidney Diseases Using DCE-MRI", *Proc. Of 9th International Conference on Medical Image Computing and Computer-Assisted Intervention - **MICCAI'06***, Denmark.

❑ **Rachid Fahmi** , Ayman S. El-Baz, Hossam E Abd El Munim, Aly A. Farag, and Manuel F. Casanova, "Classification Techniques for Autistic vs. Typically developing Brain using MRI data", *IEEE Int. Symposium on Biomedical Imaging: from Nano to Macro, **ISBI'07***. **Oral Presentation**.

❏ **Rachid Fahmi** and Aly A. Farag,"A Global-to-Local 2D Shape Registration in Implicit Spaces Using Level Sets", *IEEE Int. Conf. on Image Processing, ICIP'07*.

❏ **Rachid Fahmi**, Ayman S. El-Baz, Hossam E Abd El Munim, Aly A. Farag, and Manuel F. Casanova, "Structural MRI-based discrimination between autistic and typically developing brain". *Computer Assisted Radiology and Surgery, CARS'07*. **Oral Presentation**

❏ **Rachid Fahmi**, Anna Jerebko, Matthias Wolf, and Aly A. Farag, "Robust segmentation of tubular structures in medical images." *Accepted at SPIE Symposium on Medical Imaging 2008, San Diego, CA*.

❏ **Rachid Fahmi**, Aly A. Farag, and Manuel F. Casanova, "A new approach for automatic classification of dyslexic brain based on 3D elastic registration." Accepted at the 22nd International conference on Computer Assisted Radiology and Surgery (**CARS'08**).

❏ **Rachid Fahmi** and Aly A. Farag "A New Variational Approach for Global-to-Local Shape Registration", *Submitted to ECCV'08*.

❏ **Rachid Fahmi** and Aly A. Farag "A Fast Level Set Algorithm for Shape-Based Segmentation With Multiple Selective Priors", *accepted at ICIP'08*.

G. BOOK CHAPTERS

❏ Aly A. Farag, Hongjian Shi, **Rachid Fahmi**, and Michael J. Voor, "Basic Experiments and Finite Element Analysis of Soft Tissues", *In Biomechanics Applied to Computer Assisted Surgery, 2005. Editor: Yohan Payan*.

❏ **Rachid Fahmi**, Ayman S. El-Baz, Hossam E Abd El Munim, Alaa E. Abdel-Hakim, Aly A. Farag, and Manuel F. Casanova, "Robust Neuroimaging-Based Classification Techniques of Autistic vs. Typically Developing Brain", *In Parametric and Geometric Deformable Models: An Application in Biomaterials and Medical Imagery. Editors: J. S. Suri and Aly A. Farag. Springer, May 2007*.

❏ H. Abdel El Munim, **Rachid Fahmi**, N. Youssry El-Zehiry, and Aly A. Farag, "Volumetric MRI Analysis of Dyslexic Subjects Using A Level Set Framework", *In Parametric and Geometric Deformable Models: An Application in Biomaterials and Medical Imagery. Editors: J. S. Suri and Aly A. Farag. Springer, May 2007*.

H. LANGUAGES

Fluent in **English, French and Arabic**

I. TEACHING EXPERIENCE

● **University of Metz, Metz, France**
- Lecturer Assistant   **1996 - 1998**
Taught the following M.Sc. classes: Numerical Analysis and Finite Element Methods.

- **Jefferson Community College, Louisville, KY, USA**
  - *Adjunct Faculty in The Math Department*   **Summer-Fall, 2003**.
- **French Alliance of Louisville, Louisville, KY, USA**
  - *French and Math Instructor*   **Spring-Summer 2003**

J.   REVIEWER

- MICCAI
- IEEE EMBC

K.   MEMBERSHIP

- IEEE member since 2003.

L.   COMPUTER SKILLS

- Software Languages: Fortran, C, C++.
- Visualization Libraries: The visualization toolkit (VTK) and OpenGL.
- GUI Libraries: Microsoft Visual C++ and QT (trolltech).
- Non-GUI Libraries: Standard Template Library (STL) and Message Passing Interface (MPI).
- Operating Systems: Unix (SGI-IRIX 6.4), Linux, and Windows.
- Desktop Applications: Matlab, Adobe Photoshop, and FrontPage.